

UNIVERSITY OF HULL

DOCTORAL THESIS

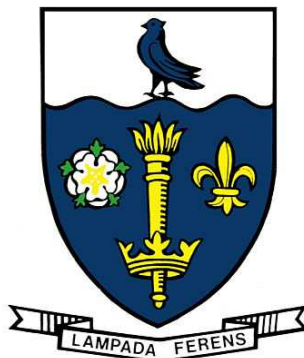
**Nucleosynthesis in Type Ia
Supernovae**

Author:

James Douglas KEEGANS

Supervisor:

Dr. Marco PIGNATARI



*A thesis submitted in fulfillment of the requirements
for the degree of Doctor of Philosophy*

in the

E. A. Milne Center for Astrophysics
School of Mathematics and Physical Sciences

April 13, 2022

Declaration of Authorship

I, James Douglas KEEGANS, declare that this thesis titled, “Nucleosynthesis in Type Ia Supernovae” and the work presented in it are my own. I confirm that:

- This work was done wholly or mainly while in candidature for a research degree at this University.
- Where any part of this thesis has previously been submitted for a degree or any other qualification at this University or any other institution, this has been clearly stated.
- Where I have consulted the published work of others, this is always clearly attributed.
- Where I have quoted from the work of others, the source is always given. With the exception of such quotations, this thesis is entirely my own work.
- I have acknowledged all main sources of help.
- Where the thesis is based on work done by myself jointly with others, I have made clear exactly what was done by others and what I have contributed myself.

Signed:

Date:

“So much universe, and so little time.”

Terry Pratchett, *The Last Hero*

UNIVERSITY OF HULL

Abstract

Faculty of Science and Engineering
School of Mathematics and Physical Sciences

Doctor of Philosophy

Nucleosynthesis in Type Ia Supernovae

by James Douglas KEEGANS

This thesis presents the post-processed isotopic yields from 39 SNIa models with masses of 1.4, 1.0 and 0.8 M_{\odot} and metallicities ranging from a ^{22}Ne mass fraction of 0 to 0.1. In chapter 3 the full yields are presented, along with a description of the major production sites of relevant isotopes and a discussion of the metallicity dependency of the yields. We discuss, in detail, the production site of each isotope and its significance in relation to GCE.

In chapter 4 we compare our post processed results with source models and with the literature to verify our yields.

In chapter 5, potential isotopic diagnostics of progenitor WD masses are identified from the post-processed results. We find that there are isotopic tracers which distinguish the Chandresakar and sub-Chandresakar mass models, and that if these ratios are able to be investigated, either in the bulk solar material or through isotopic grain data, then the progenitors of SNIa, or the relative ratios of sub- to Chandresakar mass WD progenitors, may be determined through this method with further galactic chemical evolution modeling.

Acknowledgements

Perhaps the most difficult section of this thesis to write is this one. Naturally, when these are written, the list of people to thank is enormous, and inevitably names are misplaced. I can only apologise to my friends and colleagues if your name is omitted, as each of you has helped in some way - tangible or otherwise. First, however, is my most important acknowledgment.

In November 2019, my mother passed away from complications following surgery. It is my enduring regret that she will never see this thesis. She would have been beyond proud to see it complete, and a significant driving force in my efforts to finish is rooted in my wish that she should have seen this for herself. This thesis stands, in part, as a memorial to her tireless support.

I would like to thank my supervisor, Marco, for his patience, his expertise, and his humour over the last 4-and-something years of work. I would also like to thank Richard Stancliffe, for very much the same things. Thanks to Brad Gibson, for advice both scientific and otherwise. Thanks to Gareth Few, particularly for his help when I was a clueless 1st year, and then as I was a clueless 2nd, 3rd and 4th year. Almost everyone in the Milne Center should be acknowledged here, students and staff. Please forgive me if you've been skimmed over here.

I would like to thank my colleagues in the NuGrid collaboration, particularly Sam Jones who wrote the code and supported me with an extraordinary patience. Thanks, too, to Dean Townsley, Broxton Miles and Ken Shen for the use of their data and their correspondence, without which I would not have been able to complete anything.

My thanks to my examiners, Stewart Sim and David Benoit. For their feedback which has improved this manuscript greatly, and for their tenacity

x

in reading particularly chapter three.

My special thanks to Katherine Wilson, the only non-specialist who will ever have to endure this, for proofreading and laughing at my terrible spelling.

Contents

Declaration of Authorship	iii
Abstract	vii
Acknowledgements	ix
1 An Overview of Type Ia Supernovae	1
1.1 What are Supernovae?	1
1.1.1 Types of Supernovae	2
Double Degenerate Scenario	11
Core Degenerate Mechanism	11
WD WD Collision	12
1.1.2 Modeling the Explosion	13
1.1.3 Chandrasekhar Mass Deflagration Detonation	13
1.1.4 Sub-Chandrasekhar Mass C/O Detonation	16
1.1.5 Miles	18
1.2 Nucleosynthesis in SNIa	18
1.3 Reference Yields	20
1.3.1 W7	20
1.3.2 Seitenzahl 2013	21
1.3.3 Sim 2010	21
1.3.4 Gronow 2020	22
1.4 Galactic Chemical Evolution	22
1.5 Review of Models	24

1.6	Determination of Abundances	27
1.6.1	Stellar Spectroscopy	28
1.6.2	Mass Spectrometry	28
1.6.3	Gamma Ray Spectroscopy	29
1.7	Aims of This Thesis	30
2	Post Processing and Model Description	31
2.1	Tppnp - Parallelised Post-Processing	31
2.2	Solving The Network	33
2.3	Nuclear Networks	37
2.4	Initial Abundances	40
3	Results of SNIa Post-Processing	43
3.1	Selected Tables of Data	43
3.2	Yields Analysis By Element	54
3.2.1	Oxygen	54
3.2.2	Neon	61
3.2.3	Magnesium	67
3.2.4	Aluminium	74
3.2.5	Silicon	78
3.2.6	Phosphorus	84
3.2.7	Sulphur	87
3.2.8	Chlorine	87
3.2.9	Argon	96
3.2.10	Potassium	102
3.2.11	Calcium	110
3.2.12	Scandium	119
3.2.13	Titanium	122
3.2.14	Vanadium	133
3.2.15	Chromium	138

3.2.16	Manganese	144
3.2.17	Iron	149
3.2.18	Cobalt	160
3.2.19	Nickel	161
3.2.20	Copper	172
3.2.21	Zinc	176
3.2.22	Germanium	182
3.2.23	Selenium	186
3.2.24	All Yields Comparison	188
4	Literature Yields Comparison	191
4.1	Comparison with T1.4Z0.014	191
4.2	Comparison with S1.0Z0.014	197
4.3	M0.8 Comparison	202
4.4	Summary	205
5	Diagnostics of SNIa Nucleosynthesis	207
5.1	Elemental and Isotopic Ratios	207
5.1.1	Three-Element Plots	208
5.1.2	Isotopic Plots	212
5.1.3	Local Isotopic Ratios	215
	^{36}Ar Vs ^{50}Ti	228
5.1.4	Further Isotopic Ratios	232
5.1.5	Summary	232
6	Conclusions	235
6.1	Conclusions	235
6.1.1	Possible Future Work	237
	Appendices	241

A	Decayed Yields	243
B	Rates	247
	Bibliography	249

List of Figures

1.1	Observational classification of supernova transients, with corresponding progenitor.	3
1.2	Evolutionary pathways for SNIa explosions. Main sequence stars are shown in blue, giant and supergiant stars are grey and yellow, common envelope phases are in green, and mass transfer events are in orange-red. Cores of stars and compact remnants are grey, the supernova events are represented by the purple boxes. Adapted from Toloza et al. (2019).	7
2.1	Diagram of the Runge-Kutter integration method. Adapted from Fadlisyah (2014).	36
2.2	A sketch of a representative charged particle capture cross-section. The black line shows an increasing probability of capture with increasing particle energy, the red spikes show sharp increases in capture cross-section due to nuclear resonances.	39
3.1	Production factors for models T1.4Z0 (top), T1.4Z0.014 (middle) and T1.4Z0.1 (bottom).	44
3.2	Production factors for models S1.0Z0 (top), S1.0Z0.014 (middle) and S1.0Z0.1 (bottom).	52
3.3	Production factors for models M0.8Z0 (top), M0.8Z0.014 (middle) and M0.8Z0.1 (bottom).	53

- 3.4 The ejected mass for the element O and its stable isotopes is shown with respect to initial metallicity. The elemental yields take into account radiogenic contributions. For isotopes, decayed and undecayed abundances are shown (continuous lines with crosses and dot-dashed lines with empty circles, respectively). Data is presented for the T1.4 (upper panel), S1.0 (middle panel) and M0.8 (lower panel). 55
- 3.5 Top panels: The ^{16}O abundance is shown with respect to the explosion temperature peak (continuous black line) for the models T1.4Z0 (left), T1.4Z0.014 (middle) and T1.4Z0.1 (right) at $Z=0$, $Z=0.014$ and $Z=0.1$, respectively. ^{16}O abundances are shown with contributions from radioactive species, which are negligible in this case. Middle Panels: As for top panels, but for models S1.0Z0, S1.0Z0.014 and S1.0Z0.1, respectively. Bottom Panels: As for top panels, but for models M0.8Z0, M0.8Z0.014 and M0.8Z0.1, respectively. 56
- 3.6 The abundance distributions of ^{17}O are shown, arranged as in figure 3.5. With metallicities of $Z = 0$, 0.014 and 0.1 from left to right, and the three categories of model - T1.4, S1.0 and M0.8 - from top to bottom. 57
- 3.7 The abundance distributions of ^{18}O are shown, arranged as in figure 3.5. With metallicities of $Z = 0$, 0.014 and 0.1 from left to right, and the three categories of model - T1.4, S1.0 and M0.8 - from top to bottom. Radiogenic contributions from ^{18}F are highlighted. 58
- 3.8 As in Figure 3.4 but for ejected mass of Ne, and its stable isotopes ^{20}Ne , ^{21}Ne and ^{22}Ne 62

3.9	The abundance distributions of ^{20}Ne are shown, arranged as in figure 3.5. With metallicities of $Z = 0, 0.014$ and 0.1 from left to right, and the three categories of model - T1.4, S1.0 and M0.8 - from top to bottom.	64
3.10	The abundance distributions of ^{21}Ne are shown, arranged as in figure 3.5. With metallicities of $Z = 0, 0.014$ and 0.1 from left to right, and the three categories of model - T1.4, S1.0 and M0.8 - from top to bottom.	65
3.11	The abundance distributions of ^{22}Ne are shown, arranged as in figure 3.5. With metallicities of $Z = 0, 0.014$ and 0.1 from left to right, and the three categories of model - T1.4, S1.0 and M0.8 - from top to bottom. Radiogenic contributions from ^{22}Na are included.	66
3.12	As in Figure 3.4 but for ejected mass of Mg, and its stable isotopes ^{24}Mg , ^{25}Mg and ^{26}Mg	68
3.13	The abundance distributions of ^{24}Mg are shown, arranged as in figure 3.5. With metallicities of $Z = 0, 0.014$ and 0.1 from left to right, and the three categories of model - T1.4, S1.0 and M0.8 - from top to bottom. Radiogenic contributions from ^{24}Na and ^{24}Ne are shown, which become significant at $Z \geq Z_{\odot}$	70
3.14	The abundance distributions of ^{25}Mg are shown, arranged as in figure 3.5. With metallicities of $Z = 0, 0.014$ and 0.1 from left to right, and the three categories of model - T1.4, S1.0 and M0.8 - from top to bottom.	71
3.15	The abundance distributions of ^{26}Mg are shown, arranged as in figure 3.5. With metallicities of $Z = 0, 0.014$ and 0.1 from left to right, and the three categories of model - T1.4, S1.0 and M0.8 - from top to bottom.	73
3.16	As in Figure 3.4 but for ejected mass of ^{27}Al	75

3.17	The abundance distributions of ^{27}Al are shown, arranged as in figure 3.5. With metallicities of $Z = 0, 0.014$ and 0.1 from left to right, and the three categories of model - T1.4, S1.0 and M0.8 - from top to bottom.	77
3.18	As in Figure 3.4 but for ejected mass of Si, and its stable isotopes ^{28}Si , ^{29}Si and ^{30}Si	79
3.19	The abundance distributions of ^{28}Si are shown, arranged as in figure 3.5. With metallicities of $Z = 0, 0.014$ and 0.1 from left to right, and the three categories of model - T1.4, S1.0 and M0.8 - from top to bottom.	80
3.20	The abundance distributions of ^{29}Si are shown, arranged as in figure 3.5. With metallicities of $Z = 0, 0.014$ and 0.1 from left to right, and the three categories of model - T1.4, S1.0 and M0.8 - from top to bottom.	82
3.21	The abundance distributions of ^{30}Si are shown, arranged as in figure 3.5. With metallicities of $Z = 0, 0.014$ and 0.1 from left to right, and the three categories of model - T1.4, S1.0 and M0.8 - from top to bottom. Note that the contribution from ^{30}P in S1.0Z0 is very nearly 100% of the ejected ^{30}S , and is therefore difficult to observe under the decayed abundance line.	83
3.22	As in Figure 3.4 but for ejected mass of ^{31}P	85
3.23	The abundance distributions of ^{31}P are shown, arranged as in figure 3.5. With metallicities of $Z = 0, 0.014$ and 0.1 from left to right, and the three categories of model - T1.4, S1.0 and M0.8 - from top to bottom.	86
3.24	As in Figure 3.4 but for ejected mass of S, and its stable isotopes ^{32}S , ^{33}S , ^{34}S and ^{36}S	88

3.25	The abundance distributions of ^{32}S are shown, arranged as in figure 3.5. With metallicities of $Z = 0, 0.014$ and 0.1 from left to right, and the three categories of model - T1.4, S1.0 and M0.8 - from top to bottom.	89
3.26	The abundance distributions of ^{33}S are shown, arranged as in figure 3.5. With metallicities of $Z = 0, 0.014$ and 0.1 from left to right, and the three categories of model - T1.4, S1.0 and M0.8 - from top to bottom.	90
3.27	The abundance distributions of ^{34}S are shown, arranged as in figure 3.5. With metallicities of $Z = 0, 0.014$ and 0.1 from left to right, and the three categories of model - T1.4, S1.0 and M0.8 - from top to bottom.	91
3.28	The abundance distributions of ^{36}S are shown, arranged as in figure 3.5. With metallicities of $Z = 0, 0.014$ and 0.1 from left to right, and the three categories of model - T1.4, S1.0 and M0.8 - from top to bottom. There is no production of ^{36}S at $Z = 0$ and so those plots have been omitted.	92
3.29	As in Figure 3.4 but for ejected mass of Cl, and its stable isotopes ^{35}Cl and ^{37}Cl	94
3.30	The abundance distributions of ^{35}Cl are shown, arranged as in figure 3.5. With metallicities of $Z = 0, 0.014$ and 0.1 from left to right, and the three categories of model - T1.4, S1.0 and M0.8 - from top to bottom.	95
3.31	The abundance distributions of ^{37}Cl are shown, arranged as in figure 3.5. With metallicities of $Z = 0, 0.014$ and 0.1 from left to right, and the three categories of model - T1.4, S1.0 and M0.8 - from top to bottom.	97
3.32	As in Figure 3.4 but for ejected mass of Ar, and its stable isotopes ^{36}Ar , ^{38}Ar and ^{40}Ar	98

3.33	The abundance distributions of ^{36}Ar are shown, arranged as in figure 3.5. With metallicities of $Z = 0, 0.014$ and 0.1 from left to right, and the three categories of model - T1.4, S1.0 and M0.8 - from top to bottom.	100
3.34	The abundance distributions of ^{38}Ar are shown, arranged as in figure 3.5. With metallicities of $Z = 0, 0.014$ and 0.1 from left to right, and the three categories of model - T1.4, S1.0 and M0.8 - from top to bottom.	101
3.35	The abundance distributions of ^{40}Ar are shown, arranged as in figure 3.5. With metallicities of $Z = 0, 0.014$ and 0.1 from left to right, and the three categories of model - T1.4, S1.0 and M0.8 - from top to bottom.	103
3.36	As in Figure 3.4 but for ejected mass of K, and its stable isotopes ^{39}K , ^{40}K and ^{41}K	105
3.37	The abundance distributions of ^{39}K are shown, arranged as in figure 3.5. With metallicities of $Z = 0, 0.014$ and 0.1 from left to right, and the three categories of model - T1.4, S1.0 and M0.8 - from top to bottom.	106
3.38	The abundance distributions of ^{40}K are shown, arranged as in figure 3.5. With metallicities of $Z = 0, 0.014$ and 0.1 from left to right, and the three categories of model - T1.4, S1.0 and M0.8 - from top to bottom. There are no data for the $Z = 0$ models, these panels have therefore been omitted.	108
3.39	The abundance distributions of ^{41}K are shown, arranged as in figure 3.5. With metallicities of $Z = 0, 0.014$ and 0.1 from left to right, and the three categories of model - T1.4, S1.0 and M0.8 - from top to bottom. Radiogenic contributions from ^{41}Ca account for nearly 100% of production at low metallicities, and is therefore obscured by the decayed abundance line.	109

3.40	As in Figure 3.4 but for ejected mass of Ca, and its stable isotopes ^{40}Ca , ^{42}Ca , ^{43}Ca and ^{44}Ca	111
3.41	The abundance distributions of ^{40}Ca are shown, arranged as in figure 3.5. With metallicities of $Z = 0, 0.014$ and 0.1 from left to right, and the three categories of model - T1.4, S1.0 and M0.8 - from top to bottom.	113
3.42	The abundance distributions of ^{42}Ca are shown, arranged as in figure 3.5. With metallicities of $Z = 0, 0.014$ and 0.1 from left to right, and the three categories of model - T1.4, S1.0 and M0.8 - from top to bottom.	114
3.43	The abundance distributions of ^{43}Ca are shown, arranged as in figure 3.5. With metallicities of $Z = 0, 0.014$ and 0.1 from left to right, and the three categories of model - T1.4, S1.0 and M0.8 - from top to bottom.	116
3.44	The abundance distributions of ^{44}Ca are shown, arranged as in figure 3.5. With metallicities of $Z = 0, 0.014$ and 0.1 from left to right, and the three categories of model - T1.4, S1.0 and M0.8 - from top to bottom.	118
3.45	As in Figure 3.4 but for ejected mass of ^{45}Sc	120
3.46	The abundance distributions of ^{45}Sc are shown, arranged as in figure 3.5. With metallicities of $Z = 0, 0.014$ and 0.1 from left to right, and the three categories of model - T1.4, S1.0 and M0.8 - from top to bottom.	121
3.47	As in Figure 3.4 but for ejected mass of Ti, and its stable isotopes ^{46}Ti , ^{47}Ti , ^{48}Ti , ^{49}Ti and ^{50}Ti	123
3.48	The abundance distributions of ^{46}Ti are shown, arranged as in figure 3.5. With metallicities of $Z = 0, 0.014$ and 0.1 from left to right, and the three categories of model - T1.4, S1.0 and M0.8 - from top to bottom.	125

3.49	The abundance distributions of ^{47}Ti are shown, arranged as in figure 3.5. With metallicities of $Z = 0, 0.014$ and 0.1 from left to right, and the three categories of model - T1.4, S1.0 and M0.8 - from top to bottom.	126
3.50	The abundance distributions of ^{48}Ti are shown, arranged as in figure 3.5. With metallicities of $Z = 0, 0.014$ and 0.1 from left to right, and the three categories of model - T1.4, S1.0 and M0.8 - from top to bottom.	128
3.51	The abundance distributions of ^{49}Ti are shown, arranged as in figure 3.5. With metallicities of $Z = 0, 0.014$ and 0.1 from left to right, and the three categories of model - T1.4, S1.0 and M0.8 - from top to bottom.	130
3.52	The abundance distributions of ^{50}Ti are shown, arranged as in figure 3.5. With metallicities of $Z = 0, 0.014$ and 0.1 from left to right, and the three categories of model - T1.4, S1.0 and M0.8 - from top to bottom.	132
3.53	As in Figure 3.4 but for ejected mass of V, and its stable isotopes ^{50}V and ^{51}V	134
3.54	The abundance distributions of ^{50}V are shown, arranged as in figure 3.5. With metallicities of $Z = 0, 0.014$ and 0.1 from left to right, and the three categories of model - T1.4, S1.0 and M0.8 - from top to bottom.	135
3.55	The abundance distributions of ^{51}V are shown, arranged as in figure 3.5. With metallicities of $Z = 0, 0.014$ and 0.1 from left to right, and the three categories of model - T1.4, S1.0 and M0.8 - from top to bottom.	137
3.56	As in Figure 3.4 but for ejected mass of Cr, and its stable isotopes ^{50}Cr , ^{52}Cr , ^{53}Cr and ^{54}Cr	139

3.57	The abundance distributions of ^{50}Cr are shown, arranged as in figure 3.5. With metallicities of $Z = 0, 0.014$ and 0.1 from left to right, and the three categories of model - T1.4, S1.0 and M0.8 - from top to bottom.	141
3.58	The abundance distributions of ^{52}Cr are shown, arranged as in figure 3.5. With metallicities of $Z = 0, 0.014$ and 0.1 from left to right, and the three categories of model - T1.4, S1.0 and M0.8 - from top to bottom.	142
3.59	The abundance distributions of ^{53}Cr are shown, arranged as in figure 3.5. With metallicities of $Z = 0, 0.014$ and 0.1 from left to right, and the three categories of model - T1.4, S1.0 and M0.8 - from top to bottom.	143
3.60	The abundance distributions of ^{54}Cr are shown, arranged as in figure 3.5. With metallicities of $Z = 0, 0.014$ and 0.1 from left to right, and the three categories of model - T1.4, S1.0 and M0.8 - from top to bottom.	145
3.61	As in Figure 3.4 but for ejected mass of ^{55}Mn	146
3.62	The abundance distributions of ^{55}Mn are shown, arranged as in figure 3.5. With metallicities of $Z = 0, 0.014$ and 0.1 from left to right, and the three categories of model - T1.4, S1.0 and M0.8 - from top to bottom.	148
3.63	As in Figure 3.4 but for ejected mass of Fe, and its stable isotopes ^{54}Fe , ^{56}Fe , ^{57}Fe and ^{58}Fe	150
3.64	The abundance distributions of ^{54}Fe are shown, arranged as in figure 3.5. With metallicities of $Z = 0, 0.014$ and 0.1 from left to right, and the three categories of model - T1.4, S1.0 and M0.8 - from top to bottom.	152

3.65	The abundance distributions of ^{56}Fe are shown, arranged as in figure 3.5. With metallicities of $Z = 0, 0.014$ and 0.1 from left to right, and the three categories of model - T1.4, S1.0 and M0.8 - from top to bottom.	153
3.66	The abundance distributions of ^{57}Fe are shown, arranged as in figure 3.5. With metallicities of $Z = 0, 0.014$ and 0.1 from left to right, and the three categories of model - T1.4, S1.0 and M0.8 - from top to bottom.	155
3.67	The abundance distributions of ^{58}Fe are shown, arranged as in figure 3.5. With metallicities of $Z = 0, 0.014$ and 0.1 from left to right, and the three categories of model - T1.4, S1.0 and M0.8 - from top to bottom.	156
3.68	Ejected mass of ^{56}Ni as a function of initial metallicity.	157
3.69	As in Figure 3.4 but for ejected mass of ^{59}Co	158
3.70	The abundance distributions of ^{59}Co are shown, arranged as in figure 3.5. With metallicities of $Z = 0, 0.014$ and 0.1 from left to right, and the three categories of model - T1.4, S1.0 and M0.8 - from top to bottom.	159
3.71	As in Figure 3.4 but for ejected mass of Ni, and its stable isotopes ^{58}Ni , ^{60}Ni , ^{61}Ni , ^{62}Ni and ^{64}Ni	162
3.72	The abundance distributions of ^{58}Ni are shown, arranged as in figure 3.5. With metallicities of $Z = 0, 0.014$ and 0.1 from left to right, and the three categories of model - T1.4, S1.0 and M0.8 - from top to bottom.	164
3.73	The abundance distributions of ^{60}Ni are shown, arranged as in figure 3.5. With metallicities of $Z = 0, 0.014$ and 0.1 from left to right, and the three categories of model - T1.4, S1.0 and M0.8 - from top to bottom.	165

- 3.74 The abundance distributions of ^{61}Ni are shown, arranged as in figure 3.5. With metallicities of $Z = 0, 0.014$ and 0.1 from left to right, and the three categories of model - T1.4, S1.0 and M0.8 - from top to bottom. 168
- 3.75 The abundance distributions of ^{62}Ni are shown, arranged as in figure 3.5. With metallicities of $Z = 0, 0.014$ and 0.1 from left to right, and the three categories of model - T1.4, S1.0 and M0.8 - from top to bottom. Model M0.8Z0 produces no ^{62}Ni , and so the subplot for this model is omitted. 169
- 3.76 The abundance distributions of ^{64}Ni . Only models T1.4Z0, T1.4Z0.014 and T1.4Z0.1 produce ^{64}Ni . Only the T1.4 models show production of ^{64}Ni , as such the other models have been omitted. 171
- 3.77 As in Figure 3.4 but for ejected mass of Cu, and its stable isotopes ^{63}Cu and ^{65}Cu . The M0.8 models are excluded as copper is not produced efficiently in these low. 172
- 3.78 The abundance distributions of ^{63}Cu are shown, arranged as in figure 3.5. With metallicities of $Z = 0, 0.014$ and 0.1 from left to right, and the three categories of model - T1.4, S1.0 and M0.8 - from top to bottom. The models M0.8Z0 and M0.8Z0.014 do not produce ^{63}Cu and are therefore omitted. 174
- 3.79 The abundance distributions of ^{65}Cu are shown, arranged as in figure 3.5. With metallicities of $Z = 0, 0.014$ and 0.1 from left to right, and the three categories of model - T1.4, S1.0 and M0.8 - from top to bottom. There is no production of ^{65}Cu in the M0.8 models, these are therefore omitted. 175
- 3.80 As in Figure 3.4 but for ejected mass of Zn, and its stable isotopes ^{64}Zn , ^{66}Zn , ^{67}Zn and ^{68}Zn . There is no production of zinc in the M0.8 models and therefore the plot is omitted. 177

- 3.81 The abundance distributions of ^{64}Zn are shown, arranged as in figure 3.5. With metallicities of $Z = 0, 0.014$ and 0.1 from left to right, and the three categories of model - T1.4, S1.0 and M0.8 - from top to bottom. from the M0.8 models, only M0.8Z0.1 has even a trace production of ^{64}Zn . Because of this, we omitted the M0.8 plots at lower metallicities. 179
- 3.82 The abundance distributions of ^{66}Zn are shown, arranged as in figure 3.5. With metallicities of $Z = 0, 0.014$ and 0.1 from left to right, and the three categories of model - T1.4, S1.0 and M0.8 - from top to bottom. M0.8 models do not produce ^{66}Zn and are therefore omitted. 180
- 3.83 The abundance distributions of ^{67}Zn are shown, arranged as in figure 3.5. With metallicities of $Z = 0, 0.014$ and 0.1 from left to right, and the three categories of model - T1.4, S1.0 and M0.8 - from top to bottom. The M0.8 models do not produce ^{67}Zn and are therefore omitted. 181
- 3.84 The abundance distributions of ^{68}Zn are shown, arranged as in figure 3.5. With metallicities of $Z = 0, 0.014$ and 0.1 from left to right, and the three categories of model - T1.4, S1.0 and M0.8 - from top to bottom. The M0.8 models do not produce ^{67}Zn and are therefore omitted. 183
- 3.85 As in Figure 3.4 but for ejected mass of Ge, and its stable isotopes ^{70}Ge and ^{72}Ge . The M0.8 models do not produce Ge and so that figure has been omitted. 184
- 3.86 The abundance distributions of ^{70}Ge are shown, arranged as in figure 3.5. With metallicities of $Z = 0, 0.014$ and 0.1 from left to right, and the three categories of model - T1.4, S1.0 and M0.8 - from top to bottom. 185

3.87	The ejected mass for the element Se and its stable isotopes is shown for the model set T1.4. The elemental yields take into account the radiogenic contribution. For isotopes, decayed and undecayed abundances are shown (continuous lines with crosses and dot-dashed lines with empty circles, respectively). There is no production in either of the other two categories of model.	186
3.88	The abundance distributions of ^{74}Se are shown, arranged as in figure 3.5. With metallicities of $Z = 0, 0.014$ and 0.1 from left to right, and the three categories of model - T1.4, S1.0 and M0.8 - from top to bottom.	187
3.89	This plot shows the ejected mass of each stable isotope for all three models, at all metallicities. Stable isotopes with significant metallicity trends are easily identified.	189
4.1	Decayed isotopic yields from Townsley et al. (2016) are compared with this work (T1.4Z0.02). Townsley et al. (2016) yields are denoted by circle markers.	192
4.2	Published elemental yields of Townsley et al. (2016) (square markers) are compared with T1.4Z0.02 (green circles).	194
4.3	W7 decayed elemental abundances from Nomoto and Leung (2018) represented by the green line with circle markers, compared with T1.4Z0.014 (black line, square markers).	194
4.4	Seitenzahl et al. (2013b) ejected elemental abundances (green circles) compared with T1.4Z0.014 (black squares).	196
4.5	Isotopic yields for models S1.0Z0.014 and Shen et al., 2018 (published and post-processed yields). Published yields are denoted by circle markers, the S1.0Z0.014 by square markers.	198

4.6	(Shen et al., 2018) yields (black squares) compared with S1.0Z0.014 (green circles). Decayed ejected elemental abundances are shown for both models.	199
4.7	Yields S1.0Z0 (black squares) compared with the 0.97 M_{\odot} (green circles) model of Sim et al. (2010).	200
4.8	Shen ejected elemental abundances compared with Leung and Nomoto (2020)	200
4.9	S1.0Z0.0 ejected elemental abundances compared with Gronow et al. (2020) data.	201
4.10	Isotopic abundances of Miles et al. (2019) (circle markers) compared with post-processed model M0.8Z0.014 (squares).	203
4.11	M0.8 ejected elemental abundances compared with this post-processing work.	204
4.12	Our post-processed ejected elemental masses for model M0.8Z0 compared with the 0.81 M_{\odot} model of Sim et al. (2010). Both models have an initial ^{22}Ne mass fraction of 0.	204
5.1	Elemental ratio plot [Si/Fe] and [S/Fe]. The blue circle line corresponds to the T1.4 model, the orange to the S1.0 and the green to the M0.8. Black circles on the datapoints indicated the position of the $Z = 0$ and $Z = 0.014$ to show the metallicity trends within a model. For comparison, the models of Sim et al. (2010) ((purple triangles) and Seitzzahl et al. (2013b) (red triangles). Ratios are shown normalised to the solar values, shown by the large yellow circle.	209
5.2	As figure 5.1, but for the ratios [Ti/Fe] and [Ca/Fe].	210
5.3	As figure 5.1, but for the ratios [Mn/Fe] and [Co/Fe].	211
5.4	Isotopic ratios [$^{29}\text{Si}/^{28}\text{Si}$] with respect to [$^{30}\text{Si}/^{28}\text{Si}$], normalised to solar values.	216

5.5	Local isotopic ratio diagnostic plot for ^{34}S	216
5.6	Local isotopic ratio diagnostic plot for ^{36}S	217
5.7	Local isotopic ratio diagnostic plot for ^{43}Ca	218
5.8	Local isotopic ratio diagnostic plot for ^{44}Ca	218
5.9	Local isotopic ratio diagnostic plot for ^{46}Ca	219
5.10	Local isotopic ratio diagnostic plot for ^{48}Ca	219
5.11	Local isotopic ratio diagnostic plot for ^{47}Ti	220
5.12	Local isotopic ratio diagnostic plot for ^{49}Ti	221
5.13	Local isotopic ratio diagnostic plot for ^{50}Ti	221
5.14	Local isotopic ratio diagnostic plot for ^{53}Cr	223
5.15	Local isotopic ratio diagnostic plot for ^{54}Cr	223
5.16	Local isotopic ratio diagnostic plot for ^{57}Fe	224
5.17	Local isotopic ratio diagnostic plot for ^{58}Fe	225
5.18	Local isotopic ratio diagnostic plot for ^{61}Ni	226
5.19	Local isotopic ratio diagnostic plot for ^{62}Ni	226
5.20	Local isotopic ratio diagnostic plot for ^{64}Ni	227
5.21	Example diagnostic plot showing the large spread in isotopic ratios between T1.4 and S1.0 in both $^{38}\text{Ar}/^{50}\text{Ti}$ and $^{51}\text{V}/^{58}\text{Fe}$	229
5.22	Example diagnostic plot showing the large spread in isotopic ratios between T1.4 and S1.0 in both $^{38}\text{Ar}/^{50}\text{Ti}$ and $^{51}\text{V}/^{58}\text{Fe}$	231
5.23	Example diagnostic plot showing the large spread in isotopic ratios between T1.4 and S1.0 in both $^{38}\text{Ar}/^{50}\text{Ti}$ and $^{51}\text{V}/^{58}\text{Fe}$	231

List of Tables

1.1	Number of particles, maximum peak temperature and number of timesteps for each of the three classes of model investigated in this work. Note that particles are only equally weighted in the M0.8 model.	24
2.1	All of the reactions present in the tppnp code.	35
3.1	Table showing the models presented in this chapter, from lowest metallicity to highest. Initial metallicity is exclusively represented by ^{22}Ne	45
3.2	Production factors for T1.4 from $Z = 0$ to 0.1	46
3.3	Production factors for S1.0 from $Z = 0$ to 0.1	47
3.4	Production factors for M0.8 from $Z = 0$ to 0.1	48
5.1	Table showing largest isotopic ratio shifts with pros and cons of each.	213
A.1	Decayed Post Processed Yields: T1.4	244
A.2	Decayed Post Processed Yields: S1.0	245
A.3	Decayed Post Processed Yields: M0.8	246
B.1	Selection of KADONIS rates comprising of (n,γ)	248

Dedicated To my Mam

Chapter 1

An Overview of Type Ia Supernovae

“How far that little candle throws his beams! So shines a good deed in a naughty world.”

Portia, *The Merchant of Venice*, William Shakespeare

1.1 What are Supernovae?

Transient events in astronomy have been recorded for thousands of years. The first observation of a supernova has been suggested to have occurred at around 4500 BC, in the Kashmir region of India (Joglekar et al., 2011). The brightest stellar object in the night sky in recorded history, SN 1006, was observed around the world. Detailed records of SN 1006 survive to this day (Stephenson, 2010), and serve to illustrate our enduring fascination with transient astronomical events. The invention of the telescope in 1609 revolutionised all astronomy, and over time many extragalactic observations were made of transient stellar events, some of which would out-shine entire galaxies.

Baade and Zwicky (1934) first described the "super-novae", but at this time the nature of these objects was still not known. In addition to this, spectra were poor and scarce. Surveys were undertaken which saw an explosion in the number of recorded SN events and, with this new data, a description of the mechanism of SN explosions began to be formed. Minkowski (1941) first categorised SN events into two types: Type I were a homogeneous group of explosions without hydrogen lines in their spectra; Type II were more diverse and contained H-lines.

In 1961, P. Wild discovered a new type of Supernova, with a spectrum different to the Type I previously observed (Zwicky, 1964). Further work by Zwicky ("*Supernovae.*") proposed Types III, IV and V as possible new supernovae; however, these fell out of favour. The naming convention adopted was SN Ia, Ib after the observations of distinct SN spectra which do not show the SiII $\lambda 6150$ absorption line (Da Silva, 1993). Ic was identified later, with a theoretical description of the origins of Ib and Ic as core collapse supernovae (CCSN) presented in Wheeler and Harkness (1990).

The homogeneity of Type Ia supernovae became a cornerstone of cosmology, following the work of Phillips et al. (1987), which further drove efforts to understand the mechanism by which these dramatic events occur. Not only are SNIa a key tool for cosmological studies, but their effect on galactic dynamics and morphology of the low mass dwarf spheroidals (Cashmore et al., 2017), on enrichment of galaxies and the intergalactic medium, and their being host to some of the most violent and extreme conditions in the Universe, make them an object of intense interest.

1.1.1 Types of Supernovae

Observational classifications of supernova events are shown in figure 1.1. There are two general types of supernova explosions, namely the CCSN and

Supernovae Classifications

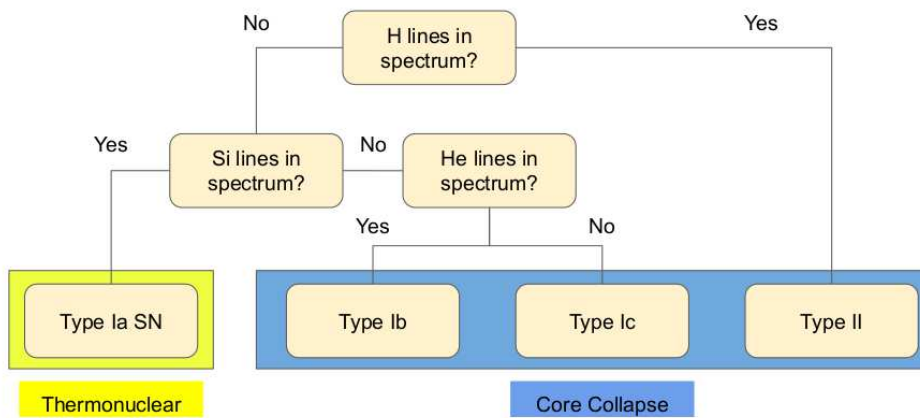


FIGURE 1.1: Observational classification of supernova transients, with corresponding progenitor.

the thermonuclear supernova (SNIa). These categories represent fundamental differences in the explosion mechanisms, with further sub-categories existing within this.

A core collapse supernova occurs when a massive star (more than $8 M_{\odot}$) reaches the end of its life. Burning has proceeded throughout the life of the star, first converting H to He, forming a He core with a H burning envelope enclosing it. This produces energy which prevents the star from collapsing under its own weight. However, once all of the H fuel is consumed, the core begins to contract and collapse. This contraction heats the He ashes which then ignite, burning to carbon. Subsequent burning occurs, producing C, Ne, O and Si shells, with a final inert core of Fe. As Fe-nuclei are some of the most tightly bound, no further energy can be liberated from fusion. This results in a final catastrophic collapse of the star as the weight of the iron core continues to grow from burning in the shells above. Once degeneracy pressure can no longer support the weight of the iron core, it collapses.

Historically, it was believed that the Fe core would reach super-nuclear densities, at which point it rebounds due to the repulsive effect of the strong

force at very small distances. This sends a shock wave back through the imploding core resulting in the ejection of the outer core and envelope of the star. However, this mechanism is no longer considered a good model of the core collapse. Currently, two favoured models describe this explosion - in the case of a 'normal' CCSN kinetic energies close to the binding energy of the material are believed to originate from neutrino driven explosions, much more energetic explosions are likely to be driven by magnetorotational explosions (Janka et al., 2007; Janka, 2012). Other explosion mechanisms are described in the literature, however we will not discuss these here. A neutron star or black hole remnant can remain - dependent on the core mass - or complete disruption of the star can occur as in the case of pair-instability supernovae, in stars with masses of around $150 M_{\odot}$ (see for example Fryer, Woosley, and Heger, 2001; Heger et al., 2003).

Type Ia supernova originate from lower mass stars which end their lives as C/O white dwarfs. In isolation these white dwarfs are unconditionally stable on time scales much longer than the age of the Universe. SNIa explosions therefore occur in binary systems, where a transfer of mass from the companion star to the primary star causes an explosion in the C/O WD. The exact mechanism by which this occurs is currently not well known, and may vary between different SNIa events.

Binary star systems have been known to exist for over 250 years with the first statistical analysis by Mitchell in 1767 (Kratter, 2011). Abt and Levy (1976) found that solar-like stars are distributed with a 42:46:9:2 frequency of single:double:triple:quadruple. More recent work revises this figure, with an average number of companions for solar-like stars being close to 1.4, and the number of stars with a companion being closer to 44% (see Duchêne and Kraus, 2013, and references therein). More than half of stars in the $1.5\text{-}5 M_{\odot}$ mass range are in systems with companions (Duchêne and Kraus, 2013).

Figure 1.2 shows the evolution of a close binary system, adapted from

Toloza et al. (2019). In (i) we begin with a main sequence binary system. Both of the main sequence stars burn hydrogen, until the more massive star exhausts H fuel in its core which then contracts. The outer layers of the star continue to burn hydrogen in a shell, which increases the luminosity of the star and causes it to expand. This leads to stage (ii) where we have a main sequence companion star and a giant or supergiant primary. At this point, if the system is close enough, the expanding hydrogen envelope of the primary engulfs the main sequence companion (iii). This leads to the first common envelope phase. A full description of the physics involved in common envelope evolution is not currently available, and significant uncertainties remain. Merger rates of compact binaries are highly sensitive to modeling parameters, with rates changing by over two orders of magnitude when considering realistic conditions for common envelopes (Aasi et al., 2015; Belczynski et al., 2007). The conditions required to initiate the common envelope phase are not well constrained, the range of systems which transition from Roche lobe overflow to the common envelope are not known (Toloza et al., 2019) and, depending on the treatment of accretion in these systems, it is possible that significant processing of envelope material occurs through accretion onto the compact object (Keegans et al., 2019). The ejection of the envelope is not certain for all systems; the treatment of viscosity and its effect on envelope ejection and a variety of other open questions remain. Despite this, it seems necessary that a common envelope event happen in the evolution of our binary SNIa progenitor.

The envelope of the more evolved star is eventually ejected (iv), which leads to a potential branching point in the evolution of our system. In (c.i) the WD accretes material from its main sequence companion, following Roche lobe overflow. This accretion continues until the Chandrasekhar mass is reached (c.ii, c.iii) during which time the system appears as a super soft x-ray

source (Southwell et al., 1996; Toloza et al., 2019). Upon reaching the Chandrasekhar mass, the WD explodes as a single degenerate SNIa. If the companion star does not undergo Roche-lobe overflow before its giant phase (v), the system will instead undergo a second common envelope phase. There are two possible scenarios if this occurs: the companion star may become a C/O core or He core (a.i). This phase results in a close compact binary of two WDs (a.ii). One may either become disrupted, causing material to be accreted on to the primary (a.iii), or direct merger of the two WDs can occur, in both cases this results in the SNIa explosion. In the event where the companion star is non-degenerate (b.i), the common envelope phase occurs and, after ejection of the envelope, a helium star and a WD remain (b.ii). The companion helium star is accreted onto the compact primary through Roche-lobe overflow and, after reaching the Chandrasekhar mass, explodes in the SNIa event.

The Chandrasekhar mass determines the maximum possible mass that a WD may achieve. This occurs when the WD is supported by relativistic electron degeneracy pressure and for a stellar object is given by the equation:

$$M_{Ch} = 5.836Y_e^2 M_{\odot}, \quad (1.1)$$

Where Y_e is the electron fraction. This gives a value for M_{Ch} of $1.46 M_{\odot}$ for a C/O WD. Above the Chandrasekhar mass, addition of further mass causes the nuclei to undergo electron captures as the Fermi energy of the electrons exceeds the electron capture threshold on the C/O nuclei. This leads to a contraction of the WD, driving further captures. Hydrostatic balance is lost during this process and results in total collapse (Arnett, 1996).

Electron captures on ^{24}Mg leads to an effective reduction in the Chandrasekhar mass, through lowering of the Fermi energy (Nomoto and Kondo, 1991; Hurley, Tout, and Pols, 2002). Whether the system subsequently forms

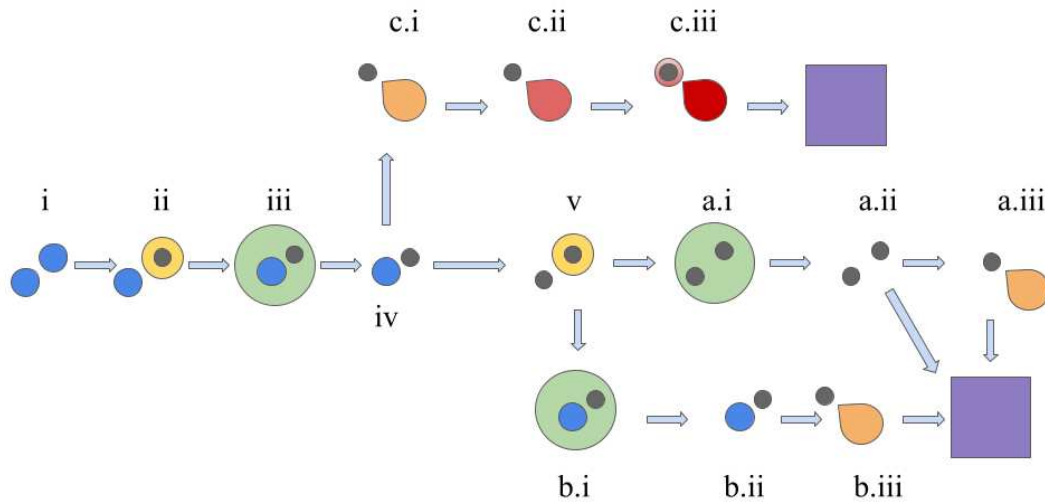


FIGURE 1.2: Evolutionary pathways for SNIa explosions. Main sequence stars are shown in blue, giant and supergiant stars are grey and yellow, common envelope phases are in green, and mass transfer events are in orange-red. Cores of stars and compact remnants are grey, the supernova events are represented by the purple boxes. Adapted from Toloza et al. (2019).

a neutron star or explodes is dependent on the interplay of the electron captures and nuclear burning in the system (Nomoto and Kondo, 1991).

Depending on the evolutionary pathway of the SNIa event, the collapse of the WD may occur through several different mechanisms. For example the primary C/O white dwarf may reach the Chandrasekhar mass which is the critical value (approximately $1.44M_{\odot}$) beyond which the WD can no longer be supported through electron degeneracy pressure. Ignition of the C/O core can be initiated through compressional heating from accreted layers, leading to a deflagration front. This deflagration front becomes a detonation due to turbulent effects (Hillebrandt and Niemeyer, 2000; Khokhlov, 1991) or may lead to a delayed detonation (Arnett and Livne, 1994). Carbon may also be ignited in the core of the WD through a detonation in an accreted helium layer, as well as other formation scenarios discussed in this chapter.

Why must the progenitor of a SNIa explosion be a C/O white dwarf? Helium white dwarfs are formed with initial masses of between ~ 0.5 and

0.2 M_{\odot} (Livio, 2000; Iben Jr and Tutukov, 1985). Ignition occurs centrally in these objects at a mass of 0.7 M_{\odot} resulting in spectra rich in He and Ni decay products and little to no intermediate mass elements (Nomoto and Sugimoto, 1977; Woosley, Taam, and Weaver, 1986). Branch et al. (1995) separate the evolution of progenitors of SNIa into two categories: those models which ignite carbon first during the explosion, and those which ignite helium followed by a carbon ignition. These two pathways correspond to the Chandrasekhar and sub-Chandrasekhar models respectively. They identify seven candidate systems for the carbon igniting Chandrasekhar mass models, and four for the helium igniting sub-Chandrasekhar mass.

The double detonation scenario was not favoured initially, as the expected spectra and lightcurves of these explosion channels were not computed to resemble those of a standard SNIa spectra (Ruiter et al., 2014; Hoefflich et al., 1996). For instance, the peak light of the explosion was predicted to be incorrect (García Senz, Bravo Guil, and Woosley, 1999). By constraining the accreted helium shell to be minimally thick however, Fink et al. (2010) show that this a viable method for initiating the explosion and Kromer et al. (2010) show that with this thin shell the spectra is in good agreement with normal SNIa spectra.

O/Ne white dwarfs are expected to form from main sequence stars at around 10 M_{\odot} (eg. Doherty et al., 2015) making them less numerous than the SNIa progenitors required to match the observed Ia rate (Livio, 2000). It is also likely that these white dwarfs will preferentially form neutron stars through accretion induced collapse, which occurs when the WD exceeds the Chandrasekhar mass.

The delay time distribution (DTD) of the progenitor systems is also an important constraint. Different evolutionary pathways require different timescales to reach SNIa explosion. Greggio (2005) presents a formulation for the DTD of SNIa, and shows that the single degenerate timescale is determined by the

evolutionary lifetime of the companion. Greggio therefore concludes that the total delay time for single degenerate systems is equal to the main sequence lifetime of the companion star, and therefore depends on the mass of the companion. In the double degenerate scenario, the delay time is the sum of the lifetime of the secondary and the time it takes for the two compact objects to coalesce, due to the radiation of gravitational waves. The gravitational wave component depends on the initial separation of the two compact objects and their masses. There is expected to be a wide range of values for the gravitational component, due to the wide possible range of separations and combined binary masses.

The observed rate of SNIa explosions offers a useful constraint on the possible progenitor systems. Maoz and Mannucci (2012) present a review of formation channels and find that the double degenerate channel most closely reproduces the observed delay-time distribution of SNIa events. A short-delay component is suggested for the single degenerate channel, however the double degenerate channel is considered to be the more likely pathway, particularly at longer timescales. Mennekens et al. (2010) also discuss the delay-time distribution of single and double degenerate progenitors of SNIa and find that the single degenerate model cannot reproduce the observed delay-time distribution of SNIa without a contribution from the double degenerate scenario. Population synthesis models can reproduce the observed distribution of SNIa from combinations of WD progenitors and therefore C/O white dwarfs are the only progenitors with the correct statistics and spectral features to match observations of SNIa.

The modeling of the evolution of intermediate mass stars with mass $\lesssim 8 M_{\odot}$ is a complicated and computationally expensive process. Burning in the stellar object continues to core helium burning, much as in the early stage of the massive stars. Karakas and Lattanzio (2014) identify stars with an initial

mass of between approximately 0.8 and 7 M_{\odot} as being capable of producing a C/O white dwarf remnant. Once the hydrogen fuel of these stars is exhausted within the core, the core contracts.

Hydrogen burning continues in a shell around the helium core, while the outer layers of the star expand and cool connectively. First dredge up occurs when the star is no longer able to cool, with the connective envelope extending deeper and mixing with more processed material. At this stage, much of the envelope may be lost to stellar winds due to the very extended nature of the star. During this process, the helium core continues to contract, and cooling becomes dominated by neutrinos in the dense centers of the cores.

Eventually, the necessary temperature for helium ignition is reached (approximately 10^8 K). Ignition occurs at different points in the star depending on the initial mass. We now have a star with a helium burning convective core and a hydrogen burning shell (Arnett, 1996). Helium breathing pulses determine, in part, the mass of the final C/O core, as they mix new unburnt material into the helium core as it is depleted. This new material extends the helium burning phase. However there is no observational data to support the occurrence of these events (Karakas and Lattanzio, 2014). The star now undergoes thermal pulses, described by Schwarzschild and Härm (1965).

At this stage, we are left with a C/O core with thermal pulsing shells above. These pulses do not effect the core, and gradual burning of the He shell decreases the envelope mass and increases the C/O core mass. As this continues, the shells extinguish and a C/O white dwarf remains (Kippenhahn, Weigert, and Weiss, 1990; Shapiro and Teukolsky, 2008).

There are a number of other possible evolutionary pathways after the formation of the white dwarf:

Double Degenerate Scenario

This progenitor model consists of two compact objects merging, whether through tidal interaction causing the WDs to spiral and merge or through three-body interactions. Observational counterparts to double degenerate systems have been identified - see, for example Roelofs et al. (2010). The merger time for a double degenerate scenario also follows the t^{-1} DTD observed in SNIa (Yungelson and Livio, 2000). Difficulties with this model, however, include the relatively high symmetry of SNIa explosions. Bravo, Badenes, and García-Senz (2005) identify a number of features of SNIa observations which suggests that the explosions are largely spherical. calling into question the usefulness of three dimensional models of the explosions. In the DD scenario there are expected to be some significant deviations from this spherical symmetry due to the accretion from the companion star. Because of this and the possibility of accretion induced collapse as an endpoint to evolution, there are open questions as to the validity of the DD scenario as a precursor to SNIa explosions.

Core Degenerate Mechanism

Originally developed to explain the observations of $H\alpha$ emission in SN 2002ic by Livio and Riess (2003), the core degenerate scenario supposes that a degenerate WD spirals inward through the envelope of an AGB star, eventually merging with the AGB core. $H\alpha$ emissions therefore originate in the envelope of the AGB star, which is largely ejected during any potential in-spiral, in agreement with the observations of Hamuy et al. (2003). While this observation and model is successful in describing the spectra of SN 2002ic, the complete absence of H features in other SNIa spectra makes the presence of a large mass of ejected H-material from the AGB companion highly unlikely. Livio and Riess (2003) suggests that in the specific example of SN 2002ic, the

SN explosion happens during the common envelope phase, before ejection of the envelope is complete. If the in-spiral and merger of the C/O remnants is over a long time period, then the ejected envelope could be dispersed; however, this may not be the case and much shorter timescales for the merger of the C/O WDs - on the order of 10^7 yrs as calculated by Meng and Podsiadlowski (2013) - means that H would still be detectable in the spectra. Currently, simulations of this process are not available and therefore predictions of the ejected composition of material are not possible. In addition to this, a number of other difficulties including the theoretical DTD, the final mass of the merged WDs, and the possibility of accretion induced collapse, leave doubts as to the viability of this progenitor system.

WD WD Collision

A possible evolutionary pathway to SNIa explosion involves the head-on collision of two WDs. Kushnir et al. (2013) show that direct collisions of WDs in triple systems give the correct synthesised mass of ^{56}Ni , the correct features of the late-time light curve and the correct distributions of velocities for the ejected ^{56}Ni , independent of the masses of the colliding white dwarfs and without the need for a deflagration to detonation transition. Previous work by Katz and Dong (2012) suggests that the number of colliding WD systems is comparable to the observed rates of SNIa explosions, however this is not supported by other works (e.g. Hamers et al., 2013; Toonen, Perets, and Hamers, 2018) where the rate is much lower. Toonen, Perets, and Hamers (2018) find an expected contribution to SNIa events of around 0.1% from these triple WD systems.

1.1.2 Modeling the Explosion

Hoyle and Fowler (1960) first suggested the detonation of a degenerate carbon core as the mechanism by which SNIa could be produced. Pure proton captures are impossible on the short timescales of the explosion, and proton captures on light nuclei (such as in the CNO cycle) provide insufficient energy generation due to the limited number of proton captures that can occur, even at very high temperatures. Helium burning is likewise slow due to the very low abundances of ^8Be . It is concluded therefore, that in explosive nucleosynthesis, fusion of light nuclei such as ^{12}C is necessary to provide the huge energy output needed for a SN event.

We now move to a description of the three models investigated in this work, which are the $1.4 M_{\odot}$ model of Townsley et al. (2016) (T1.4), the $1.0 M_{\odot}$ model of Shen et al. (2018), and the $0.8 M_{\odot}$ model of Miles et al. (2019).

1.1.3 Chandrasekhar Mass Deflagration Detonation

Accretion onto the WD raises the temperature of the core due to compressional heating, which ignites a slow carbon burning known as the simmering phase, which changes the Y_e of the WD. This nuclear energy generation further increases the core's temperature. As the $(^{12}\text{C}, ^{12}\text{C})$ rate is highly sensitive to the temperature of the system, the energy generation increases until neutrino cooling processes can no longer keep the core in equilibrium. Convective instabilities are then formed, causing the whole of the core of the WD to become convective until even this can no longer keep the reaction rate in check.

When the nuclear burning and convective timescales are approximately the same, a thermonuclear runaway occurs (Iliadis, 2015). Arnett (1996) describes the effect of degeneracy pressure in this event, which drives the detonation. Without degenerate matter, the star would simply expand during

the deflagration stage, allowing it to cool. As the material is degenerate, this cannot occur and the temperature continues to increase until the runaway (^{12}C , ^{12}C) reactions occur. During the detonation, it is the passage of the shock, compressing unburnt fuel, which drives the further reactions which power the shockwave. A pure detonation or shock is insufficient to reproduce the observed SNIa abundances. This transition from deflagration to detonation is therefore a crucial consideration of the nucleosynthesis and dynamics of any SNIa model.

The first description of the deflagration-detonation model was presented in Khokhlov (1991). Townsley et al. (2016) presents a deflagration-detonation model adapted from the earlier Calder et al. (2007), with improved treatments of the flame fronts which remain unresolved in hydrodynamical modeling. Pure detonation models convert the whole C/O WD into iron peak elements (Arnett, 1969), giving a good match to abundance patterns for iron group elements but severe under-production of intermediate mass elements ($6 \leq Z \leq 21$), resulting in yields incompatible with galactic chemical evolution models (Arnett, Truran, and Woosley, 1971). The detonation is a supersonic burning front which propagates through the WD (Townsley et al., 2016; Khokhlov, 1989), caused by a shock-wave moving through the C/O fuel. A deflagration is a subsonic burning front which propagates through the C/O fuel through conduction (Timmes and Woosley, 1992; Townsley et al., 2016).

The deflagration produces more intermediate mass elements due to the expansion of the fuel and subsequent lowering of density. The iron group distribution of the burning products in this scenario is significantly different to the observed Solar System abundances. Khokhlov (1991) suggests a regime whereby the explosion begins as a deflagration front in the WD and then evolves to a detonation due to sub-grid effects in the turbulent flame front of the deflagration, which are unresolved in current models. In deflagration fronts in the T1.4 model, the temperature experienced by the tracer

particles is not physical, due to the thickness of the front. Reconstruction is used to give a more physical description of the actual thermodynamic conditions that these particles experience in order to better model the burning processes in the fuel.

Sufficient expansion of the WD material is necessary to produce intermediate mass elements in the outer, less dense regions of the progenitor ($\rho \lesssim 10^7 \text{gcm}^{-3}$), whilst in the more dense inner regions of the WD the Fe-group nucleosynthesis of the detonation model is preserved. Röpke (2007) found that large patches of turbulent flame fronts are viable sites for the transition to a deflagration front, supporting the theory that deflagration to detonation events may occur in SNIa explosions.

Comparison of predicted yields of pure deflagration explosions from three dimensional models with observations has been investigated in Röpke et al. (2007). Despite reproducing the light-curve of typical SNIa closely, there were still found to be discrepancies. The deflagration-detonation model is therefore a strong candidate for the explosion mechanism in SNIa.

Whether an accreting white dwarf is capable of growing to the Chandrasekhar mass is disputed. Hillman et al. (2016) found a broad range of accretion rates for which growth to the Chandrasekhar mass is possible due to heating of the WD core, which results in the partial lifting of degeneracy and subsequent quasi-steady state He burning. However it is not clear that the C/O WD grows in mass during accretion phases.

Livio and Mazzali (2018) highlight the potential diversity of progenitor systems for the single degenerate scenario: the companion star could be any main sequence, giant or AGB star; the progenitor systems could be classical or recurrent novae (along with other possibilities); this leads naturally to a diversity in the explosive conditions in the SNIa, and so a spread in the observed characteristics of the SNIa event, as is observed in Ia lightcurves.

Some observations of early blue excesses in the lightcurves of SNIa (Hosseinzadeh et al., 2017; Marion et al., 2016) support the existence of a non-degenerate companion star. In addition to these, potential observations of circumstellar material around some SNIa further suggest the presence of a non-degenerate companion (Maguire et al., 2013). There are some difficulties, however, to be found within this model. Observations of interactions between the ejected SNIa material and a companion show no signs of optical and UV emission, which should be more luminous than the radioactive decay in the first days of the explosion.

If the WD were to be accreting H from its companion, there should be some evidence of H-lines in the spectra at late times. However, surveys have shown no evidence of hydrogen in SNIa spectra. Botyánszki, Kasen, and Plewa (2017) rule out main-sequence companions due to this lack of H spectra lines. We therefore see a range of issues in the observational evidence for single degenerate SNIa. The theoretical predictions of nucleosynthesis products, however, favour this progenitor model.

Hansen (2003) suggests the companion star in the single degenerate scenario may survive the SNIa event, which affords the opportunity to identify SNIa host systems after the event of an explosion. Observations by Justham et al. (2009) of low mass single white dwarfs with $M < 0.4 M_{\odot}$ suggest that at least some of the observed SNIa explosions originates with a single degenerate scenario.

1.1.4 Sub-Chandrasekhar Mass C/O Detonation

The models of Shen et al. (2018) investigated in this work are of a $1.0 M_{\odot}$ single C/O detonation explosion. The model is the limiting case for a double detonation, whereby the accreted helium layer is argued to be of a very

small mass, and so inconsequential for the burning and nucleosynthesis output. In a standard double detonation scenario, rapid transfer of He from a binary companion initiates a He detonation in the accreted outer layers of the star. This subsequently triggers a second explosion in the C/O core of the white dwarf. In this model, the detonation is triggered only in the C/O core. While this leads to a WD explosion which matches observable reasonably well. Neglecting to include the helium shell ashes in the models can lead to inconsistencies however - Fink et al. (2010) show significant production of some iron group material in the helium ashes such as ^{52}Fe .

Nomoto (1982) identifies a range of accretion rates in the SNIa progenitor system which may give rise to a DD event. For strong helium flashes with accretion rates between 4×10^{-8} and $10^{-9} M_{\odot}\text{yr}^{-1}$. In these models the DD explosion synthesises almost exclusively ^{56}Ni , with only a few thousandths of a solar mass of intermediate mass elements. Further work by Woosley and Weaver (1994) demonstrates that accretion of 0.15-0.2 M_{\odot} of helium is sufficient to cause a DD event to occur. Fink et al. (2010) finds significantly smaller He shell masses are sufficient to ignite the C core - down to $3.5 \times 10^{-3} M_{\odot}$.

Kushnir, Wygoda, and Sharon (2020) find that the amount of synthesised ^{56}Ni differs significantly from observed values for DD models, with the discrepancies in results being larger than the observational uncertainties.

The number of tracer particles for the S1.0 models is much lower than in the T1.4 and M0.8 cases. This is due to the Shen models being one dimensional, as opposed to the two dimensional models in the T1.4 and M0.8 cases. The tracers in this model are therefore points in the one dimensional star, and fewer tracers are needed to have a resolved model. For the purposes of this thesis, the dimensionality of the progenitors is not important as we do not investigate the effect of this on the nucleosynthesis products.

1.1.5 Miles

The detonation of the Miles et al. (2019) model is initiated by inserting a hot spot into the core of the C/O WD, with a temperature of 1.98×10^9 K. This model therefore does not correspond to a particular progenitor system, with only the initial mass of the C/O core and the initial abundances determining the explosion.

The Miles models are very sub luminous due to the small amount of ^{56}Ni produced in the explosion. Because of this, they do not produce lightcurves which would be classified as a normal SNIa. Sub-luminous Type Ia events have been observed - e.g. Höflich et al. (2002), and various explanations for their origin are available in the literature (Howell, 2001; Pakmor et al., 2010). This model may therefore be useful as a test of sub-luminous SNIa, but is not representative of a typical explosion.

1.2 Nucleosynthesis in SNIa

When describing the explosion of the C/O WD, we must first consider the composition. The core of the WD is formed during convective He burning, and the outer layers during shell burning on the AGB (Iliadis, 2015). This composition can be described in terms of ^{12}C , ^{16}O and ^{22}Ne abundances (Timmes, Brown, and Truran, 2003). Domínguez, Höflich, and Straniero (2001) identify that the initial composition of the WD impacts the nucleosynthesis in the outer layers only, as we find in our post-processed models.

Different stages of burning are experienced at different depths in the white dwarf, which correspond to different peak temperatures and densities experienced in these various fluid elements, and which Iliadis (2015) models after the various burning stages in massive stars. In the most extreme central environments, complete silicon burning is experienced, producing a distribution of iron group material which is sensitive to the peak density (due to the effect

on weak reaction rates). This explosive Si-burning occurs at temperatures in excess of 9 GK and as such, the nucleosynthesis observed at the end of the explosion is through recombination of α particles and free neutrons, in either an α -rich or standard freeze-out (these are explained more fully in chapter 2). The central density is therefore a defining characteristic of the eventual ejecta, due to the weak interactions in the very dense core, which alters the electron fraction of the fuel.

Incomplete silicon burning occurs in peak temperature regions of around 5 GK, and explosive oxygen burning accounts for the outer, cooler layers of the WD (Iliadis, 2015). Explosive oxygen burning and incomplete silicon burning produce many α -chain isotopes, along with stable Fe-group nuclei. Incomplete Si burning occurs in quasi statistical equilibrium (QSE) giving two islands of production at intermediate masses and in the Fe-group. The complete conversion of intermediate mass isotopes to Fe-group material is halted by the expansion and cooling of the material as the shock wave passes, causing a freeze-out. Iliadis (2015) therefore notes that the expansion timescales and the initial electron fraction are likely to dictate the relative abundances of Fe-group to intermediate mass elements (IMEs). The explosive oxygen burning follows a similar trend to the incomplete Si burning; however, as the peak temperatures are lower the total amount of material that is processed to the Fe-group is severely reduced. In the outermost layers, explosive Ne-C burning occurs. These burning regimes are discussed in the context of our results in Chapter 3 where they are identified as the hot (complete-Si), intermediate (incomplete-Si and exp-O) and cool components (exp-Ne/C).

1.3 Reference Yields

A selection of SNIa yields available in the literature are used to benchmark our results in Chapter 4. Here we give a brief overview of the various reference models.

1.3.1 W7

Special consideration must be shown for the yields of Nomoto, Thielemann, and Yokoi (1984), which have been updated in Iwamoto et al. (1999) and Nomoto and Leung (2018). These yields have been the benchmark for SNIa yields in GCE and lightcurves for almost 40 years.

The carbon deflagration in the original W7 model is triggered by rapid accretion of material from the companion star, at rates greater than $4 \times 10^{-8} M_{\odot} \text{yr}^{-1}$. The passage of the deflagration wave through the outer material of the W7 model synthesises the intermediate mass elements such as Ca and S, while the ^{56}Ni and ^{56}Co necessary for the observed light curve are synthesised in the inner regions. The WD is completely disrupted in this explosion.

A network of 205 species is used in the original Nomoto, Thielemann, and Yokoi (1984) paper. In Nomoto, Thielemann, and Wheeler (1984) some difficulties with the abundances of some isotopes are discussed, with overproduction of intermediate mass elements evident from the original paper, due to the high central density of the original W7 model. Comparisons with the observations of Anders and Ebihara (1982) were in good agreement with W7 due to the lower central density experienced during the explosion; however, it is mentioned that production of ^{54}Fe is a factor of 4 larger than expected, largely due to excess neutronisation.

The '7' in the W7 models correspond to the value of the mixing length scale to pressure scale height, the W to the white dwarf progenitor (as opposed to the 'C' cases with a stellar core).

1.3.2 Seitenzahl 2013

The models from Seitenzahl et al., 2013b have been used to benchmark against our Chandrasekhar mass models. These models are three dimensional, and vary mostly in the method of ignition. Different models have different numbers and distributions of ignition kernels, ranging from 1 to 1600, with three different central densities for the progenitor WD. They find that the delayed-detonation models all unbind the WD progenitor and produce masses of ^{56}Ni between 0.32 and 1.11 M_{\odot} . The results of this paper support a central ignition with symmetrical distribution of ignition kernels as the closest match to observational data in order to ensure the necessary pre-expansion of the WD progenitor. Due to the computational complexity of the simmering phase the paper presents the ignition conditions of the system as a free parameter and investigates the difference in isotopic yields due to this.

1.3.3 Sim 2010

These models are used to benchmark against our 1.0 M_{\odot} . Good agreement with observations are seen in this paper for WDs with masses between 0.97 and 1.15 M_{\odot} . In these models a WD primary accretes a He envelope from a companion and subsequently detonates, triggering the carbon detonation in the WD. This He shell component is missing from our sub-Chandrasekhar mass models. As we discuss in chapter 4 and 5, inclusion of this accreted helium layer is an important next step in these studies, and is likely to strengthen our results. This paper does not address the method by which the detonation is initiated, only that the C/O WD are ignited centrally with a specific mass. In this way, the paper presents an excellent analogue to the S1.0 models, which also neglect the pathway to explosion.

1.3.4 Gronow 2020

We take our reference for the M0.8 models from Gronow et al. (2020). This paper gain follows burning in the accreted helium shell, capturing the detailed nucleosynthesis there with high resolution hydrodynamical simulations. The explosion mechanism in this case is again a double detonation, in this case it is not treated as a free parameter but arises following the helium detonation. The minimum mass investigated in this paper is $0.91 M_{\odot}$, including the accreted helium layer. This is close to the M0.8 model of our work.

1.4 Galactic Chemical Evolution

Matteucci and Greggio (1986) first investigated the impact of SNIa yields on the solar abundances of 5 key isotopes - ^{12}C , ^{16}O , ^{24}Mg , ^{28}Si and ^{56}Fe . They highlight the importance of the delay time distribution as a diagnostic tool for the differentiation of SNIa progenitors, selecting a supernovae rate from Greggio and Renzini (1983) for the single degenerate scenario, and use the yields of Nomoto, Thielemann, and Yokoi (1984). Given these conditions, they find that SNIa contribute $\sim 70\%$ of solar iron, and that SNIa are necessary to match the observed $[\text{Fe}/\text{H}]$ evolution of the Milky Way. They also find an overproduction of C, Si and Mg. Work by Mannucci et al. (2005) refined the SNIa rate, and demonstrated that this was dependent on morphology and colour of the host galaxy - and therefore the star formation rate. Further work by Mannucci, Della Valle, and Panagia (2006) supports the use of two distinct delay time distributions for SNIa rates - one with a delay time on the order of 3-4 Gy in distant galaxies (with high redshift), and one for local SNIa which retain the dependency on colour and radio luminosity described in other works (Mannucci et al., 2005; Della Valle et al., 2005).

Inclusion of these new rates in Matteucci et al. (2006) lead to the conclusion that $\sim 50\%$ of SNIa progenitors are formed from progenitors with

initial mass $> 5M_{\odot}$ which explode soon after the beginning of star formation (although this may be as low as 35 or 40%). The remaining systems are predicted to originate from lower mass progenitors. The $[O/Fe]$ vs $[Fe/H]$ evolution of this DTD is compared with observations and a decrease in O with respect to $[Fe/H]$ is found.

Matteucci et al. (2009) discuss the effect of varying the progenitor of the SNIa. The effect on the $[O/Fe]$ evolution is negligible between their double or single degenerate models; instead, this is dependent on the percentage of prompt explosions. Here they find $<30\%$ to be the proportion of prompt explosions needed to match observations. These prompt events correspond to the upper limits of the mass range which result in a final C/O WD remnant.

SNIa are known to contribute significantly to the abundances of the iron group elements, along with some α elements (Maiolino and Mannucci, 2019). Their explosions also affect the morphology of low mass host galaxies, along with their enrichment. Cr, Mn, Fe, Ni, Co, Cu and Zn are all identified as being primarily produced from SNIa (Kobayashi, Karakas, and Lugaro, 2020), along with the production of odd-Z elements, dependent on the initial metallicity of the SNIa progenitor. This metallicity dependence is due to the neutron excess of the ^{22}Ne produced during He burning. Kobayashi, Leung, and Nomoto (2020) find that more than 75% of SNIa progenitors should reach the Chandrasekhar mass, while Seitzzahl et al. (2013a) find a value close to 50%.

From the conflicting and sometimes contradictory results in the literature, we can conclude that the proportion of Chandrasekhar mass progenitors of SNIa can not currently be reliably determined, and may lie between 20% and 75%. In this work, we aim to provide a new diagnostic by which this fraction of Chandrasekhar mass progenitors may be determined - namely the isotopic ratio of various products of explosive burning in these events.

SNIa are one of the primary contributing factors of the solar abundances,

Parameter	T1.4	S1.0	M0.8
No. of Particles	7856	107	9996
T_{peak} Max (GK)	10.28	6.32	5.21
No. Timesteps	6872	58738	1347

TABLE 1.1: Number of particles, maximum peak temperature and number of timesteps for each of the three classes of model investigated in this work. Note that particles are only equally weighted in the M0.8 model.

along with CCSN, planetary nebulae and winds from intermediate and low mass stars (Gibson et al., 2003). Understanding their nucleosynthesis is therefore vital to our description of the evolution of the Milky Way. The use of $[O]/[Fe]$ vs $[Fe]/H$ (or indeed any combination of elements relative to H) to describe the chemical evolution of a given galaxy is a common tool (Wyse and Gilmore, 1988). Oxygen and iron are often used due to the ease of observation, although other elements are substituted frequently. The evolution of $[O/Fe]$ with respect to chemical enrichment (where $[Fe]/[H]$ becomes a proxy for evolutionary time) shows a decrease in the $[O/Fe]$ abundance at $[Fe]/[H] \sim 0.1$. This is caused by early contributions from massive stars in the form of CCSN which are rich in α -elements. Although SNIa also contribute to the production of most α -elements, their contribution to iron is larger, and so we see a decrease with respect to time of the $[O/Fe]$ ratio. Similar work to that presented here has recently been carried out using the HESMA models (Lach et al., 2020).

1.5 Review of Models

Table 1.1 shows some of the key parameters of each of the three models investigated in this work; namely the number of tracer particles post processed, the maximum peak temperature of any particle in that set of tracer particles and the number of timesteps in each trajectory. The method by which explosions were initiated in the hydrodynamical modelling is via a hot spot in

all cases. M0.8 has the greatest number of particles, with approximately 10^4 being extracted for the post-processing step. T1.4 has a similar number of particles; S1.0 has only $107 \cdot 10^5$ particles were available for post-processing in the T1.4 models. Convergence studies showed that the total abundances were converged at around 1:10 particles being post-processed. We therefore chose to omit the extra particles. Due to the sparse nature of the S1.0 yields, many of the diagnostic plots presented later in this work appear to have missing data for the S1.0 models, but this is only an artifact of the difference in the density of the data. The large difference in the number of tracer particles between the T1.4 and S1.0 models suggests is mostly due to the reduction to one dimension in the S1.0 case.

Time resolution in the three models varies significantly. The S1.0 model is highly over resolved, with close to 6×10^5 timesteps. This results in the particles taking longer to post-process; however, since convergence of yields with respect to time resolution was not investigated, the trajectories remain as they were when extracted from the hydrodynamical modelling. This is in order to not introduce inconsistencies in the yields with respect to those published for S1.0. The number of timesteps for the M0.8 and T1.4 models is comparable at around 10^3 per trajectory, and each particle completed post-processing in approximately 30 minutes.

For the T1.4 model, resolution in the hotter parts of the explosion is very high; however, the resolution in the outer layers of the WD is not as high as that found in Travaglio et al. (2004). There may therefore be some loss of accuracy in the outer layers, where the dominant contribution to the yields of the intermediate mass elements is. In the models of Townsley et al. (2016), based on the earlier work Calder et al. (2007) and Townsley et al. (2007), the explosion in the WD progenitor is initiated through the introduction of an artificial hot spot at a predetermined radius. This artificial hot spot is referred to as the "match head" where the temperature is raised to 10 GK. Heat

diffuses from this region, igniting the flame in the C/O material.

There are a number of important improvements to the the original models, including the ability to change the Y_e of the fuel. The most notable feature of the Townsley et al. (2016) models, however, is the introduction of reconstruction of the trajectories. The flame front of the shockwave during the SNIa explosion is artificially thick in the raw data from the hydrodynamic modelling. In order to account for this, the reconstruction process narrows the flame by reducing the effective time that the material spends at the peak temperatures in the simulation. This is achieved by calibrating the burning products of the flame front (Townsley et al., 2016).

The S1.0 models utilise the flash code in order to model 3d spherically symmetric explosion, using density profiles from MESA for the initial conditions of their WD progenitor. The explosion in this model is also initialised by a hotspot, here with a central temperature of 2 GK. The hot spot is relatively large compared to the minimum detonatable region; however, the mass of the spot is small. Shen et al. (2018) argue that this also therefore minimises the impact on the ejected yields.

The M0.8 model uses a uniform composition throughout the WD progenitor, with 1.4% of metals. The ignition of this model is again achieved with the introduction of a hotspot, this time at 1.98 GK. Flash is used to evolve the system, through the initial helium detonation, leading to the triggering of the C/O detonation.

With the W7 model as a benchmark, Iliadis (2015) describe the nucleosynthesis during the propagation of the SN shock-wave. This shock-wave determines the burning conditions experienced by the material in the progenitor. In the innermost most extreme conditions, the material reaches densities of over $8.0 \times 10^8 \text{ g cm}^{-3}$. Under these conditions electron captures proceed rapidly, altering the Y_e of the material. The Y_e is the electron fraction, which is the ratio of electrons to baryons. This changes during the SNIa through

β -decays or electron captures. Below these extreme density conditions, but still at peak temperatures in excess of 5 GK, the material enters nuclear statistical equilibrium (NSE). NSE is a state in which all of the reaction rates, aside from the weak reactions, are in equilibrium in the system. NSE abundances are determined exclusively by three factors: the temperature, density and initial Y_e . Iliadis (2015) describes the further burning regimes experienced by material farther out in the WD, as the shockwave propagates forward and cools. Incomplete silicon burning, oxygen burning and neon-carbon burning proceed outwards from the center in mass shells as the peak temperature of the shockwave decreases as it moves outwards in the exploding WD. This is true for the higher mass models we investigate - T1.4 and S1.0 reach higher peak temperatures than the M0.8 model, due to their larger explosion energy. In M0.8 we see that the explosion energy is not sufficient to raise the temperature of any portion of the material above 5 GK. This results in only products from incomplete silicon, oxygen and carbon-neon burning. A detailed discussion of the isotopic and elemental ejecta are presented in section 3.2.

1.6 Determination of Abundances

In order to determine the contributions from SNIa some physical property must be measured which may be correlated with the abundance of a given element or isotope. Most information on SNIa to date has been available through the examination of optical or near optical light curves however or through the determination of solar isotopic abundances. Gamma ray spectroscopy also offerers a path to investigating the abundances of certain radioactive isotopes present shortly after the SNIa explosion. In this section, we describe these categories of observation - stellar spectroscopy, mass spectrometry and gamma ray spectroscopy and the experimental methods by

which these are achieved.

1.6.1 Stellar Spectroscopy

Determination of elemental abundances in stars is achieved through spectroscopy. The emission of light from a stellar surface is determined through the use of a spectrograph and emission or absorption lines are detected, depending on the environment and the object being observed. Each element has unique electronic transitions determined by the nuclear charge and the ionisation state of the atom, which gives rise to unique transmission lines superimposed on the continuum emission of the star. The relative strengths of these lines gives the relative abundance of an element in the star's surface. Using these spectral features, the abundances of elements can be determined. For the case of SNIa, optical and near infra-red spectra have been fundamental in determining physical properties of the explosion (Leibundgut and Suntzeff, 2003), while early light curve observations in the ultra violet have presented some constraints on the nature of the progenitors of Type Ia's (Hosseinzadeh et al., 2017).

1.6.2 Mass Spectrometry

Determination of isotopic abundances in the laboratory is achieved through mass spectrometry. In the case of presolar grains, the source of the isotopic abundances being investigated may be a single stellar event. For the case of bulk solar abundances, the isotopic ratios determined are an aggregate of all of the events which have enriched the solar environment. As there have been no presolar grains unambiguously identified as originating in a SNIa explosion, we must therefore compare isotopic abundances with the solar material for now. This introduces a level of uncertainty however, which is tied to the collective uncertainty on the yields and the evolution of the yields

of all sources of the isotopes we are concerned with. Baring this limitation in mind, the application of mass spectrometry is not trivial. It also necessarily relies on the chemical makeup of the solar neighborhood which may have been enriched with a peculiar event at some epoch. Baring these limitations in mind, mass spectrometry is still a powerful and useful tool. Through it, we gain access to isotopic abundances, which are generally not possible to determine from stellar spectroscopy (except for very close objects and for light elements). Because the bulk solar material has many contributions from a number of sources, if the contributions from SNIa are small there is difficulty in disentangling any information on the progenitors from these readings - as the small differences in abundances from differences in progenitor would be swamped by the uncertainties in GCE and yields from other sources.

In order to determine isotopic abundances, a sample of material is first vaporised to give free ions from a sample. These ions are accelerated through a spectrometer with a magnetic field perpendicular to the motion of the ions. This field bends the ions, with the trajectory determined by their velocity, mass and their charge. Detectors determine the point of impact of the ionised material and so the mass of the isotope is determined.

1.6.3 Gamma Ray Spectroscopy

Gamma ray spectroscopy is similar to stellar spectroscopy in that it is the detection of photons however, for the case of γ -ray spectroscopy, the photon is emitted due to nuclear transitions, not electronic transitions. When radioactive nuclei in the ejecta of SNIa decay, through $\beta +$ or $-$ reactions, the daughter nuclei are in an excited state. The de-excitation emits a photon with an energy unique to that isotope, which is then detected (often in germanium detectors). This method provides information on the isotopic abundances in

the ejecta of the Type Ia explosion, which is a stronger constraint on the nucleosynthesis in these objects however improvements in current generations of gamma telescopes are needed.

1.7 Aims of This Thesis

In this work we aim to first describe the effect of initial ^{22}Ne mass fraction on the nuclear burning in our three classes of model. While the effect of progenitor mass on the ejected elemental abundances of SNIa is well documented and extensively researched, the inclusion of the metallicity dependence and isotopic abundances is less well explored, being largely limited to the case of ^{56}Ni in, e.g., Timmes, Brown, and Truran, 2003 and p-process nucleosynthesis in, e.g., Travaglio, Hillebrandt, and Reinecke (2005). Taking these isotopic abundances, we then investigate which of these is most reliable as a tracer of initial progenitor mass over a wide range of the metallicities involved, which come with a variety of practical challenges.

We discuss the various means by which these isotopic abundances might be probed - γ -ray astronomy, isotopic abundance measurements of solar-system material, and effects on the SNIa lightcurves and suggest which isotopes might be best answer the question - what are the progenitors of Type Ia supernovae?

Chapter 2

Post Processing and Model

Description

*“TAKE THE UNIVERSE AND GRIND IT DOWN TO THE FINEST POWDER AND SIEVE IT THROUGH THE FINEST SIEVE AND THEN **SHOW ME ONE ATOM OF JUSTICE, ONE MOLECULE OF MERCY.**”*

Death, The Hogfather, Terry Pratchett

2.1 Tppnp - Parallelised Post-Processing

Post-processing is a vital tool in astrophysical modeling, separating large reaction networks from the hydrodynamical modeling of a system. A small reaction network is used during the stellar evolution or the modeling of the explosion in a stellar environment, with key reactions and isotopes concerned with energy generation. After the energy evolved by the system has been calculated, post-processing with the full nuclear network is done, using the temperature and density profiles obtained through the initial modeling step. This increases the speed at which the evolution of a stellar object can be computed, and reduces the computational cost. Because of this approach, variations of key reaction rates (for example ^{12}C - ^{12}C for SNIa) for sensitivity

purposes are not possible, as this changes the energy generation and consequently the dynamics of the system.

This work was completed using the post-processing code `tpnpn` - Tracer Particle Post-Processing Network - Parallel, based on previous codes `ppn` and `mppnp`. A full description of the `tpnpn` code can be found in Jones et al. (2019), along with details in Ritter et al. (2018) and Pignatari et al. (2016). A description of the key features of the code is presented here: integration methods and nuclear networks, the treatment of initial abundances, and the explosion mechanisms of the three classes of model.

`Tpnpn` takes Lagrangian tracer particles from hydrodynamical simulations which do not mix material between those particles. Mixing between particles would result in a changing chemical composition, as well as changing thermodynamic conditions, and can significantly change the nucleosynthesis in a given fluid element - as is seen in convective burning environments such as AGB stars. The post-processing code `mppnp` deals with mixing between cells in a stellar model by the inclusion of a diffusion coefficient and mixing length theory. However, during the course of the SNIa explosion, there is not expected to be exchange of material between any of the tracer particles. We are therefore justified in the approach of `tpnpn`, where each particle is treated as an independent thermodynamic trajectory with initial chemical composition, and time varying temperature and density conditions. The temperature and density conditions, along with the initial chemical composition at the onset of the explosion, determine the nuclear burning experienced in the flame front and during the subsequent freeze-out.

In this work we use the new integration methods implemented in Jones et al. (2019) - the semi-implicit Bader-Deuffhard method for rate calculation during explosive burning, and the Cash-Karp Runge-Kutta method for nuclear statistical equilibrium. The specifics of the integration method can impact the final yields significantly. Reverse reaction rates are calculated for the

majority of reactions using the principle of detailed balance in order to retain consistency between the calculated rates and the NSE solver. Those reactions for which there are experimental data are generally considered to be the forward reactions for the purposes of computing the rates. Forward reactions are always consistent with the forward rates identified in the JINA reaclib database. Use of the Bader-Deuffhard method increases the accuracy of the computations, compared with the standard integration method described in Pignatari et al. (2016) (the backward Euler Newton-Raphson method), with typically a 30-300% increase in computational time.

Our reaction network consists of over 5200 isotopes and 75,000 reactions. Although this is far larger number of isotopes than are necessary for the complete description of burning in SNIa, the adaptive solver of tppnp ensures that any unnecessary reactions or isotopes are not carried forward in computation. Time savings on these models from decreased reaction networks are likely to be minimal, and total computation time for even the largest models (T1.4 with 10^5 particles) take only on the order of 1000 CPU hours. Further post-processing with tracers from three-dimensional models may require refinement of the network, as well as methods for selecting weighted subsamples of trajectories from possibly many millions of particles. Presently the complete post-processing of all particles is relatively cheap and ensures that errors from convergence of yields with respect to particle number are not a concern.

2.2 Solving The Network

The change in a nuclear species N_i is given by equation 2.1:

$$\frac{dN_i}{dt} = \left[\sum_{j,k} N_j N_k \langle \sigma v \rangle_{jk \rightarrow i} + \sum_l \lambda_{\beta, l \rightarrow i} N_l + \sum_m \lambda_{\gamma, m \rightarrow i} N_m \right] - \left[\sum_n N_n N_i \langle \sigma v \rangle_{ni} + \sum_o \lambda_{\beta, i \rightarrow o} N_i + \sum_p \lambda_{\gamma, i \rightarrow p} N_i \right] \quad (2.1)$$

which has been reproduced from Iliadis, 2015. The terms in the first set of brackets are all reactions producing the isotope N_i , the first term being reactions between species j and k . In the tppnp code, this is one of 4 reactions - (p, γ) , (p, α) , (α, γ) or (α, p) . The second term represents all β -decay processes which lead to isotope N_i , and the third term is any photodisintegration reaction which had isotope N_i as a product, usually (γ, p) or (γ, α) in the tppnp reaction network. This is the same for the terms in the second set of brackets - however, these are destruction reactions. Iliadis (2015) describes two modifications which are necessary when non-identical particles produce two nuclei, or identical particles produce one nucleus. In these two cases the sum over the first term then becomes:

$$2N_j N_k \langle \sigma v \rangle_{jk \rightarrow i} \quad (2.2)$$

and

$$\frac{1}{2} N_j^2 \langle \sigma v \rangle_{jj \rightarrow i} \quad (2.3)$$

respectively. Further to this, three particle reactions such as the triple- α process must be considered. Table 2.1 describes all of the possible stellar reactions in tppnp in terms of their reactants and products.

Each species which is produced or destroyed in our SNIa models will

Charged Particle	β -decay	Photodisintegration
(p, γ)		(γ ,p)
(p, α)		(γ , α)
(α , γ)		
(α ,p)		

TABLE 2.1: All of the reactions present in the tppnp code.

have a similar expression. The number of isotopes relevant to SNIa nucleosynthesis is around 250 individual nuclides, as seen in the work of Townsley et al. (2016). This results in thousands of coupled ordinary differential equations. A reaction network solves these simultaneously for the final abundances of the system, given the initial conditions and temperature and density evolution. Various numerical techniques are employed to achieve this; for example, the forward Euler method of numerical integration; the Bader-Doeflhad method; and the Runge-Kutter method, mentioned earlier in this work. The process of computing the nucleosynthesis of these species goes as follows:

1. At time $t = 0$, the initial abundances of all isotopes are specified.
2. The current temperature and density, and abundances of relevant isotopes are used to calculate all reaction rates producing or destroying a given species over a time-step δt .
 - (a) If the abundances do not converge after evolving the species for a time δt - i.e. if when checked against a smaller time step the final abundances do not match - then a sub-timestep is taken, where δt is reduced. T and ρ values are then interpolated between the original timestep.
 - (b) This process continues until the change in abundance is resolved
3. The new abundances are then used in step 1. at $t = t + \delta t$

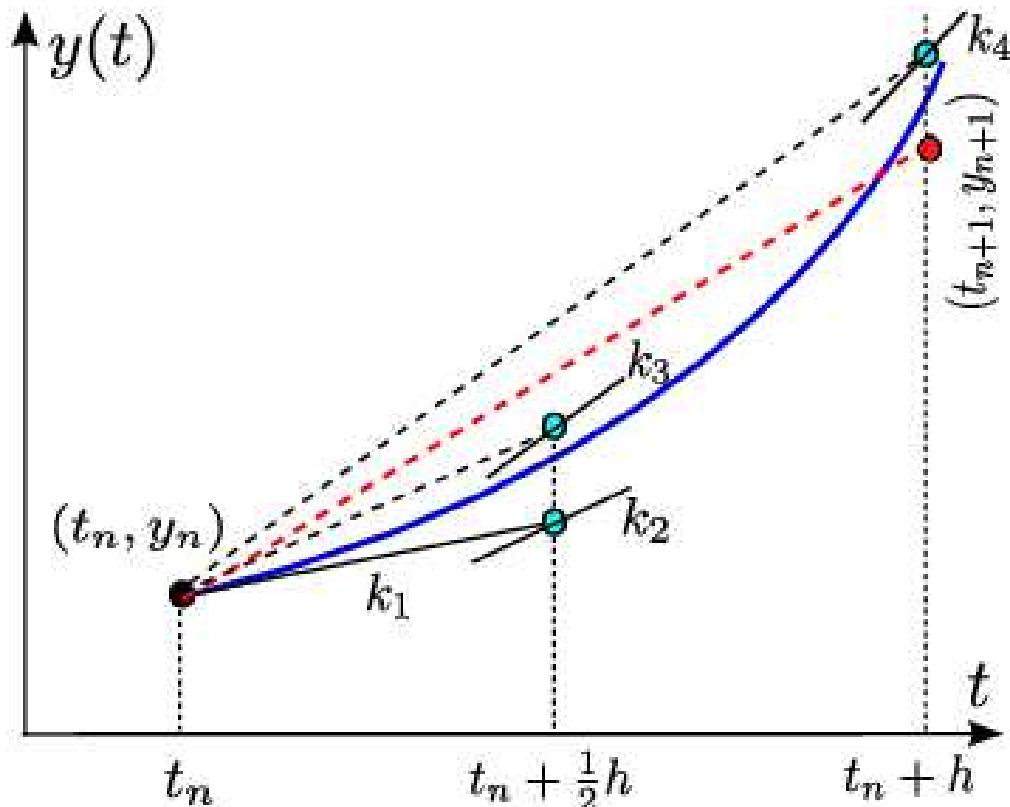


FIGURE 2.1: Diagram of the Runge-Kutter integration method.

Adapted from Fadlisyah (2014).

Determination of the new values at $t = t + \delta t$ are found by determining the slope of the function, either at that time or at a time later than the current timestep (depending on the integration method). In the Runge-Kutter method intermediate slopes are used to improve accuracy, as shown in figure 2.1. At K_1 the slope is calculated and using the point K_2 is computed. Using the slope as calculated at K_2 , we return to our initial conditions and compute K_3 . This is then used to compute across the whole timestep to K_4 . After this, a weighting of all of the slopes is used to reduce the error on the integration step as far as possible. Tppnp uses the RK4 method for its much improved accuracy compared to a small increase in computational cost versus the Euler method.

While the formulation presented here appears simple, each of the production and destruction terms in equation 2.1 rely on experimental and theoretical determinations of reaction rates, which are often challenging to produce. The majority of reaction rates relevant to SNIa nucleosynthesis are well known experimentally - see, for example, Iliadis et al. (2001), Dillmann et al. (2006), Angulo et al. (1999); theoretical predictions of rates become more common as nuclei become more unstable away from the valley of stability, where experiments are much more difficult to conduct. Nuclear uncertainties, however, may still play an important role in the final post-processed abundances. The cross-section of the reactions is determined at discrete temperatures, and an interpolation is required to provide a rate at intermediate temperatures for which there may be no experimental data. The interpolation carried out in the tppnp code is a cubic spline.

2.3 Nuclear Networks

As discussed in the introduction, the sets of trajectories T1.4, S1.0 and M0.8 are based on hydrodynamics simulations using limited networks. For these three models, post-processing is then carried out on the trajectories to produce final yields in their respective publications. We find in this work that those networks used for post-processing are sufficient to capture the nucleosynthesis in these models, as our results differ at most within a factor of 2-3 for almost all abundances. We do see some leakage of material to isotopes not included in the T1.4 models; however, abundances are low (see Chapter 3). The benefits of post-processing these models again comes with the use of a consistent nuclear reaction network between them. With this, we disentangle the nuclear physics uncertainties from hydrodynamical modeling considerations.

The network used in the post-processing of T1.4 is quite large, using 225 nuclides in the reconstruction of the thin flame front (Townesley et al., 2016). These include weak reactions discussed in Calder et al. (2007), which are necessary for the computation of the neutronisation in the flame front and are taken from Langanke and Martínez-Pinedo (2000) and Langanke and Martínez-Pinedo (2001). Where newer rates are not available, they use those found in Fuller, Fowler, and Newman (1985) and Oda et al. (1994). The standard TORCH network is extended in their work, including 25 rates pertaining to neutron rich Fe-group isotopes. Our large network includes many rates which are not relevant to the SNIa explosion; however, due to the adaptive solver, the computational expense of post-processing is not increased significantly relative to a more restricted network. We also see production of trace amounts of higher-Z material not found in Townesley et al. (2016) because of our more extended network, with total ejected mass of order $10^{-9} M_{\odot}$.

A sketch of a representative charged particle reaction crosssection is shown in figure 2.2. In this sketch it can be seen that the crosssection increases with particle energy, as the incident particles have a higher probability of overcoming the coulomb barrier. The sharp spikes in the crosssection arise from nuclear physics considerations, such as excited nuclear states in the daughter nucleus, which increase the probability of particle capture by orders of magnitude.

The network in Shen et al. (2018) used for the hydrodynamical modeling consists of 41 isotopes and 190 reactions, all of which were taken from the JINA reaclib (Cyburt et al., 2010). With errors of only a few percent in energy generation, they find that this network is sufficient to follow the explosion dynamics. Post-processing in this work was carried out with a 205 isotope network using MESA, again with all reactions being taken from the JINA reaclib.

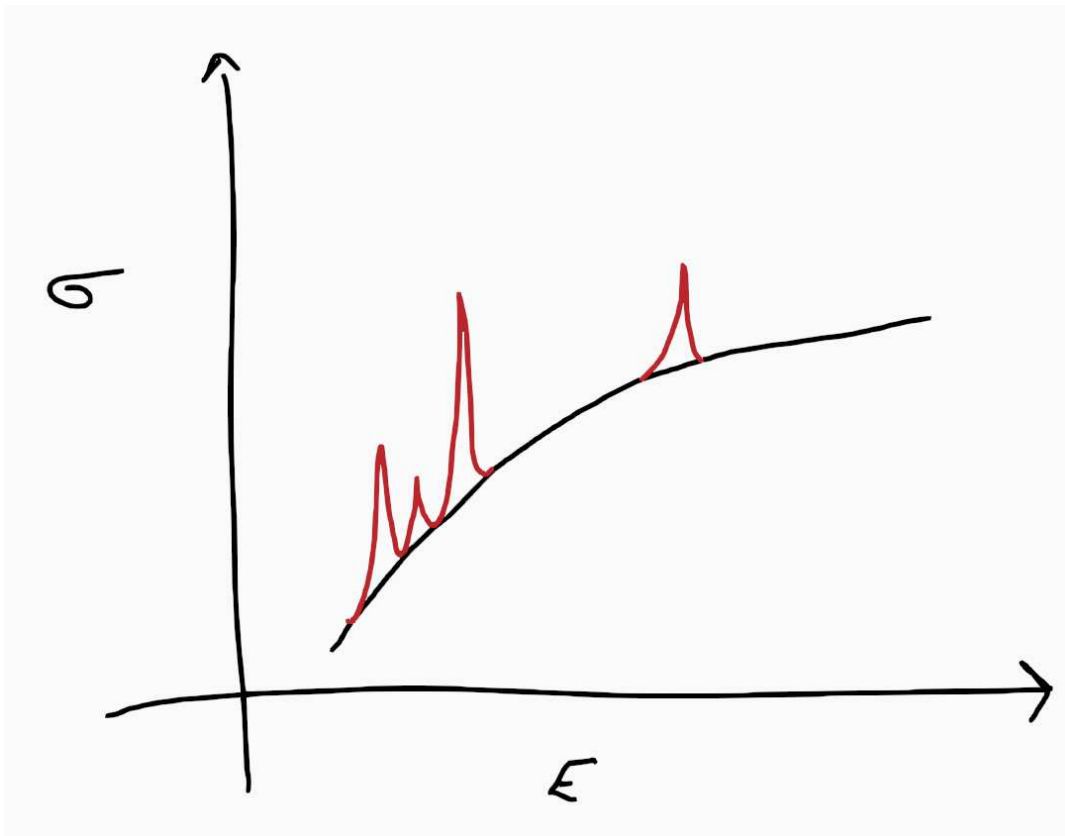


FIGURE 2.2: A sketch of a representative charged particle capture cross-section. The black line shows an increasing probability of capture with increasing particle energy, the red spikes show sharp increases in capture cross-section due to nuclear resonances.

Finally, the network in Miles et al. (2019) is again 205 isotopes, also with JINA reaclib rates. In each case, the hydrodynamics have been calculated separately, with the final yields being post-processed.

Whilst both the S1.0 and M0.8 models post process using the JINA rates, these may not be consistent between the works due to different rate compilations and releases from JINA. Because of this, our present work is a necessary and useful investigation, ensuring that nuclear uncertainties are eliminated in a comparison between the various progenitor models of SNIa.

Reaction rates are taken from a variety of different sources. The Rauscher and Thielemann (2000) JINA reaclib, Cyburt et al. (2010) Basel reaclib, Dillmann et al. (2006) KADoNIS, Angulo et al. (1999), Caughlan and Fowler (1988) and Iliadis et al. (2001) compilations between them constitute the majority of reactions other than the weak reaction rates, which are compiled from Fuller, Fowler, and Newman (1985), Oda et al. (1994), Goriely (1999) and Langanke and Martinez-Pinedo (2000), along with rates from Takahashi and Yokoi (1987) as discussed in Jones et al. (2019) and Pignatari et al. (2016). See appendix B for a selection key rates and their sources.

In NSE the prescription outlined in Calder et al. (2007), correcting for coulomb screening, is used along with the partition functions described in the JINA reaclib. This is calculated at 6 GK in these models; however, the exact temperature at which it is appropriate to use these as opposed to solving the full network is contended.

2.4 Initial Abundances

In this present work we select an initial abundance of metals determined by the mass fraction of ^{22}Ne . ^{22}Ne acts as a proxy for the metallicity of the progenitor in this work, as the weak interactions in the CNO cycle $^{18}\text{F}(\beta^+)^{18}\text{O}$ convert protons to neutrons and changes the Y_e of the system. Note that this

definition of Z is distinct from the usual astronomical meaning, that being the mass fraction of any element heavier than helium. Here Z refers to the change in electron fraction Y_e .

In the extreme temperature conditions of SNIa explosions, any seed nuclei in the interior of the stars will be photodisintegrated to protons and He nuclei. This leaves the composition of outer layers of the star - those which do not reach a temperature of above around 5GK - with a non-zero abundance of seed nuclei. Initial composition, beyond the electron fraction, is not important in those particles which reach NSE and, as discussed previously, the composition of the outer, cooler layers of the white dwarf are unlikely to resemble scaled solar abundances. We have therefore chosen to treat our white dwarf as having neutron excess only in the form of ^{22}Ne .

The use of ^{22}Ne as a tracer of metallicity in SNIa is well established (Timmes, Brown, and Truran, 2003; Howell et al., 2009) with the effect of initial metallicity accounting for up to 10% of the dispersion observed in SNIa found in environments of differing metallicities. The results of Howell et al. (2009) show a significantly reduced spread in the synthesised ^{56}Ni abundance due to host galaxies not achieving the extreme enrichment required to produce the large variations seen in Timmes, Brown, and Truran (2003). ^{56}Fe 's linear dependence on the initial metallicity and the dependence of other elements is explored in chapter 3.

T1.4 choose a scaled solar abundance for their models, except for the CNO material, which is treated as ^{22}Ne as in Timmes, Brown, and Truran (2003), with a constant abundance throughout the WD. The rest of the material is composed of C and O, and convective burning ashes: ^{20}Ne , ^{16}O , ^{13}C and ^{23}Ne . S1.0 includes ^{22}Ne and ^{56}Fe as proxies for the abundances of non-C/O isotopes and as a tracer of metallicity, again with a uniform distribution of abundances in the WD. M0.8 use solar abundances taken from Asplund et al. (2009).

Initial abundances in SNIa models are not treated with exact consistency between research groups. Many use a scaled solar value of abundances along with a proportion of ^{22}Ne ; however, recent work by Battino et al. (2020) suggests a significantly different composition can be achieved in the outer layers of the WD, leading to production of p-nuclei. In order to be consistent across all models, initial abundances in the post-processed models consist of only ^{12}C , ^{16}O and ^{22}Ne . Whilst this undoubtedly introduces some discrepancies with the published data of T1.4, S1.0 and M0.8, these differences are shown to be relatively small even when considering other uncertainties that are convolved between this work and those published results, such as differences in reaction networks used. For example, see figures 4.2, 4.6 and 4.10 where the abundances distributions of these models follow very closely the results in the published parent models (although see discussion of M0.8 in Chapter 4).

Chapter 3

Results of SNIa Post-Processing

“Through me you go into eternal pain; through me you go amongst the lost people”

Dante Alighieri, *The Inferno*

Here we present an overview of the isotopes which are over-produced relative to solar abundances in our various models. Models are labeled according to the initial mass of the progenitor and the metallicity. T1.4 corresponds to the Townsley et al. (2016) 1.4 M_{\odot} deflagration detonation model, S1.0 the Shen et al. (2018) 1.0 M_{\odot} double detonation model, and M0.8 the Miles et al. (2019) 0.8 M_{\odot} model. Metallicities range from $Z = 0$ to $Z = 0.1$, with the initial fraction of metals being represented by the mass fraction of ^{22}Ne with a uniform distribution through all tracer particles. For example, T1.4Z0 corresponds to a zero metallicity, 1.4 M_{\odot} model. The full list of models is shown in table 3.1.

3.1 Selected Tables of Data

Tables 3.2, 3.3 and 3.4 show the production factors for the three models T1.4, S1.0 and M0.8 at all metallicities, C ($Z = 6$) to As ($Z = 33$) (where Z is the proton number). Yields are taken at $t = \infty$ meaning all radioactive isotopes

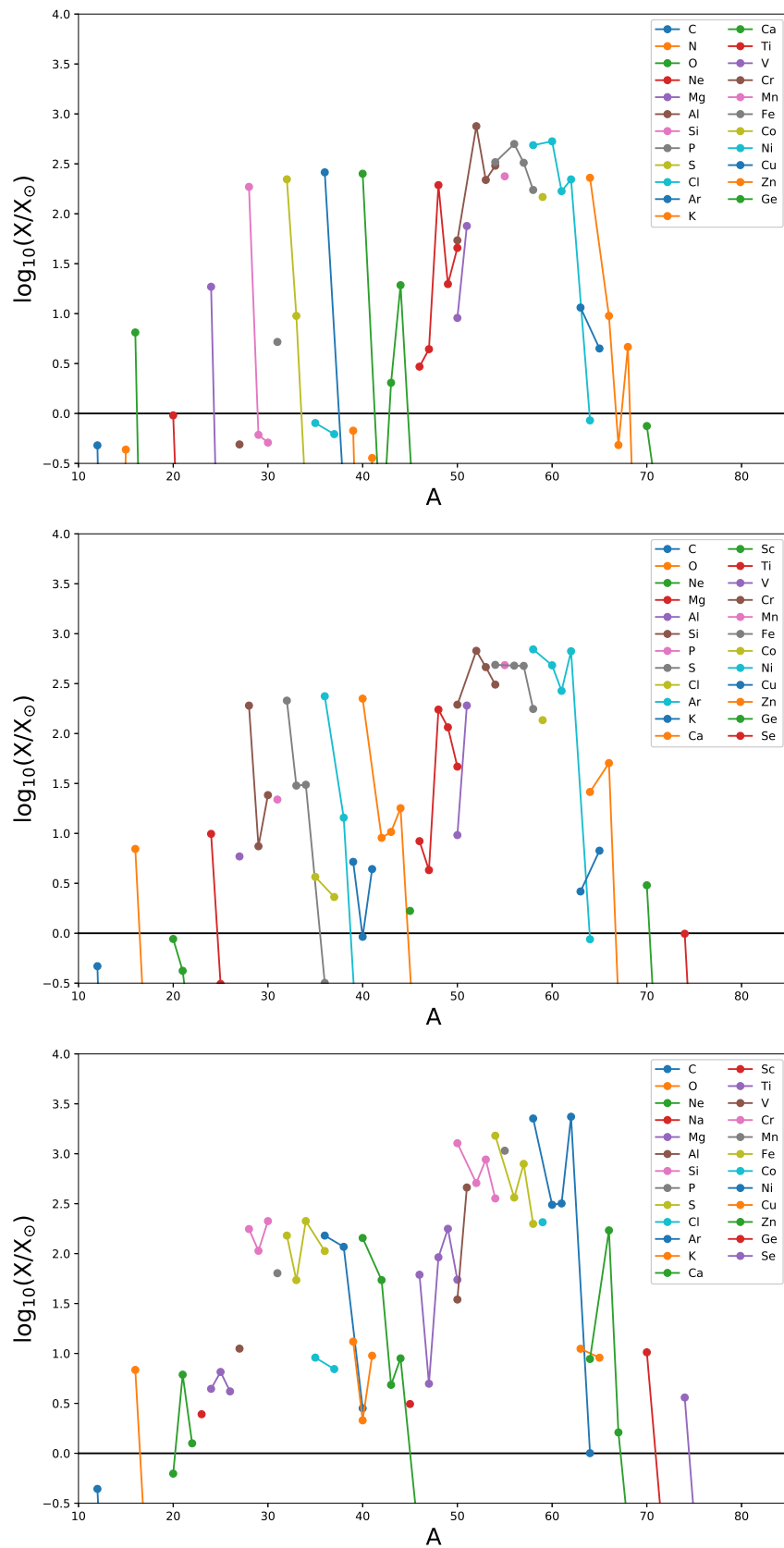


FIGURE 3.1: Production factors for models T1.4Z0 (top), T1.4Z0.014 (middle) and T1.4Z0.1 (bottom).

T1.4Z0	S1.0Z0	M0.8Z0
T1.4Z0.0000001	S1.0Z0.0000001	M0.8Z0.0000001
T1.4Z0.000001	S1.0Z0.000001	M0.8Z0.000001
T1.4Z0.00001	S1.0Z0.00001	M0.8Z0.00001
T1.4Z0.0001	S1.0Z0.0001	M0.8Z0.0001
T1.4Z0.001	S1.0Z0.001	M0.8Z0.001
T1.4Z0.002	S1.0Z0.002	M0.8Z0.002
T1.4Z0.005	S1.0Z0.005	M0.8Z0.005
T1.4Z0.014	S1.0Z0.014	M0.8Z0.014
T1.4Z0.01	S1.0Z0.01	M0.8Z0.01
T1.4Z0.02	S1.0Z0.02	M0.8Z0.02
T1.4Z0.05	S1.0Z0.05	M0.8Z0.05
T1.4Z0.1	S1.0Z0.1	M0.8Z0.1

TABLE 3.1: Table showing the models presented in this chapter, from lowest metallicity to highest. Initial metallicity is exclusively represented by ^{22}Ne .

are decayed. We now discuss the effect of metallicity of each of the three models.

In figure 3.1, the isotopic production factors for models T1.4Z0, T1.4Z0.014 and T1.4Z0.1 are shown. We observe a large overproduction in the iron group region as compared with solar abundances (Asplund et al., 2009), as well as peaks in production of Mg, Si, S, Ar and Ca isotopes. Here, the production factor is given by the log of the ejected mass of isotope X, divided by the abundance of that isotope in the sun:

$$\log_{10}(X_{ejc}/X_{\odot})$$

We have here chosen to use production factor as it easily allows us to estimate the contribution from SNIa to the solar abundance of an isotope, considering that SNIa contribute around 70% of solar iron.

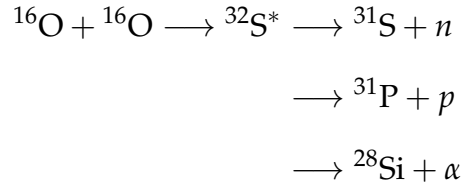
Explosive oxygen burning accounts for the majority of the production of the intermediate mass elements (Mg, Si, S and Ar) in these models, with a small contribution from trajectories reaching NSE for sulphur and argon (see

Element	A	$^{22}\text{Ne} = 0$	1e-7	1e-6	1e-5	1e-4	1e-3	2e-3	5e-3	1e-2	1.4e-2	2e-2	5e-2	1e-1
C	12	6.55e-01	6.55e-01	6.55e-01	6.55e-01	6.55e-01	6.53e-01	6.51e-01	6.47e-01	6.42e-01	6.39e-01	6.35e-01	6.21e-01	6.01e-01
C	13	2.12e-05	2.12e-05	2.11e-05	2.09e-05	2.04e-05	2.89e-05	4.80e-05	1.34e-04	2.92e-04	4.28e-04	6.49e-04	2.05e-03	5.31e-03
N	14	3.44e-05	3.44e-05	3.44e-05	3.42e-05	3.88e-05	1.90e-04	3.83e-04	9.01e-04	1.63e-03	2.14e-03	2.81e-03	5.29e-03	7.69e-03
N	15	5.94e-01	5.94e-01	5.92e-01	5.74e-01	3.98e-01	2.97e-02	1.13e-02	3.60e-03	2.22e-03	2.02e-03	2.07e-03	4.02e-03	1.44e-02
O	16	8.84e+00	8.84e+00	8.84e+00	8.85e+00	8.86e+00	8.94e+00	9.02e+00	9.21e+00	9.43e+00	9.54e+00	9.67e+00	9.80e+00	9.35e+00
O	17	2.36e-04	2.36e-04	2.38e-04	2.58e-04	5.23e-04	1.08e-02	2.66e-02	6.61e-02	1.08e-01	1.31e-01	1.56e-01	1.99e-01	1.98e-01
O	18	4.19e-07	4.19e-07	4.21e-07	4.43e-07	7.37e-07	1.22e-05	3.03e-05	8.16e-05	1.60e-04	2.19e-04	3.07e-04	8.38e-04	3.02e-03
F	19	1.70e-03	1.70e-03	1.69e-03	1.62e-03	1.19e-03	3.59e-04	2.47e-04	2.67e-04	4.52e-04	6.34e-04	9.34e-04	2.49e-03	4.18e-03
NE	20	1.31e+00	1.31e+00	1.31e+00	1.31e+00	1.31e+00	1.30e+00	1.29e+00	1.27e+00	1.23e+00	1.20e+00	1.15e+00	9.96e-01	8.55e-01
NE	21	3.50e-03	3.50e-03	3.50e-03	3.55e-03	4.13e-03	2.13e-02	5.44e-02	1.74e-01	3.87e-01	5.75e-01	8.85e-01	2.94e+00	8.38e+00
NE	22	1.99e-04	1.99e-04	2.01e-04	2.23e-04	4.83e-04	3.71e-03	8.01e-03	2.42e-02	5.94e-02	9.34e-02	1.53e-01	5.73e-01	1.72e+00
NA	23	2.14e-01	2.14e-01	2.14e-01	2.13e-01	2.09e-01	1.92e-01	1.94e-01	2.17e-01	2.82e-01	3.45e-01	4.49e-01	1.16e+00	3.36e+00
MG	24	2.54e+01	2.54e+01	2.54e+01	2.54e+01	2.55e+01	2.46e+01	2.32e+01	1.98e+01	1.58e+01	1.35e+01	1.11e+01	6.26e+00	6.04e+00
MG	25	2.33e-03	2.33e-03	2.34e-03	2.37e-03	2.90e-03	3.61e-02	5.86e-02	1.34e-01	2.84e-01	4.25e-01	6.67e-01	2.47e+00	8.92e+00
MG	26	9.78e-03	9.78e-03	9.79e-03	9.90e-03	1.12e-02	2.75e-02	4.50e-02	9.65e-02	1.81e-01	2.49e-01	3.56e-01	1.08e+00	5.70e+00
AL	27	6.69e-01	6.69e-01	6.69e-01	6.67e-01	6.57e-01	1.51e+00	2.72e+00	5.07e+00	7.13e+00	8.03e+00	8.78e+00	1.02e+01	1.53e+01
SI	28	2.54e+02	2.54e+02	2.54e+02	2.54e+02	2.55e+02	2.58e+02	2.60e+02	2.61e+02	2.61e+02	2.60e+02	2.59e+02	2.53e+02	2.41e+02
SI	29	8.34e-01	8.34e-01	8.34e-01	8.31e-01	8.66e-01	2.99e+00	3.91e+00	5.83e+00	8.29e+00	1.02e+01	1.32e+01	3.96e+01	1.46e+02
SI	30	6.98e-01	6.97e-01	6.94e-01	6.63e-01	4.45e-01	6.31e-01	2.15e+00	8.91e+00	2.22e+01	3.30e+01	4.92e+01	1.35e+02	2.89e+02
P	31	7.11e+00	7.11e+00	7.09e+00	6.91e+00	5.30e+00	4.06e+00	6.24e+00	1.28e+01	2.27e+01	2.98e+01	3.94e+01	7.60e+01	8.70e+01
S	32	3.03e+02	3.03e+02	3.02e+02	3.02e+02	3.02e+02	2.99e+02	2.98e+02	2.96e+02	2.94e+02	2.92e+02	2.88e+02	2.60e+02	2.07e+02
S	33	1.30e+01	1.30e+01	1.30e+01	1.31e+01	1.38e+01	1.38e+01	1.53e+01	2.32e+01	3.42e+01	4.11e+01	4.94e+01	7.07e+01	7.42e+01
S	34	1.88e-01	1.88e-01	1.87e-01	1.77e-01	1.05e-01	1.20e+00	3.70e+00	1.21e+01	2.80e+01	4.19e+01	6.42e+01	1.74e+02	2.89e+02
S	36	5.32e-05	5.32e-05	5.32e-05	5.32e-05	5.33e-05	6.43e-04	4.58e-03	4.34e-02	2.06e-01	4.35e-01	1.01e+00	1.57e+01	1.45e+02
CL	35	1.10e+00	1.10e+00	1.09e+00	1.06e+00	8.20e-01	7.03e-01	9.89e-01	2.00e+00	3.67e+00	5.01e+00	6.89e+00	1.20e+01	1.24e+01
CL	37	8.48e-01	8.48e-01	8.49e-01	8.51e-01	8.77e-01	9.76e-01	1.17e+00	1.76e+00	2.59e+00	3.15e+00	3.89e+00	7.08e+00	9.53e+00
AR	36	3.55e+02	3.55e+02	3.55e+02	3.55e+02	3.54e+02	3.46e+02	3.43e+02	3.36e+02	3.29e+02	3.23e+02	3.14e+02	2.69e+02	2.07e+02
AR	38	2.15e-01	2.15e-01	2.12e-01	2.14e-01	1.97e-01	7.09e-01	1.69e+00	5.44e+00	1.29e+01	1.96e+01	3.04e+01	8.77e+01	1.60e+02
AR	40	5.04e-05	5.04e-05	5.04e-05	5.04e-05	5.05e-05	6.78e-05	1.58e-04	9.86e-04	5.13e-03	1.29e-02	3.83e-02	7.90e-01	3.86e+00
K	39	9.18e-01	9.18e-01	9.12e-01	9.12e-01	8.52e-01	1.07e+00	1.63e+00	3.62e+00	5.71e+00	7.09e+00	8.88e+00	1.58e+01	1.80e+01
K	40	3.21e-04	3.20e-04	3.21e-04	3.24e-04	3.87e-04	2.20e-02	5.36e-02	1.95e-01	6.57e-01	1.26e+00	2.47e+00	6.23e+00	2.92e+00
K	41	4.89e-01	4.89e-01	4.91e-01	5.10e-01	6.92e-01	1.38e+00	1.88e+00	3.14e+00	4.87e+00	6.00e+00	7.42e+00	1.23e+01	1.30e+01
CA	40	3.44e+02	3.44e+02	3.44e+02	3.44e+02	3.42e+02	3.35e+02	3.30e+02	3.22e+02	3.13e+02	3.06e+02	2.96e+02	2.52e+02	1.96e+02
CA	42	5.96e-02	5.95e-02	5.95e-02	5.95e-02	5.89e-02	3.30e-01	8.68e-01	3.33e+00	8.14e+00	1.23e+01	1.89e+01	5.05e+01	7.42e+01
CA	43	2.77e+00	2.77e+00	2.76e+00	2.76e+00	2.65e+00	2.86e+00	4.57e+00	1.16e+01	1.39e+01	1.41e+01	1.37e+01	1.06e+01	6.62e+00
CA	44	2.63e+01	2.63e+01	2.63e+01	2.63e+01	2.63e+01	2.68e+01	2.69e+01	2.64e+01	2.52e+01	2.44e+01	2.32e+01	1.81e+01	1.22e+01
CA	46	1.35e-02	1.35e-02	1.35e-02	1.35e-02	1.35e-02	1.36e-02	1.36e-02	1.36e-02	1.39e-02	1.42e-02	1.53e-02	4.43e-02	1.62e-01
CA	48	1.05e-05	1.05e-05	1.05e-05	1.05e-05	1.05e-05	1.06e-05	1.06e-05	1.07e-05	1.08e-05	1.10e-05	1.12e-05	1.26e-05	4.55e-05
SC	45	2.79e-01	2.79e-01	2.80e-01	2.92e-01	4.16e-01	9.32e-01	1.06e+00	1.41e+00	1.94e+00	2.29e+00	2.73e+00	3.90e+00	4.26e+00
TI	46	4.02e+00	4.02e+00	3.99e+00	4.02e+00	3.70e+00	1.64e+00	1.10e+00	3.02e+00	7.49e+00	1.14e+01	1.76e+01	4.97e+01	8.40e+01
TI	47	6.02e+00	6.02e+00	5.96e+00	6.02e+00	5.58e+00	2.84e+00	2.16e+00	3.95e+00	5.31e+00	5.86e+00	6.31e+00	6.80e+00	6.80e+00
TI	48	2.65e+02	2.64e+02	2.64e+02	2.65e+02	2.65e+02	2.65e+02	2.65e+02	2.58e+02	2.46e+02	2.37e+02	2.25e+02	1.78e+02	1.25e+02
TI	49	2.70e+01	2.70e+01	2.70e+01	2.78e+01	3.96e+01	7.76e+01	8.59e+01	1.09e+02	1.39e+02	1.58e+02	1.78e+02	2.25e+02	2.42e+02
TI	50	6.22e+01	6.22e+01	6.22e+01	6.22e+01	6.22e+01	6.23e+01	6.24e+01	6.27e+01	6.33e+01	6.37e+01	6.44e+01	6.79e+01	7.47e+01
V	50	1.24e+01	1.24e+01	1.24e+01	1.24e+01	1.24e+01	1.24e+01	1.24e+01	1.25e+01	1.28e+01	1.31e+01	1.36e+01	1.74e+01	4.74e+01
V	51	1.03e+02	1.03e+02	1.03e+02	1.03e+02	9.75e+01	9.86e+01	1.13e+02	1.63e+02	2.23e+02	2.61e+02	3.07e+02	4.52e+02	6.28e+02
CR	50	7.39e+01	7.39e+01	7.38e+01	7.40e+01	7.37e+01	7.52e+01	8.36e+01	1.25e+02	2.01e+02	2.66e+02	3.68e+02	9.25e+02	1.74e+03
CR	52	1.03e+03	1.03e+03	1.03e+03	1.03e+03	1.03e+03	1.02e+03	1.01e+03	9.82e+02	9.45e+02	9.20e+02	8.87e+02	7.69e+02	6.95e+02
CR	53	2.98e+02	2.98e+02	2.98e+02	3.01e+02	3.25e+02	3.85e+02	4.09e+02	4.78e+02	5.72e+02	6.32e+02	7.04e+02	9.35e+02	1.20e+03
CR	54	4.14e+02	4.14e+02	4.14e+02	4.14e+02	4.14e+02	4.15e+02	4.15e+02	4.17e+02	4.20e+02	4.22e+02	4.26e+02	4.46e+02	4.88e+02
MN	55	3.24e+02	3.24e+02	3.24e+02	3.24e+02	3.25e+02	3.72e+02	4.11e+02	4.94e+02	5.95e+02	6.61e+02	7.47e+02	1.07e+03	1.47e+03
FE	54	4.49e+02	4.49e+02	4.49e+02	4.49e+02	4.49e+02	4.60e+02	4.74e+02	5.20e+02	6.00e+02	6.66e+02	7.66e+02	1.27e+03	2.07e+03
FE	56	6.83e+02	6.83e+02	6.83e+02	6.83e+02	6.82e+02	6.80e+02	6.78e+02	6.72e+02	6.62e+02	6.54e+02	6.42e+02	5.86e+02	4.98e+02
FE	57	4.43e+02	4.43e+02	4.43e+02	4.43e+02	4.47e+02	4.82e+02	5.14e+02	5.56e+02	6.11e+02	6.50e+02	7.04e+02	9.02e+02	1.08e+03
FE	58	2.36e+02	2.36e+02	2.36e+02	2.36e+02	2.37e+02	2.37e+02	2.37e+02	2.38e+02	2.40e+02	2.41e+02	2.43e+02	2.53e+02	2.71e+02
CO	59	2.01e+02	2.01e+02	2.01e+02	2.01e+02	1.94e+02	1.36e+02	1.15e+02	1.44e+02	1.71e+02	1.86e+02	2.03e+02	2.52e+02	2.82e+02
NI	58	6.64e+02	6.64e+02	6.64e+02	6.64e+02	6.65e+02	6.66e+02	6.71e+02	7.34e+02	8.55e+02	9.52e+02	1.10e+03	1.84e+03	3.08e+03
NI	60	7.26e+02	7.26e+02	7.25e+02	7.26e+02	7.26e+02	7.28e+02	7.31e+02	7.09e+02	6.79e+02	6.59e+02	6.33e+02	5.33e+02	4.21e+02
NI	61	2.30e+02	2.30e+02	2.30e+02	2.30e+02	2.33e+02	2.65e+02	2.98e+02	3.26e+02	3.49e+02	3.65e+02	3.85e+02	4.39e+02	4.34e+02
NI	62	3.02e+02	3.02e+02	3.02e+02	3.02e+02	3.03e+02	3.28e+02	3.93e+02	5.45e+02	7.52e+02	9.11e+02	1.14e+03	2.13e+03	3.21e+03
NI	64	1.16e+00	1.16e+00	1.16e+00	1.16e+00	1.16e+00	1.17e+00	1.17e+00	1.17e+00	1.18e+00	1.19e+00	1.20e+00	1.26e+00	1.37e+00
CU	63	1.57e+01	1.57e+01	1.57e+01	1.57e+01	1.56e+01	1.93e+01	1.70e+01	3.53e+00	3.44e+00	3.58e+00	3.93e+00	7.45e+00	1.52e+01
CU	65	6.11e+00	6.11e+00	6.10e+00	6.13e+00	6.22e+00	6.96e+00	6.99e+00	7.13e+00	8.24e+00	9.16e+00	1.04e+01	1.37e+01	1.24e+01
ZN	64	3.13e+02	3.13e+02	3.12e+02	3.14e+02	3.16e+02	3.00e+02	1.78e+02	5.93e+01	4.05e+01	3.55e+01	3.11e+01	2.06e+01	1.20e+01
ZN	66	1.30e+01	1.30e+01	1.30e+01	1.30e+01	1.35e+01	1.79e+01	2.25e+01	3.43e+01	5.38e+01	6.91e+01	9.0		

Element	A	²² Ne = 0	1e-7	1e-6	1e-5	1e-4	1e-3	2e-3	5e-3	1e-2	1.4e-2	2e-2	5e-2	1e-1
C	12	3.62e-01	3.62e-01	3.62e-01	3.62e-01	3.61e-01	3.59e-01	3.58e-01	3.54e-01	3.51e-01	3.50e-01	3.48e-01	3.41e-01	3.31e-01
C	13	2.01e-05	2.01e-05	2.03e-05	1.99e-05	2.01e-05	4.03e-05	8.18e-05	2.83e-04	6.85e-04	1.03e-03	1.57e-03	4.22e-03	8.07e-03
N	14	1.75e-05	1.75e-05	1.75e-05	1.74e-05	2.35e-05	1.26e-04	2.15e-04	4.14e-04	6.31e-04	7.41e-04	8.64e-04	1.34e-03	1.93e-03
N	15	3.74e-01	3.74e-01	3.72e-01	3.53e-01	1.71e-01	6.17e-03	2.26e-03	8.22e-04	5.57e-04	5.22e-04	5.69e-04	2.68e-03	1.13e-02
O	16	7.91e+00	7.91e+00	7.91e+00	7.92e+00	7.98e+00	8.19e+00	8.30e+00	8.55e+00	8.80e+00	8.91e+00	9.01e+00	9.01e+00	8.42e+00
O	17	1.37e-04	1.37e-04	1.39e-04	1.61e-04	5.67e-04	9.53e-03	1.74e-02	2.90e-02	3.53e-02	3.78e-02	4.07e-02	4.32e-02	3.91e-02
O	18	3.65e-07	3.66e-07	3.70e-07	4.12e-07	1.01e-06	8.53e-06	1.39e-05	2.66e-05	4.54e-05	5.80e-05	8.16e-05	5.38e-04	2.27e-03
F	19	2.80e-04	2.80e-04	2.78e-04	2.64e-04	1.78e-04	5.22e-05	6.47e-05	1.30e-04	2.05e-04	2.67e-04	4.03e-04	8.94e-04	9.81e-04
NE	20	4.24e-01	4.24e-01	4.24e-01	4.24e-01	4.24e-01	4.18e-01	4.12e-01	3.99e-01	3.82e-01	3.71e-01	3.57e-01	3.12e-01	2.67e-01
NE	21	1.16e-03	1.16e-03	1.16e-03	1.19e-03	1.55e-03	1.48e-02	4.15e-02	1.15e-01	1.99e-01	2.72e-01	4.38e-01	1.50e+00	3.43e+00
NE	22	6.23e-05	6.23e-05	6.24e-05	6.27e-05	9.00e-05	1.31e-03	3.46e-03	1.31e-02	3.57e-02	5.69e-02	9.32e-02	3.50e-01	9.76e-01
NA	23	8.94e-02	8.94e-02	8.93e-02	8.91e-02	8.63e-02	7.59e-02	7.65e-02	9.21e-02	1.25e-01	1.56e-01	2.18e-01	5.64e-01	1.43e+00
MG	24	1.27e+01	1.27e+01	1.27e+01	1.27e+01	1.28e+01	1.19e+01	1.07e+01	7.81e+00	5.14e+00	3.95e+00	2.92e+00	1.54e+00	2.04e+00
MG	25	1.03e-03	1.03e-03	1.04e-03	1.05e-03	1.45e-03	1.63e-02	2.59e-02	5.77e-02	1.19e-01	1.77e-01	2.74e-01	9.18e-01	2.88e+00
MG	26	3.68e-03	3.68e-03	3.68e-03	3.74e-03	4.43e-03	1.17e-02	1.90e-02	3.90e-02	7.09e-02	9.57e-02	1.33e-01	3.86e-01	1.49e+00
AL	27	2.95e-01	2.95e-01	2.94e-01	2.92e-01	2.71e-01	7.11e-01	1.21e+00	2.02e+00	2.51e+00	2.64e+00	2.69e+00	3.02e+00	5.09e+00
SI	28	2.91e+02	2.91e+02	2.91e+02	2.91e+02	2.92e+02	2.96e+02	2.98e+02	3.00e+02	2.99e+02	2.99e+02	2.98e+02	2.94e+02	2.85e+02
SI	29	7.44e-01	7.44e-01	7.43e-01	7.37e-01	7.67e-01	7.67e-01	7.67e-01	3.50e+00	4.69e+00	5.80e+00	6.53e+00	7.67e+00	6.93e+01
SI	30	5.67e-01	5.67e-01	5.63e-01	5.21e-01	2.34e-01	4.98e-01	1.64e+00	5.86e+00	1.29e+01	1.81e+01	2.59e+01	7.82e+01	2.47e+02
P	31	4.71e+00	4.71e+00	4.69e+00	4.53e+00	3.19e+00	3.72e+00	5.77e+00	1.12e+01	1.84e+01	2.32e+01	2.96e+01	5.71e+01	8.64e+01
S	32	3.52e+02	3.52e+02	3.52e+02	3.52e+02	3.51e+02	3.45e+02	3.43e+02	3.42e+02	3.39e+02	3.35e+02	3.29e+02	2.91e+02	2.29e+02
S	33	6.15e+00	6.15e+00	6.17e+00	6.30e+00	7.58e+00	1.30e+01	1.68e+01	2.65e+01	3.86e+01	4.63e+01	5.60e+01	8.94e+01	1.04e+02
S	34	1.36e-01	1.36e-01	1.34e-01	1.23e-01	4.78e-02	2.39e+00	7.00e+00	2.22e+01	4.94e+01	7.20e+01	1.06e+02	2.80e+02	5.11e+02
S	36	9.28e-08	9.28e-08	9.32e-08	9.75e-08	1.78e-07	5.42e-04	3.23e-03	2.55e-02	1.07e-01	2.30e-01	5.37e-01	8.02e+00	7.19e+01
CL	35	8.07e-01	8.07e-01	8.04e-01	7.74e-01	5.74e-01	1.03e+00	1.67e+00	3.35e+00	5.85e+00	7.71e+00	1.02e+01	1.77e+01	1.97e+01
CL	37	6.07e-01	6.07e-01	6.09e-01	6.29e-01	8.00e-01	1.50e+00	2.01e+00	3.26e+00	4.87e+00	5.96e+00	7.33e+00	1.18e+01	1.35e+01
AR	36	3.99e+02	3.99e+02	3.99e+02	3.99e+02	3.96e+02	3.83e+02	3.76e+02	3.66e+02	3.55e+02	3.47e+02	3.35e+02	2.77e+02	2.06e+02
AR	38	4.87e-02	4.92e-02	4.95e-02	4.70e-02	4.10e-02	1.58e+00	4.09e+00	1.30e+01	3.06e+01	4.63e+01	7.09e+01	1.88e+02	3.13e+02
AR	40	9.23e-09	9.23e-09	9.27e-09	9.64e-09	1.46e-08	2.85e-05	1.47e-04	1.03e-03	5.09e-03	1.24e-02	3.50e-02	5.66e-01	3.30e+00
K	39	5.51e-01	5.52e-01	5.51e-01	5.37e-01	4.77e-01	1.89e+00	3.31e+00	6.64e+00	1.11e+01	1.42e+01	1.81e+01	2.96e+01	2.93e+01
K	40	9.10e-05	9.10e-05	9.14e-05	9.49e-05	1.67e-04	4.73e-02	1.08e-01	3.51e-01	1.00e+00	1.73e+00	3.02e+00	6.90e+00	5.46e+00
K	41	8.71e-01	8.71e-01	8.75e-01	9.16e-01	1.30e+00	2.70e+00	3.78e+00	6.39e+00	9.73e+00	1.19e+01	1.45e+01	2.10e+01	1.91e+01
CA	40	3.68e+02	3.68e+02	3.68e+02	3.68e+02	3.65e+02	3.50e+02	3.42e+02	3.30e+02	3.16e+02	3.06e+02	2.93e+02	2.41e+02	1.83e+02
CA	42	9.93e-03	9.94e-03	9.94e-03	9.64e-03	5.63e-03	6.98e-01	2.01e+00	7.19e+00	1.82e+01	2.82e+01	4.42e+01	1.12e+02	1.52e+02
CA	43	7.27e-01	7.26e-01	7.16e-01	6.96e-01	5.03e-01	8.55e-01	1.90e+00	3.30e+00	3.62e+00	3.50e+00	3.35e+00	2.35e+00	1.62e+00
CA	44	1.58e+01	1.56e+01	1.57e+01	1.59e+01	1.57e+01	1.53e+01	1.50e+01	1.41e+01	1.32e+01	1.26e+01	1.18e+01	8.76e+00	5.86e+00
CA	46	2.02e-13	2.02e-13	2.05e-13	2.34e-13	9.31e-13	9.10e-09	1.55e-07	5.43e-06	8.34e-05	3.37e-04	1.47e-03	3.01e-02	1.98e-01
CA	48	3.81e-23	3.82e-23	3.92e-23	5.04e-23	5.05e-22	1.15e-16	7.93e-15	7.06e-13	2.48e-11	2.04e-10	1.19e-09	3.13e-07	3.03e-05
SC	45	3.23e-01	3.22e-01	3.24e-01	3.44e-01	5.68e-01	1.16e+00	1.37e+00	1.87e+00	2.45e+00	3.21e+00	4.22e+00	4.00e+00	3.96e+00
TI	46	5.63e-01	5.72e-01	5.77e-01	5.43e-01	5.01e-01	6.17e-01	1.65e+00	6.44e+00	1.66e+01	2.54e+01	3.87e+01	9.41e+01	1.31e+02
TI	47	1.10e+00	1.11e+00	1.11e+00	1.06e+00	9.63e-01	5.31e-01	7.65e-01	1.37e+00	1.93e+00	2.24e+00	2.66e+00	4.03e+00	5.87e+00
TI	48	2.15e+02	2.15e+02	2.15e+02	2.15e+02	2.15e+02	2.12e+02	2.10e+02	2.03e+02	1.93e+02	1.85e+02	1.76e+02	1.38e+02	9.77e+01
TI	49	1.66e+01	1.66e+01	1.67e+01	1.75e+01	3.03e+01	6.10e+01	6.80e+01	8.75e+01	1.13e+02	1.28e+02	1.45e+02	1.82e+02	1.97e+02
TI	50	2.35e-13	2.35e-13	2.38e-13	2.66e-13	7.41e-13	1.24e-07	1.99e-06	5.20e-05	4.53e-04	1.07e-03	2.11e-03	6.03e-03	3.74e-02
V	50	1.57e-07	1.57e-07	1.60e-07	1.71e-07	3.92e-07	1.51e-03	9.55e-03	1.19e-01	7.39e-01	1.47e+00	2.38e+00	7.72e+00	4.64e+01
V	51	2.35e+01	2.36e+01	2.36e+01	2.31e+01	1.83e+01	3.17e+01	5.14e+01	9.49e+01	1.46e+02	1.78e+02	2.18e+02	3.43e+02	5.19e+02
CR	50	2.92e+00	2.95e+00	3.00e+00	2.88e+00	3.13e+00	9.22e+00	2.15e+01	6.47e+01	1.45e+02	2.13e+02	3.21e+02	9.18e+02	1.73e+03
CR	52	7.69e+02	7.69e+02	7.69e+02	7.70e+02	7.68e+02	7.59e+02	7.50e+02	7.27e+02	6.95e+02	6.72e+02	6.43e+02	5.44e+02	5.17e+02
CR	53	1.19e+02	1.19e+02	1.19e+02	1.22e+02	1.48e+02	1.89e+02	2.10e+02	2.71e+02	3.51e+02	4.01e+02	4.61e+02	6.59e+02	9.21e+02
CR	54	9.15e-09	9.18e-09	9.47e-09	1.02e-08	4.59e-08	9.17e-05	4.74e-04	3.97e-03	1.81e-02	3.77e-02	8.36e-02	8.76e-01	6.41e+00
MN	55	1.04e+01	1.04e+01	1.04e+01	1.04e+01	1.15e+01	5.80e+01	9.13e+01	1.63e+02	2.49e+02	3.02e+02	3.70e+02	6.06e+02	8.91e+02
FE	54	5.86e-01	5.87e-01	5.93e-01	6.02e-01	7.65e-01	1.07e+01	2.40e+01	6.64e+01	1.40e+02	2.00e+02	2.91e+02	7.27e+02	1.35e+03
FE	56	4.49e+02	4.49e+02	4.49e+02	4.49e+02	4.49e+02	4.47e+02	4.46e+02	4.41e+02	4.33e+02	4.28e+02	4.19e+02	3.81e+02	3.24e+02
FE	57	1.56e+02	1.56e+02	1.55e+02	1.57e+02	1.59e+02	1.87e+02	2.07e+02	2.33e+02	2.73e+02	3.02e+02	3.40e+02	4.81e+02	6.16e+02
FE	58	7.20e-09	7.22e-09	7.29e-09	7.86e-09	2.59e-08	4.90e-06	2.07e-05	1.47e-04	6.21e-04	1.26e-03	2.67e-03	2.10e-02	9.70e-02
CO	59	6.40e+01	6.43e+01	6.49e+01	6.26e+01	5.81e+01	1.75e+01	1.83e+01	3.49e+01	5.07e+01	5.99e+01	7.07e+01	9.89e+01	1.07e+02
NI	58	1.40e+01	1.40e+01	1.42e+01	1.38e+01	1.37e+01	9.50e+00	1.28e+01	5.65e+01	1.31e+02	1.92e+02	2.84e+02	7.67e+02	1.61e+03
NI	60	2.94e+02	2.93e+02	2.94e+02	2.94e+02	2.95e+02	2.99e+02	2.99e+02	2.81e+02	2.63e+02	2.51e+02	2.36e+02	1.70e+02	9.16e+01
NI	61	9.87e+01	9.83e+01	9.81e+01	9.91e+01	1.01e+02	1.22e+02	1.37e+02	1.45e+02	1.58e+02	1.66e+02	1.77e+02	1.95e+02	1.64e+02
NI	62	1.54e+01	1.55e+01	1.40e+01	1.56e+01	1.53e+01	4.79e+01	8.64e+01	1.59e+02	2.75e+02	3.64e+02	4.92e+02	9.76e+02	1.24e+03
NI	64	4.81e-17	4.77e-17	4.86e-17	4.85e-17	5.14e-17	1.07e-13	2.20e-12	2.96e-11	3.36e-11	3.62e-11	4.40e-11	3.32e-10	6.04e-09
CU	63	9.72e+00	9.73e+00	9.33e+00	9.76e+00	9.87e+00	1.30e+01	1.34e+00	5.96e-01	6.19e-01	7.16e-01	9.39e-01	2.47e+00	4.55e+00
CU	65	2.73e+00	2.71e+00	2.75e+00	2.74e+00	2.80e+00	2.71e+00	2.48e+00	2.60e+00	2.99e+00	3.24e+00	3.60e+00	3.77e+00	2.07e+00
ZN	64	1.72e+02	1.71e+02	1.76e+02	1.72e+02	1.76e+02	1.05e+02	4.14e+01	2.10e+01	1.52e+01	1.32e+01	1.15e+01	6.43e+00	2.37e+00
ZN	66	4.60e+00	4.55e+00	4.56e+00	4.64e+00	4.80e+00	6.59e+00	8.26e+00	1.33e+01	2.16e+01	2.76e+01			

Element	A	$^{22}\text{Ne} = 0$	1e-7	1e-6	1e-5	1e-4	1e-3	2e-3	5e-3	1e-2	1.4e-2	2e-2	5e-2	1e-1
C	12	2.85e+00	2.85e+00	2.85e+00	2.85e+00	2.85e+00	2.84e+00	2.83e+00	2.81e+00	2.79e+00	2.78e+00	2.76e+00	2.70e+00	2.61e+00
C	13	2.17e-06	2.17e-06	2.16e-06	2.12e-06	2.64e-06	4.90e-05	1.31e-04	4.17e-04	9.47e-04	1.41e-03	2.19e-03	7.39e-03	1.97e-02
N	14	1.02e-04	1.02e-04	1.02e-04	1.01e-04	1.14e-04	5.51e-04	1.07e-03	2.44e-03	4.41e-03	5.83e-03	7.76e-03	1.53e-02	2.34e-02
N	15	1.65e+00	1.65e+00	1.65e+00	1.59e+00	1.04e+00	7.96e-02	3.11e-02	1.07e-02	6.42e-03	5.76e-03	5.87e-03	1.28e-02	4.90e-02
O	16	2.94e+01	2.94e+01	2.94e+01	2.94e+01	2.95e+01	2.97e+01	2.99e+01	3.07e+01	3.16e+01	3.21e+01	3.25e+01	3.30e+01	3.15e+01
O	17	7.61e-04	7.62e-04	7.67e-04	8.21e-04	1.56e-03	3.04e-02	7.10e-02	1.70e-01	2.80e-01	3.41e-01	4.08e-01	5.40e-01	5.35e-01
O	18	1.33e-06	1.33e-06	1.34e-06	1.40e-06	2.36e-06	3.60e-05	8.22e-05	2.14e-04	4.33e-04	6.11e-04	8.88e-04	2.76e-03	1.06e-02
F	19	4.90e-03	4.90e-03	4.87e-03	4.65e-03	3.29e-03	9.46e-04	6.58e-04	7.86e-04	1.51e-03	2.20e-03	3.32e-03	9.38e-03	1.54e-02
NE	20	5.22e+00	5.22e+00	5.22e+00	5.22e+00	5.22e+00	5.18e+00	5.14e+00	5.03e+00	4.85e+00	4.72e+00	4.55e+00	3.93e+00	3.39e+00
NE	21	1.17e-02	1.17e-02	1.17e-02	1.20e-02	1.42e-02	7.04e-02	1.76e-01	5.77e-01	1.36e+00	2.06e+00	3.24e+00	1.14e+01	3.27e+01
NE	22	6.86e-04	6.89e-04	7.17e-04	9.97e-04	3.82e-03	3.38e-02	6.94e-02	1.87e-01	4.08e-01	6.05e-01	9.29e-01	3.01e+00	8.28e+00
NA	23	8.75e-01	8.75e-01	8.75e-01	8.73e-01	8.56e-01	7.92e-01	7.96e-01	8.64e-01	1.09e+00	1.32e+00	1.72e+00	4.55e+00	1.31e+01
MG	24	6.45e+01	6.45e+01	6.45e+01	6.45e+01	6.45e+01	6.21e+01	5.83e+01	4.82e+01	3.67e+01	3.06e+01	2.45e+01	1.36e+01	1.29e+01
MG	25	6.67e-03	6.67e-03	6.68e-03	6.82e-03	8.79e-03	9.03e-02	1.62e-01	4.26e-01	9.88e-01	1.53e+00	2.48e+00	9.71e+00	3.24e+01
MG	26	3.91e-02	3.91e-02	3.92e-02	3.97e-02	4.49e-02	1.06e-01	1.68e-01	3.45e-01	6.47e-01	9.05e-01	1.32e+00	4.28e+00	1.76e+01
AL	27	2.36e+00	2.36e+00	2.36e+00	2.36e+00	2.33e+00	4.78e+00	8.03e+00	1.43e+01	1.96e+01	2.18e+01	2.35e+01	2.73e+01	4.14e+01
SI	28	4.68e+02	4.68e+02	4.68e+02	4.68e+02	4.69e+02	4.78e+02	4.84e+02	4.91e+02	4.94e+02	4.94e+02	4.94e+02	4.87e+02	4.70e+02
SI	29	1.77e+00	1.77e+00	1.77e+00	1.79e+00	2.19e+00	7.99e+00	1.01e+01	1.49e+01	2.14e+01	2.67e+01	3.53e+01	1.05e+02	3.96e+02
SI	30	1.27e+00	1.27e+00	1.26e+00	1.22e+00	9.63e-01	1.86e+00	6.10e+00	2.44e+01	5.96e+01	8.82e+01	1.31e+02	3.64e+02	8.52e+02
P	31	1.44e+01	1.44e+01	1.43e+01	1.38e+01	9.58e+00	9.69e+00	1.72e+01	3.81e+01	6.89e+01	9.08e+01	1.20e+02	2.30e+02	2.64e+02
S	32	5.02e+02	5.02e+02	5.02e+02	5.02e+02	4.99e+02	4.91e+02	4.88e+02	4.85e+02	4.81e+02	4.77e+02	4.69e+02	4.12e+02	3.06e+02
S	33	3.65e+01	3.65e+01	3.66e+01	3.69e+01	3.97e+01	4.52e+01	5.24e+01	8.02e+01	1.16e+02	1.38e+02	1.64e+02	2.26e+02	2.06e+02
S	34	2.89e-01	2.89e-01	2.87e-01	2.72e-01	1.70e-01	5.21e+00	1.56e+01	4.89e+01	1.09e+02	1.60e+02	2.40e+02	6.26e+02	9.83e+02
S	36	5.07e-07	5.07e-07	5.09e-07	5.29e-07	8.40e-07	2.03e-03	1.36e-02	1.17e-01	5.38e-01	1.16e+00	2.91e+00	5.25e+01	4.79e+02
CL	35	1.57e+00	1.57e+00	1.56e+00	1.49e+00	9.49e-01	1.95e+00	3.29e+00	6.94e+00	1.33e+01	1.83e+01	2.51e+01	3.97e+01	3.45e+01
CL	37	2.69e+00	2.69e+00	2.69e+00	2.71e+00	2.96e+00	3.35e+00	4.08e+00	6.24e+00	9.19e+00	1.12e+01	1.37e+01	2.18e+01	2.60e+01
AR	36	5.09e+02	5.09e+02	5.09e+02	5.09e+02	5.04e+02	4.80e+02	4.66e+02	4.43e+02	4.20e+02	4.04e+02	3.83e+02	2.90e+02	1.92e+02
AR	38	3.48e-02	3.48e-02	3.47e-02	3.39e-02	2.49e-02	3.23e+00	8.39e+00	2.60e+01	6.10e+01	9.21e+01	1.41e+02	3.77e+02	6.11e+02
AR	40	3.23e-08	3.23e-08	3.24e-08	3.36e-08	4.92e-08	8.59e-05	4.79e-04	3.54e-03	1.81e-02	4.60e-02	1.42e-01	3.12e+00	1.67e+01
K	39	4.41e-01	4.40e-01	4.39e-01	4.21e-01	3.41e-01	3.31e+00	5.73e+00	1.15e+01	1.97e+01	2.56e+01	3.33e+01	5.48e+01	5.24e+01
K	40	3.13e-04	3.13e-04	3.14e-04	3.23e-04	4.70e-04	1.06e-01	2.30e-01	7.44e-01	2.45e+00	4.68e+00	9.15e+00	2.28e+01	8.73e+00
K	41	1.62e+00	1.62e+00	1.63e+00	1.71e+00	2.47e+00	5.14e+00	6.90e+00	1.12e+01	1.69e+01	2.07e+01	2.54e+01	3.66e+01	3.20e+01
CA	40	4.11e+02	4.11e+02	4.11e+02	4.10e+02	4.06e+02	3.77e+02	3.58e+02	3.27e+02	2.97e+02	2.79e+02	2.57e+02	1.81e+02	1.15e+02
CA	42	1.03e-02	1.02e-02	1.02e-02	9.37e-03	1.47e-03	1.44e+00	4.09e+00	1.44e+01	3.68e+01	5.77e+01	9.12e+01	2.38e+02	3.13e+02
CA	43	2.40e-01	2.40e-01	2.36e-01	1.97e-01	1.63e-03	7.15e-03	2.01e-02	8.72e-02	2.72e-01	4.57e-01	7.53e-01	1.77e+00	2.38e+00
CA	44	7.95e+00	7.95e+00	7.95e+00	7.94e+00	7.82e+00	7.06e+00	6.59e+00	5.82e+00	5.13e+00	4.75e+00	4.32e+00	3.02e+00	2.01e+00
CA	46	7.65e-13	7.66e-13	7.75e-13	8.80e-13	3.08e-12	5.79e-08	9.50e-07	2.88e-05	3.67e-04	1.37e-03	5.81e-03	1.43e-01	8.16e-01
CA	48	3.21e-20	3.24e-20	3.47e-20	5.78e-20	2.00e-19	2.33e-16	1.29e-14	1.36e-12	4.99e-11	3.44e-10	3.33e-09	1.52e-06	1.52e-04
SC	45	4.51e-01	4.52e-01	4.57e-01	5.11e-01	9.85e-01	1.56e+00	1.90e+00	2.58e+00	3.35e+00	3.84e+00	4.41e+00	5.03e+00	4.17e+00
TI	46	6.07e-03	6.08e-03	6.12e-03	6.31e-03	1.35e-02	1.05e+00	3.13e+00	1.21e+01	3.16e+01	4.89e+01	7.54e+01	1.84e+02	2.38e+02
TI	47	8.17e-02	8.16e-02	8.10e-02	7.46e-02	1.78e-02	7.69e-02	1.38e-01	3.30e-01	7.29e-01	1.10e+00	1.69e+00	4.62e+00	8.48e+00
TI	48	9.19e+01	9.19e+01	9.19e+01	9.18e+01	9.13e+01	8.70e+01	8.34e+01	7.53e+01	6.56e+01	5.95e+01	5.22e+01	3.14e+01	1.98e+01
TI	49	2.32e+00	2.33e+00	2.38e+00	3.00e+00	2.32e+01	3.16e+01	3.68e+01	4.85e+01	6.03e+01	6.58e+01	7.04e+01	6.78e+01	6.64e+01
TI	50	5.51e-13	5.52e-13	5.59e-13	6.35e-13	2.03e-12	2.45e-07	4.34e-06	1.38e-04	1.41e-03	3.40e-03	6.51e-03	1.63e-02	6.51e-02
V	50	1.25e-07	1.25e-07	1.26e-07	1.40e-07	5.31e-07	3.59e-03	2.24e-02	3.02e-01	2.02e+00	3.96e+00	5.95e+00	1.24e+01	6.12e+01
V	51	8.71e+00	8.71e+00	8.70e+00	8.59e+00	1.46e+00	1.87e+01	3.02e+01	5.41e+01	8.08e+01	9.67e+01	1.15e+02	1.68e+02	3.19e+02
CR	50	2.71e-01	2.72e-01	2.75e-01	3.14e-01	4.24e-01	1.01e+01	2.40e+01	7.18e+01	1.63e+02	2.42e+02	3.69e+02	1.09e+03	2.02e+03
CR	52	2.15e+02	2.15e+02	2.15e+02	2.15e+02	2.14e+02	2.06e+02	1.98e+02	1.81e+02	1.60e+02	1.47e+02	1.32e+02	1.08e+02	2.49e+02
CR	53	2.76e+01	2.76e+01	2.78e+01	2.98e+01	5.05e+01	6.46e+01	7.64e+01	1.02e+02	1.29e+02	1.43e+02	1.58e+02	2.34e+02	5.03e+02
CR	54	8.11e-10	8.13e-10	8.37e-10	1.15e-09	4.05e-08	1.49e-04	7.23e-04	5.89e-03	2.60e-02	5.35e-02	1.19e-01	1.25e+00	9.00e+00
MN	55	1.95e+00	1.95e+00	1.93e+00	1.75e+00	1.98e+00	2.38e+01	3.67e+01	6.14e+01	8.71e+01	1.02e+02	1.19e+02	1.78e+02	2.89e+02
FE	54	1.66e-01	1.66e-01	1.66e-01	1.66e-01	1.95e-01	9.67e-00	2.11e+01	5.64e+01	1.16e+02	1.65e+02	2.36e+02	5.52e+02	8.77e+02
FE	56	3.86e+01	3.86e+01	3.86e+01	3.85e+01	3.85e+01	3.72e+01	3.61e+01	3.33e+01	3.00e+01	2.79e+01	2.55e+01	1.91e+01	1.84e+01
FE	57	5.25e+00	5.25e+00	5.25e+00	5.27e+00	5.44e+00	6.91e+00	8.22e+00	1.12e+01	1.43e+01	1.60e+01	1.78e+01	2.16e+01	2.51e+01
FE	58	6.56e-09	6.57e-09	6.69e-09	7.94e-09	4.87e-08	1.07e-05	3.63e-05	2.27e-04	9.20e-04	1.85e-03	3.91e-03	3.04e-02	1.37e-01
CO	59	5.89e-02	5.88e-02	5.84e-02	5.38e-02	4.10e-03	4.60e-03	1.10e-02	4.33e-02	1.30e-01	2.23e-01	3.96e-01	1.89e+00	4.15e+00
NI	58	4.84e-01	4.84e-01	4.86e-01	5.01e-01	6.30e-01	1.60e+00	2.69e+00	6.08e+00	1.18e+01	1.63e+01	2.27e+01	4.76e+01	7.07e+01
NI	60	1.85e-02	1.84e-02	1.81e-02	1.53e-02	2.82e-04	3.90e-04	1.60e-03	1.07e-02	5.00e-02	1.05e-01	2.32e-01	1.79e+00	7.02e+00
NI	61	7.65e-04	7.64e-04	7.53e-04	6.57e-04	3.96e-05	7.27e-06	1.62e-05	7.42e-05	2.86e-04	5.94e-04	1.32e-03	1.08e-02	5.39e-02
NI	62	1.98e-06	1.98e-06	1.99e-06	2.05e-06	2.66e-06	4.88e-06	9.59e-06	2.78e-05	6.32e-05	1.05e-04	1.99e-04	1.69e-03	1.26e-02
NI	64	3.85e-20	3.86e-20	3.91e-20	4.42e-20	1.87e-19	5.60e-13	8.06e-12	8.66e-11	7.71e-11	7.61e-11	8.80e-11	3.73e-10	6.71e-09
CU	63	1.43e-08	1.43e-08	1.45e-08	1.69e-08	6.90e-08	4.49e-08	1.04e-07	4.83e-07	2.21e-06	5.24e-06	1.32e-05	1.35e-04	6.42e-04
CU	65	1.60e-10	1.60e-10	1.57e-10	1.32e-10	1.47e-11	3.36e-10	7.34e-10	2.29e-09	5.38e-09	1.17e-08	2.81e-08	2.46e-07	9.85e-07
ZN	64	2.60e-09	2.60e-09	2.60e-09	2.64e-09	6.91e-09	5.21e-08	1.37e-07	8.19e-07	3.74e-06	7.87e-06	1.70e-05	1.08e-04	2.96e-04
ZN	66	7.12e-12	7.11e-12	7.04e-12	6.37e-12	3.00e-12	2.11e-09	1.23e-08	4.20e-08	1.83e-08	1.74e-08	3.0		

section 3.2 for a full description of the burning regimes). Explosive oxygen burning is the direct fusion of two ^{16}O nuclei, resulting in a number of possible products as described in Woosley, Heger, and Weaver (2002):



We see production of the intermediate mass elements in the range of 2-5 GK, lighter elements being produced preferentially in cooler conditions. we therefore observe both carbon burning ($T_9 \sim 2$ GK) and explosive oxygen burning ($T_9 \sim 3$ GK). In the lower peak temperature regime, rates of photodisintegration are low and fusion dominates. In the higher temperature explosive burning, these rates are similar. The majority of burning however follows the reactions stated above - the three decay channels of S^* - which have varying branching ratios which determine the most likely products. ^{28}Si and ^{32}S constitute 90% of the products of oxygen burning (Woosley, Heger, and Weaver, 2002).

The α chain isotopes are produced through freeze out from NSE. These are ^{24}Mg , ^{28}Si , ^{32}S and ^{36}Ar . The large peak in production in the iron group arises from the complete destruction of the ^{12}C and ^{16}O nuclei to α particles, and their subsequent recombination, as the temperature drops after the passing of the shock wave. For a given Z in the low to intermediate mass isotopes ($A < 45$), the lightest stable nucleus of that element is the most overproduced at low metallicities. As the metallicity of the system increases, we see a boost in production of the heavier isotopes of a given element. The bulk of the iron group material is formed in the freeze out from NSE, at high central densities.

These high density regions modify the Y_e of the material undergoing nucleosynthesis through electron capture reactions, resulting in a less pronounced dependence on the initial metallicity of the progenitor.

Brachwitz et al. (2000) discuss in detail the effect of electron capture rates and the Y_e of the progenitor on the ejected composition of the iron group ejecta, finding that their improved electron capture rates determined through a shell model monte carlo simulation changes the production of ^{48}Ca , ^{48}Ti , ^{54}Cr , $^{54,58}\text{Fe}$, and ^{58}Ni . This effect is seen in the composition of the iron group in figure 3.1, where the changing Y_e is caused by the initial composition shift from T1.4Z0.0 to T1.4Z0 rather than through a change in the electron capture rates. ^{58}Ni increases by a factor of 2 between the $Z = 0$ and $Z = 0.1$ panels. An even larger effect on the abundance of ^{54}Fe is observed - increasing by a factor of 5 between the same models. Conversely, in the lower iron group region (^{48}Ca , ^{48}Ti) we do not see this same strong dependency on the Y_e of the progenitor, for ^{48}Ti production is consistent across the range of metallicities investigated, for ^{48}Ca production is very low - going from 1.62×10^{-12} to 6.94×10^{-12} by mass fraction across the metallicity range. Although there is a factor of 4 difference in production, there is only a trace amount of ^{48}Ca ejected from the system.

Brachwitz et al. (2000) find that odd-odd nuclei and odd-A nuclei have the largest effect on the Y_e of the SNIa explosion. The choice of electron capture reactions for these nuclei in particular are therefore key to our post-processing results. Gamow-Teller back resonances in astrophysical conditions significantly boost electron capture rates (Brachwitz et al., 2000). Due to the dense conditions in the SNIa explosion, forbidden transitions are negligible and these resonances dominate (Fuller, Fowler, and Newman, 1982). In addition to this Fuller, Fowler, and Newman (1982) also highlight the importance of the neutron closed shells in SNIa nucleosynthesis, which block further electron captures.

The middle panel of figure 3.1 illustrates the effect of the decreased Y_e in this model. Through the span of our models we range from a Y_e of 0.5 at $Z = 0$, to a value of Y_e of 0.495 at $Z = 0.1$. We see a significant boost in the production of heavier isotopes in the $A < 50$ region, and some change in the production in the central region. The odd-even effect begins to appear in the isotopic chains (it is already apparent from the absence of, for example, an overproduction of Al) as the numbers of free neutrons in the supernova increases. We see that there is a larger overproduction of even-even isotopes, due to the larger neutron capture cross-section for those nuclei with odd numbers of neutrons. The odd-even effect is more pronounced in the T1.4Z0.1 run, and the nucleosynthesis shifts in all regions to more neutron rich isotopes, due to the decreased Y_e .

Comparing figures 3.1 and 3.2, S1.0Z0 shows a similar distribution to T1.4Z0 in the $A < 50$ region, the iron group region is less abundant and efficient production in a given element is spread over a smaller number of isotopes. Trends for the $A < 50$ isotopes are similar between S1.0Z0 and T1.4Z0, and S1.0Z0.014 and T1.4Z0.014, as these are produced in very similar conditions between the two sets of model. While the most abundant isotopes of a given iron group element are produced in broadly the same proportion as for the T1.4 cases, heavier isotopes of a given element are less produced than in their T1.4 counterpart - ^{64}Ni has a production factor of 1.16 in the T1.4Z0 model, 17 orders of magnitude larger than the S1.0Z0 model. Similarly, there are 11 orders of magnitude difference in the ^{58}Fe production factor.

Increasing the initial metallicity from $Z = 0$ to $Z = 0.014$ results in a small overproduction of Ge in the S1.0Z0.014 model. In the S1.0Z0.1 model it results in a further boost, however a number of different elements synthesised in the SN explosion remains the same. We see a similar distribution of the iron group isotopic production factors between T1.4Z0.1 and S1.0Z0.1 as well as in the lower mass region.

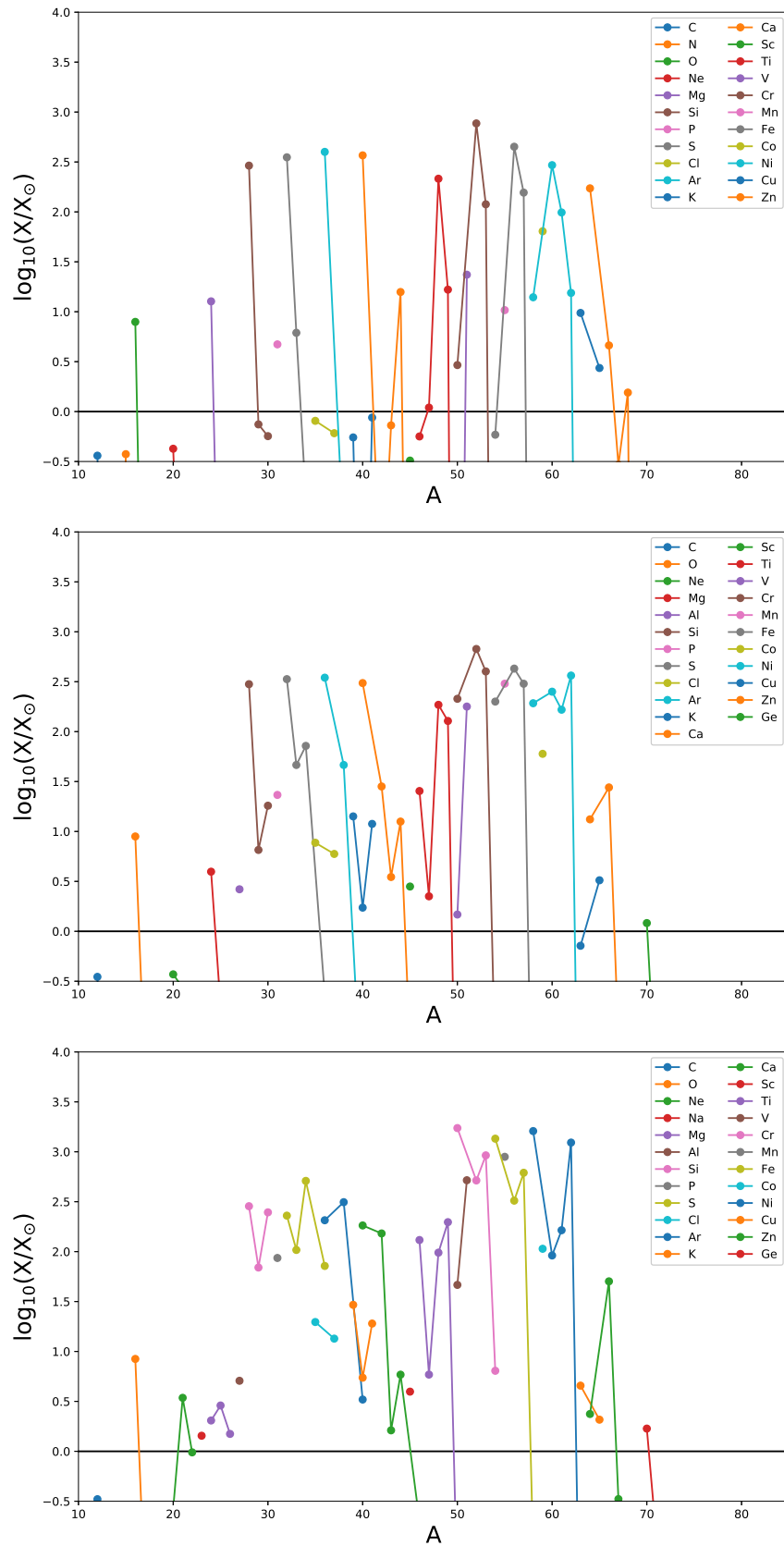


FIGURE 3.2: Production factors for models S1.0Z0 (top), S1.0Z0.014 (middle) and S1.0Z0.1 (bottom).

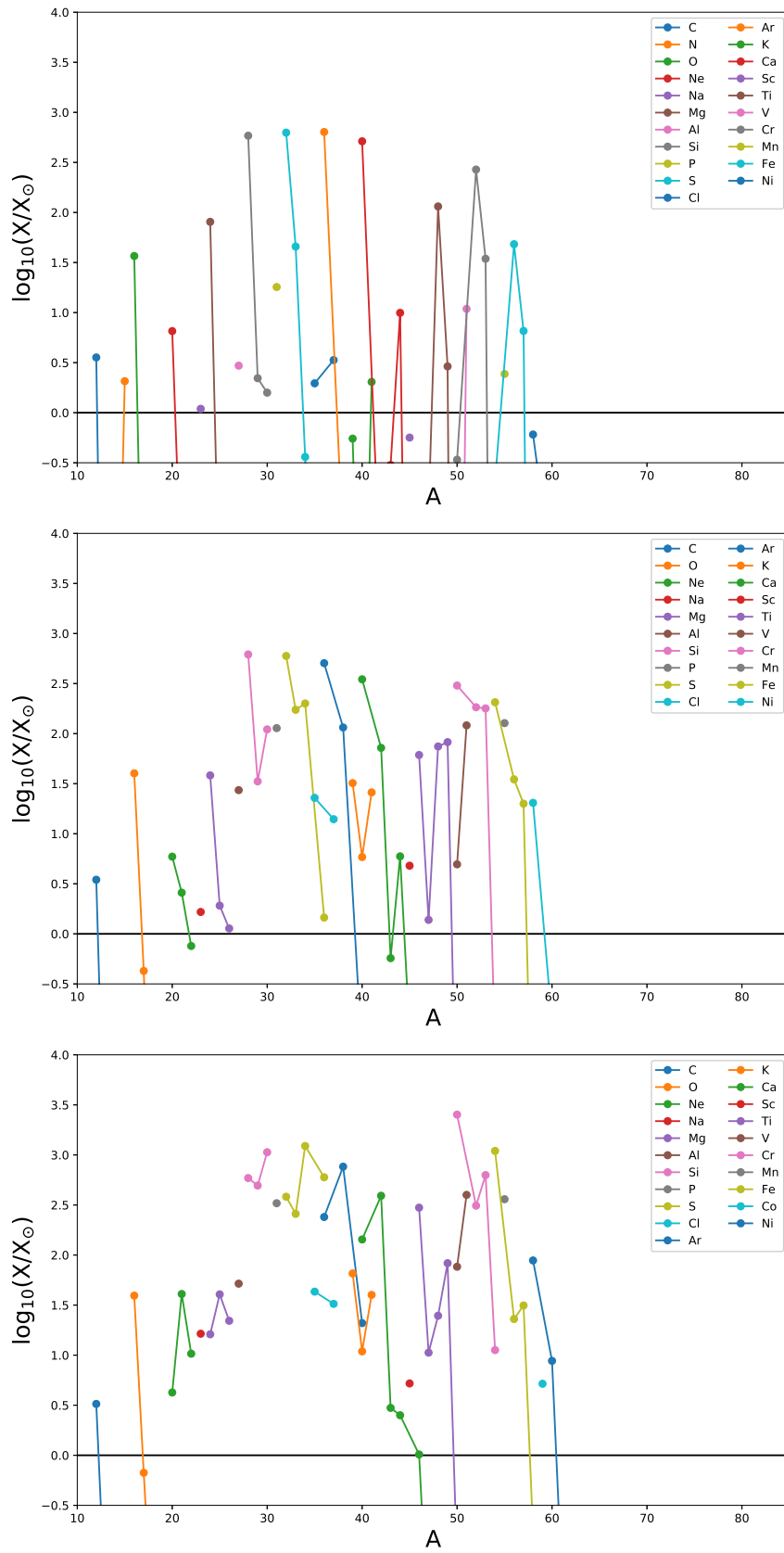


FIGURE 3.3: Production factors for models M0.8Z0 (top), M0.8Z0.014 (middle) and M0.8Z0.1 (bottom).

M0.8Z0 shows a large reduction in the production of iron group isotopes as compared with T1.4Z0 and S1.0Z0, and a reduction in the maximum proton number reached with nucleosynthesis stopping at Ni. Lower mass nuclei such as Si and S dominate, as none of the material in the explosion reaches NSE conditions. The majority of the ejecta is dominated by the products of explosive C and explosive O burning. Whilst the distributions of production factors for individual isotopes is similar, there are significant differences in the magnitude of production between the three $Z = 0.1$ models. Fe, for instance, is highly suppressed in the M0.8Z0.1 model, where as Cr remains unchanged within a factor of 5 for ^{52}Cr - the most abundant isotope of Cr.

3.2 Yields Analysis By Element

In this section we describe the production of each stable isotope of each element between C and Se, for each of the three classes of model investigated. Where possible, in the cooler non-NSE regimes, we highlight the key reactions which drive the production of the stable isotopes and their radiogenic contributions. Note that in some figures in this chapter relating to the T1.4 models, there are sharp spikes in production. This is due to the two dimensional nature of the models, which causes some particles with similar peak temperatures but different density conditions to be presented next to each other in the graphs.

3.2.1 Oxygen

Oxygen has 3 stable isotopes: ^{16}O , ^{17}O and ^{18}O . SNIa are not expected to be a significant source of oxygen - ^{16}O is largely produced in massive stars during He burning, ^{17}O is synthesised in novae in the hot CNO cycle (Romano et al., 2017), and ^{18}O is a product of partial He burning, again in massive stars (Woosley, Heger, and Weaver, 2002). Kobayashi, Karakas, and Lugaro

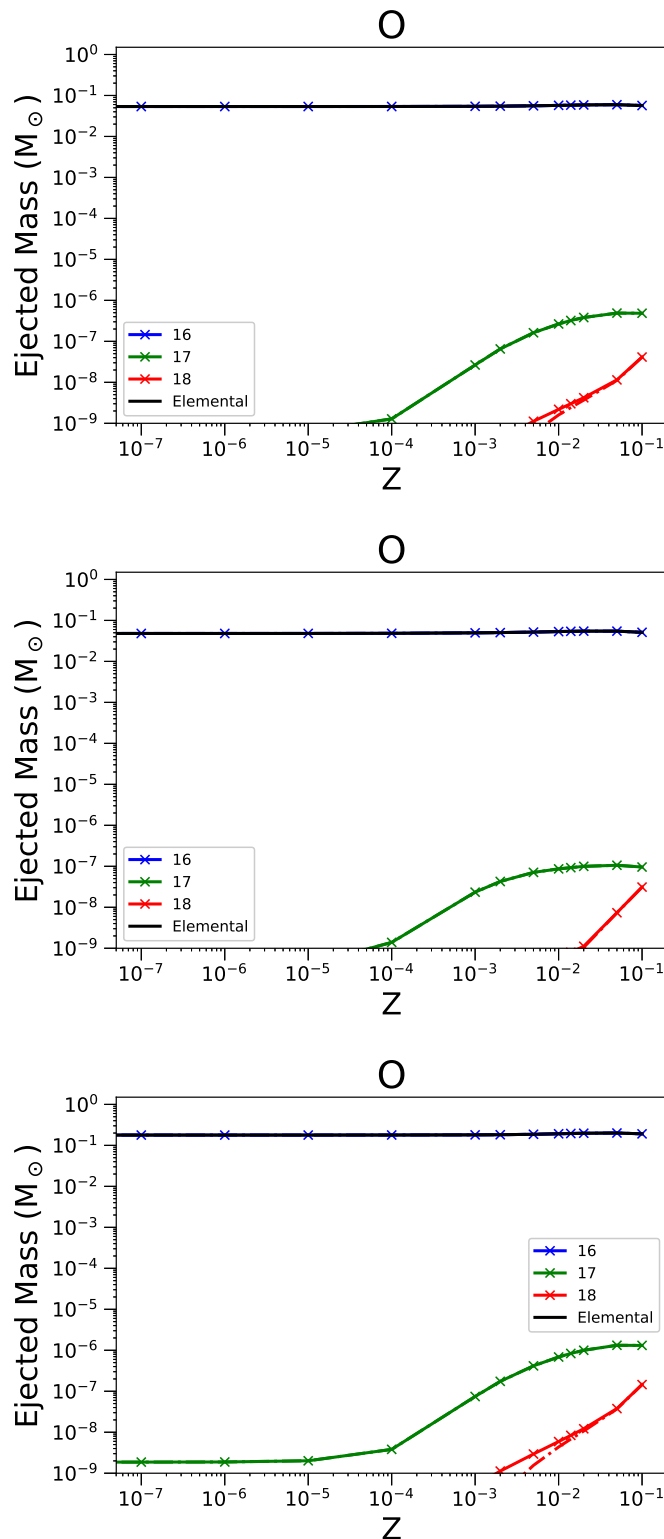


FIGURE 3.4: The ejected mass for the element O and its stable isotopes is shown with respect to initial metallicity. The elemental yields take into account radiogenic contributions. For isotopes, decayed and undecayed abundances are shown (continuous lines with crosses and dot-dashed lines with empty circles, respectively). Data is presented for the T1.4 (upper panel), S1.0 (middle panel) and M0.8 (lower panel).

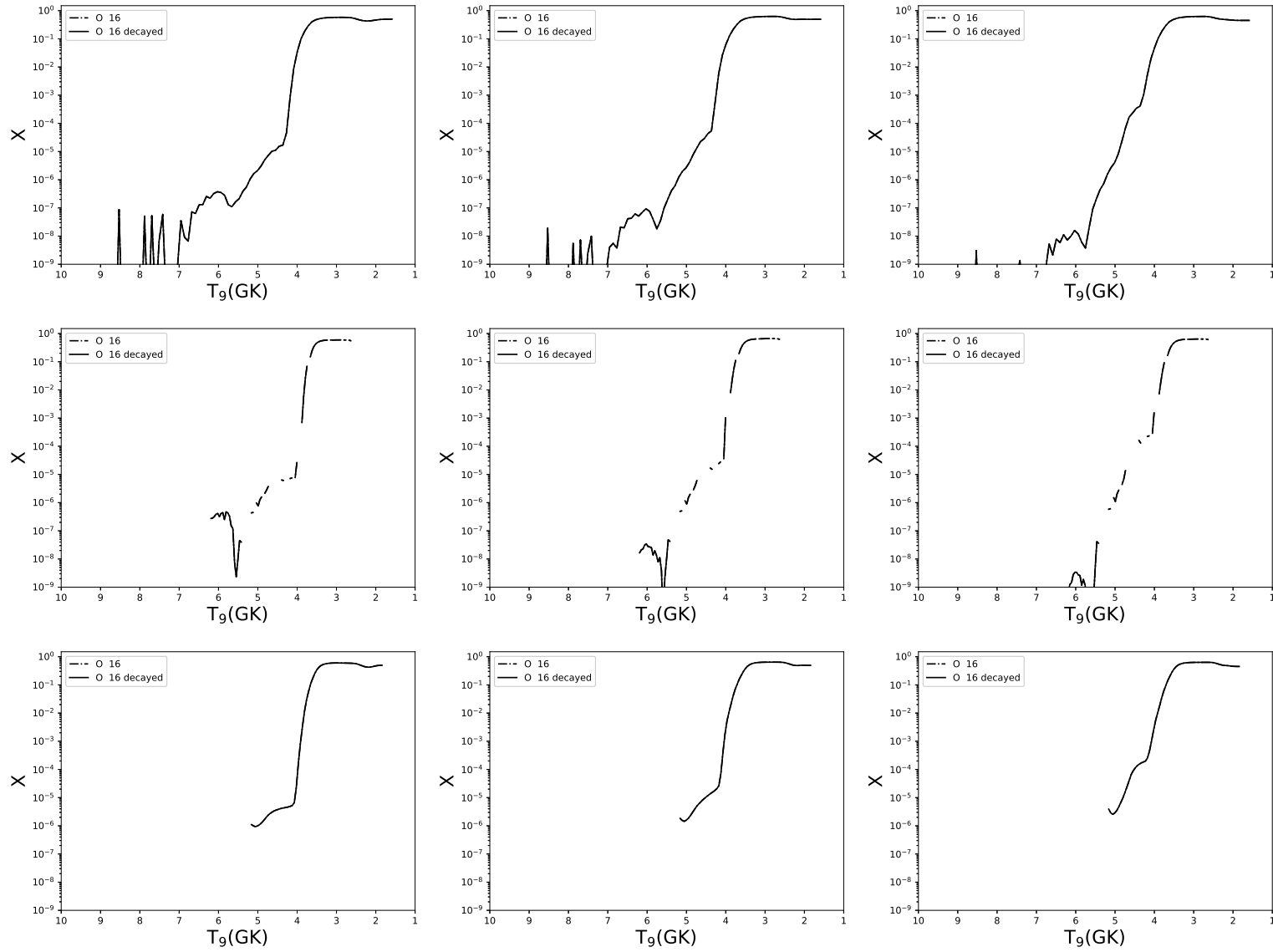


FIGURE 3.5: Top panels: The ^{16}O abundance is shown with respect to the explosion temperature peak (continuous black line) for the models T1.4Z0 (left), T1.4Z0.014 (middle) and T1.4Z0.1 (right) at $Z=0$, $Z=0.014$ and $Z=0.1$, respectively. ^{16}O abundances are shown with contributions from radioactive species, which are negligible in this case. Middle Panels: As for top panels, but for models S1.0Z0, S1.0Z0.014 and S1.0Z0.1, respectively. Bottom Panels: As for top panels, but for models M0.8Z0, M0.8Z0.014 and M0.8Z0.1, respectively.

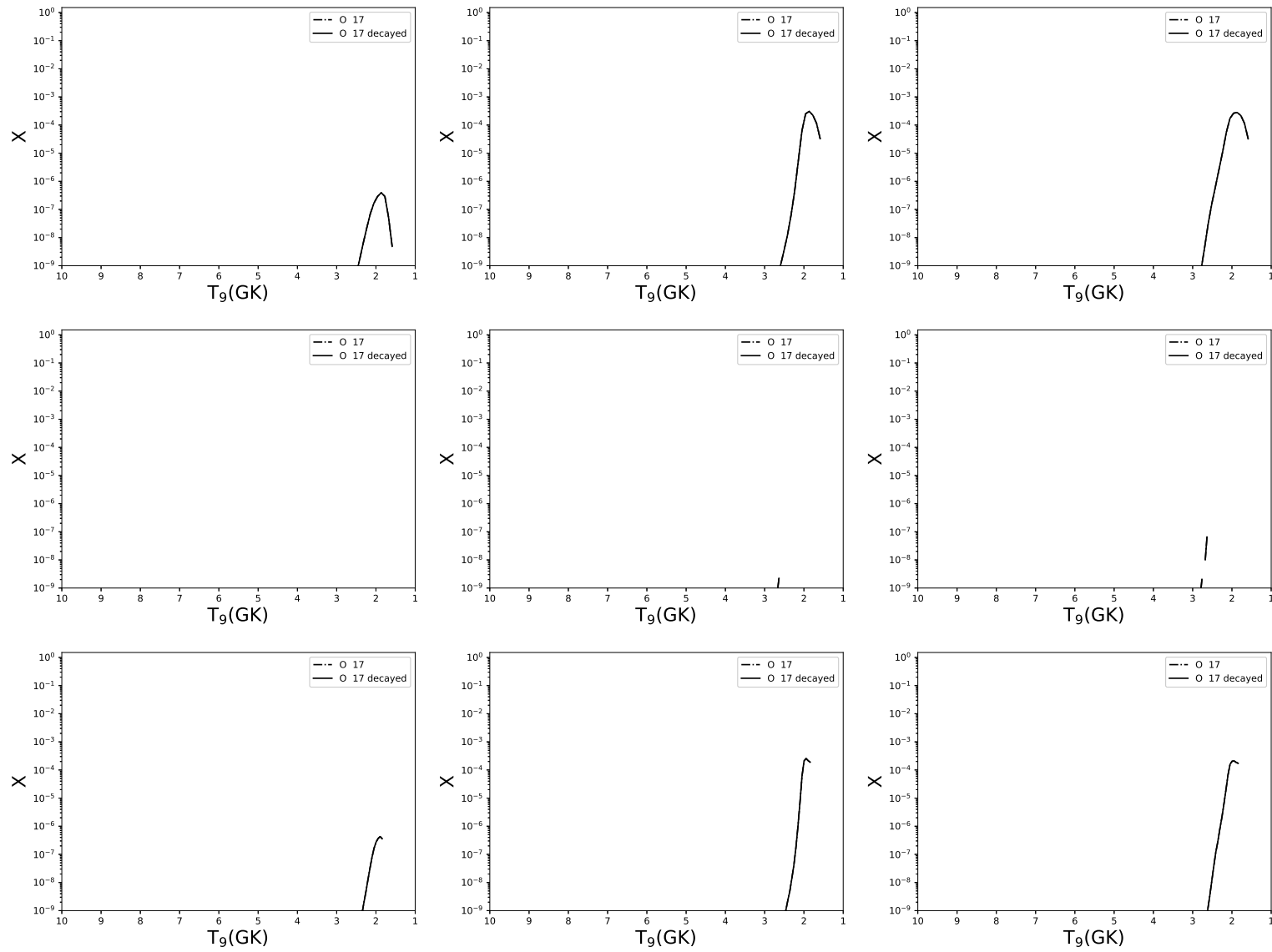


FIGURE 3.6: The abundance distributions of ^{17}O are shown, arranged as in figure 3.5. With metallicities of $Z = 0, 0.014$ and 0.1 from left to right, and the three categories of model - T1.4, S1.0 and M0.8 - from top to bottom.

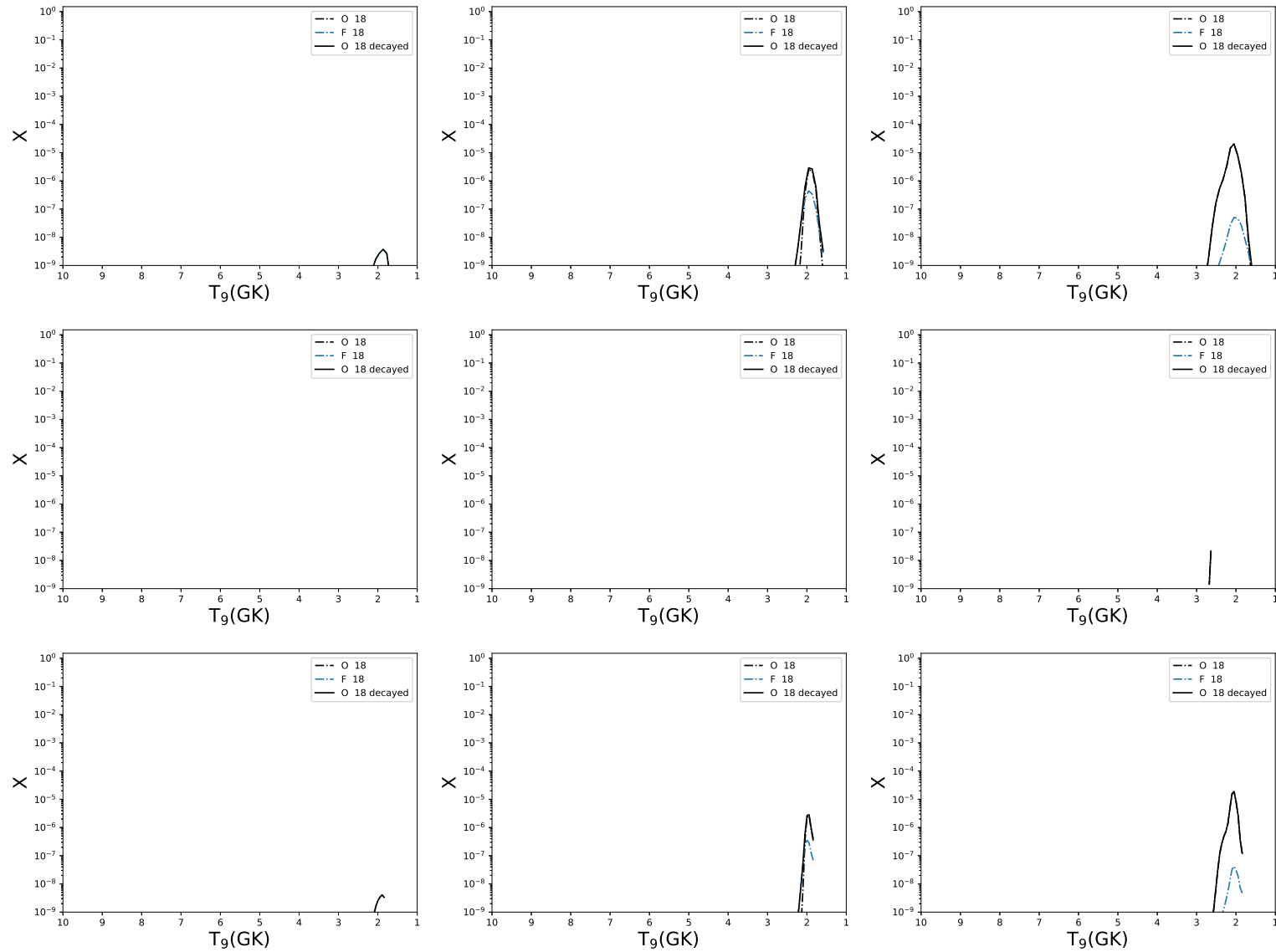


FIGURE 3.7: The abundance distributions of ^{18}O are shown, arranged as in figure 3.5. With metallicities of $Z = 0, 0.014$ and 0.1 from left to right, and the three categories of model - T1.4, S1.0 and M0.8 - from top to bottom. Radiogenic contributions from ^{18}F are highlighted.

(2020) show that without novae, the evolution of [O/H] vs [Fe/H] can be reproduced for the Milky Way, due to the relatively low abundance of ^{17}O and ^{18}O .

Figure 3.4 shows our first plot of ejected mass vs metallicity, here for oxygen. These plots are arranged with three panels, the most massive T1.4 models are shown in the top panels, next in the middle panel is the S1.0 models, and in the bottom panel the M0.8 models. Radiogenic contributions are given by the difference between the solid, decayed lines for a given isotope (i.e. the abundance at $t = \infty$) and the dashed lines showing direct production of that isotope (i.e. immediately after the last timestep of each run. NB.that there may be differences in the radiogenic yields from each model as they run for different lengths of time however this will only impact very short lived isotopes). The total ejected elemental mass is also shown with a solid black line.

In figure 3.4 we show the total ejected mass of elemental oxygen as a function of Z for each model increases with decreasing mass of the progenitor. The oxygen ejected in our models is the unburnt fuel remaining after the explosion, which there is more of in the lower mass model M0.8. We see a very weak trend with metallicity leading to a increase in the ejected mass of ^{16}O with increasing initial metallicity. In model T1.4, we go from an ejected mass of ^{16}O of 5.37×10^{-2} at $Z = 0$ to 5.68×10^{-2} at $Z = 0.1$, the S1.0 models increase from 4.81 to 5.12×10^{-2} , and the M0.8 models from 1.79 to 1.91×10^{-1} . In all models we see a secondary component contribution to ^{17}O and ^{18}O , with similar behavior for all three masses of model, a rise in abundance beginning at $Z = 10^{-4}$ and rising to an ejected mass of approximately $10^{-7} M_{\odot}$ at around solar metallicity, before plateauing.

Figure 3.5 is the first 9-panel plot in this work. In it, the models investigated are shown in three rows, from T1.4 models in the top row to S1.0 in the middle and M0.8 in the bottom row. In the columns from left to right we increase the initial metallicity from $Z = 0$ to $Z = Z_{\odot}$ to $Z = 0.1$. In each of these

9 panels, the peak temperature of each particle is shown on the x-axis, the y-axis shows the mass fraction of a given isotope at in each trajectory at the end of nucleosynthesis. We note an artefact in the plots of the S1.0 models due to the relative sparsity of data (10^2 particles compared to 10^4 for the T1.4 and M0.8 models). Because of this the data, at times, appears incomplete in these figures. Where this occurs, we discuss the trends as the would appear without these effects. The use of peak temperature as the defining characteristic for a particle is important for those trajectories in two dimensions, as a simple radial distance would not represent the trends seen in the T1.4 models correctly. Because of this, the trajectories are sorted in order of peak temperature which can be seen to give smooth trends in all models. This is due to the nucleosynthesis being largely defined by the peak temperature of a given trajectory, and to a lesser extent in the more dense models, the peak density of a trajectory.

In figures 3.5, 3.6 and 3.7 the abundance profile of the ejecta is shown with respect to the peak temperature during the WD explosion. Most of the ejected ^{16}O comes from the peak temperature range of between 1 and 3.5 GK. This is due to the oxygen fuel remaining unburnt in these relatively cooler regions, which only ignite carbon. Production of ^{17}O and ^{18}O in the 1.5 - 2.5 GK range, where 1.5 GK corresponds to the lowest peak temperatures experienced in these three models. Nucleosynthesis is very similar between our set of three models for the production of oxygen. Production of ^{17}O and ^{18}O is highly metallicity dependent and the production of ^{17}O begins at approximately $Z = 10^{-4}$ for all models. The sparsity of the data for the S1.0 models does not show production of ^{17}O at $Z = 0$ and $Z = Z_{\odot}$, or ^{18}O for the same metallicities. It can be seen in figure 3.6 however that ^{18}O has a large radiogenic contribution from ^{18}F at solar metallicity. This decreases as the initial ^{22}Ne content of the white dwarf is increased, and at super-solar metallicities it is produced directly as ^{18}O , with a very small contribution from ^{18}F of less

than 1 percent.

For ^{16}O (figure 3.5), we see that the ejected mass from unburnt ^{16}O is relatively insensitive to initial metallicity. Differences occur in the intermediate peak temperature range - between 4 and 7 GK - where destruction of ^{16}O is more efficient at higher metallicities. We see that no oxygen is ejected above approximately 4 GK in any model, due to its complete burning.

3.2.2 Neon

Neon has 3 stable isotopes: ^{20}Ne , ^{21}Ne and ^{22}Ne . ^{20}Ne is by far the dominant contributor to elemental neon abundance in the Solar System, contributing over 90% . SNIa are not a major contributor to the abundance of elemental neon in the galaxy. Pignatari et al. (2016) show that neon is mostly produced as ^{20}Ne in massive stars. Woosley, Heger, and Weaver (2002) identify neon production as occurring during carbon burning. We can see that only trace amounts of neon are produced above 4 GK in our models (that trace amount being produced as ^{20}Ne), the rest is processed in the outer, cooler layers of the WD in conditions similar to carbon burning. ^{21}Ne is also produced by carbon burning in massive stars, and ^{22}Ne in helium burning. In the models presented in this work, the mass fraction of ^{22}Ne is set as an initial condition for the composition of the WD, with a uniform distribution through all tracer particles. This is as a proxy for the metallicity of the fuel. Careful consideration must therefore be given to our reported ejected abundances of ^{22}Ne , as the initial conditions of our simulations have ^{22}Ne as the sole source of metals, and abundances of ^{22}Ne from these models may differ substantially from values obtained from the nucleosynthesis in the progenitor WD.

From figure 3.8 we see that there is a strong metallicity dependency for the production of both ^{21}Ne and ^{22}Ne , in the higher mass models a sharp

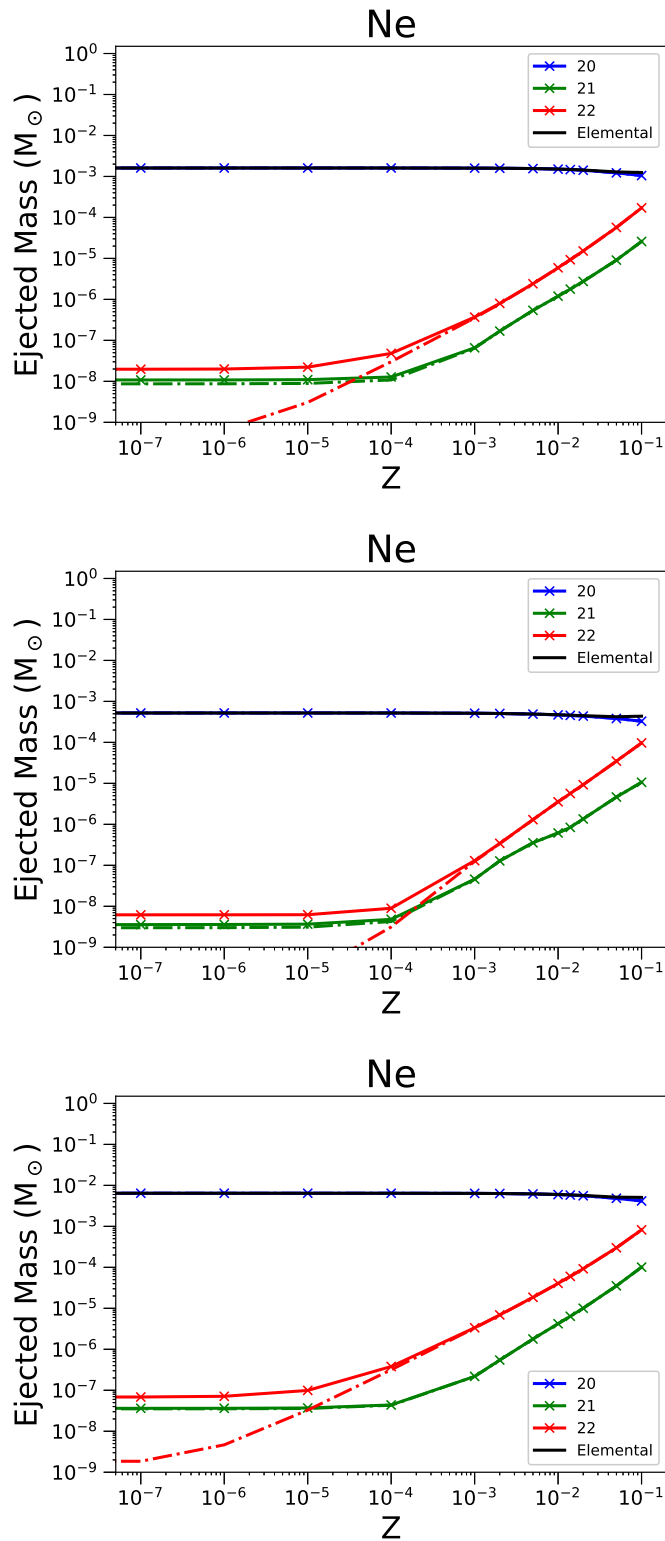


FIGURE 3.8: As in Figure 3.4 but for ejected mass of Ne, and its stable isotopes ^{20}Ne , ^{21}Ne and ^{22}Ne .

increase in the secondary production of these isotopes is observed around $Z = 10^{-4}$, where as for production of ^{22}Ne this begins at $Z = 10^{-5}$.

^{20}Ne is produced here by alpha captures on ^{16}O , as shown by its large production in the oxygen burning regions of figure 3.9. As can be seen in figure 3.9, there is a decrease in the amount of ^{20}Ne produced at intermediate peak temperatures (between 5.5 and 7 GK here) in models T1.4Z0.014, T1.4Z0.1, S1.0Z0.14 and S1.0Z0.1 and in all models at lower peak temperatures due to the increasing metallicity. This decrease is larger than the increased production of other isotopes of neon, and we see from figure 3.8 that this results in a decrease in the total ejected mass of elemental Ne. There is no significant radiogenic contribution to the abundance of ^{20}Ne in any of the models investigated here.

^{21}Ne is produced largely as a secondary isotope through the $^{20}\text{Ne}(n,\gamma)^{21}\text{Ne}$ reaction. While trace amounts are produced in the T1.4, S1.0 and M0.8 models at $Z = 0$, production increases significantly as the initial metallicity is increased due to the increased availability of neutrons in the system. We see a small primary production in the intermediate peak temperature region only in the $Z = 0$ models. This production is negligible compared to the increase in production at lower peak temperatures between 1 and 3 GK. At zero metallicity there is a non negligible contribution to the overall production from ^{21}Na of the order of a few percent. On the other hand, there is no significant radiogenic contribution to ^{21}Ne above $Z = 0$.

The total ejected mass of ^{22}Ne from our models is likely to be an overestimate, due to unprocessed ^{22}Ne in the outer layers of the WD which remain after the shockwave has passed through. We are unable to quantify the correct abundance of ^{22}Ne without a full initial abundance profile for the progenitor. Such work has been undertaken by Battino et al. (2020), who show that due to the neutron flux in the accretion phase of the WD, ^{22}Ne can be depleted in the outer layers of the WD prior to explosion. It is unlikely that

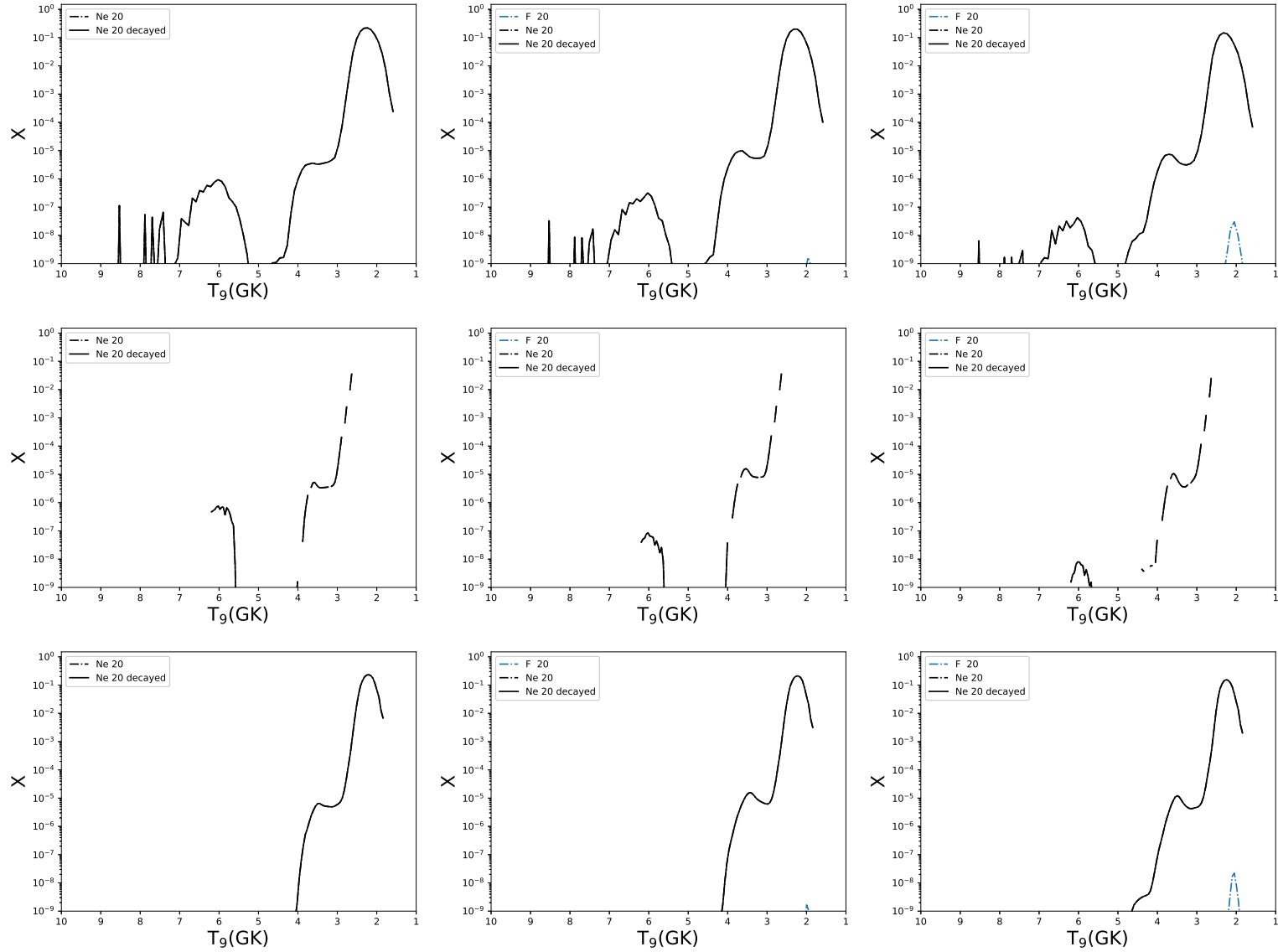


FIGURE 3.9: The abundance distributions of ^{20}Ne are shown, arranged as in figure 3.5. With metallicities of $Z = 0, 0.014$ and 0.1 from left to right, and the three categories of model - T1.4, S1.0 and M0.8 - from top to bottom.

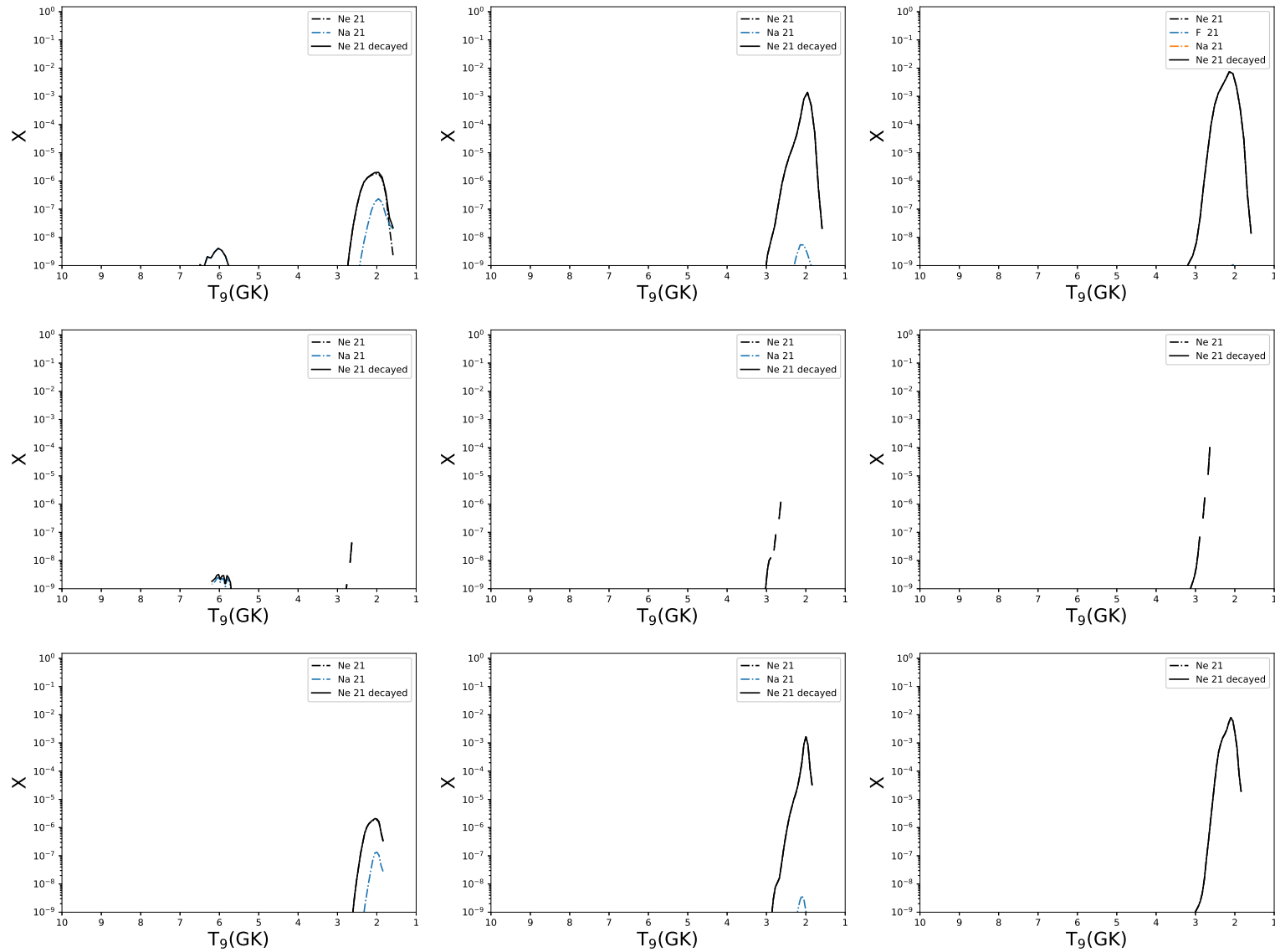


FIGURE 3.10: The abundance distributions of ^{21}Ne are shown, arranged as in figure 3.5. With metallicities of $Z = 0, 0.014$ and 0.1 from left to right, and the three categories of model - T1.4, S1.0 and M0.8 - from top to bottom.

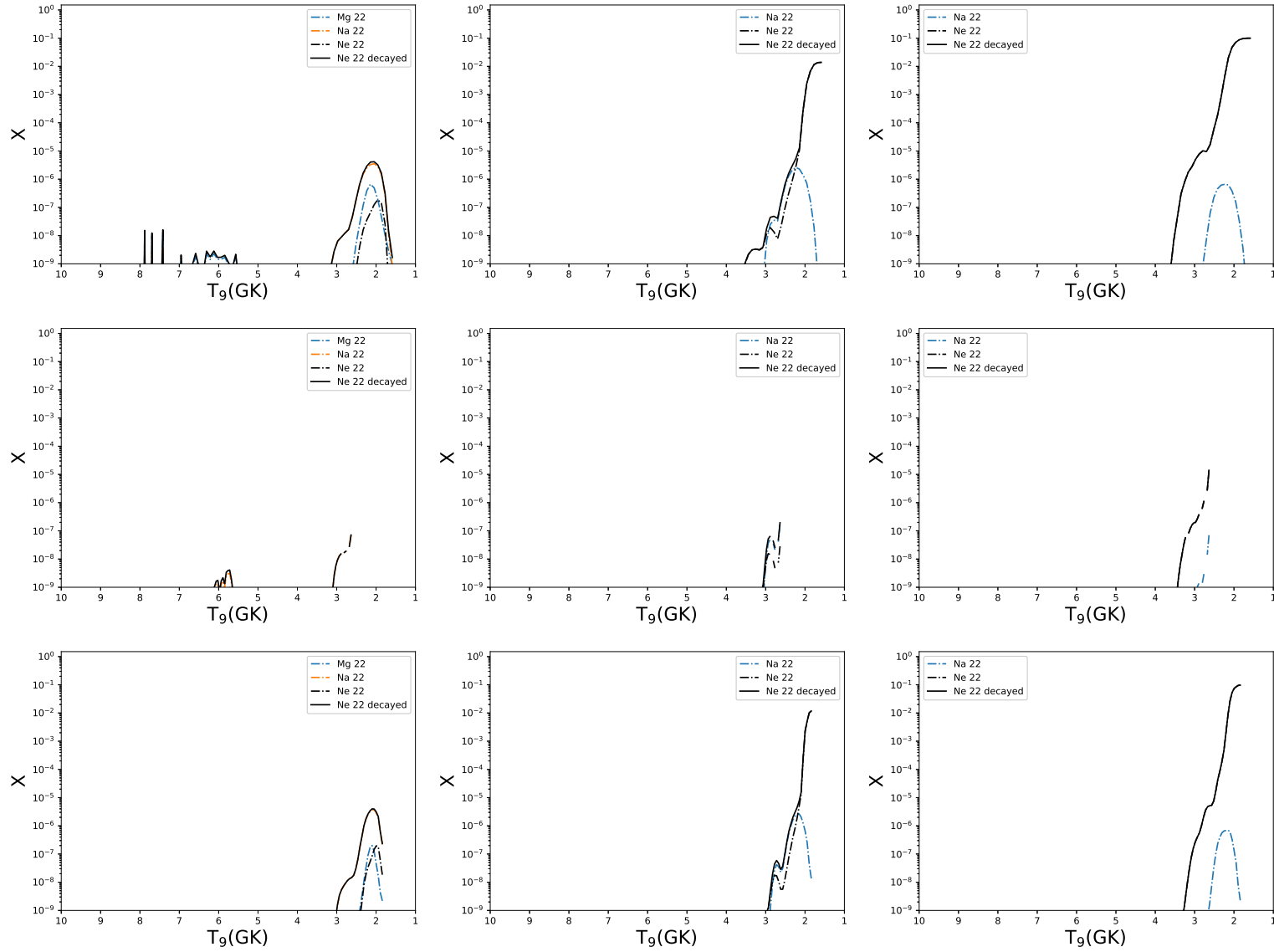


FIGURE 3.11: The abundance distributions of ^{22}Ne are shown, arranged as in figure 3.5. With metallicities of $Z = 0$, 0.014 and 0.1 from left to right, and the three categories of model - T1.4, S1.0 and M0.8 - from top to bottom. Radiogenic contributions from ^{22}Na are included.

the abundances will vary hugely from those in our outer layer however, as most of the material in the outer layers will be CNO, which is processed to ^{22}Ne .

3.2.3 Magnesium

Magnesium has 3 stable isotopes: ^{24}Mg , ^{25}Mg and ^{26}Mg . The isotopes of magnesium are primarily formed in carbon and neon burning (Woosley, Heger, and Weaver, 2002) and are not produced in SNIa efficiently. ^{24}Mg is the most abundant isotope of magnesium, and in our models magnesium is primarily ejected as ^{24}Mg . There is a strong metallicity trend for all isotopes and the relative ratios of these change significantly over the metallicity range investigated in this work.

^{24}Mg is usually a primary isotope, being formed by α captures on ^{20}Ne , however the observed trend of decreasing ^{24}Mg abundance above $Z = 10^{-3}$ in these models is due to the reaction $^{24}\text{Mg}(n, \gamma)^{25}\text{Mg}$ with the neutrons produced by the reaction $^{22}\text{Ne}(\alpha, n)^{25}\text{Mg}$. We may therefore expect the specifics of nucleosynthesis in the cooler outer layers of the WD to be dependent on both the ^{22}Ne abundance and the rate of the reaction producing neutrons. Below $Z = 10^{-3}$ the abundance of ^{22}Ne provides an insufficient flux of neutrons to change ^{24}Mg production.

Figure 3.12 presents the isotopic and elemental ejected masses of the three stable isotopes of magnesium. All models show a decrease in the ejected mass of elemental Mg at metallicities in the region of solar. As we reach super-solar metallicities, the elemental abundance of Mg increases again, as the decrease in ^{24}Mg begins to plateau and the significant increase in both ^{25}Mg and ^{26}Mg begins to compensate for the lost mass from ^{24}Mg . Secondary contributions to the abundances of ^{25}Mg and ^{26}Mg begin in the $Z=10^{-4}$ region, increasing abundances of these by over 3 orders of magnitude in all

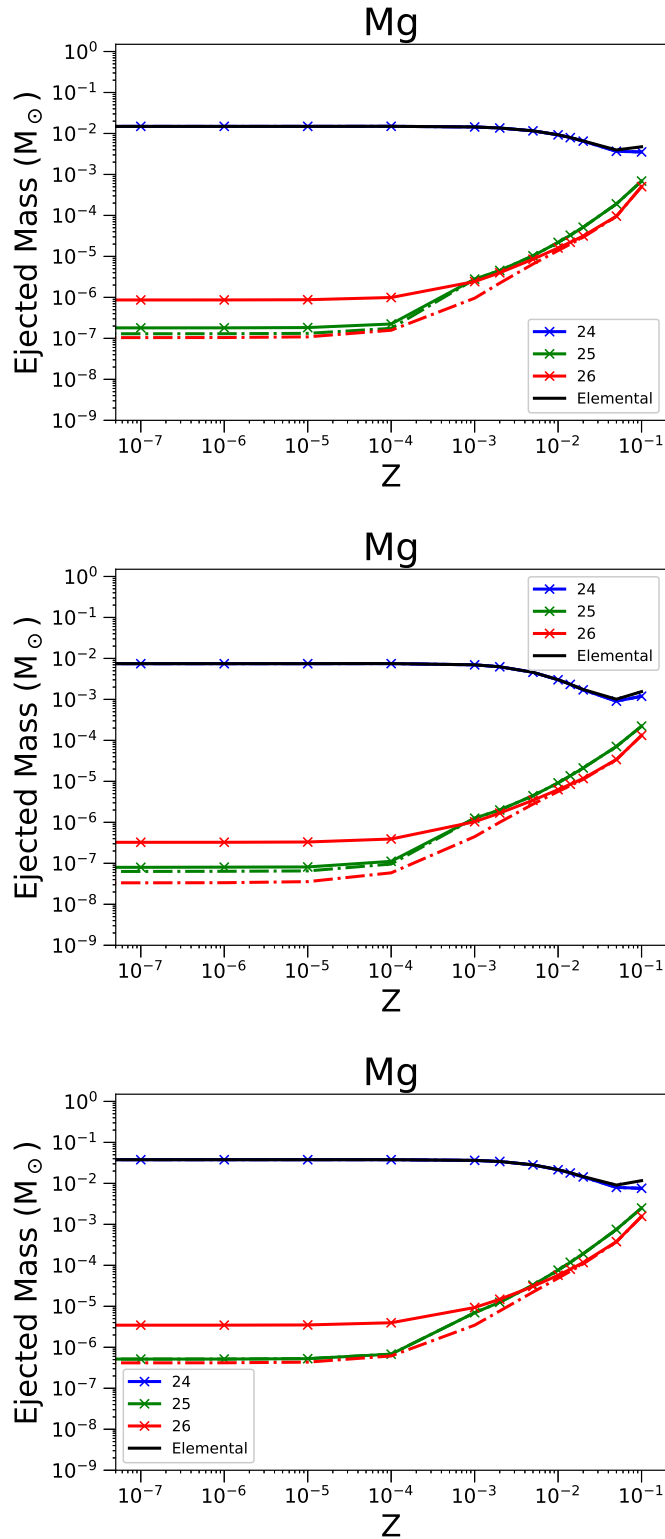
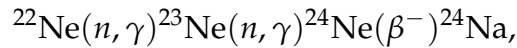


FIGURE 3.12: As in Figure 3.4 but for ejected mass of Mg, and its stable isotopes ^{24}Mg , ^{25}Mg and ^{26}Mg .

models. This is linear with the increase in ^{22}Ne for ^{25}Mg , and with a steeper increase for ^{26}Mg .

Figure 3.13 shows the contributions to the production of ^{24}Mg at different peak temperatures. The decrease with increasing metallicity comes largely from decreased production at low peak temperatures, where we see from figure 3.13 the peak production in the 2 - 3.5 GK range has fallen from a mass fraction of greater than 10% to a few percent between models T1.4Z0 and T1.4Z0.1. We see that the radiogenic contribution to ^{24}Mg increases in all models as the initial metallicity increases, with ^{24}Na becoming a contributor to the ejecta from lower peak temperature regions at $Z=0.1$, although it remains negligible. This ^{24}Na is produced in the series of reactions



the neutron flux required is again supplied by the $^{22}\text{Ne}(\alpha, n)^{25}\text{Mg}$ reaction.

From figure 3.13 we note that there is no significant contribution from radiogenic sources to the abundance of ^{24}Mg at any metallicity. There is also a small contribution from ^{24}Na but this is negligible, as seen across all models.

In the T1.4Z0 model, we see that there is a significant contribution to the ejected ^{25}Mg from ^{25}Al (Figure 3.14) in the intermediate peak temperature range. Under these conditions the majority of ^{25}Mg is produced as ^{25}Al . As can be seen in the T1.4Z0 panel, this is not the largest contributor to the ejected mass of ^{25}Mg in this model. This comes from the cooler outer layers of the explosion, where the majority of ^{25}Mg is synthesised by the $^{22}\text{Ne}(\alpha, n)^{25}\text{Mg}$ reaction.

We observe an interesting trend in the T1.4 models, whereby the intermediate temperature peak region ceases to contribute to the ejected ^{25}Mg mass as we increase the initial metallicity. This is more than compensated for by the increase in production at lower peak temperatures across the models. We

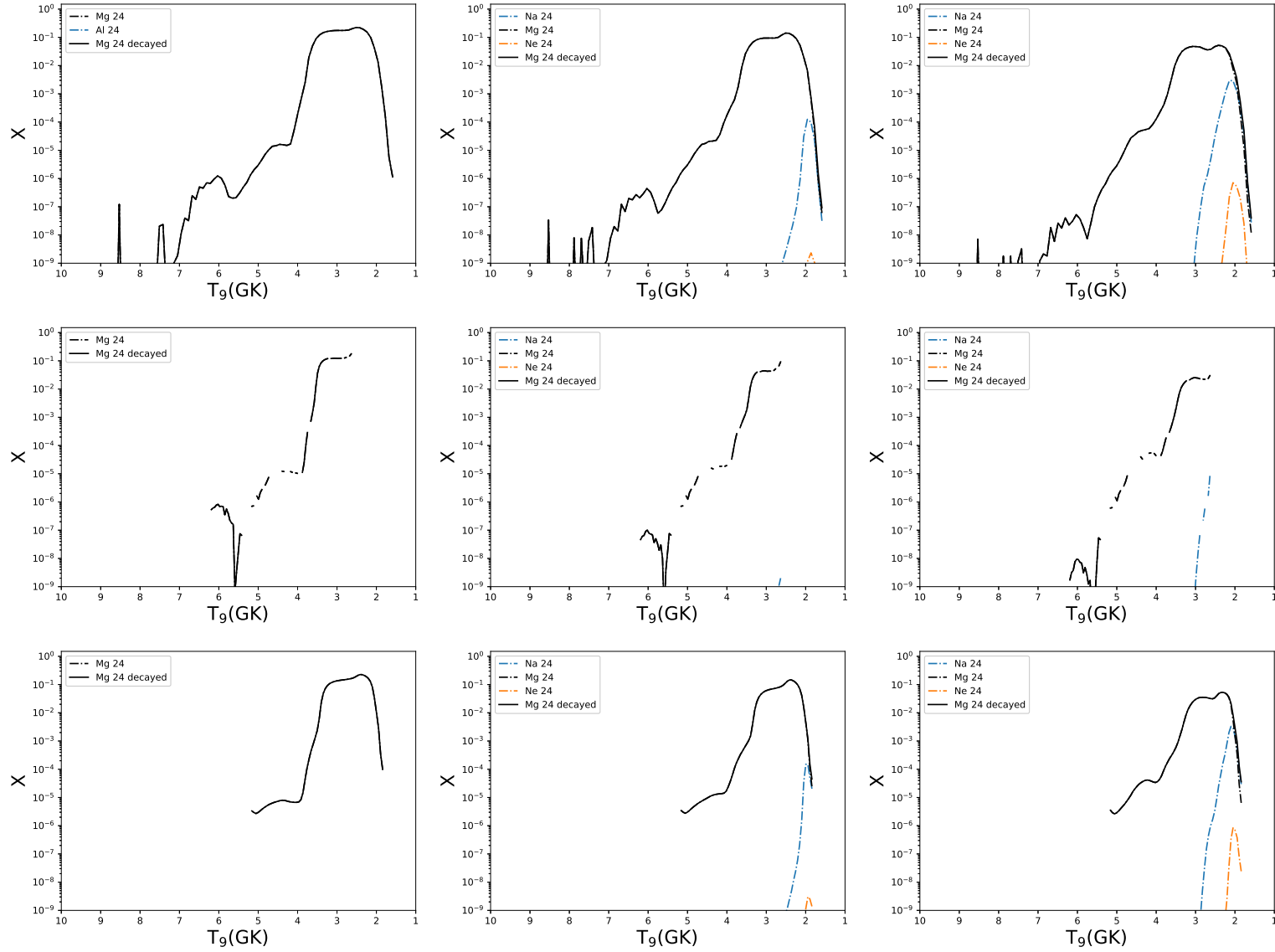


FIGURE 3.13: The abundance distributions of ^{24}Mg are shown, arranged as in figure 3.5. With metallicities of $Z = 0$, 0.014 and 0.1 from left to right, and the three categories of model - T1.4, S1.0 and M0.8 - from top to bottom. Radiogenic contributions from ^{24}Na and ^{24}Ne are shown, which become significant at $Z \geq Z_\odot$

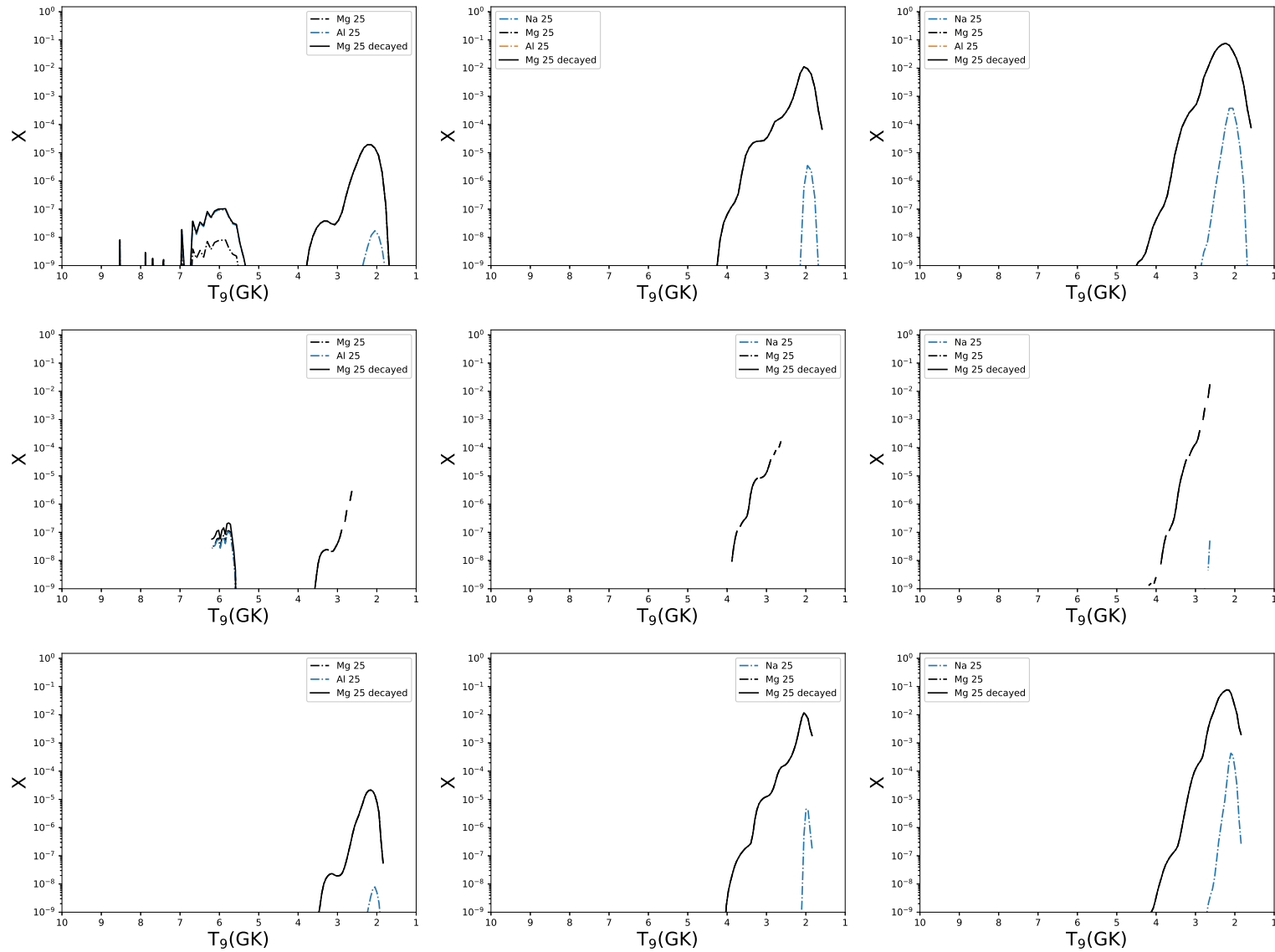


FIGURE 3.14: The abundance distributions of ^{25}Mg are shown, arranged as in figure 3.5. With metallicities of $Z = 0, 0.014$ and 0.1 from left to right, and the three categories of model - T1.4, S1.0 and M0.8 - from top to bottom.

therefore conclude that ^{25}Mg is produced as both a primary isotope, in the hotter regions, and a secondary one in the cooler outer layers.

A similar trend is observed in the S1.0 models, where we observe some production of ^{25}Al in the intermediate peak temperature layers, here around the 6 GK range (the hottest peak temperatures for this model). We observe the secondary production of ^{25}Mg , again directly as ^{25}Mg for the most part. Figure 3.14 reveals the relatively small impact these radiogenic contributions have to the overall ejected mass of ^{25}Mg across all models.

For the M0.8 models, we see that production is concentrated in the outer layers and is strongly dependent on metallicity, as is seen in the other two models. The production peak in the outer layers of M0.8Z0.1 is very similar to that of both T1.4Z0.1 and S1.0Z0.1, with the temperature range over which ^{25}Mg is produced being more similar to the S1.0 model, as we see a small shift in the tail of production from the T1.4Z0.1 model from 4.5 to 4 GK. Peak production for all models lies at approximately 2.4 GK however, so we can conclude that burning conditions in this region are very similar between the three sets.

^{26}Mg has significant radiogenic contributions to ejected mass in all models at $Z=0$. We see a broad production of ^{26}Mg as ^{26}Si and ^{26}Al in the T1.4Z0 model - ^{26}Si in the intermediate peak temperature region (4 GK - 6 GK) and ^{26}Al in the lower peak temperature region, with a more complicated interplay in the 4 - 5 GK range, where both Si and Al are produced in similar quantities. We can look at this nucleosynthesis as a superposition of the lower and intermediate peak temperature region nucleosynthesis. Direct production of ^{26}Mg does occur in the outer regions of the SNIa explosion, however it does not constitute the majority of the total ejected ^{26}Mg . As the metallicity increases in the T1.4 models, we see a dramatic change in the nucleosynthesis. Intermediate peak temperature production is eliminated, and the outer layers of the explosion dominate, with a large increase in the ejected mass from

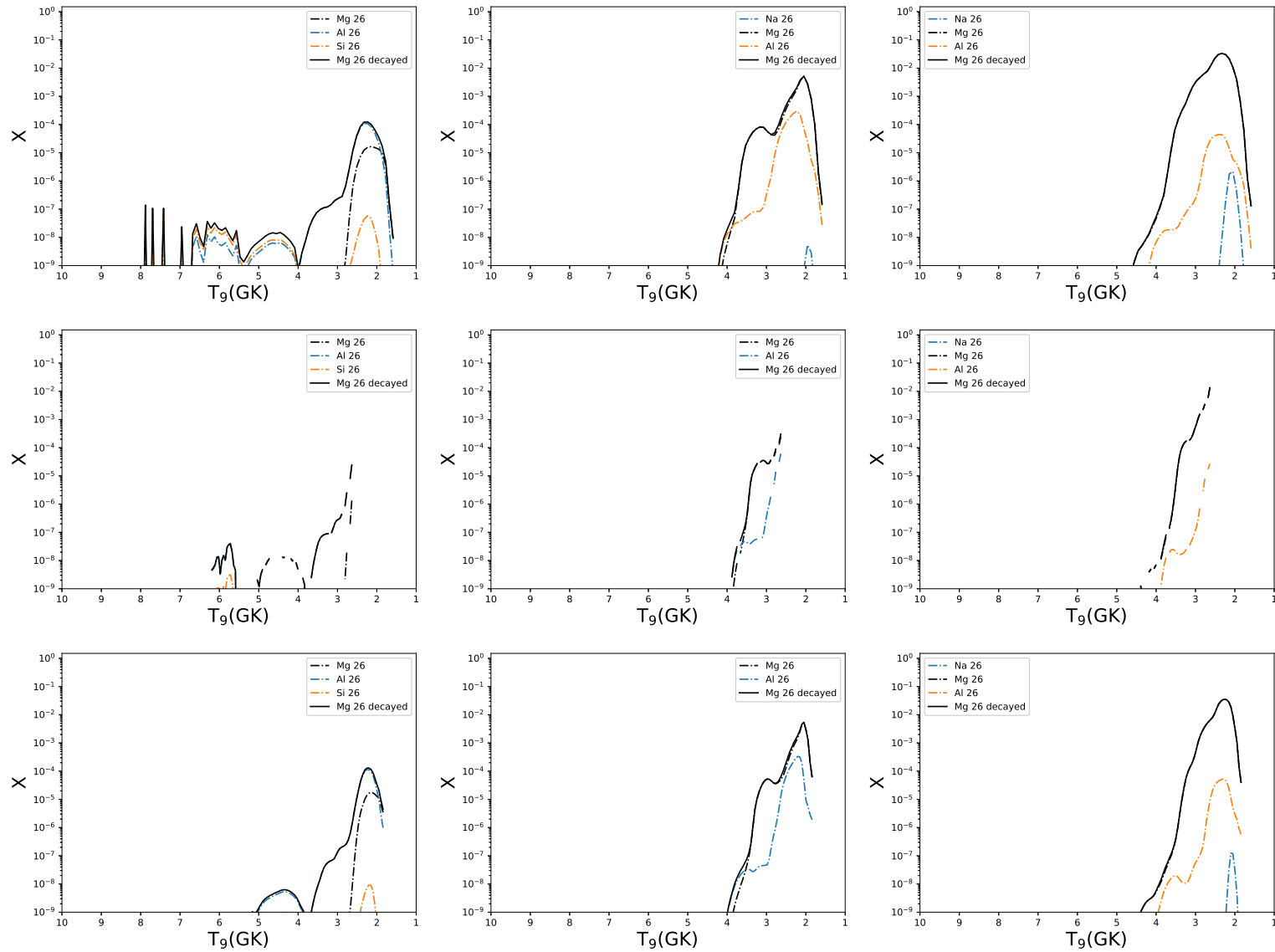


FIGURE 3.15: The abundance distributions of ^{26}Mg are shown, arranged as in figure 3.5. With metallicities of $Z = 0, 0.014$ and 0.1 from left to right, and the three categories of model - T1.4, S1.0 and M0.8 - from top to bottom.

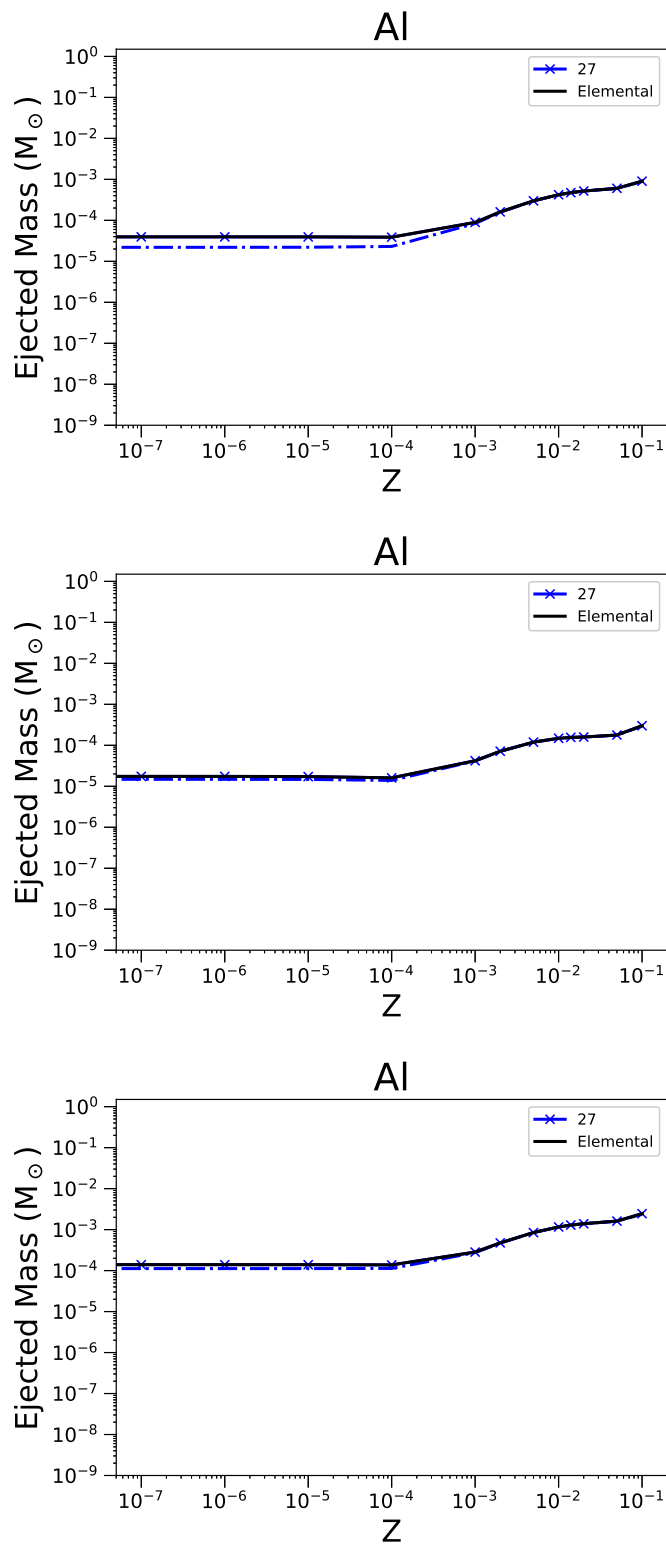
these trajectories which more than compensates for this as can be seen in figure 3.12. We also see a swap to the dominant nucleosynthesis channel being direct synthesis of ^{26}Mg , with a broad contribution from ^{26}Al . ^{26}Si production is eliminated. At super-solar metallicities (T1.4Z0.1) that direct synthesis of ^{26}Mg dominates, with a decreased contribution from ^{26}Al . We concluded that ^{26}Mg is produced directly as a secondary isotope in SNIa explosions in the T1.4 set of models.

In the S1.0Z0 models production of ^{26}Mg is dominated at all temperatures by radiogenic contributions from ^{26}Al . As we increase our initial metallicity, direct production of ^{26}Mg is again boosted by the supply of neutrons from the $^{22}\text{Ne}(\alpha, n)$ reaction. Contributions from the $^{22}\text{Ne}(\alpha, \gamma)^{26}\text{Mg}$ channel are negligible at the temperatures where ^{26}Mg is produced in this model, as the cross section for the (α, γ) reaction are three orders of magnitude smaller than for the (α, n) , due to resonances. We also observe an increase in the amount of ^{26}Al produced, due to the increased production of ^{25}Mg and subsequent (p, γ) reactions. As with the T1.4Z0.1 model, the production of ^{26}Al decreases again in the S1.0Z0.1 model, and ^{26}Mg is dominated by direct synthesis.

Similar trends are observed in the M0.8 models, with an increase in the production of radiogenic ^{26}Al boosting production of ^{26}Mg in the $Z = Z_{\odot}$ model. This decreases as the metallicity increases to super-solar values. In all models at $Z > 0.014$, there is no production in the intermediate peak temperature range as identified in the $Z = 0$ models.

3.2.4 Aluminium

Aluminium is mono-isotopic, with only ^{27}Al being stable. the primary production site of aluminium is carbon and neon burning in CCSN (Woosley, Heger, and Weaver, 2002) with similar conditions for production to ^{25}Mg and ^{26}Mg (Pignatari et al., 2016). Figure 3.16 shows the dependence of the

FIGURE 3.16: As in Figure 3.4 but for ejected mass of ^{27}Al .

elemental aluminium production on initial metallicity. Al production does generally increase with increasing metallicity for all models, with a plateau around the solar metallicity region. Production is nearly flat for $Z \leq 10^{-4}$ with a significant radiogenic contribution from ^{27}Si . This radiogenic contribution decreases with increasing metallicity. We see that there is a significant radiogenic contribution only in the lower metallicity T1.4 models, above $Z=10^{-4}$ almost all material is produced directly as ^{27}Al . At lower metallicities, particularly in the T1.4Z0 model, the radiogenic contribution is on the order of 50% of the total ejected mass of ^{27}Al . The primary radiogenic contribution shifts both in species from ^{27}Si to ^{27}Mg and in temperature range, from peak production of radioisotopes in the 2-4 GK range down to a more localised production around 2 GK. This is the odd even effect, observed in a variety of SN scenarios (see, for example Kozyreva, Yoon, and Langer (2014))

We see from figure 3.17 that there is a significant contribution to the abundance of ^{27}Al in the T1.4Z0 model from ^{27}Si over a broad range of temperatures. Production of ^{27}Si ranges from around 1.5 to 5.5 GK, over the majority of which this silicon component is comparable to the direct production of ^{27}Al and is the dominant source of ^{27}Al over much of this temperature range. In the S1.0Z0 and M0.8Z0 models, while there is a significant contribution from ^{27}Si , direct synthesis of ^{27}Al remains the dominant channel for production of Al.

In the models T1.4Z0.014, S1.0Z0.014 and M0.8Z0.014 show a reduction in the production of ^{27}Al in all channels in the range of 4-5 GK, as well as a smaller reduction in the higher temperature range of T1.4Z0.014. There is also a boost to direct production of ^{27}Al at peak temperatures between 2 and 4GK. We see for all solar models that ^{27}Al is primarily ejected directly, however there is a non-negligible contribution from some radioisotopes, not only at solar metallicities. There is a reduction in the radiogenic contribution from ^{27}Si at solar metallicity, similar to other intermediate mass elements

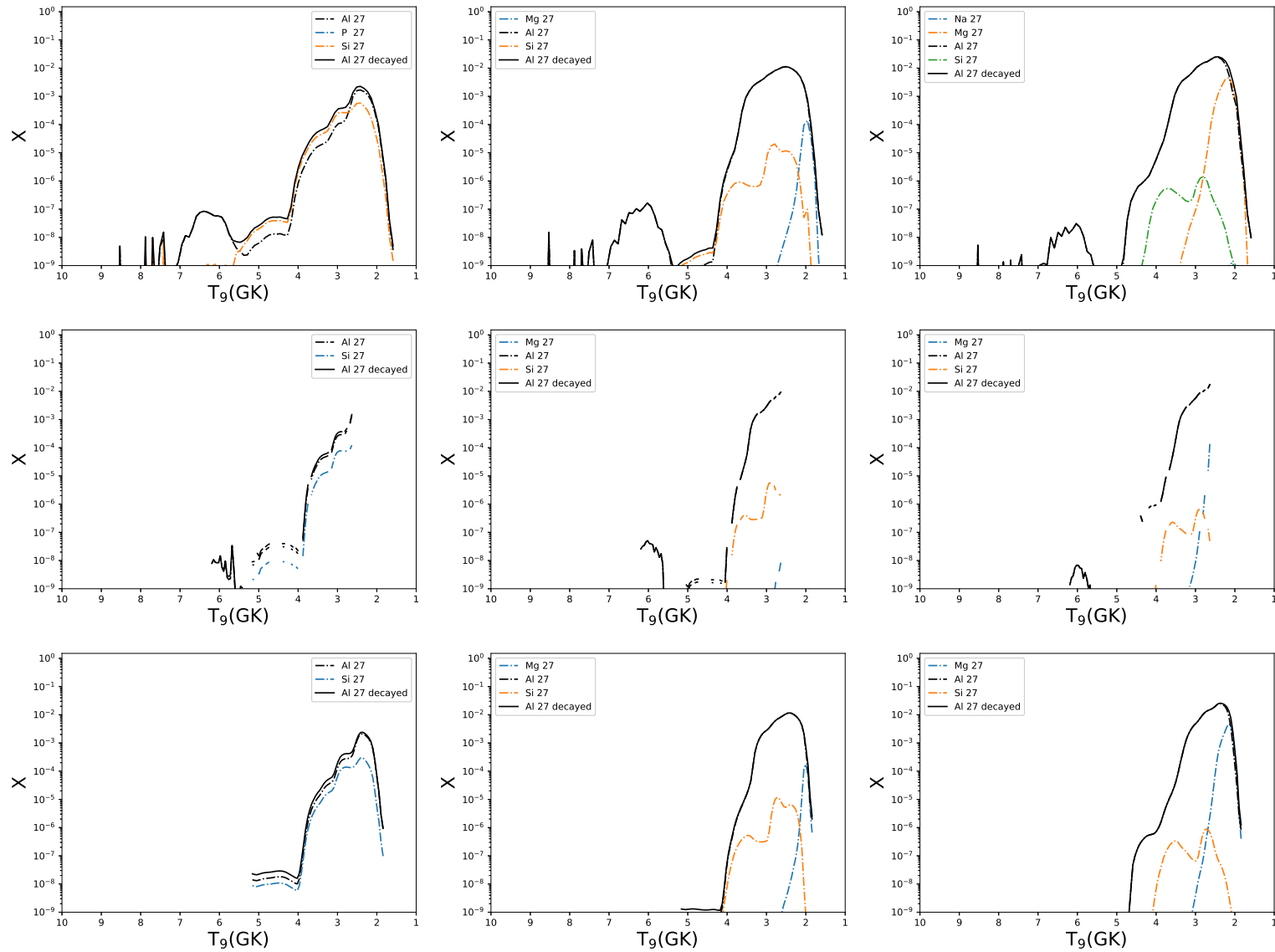


FIGURE 3.17: The abundance distributions of ^{27}Al are shown, arranged as in figure 3.5. With metallicities of $Z = 0, 0.014$ and 0.1 from left to right, and the three categories of model - T1.4, S1.0 and M0.8 - from top to bottom.

discussed previously. This is due to reaction pathways shifting towards more neutron rich species as the flux of neutrons increases due to the $^{22}\text{Ne}(\alpha, n)$ reaction. This is also why we see the increase in ^{27}Mg , as it is a product of neutron captures on the stable ^{26}Mg . Most ^{27}Al is ejected directly, although there are major contributions from radiogenic sources such as ^{27}Si and ^{27}Mg . There is still a significant proportion of ^{27}Mg which contributes at the lowest peak temperatures.

3.2.5 Silicon

Silicon consists of 3 stable isotopes: ^{28}Si , ^{29}Si and ^{30}Si and is mostly made in CCSN. ^{28}Si is the most abundant naturally occurring stable isotope, and is a product of oxygen fusion through the reaction



Contributions from SNIa events are needed however to fit the observed solar system abundances (see, for example Seitzzahl et al., 2013b; Kobayashi, Karakas, and Lugaro, 2020).

^{28}Si is by far the most abundant isotopic contributor to elemental Si production, as shown in figure 3.18. In all models, Si is produced in large quantities, with ejected masses above 0.2-0.3 M_{\odot} . The largest producers of Si are the M0.8 models, with a factor of around 2 larger ejected mass than compared with the other two classes of model across all metallicities (Figure 3.19).

^{28}Si has no trend with metallicity until we reach super-solar models. After this there is a small dip in production of all classes of model, arising from reduced production of ^{28}Si at the lowest peak temperatures due to neutron captures. We do see a strong metallicity dependence in ^{29}Si and ^{30}Si contributions to elemental silicon, resulting in a flat ejected elemental mass. ^{28}Si has a broad peak of production in all models, stretching from 1.8 to 6 GK

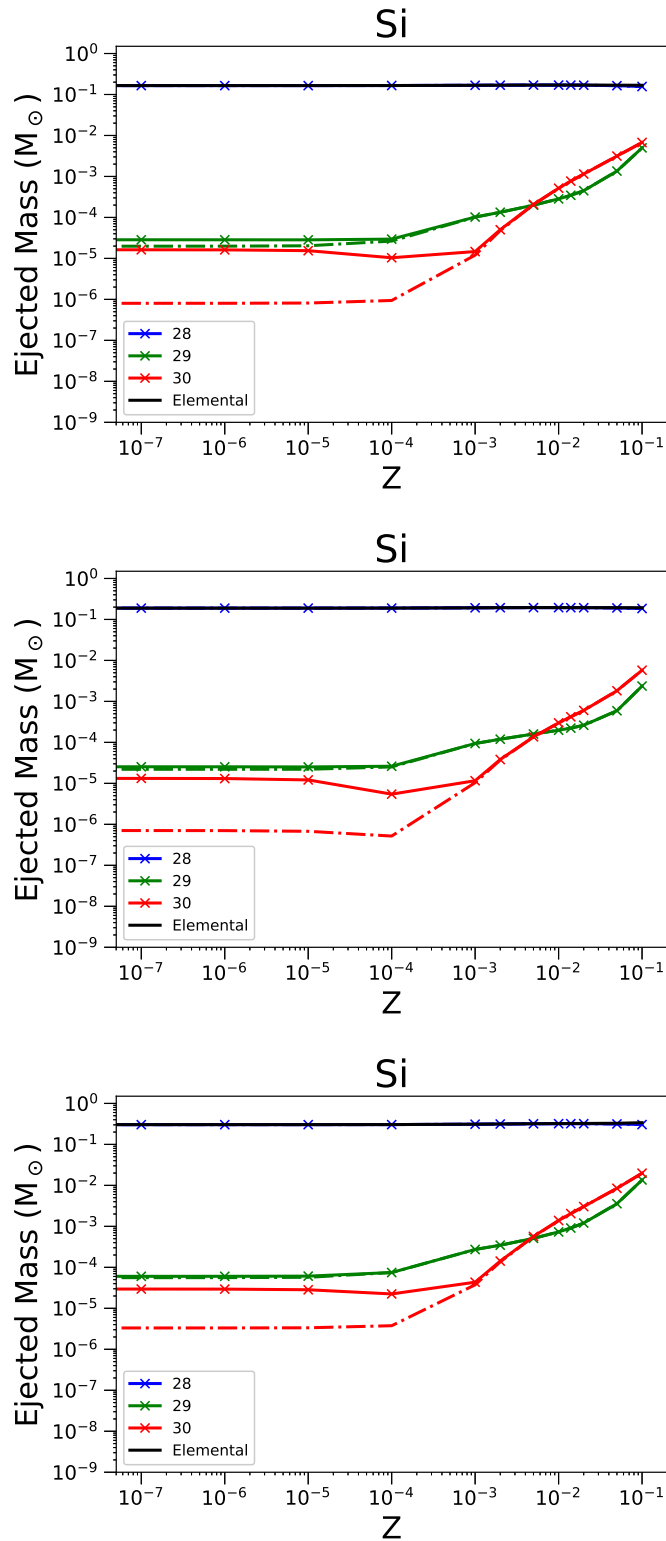


FIGURE 3.18: As in Figure 3.4 but for ejected mass of Si, and its stable isotopes ^{28}Si , ^{29}Si and ^{30}Si .

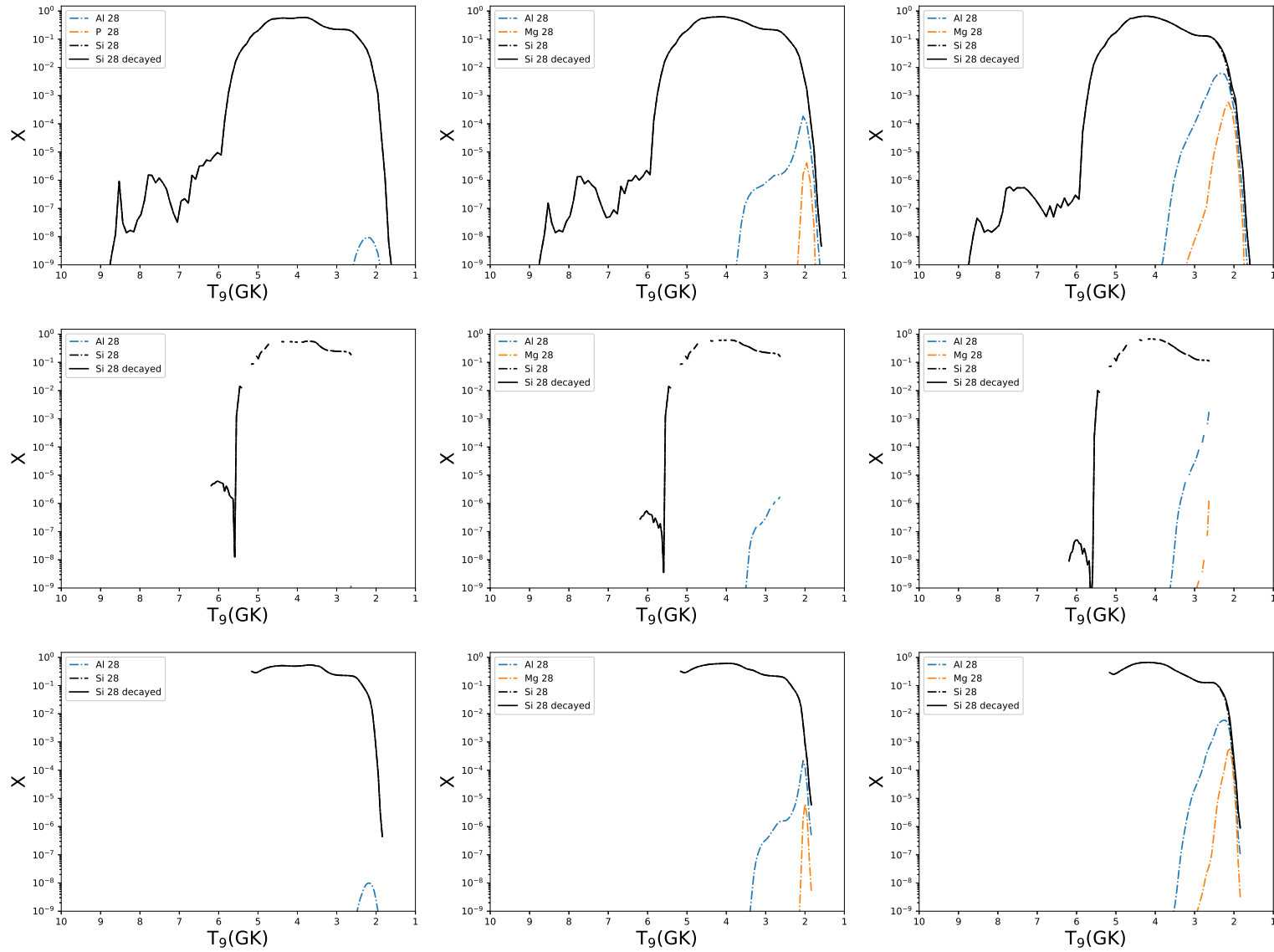


FIGURE 3.19: The abundance distributions of ^{28}Si are shown, arranged as in figure 3.5. With metallicities of $Z = 0, 0.014$ and 0.1 from left to right, and the three categories of model - T1.4, S1.0 and M0.8 - from top to bottom.

(slightly lower in the S1.0 and M0.8 models, due to the lower density of these tracer particles). Production of ^{28}Si in the lowest temperature range is dominated by radiogenic contributions, mostly from neutron rich Al although the impact on the integrated abundances is negligible, as can be seen in figure 3.18.

From figure 3.19 we see that models T1.4Z0, T1.4Z0.014 and T1.4Z0.1 have a higher temperature production peak for ^{28}Si , which is relatively insensitive to the initial metallicity. This is due to the high density region in the SNIa causing electron capture reactions. For stellar conditions where nuclear reaction rates are approaching NSE, charged particle reaction rates are in equilibrium, and so it is the weak interactions which govern the shift in distribution from normal NSE to a more neutron rich distribution (Langanke and Martinez-Pinedo, 2000). The density of these hottest particles ensure that the Y_e is similar between all T1.4 models in the high temperature region. Despite this, production is negligible compared to trajectories at lower peak temperatures.

^{29}Si has a similar trend with metallicity across the three class of models, as does ^{30}Si . We see that the ^{29}Si to ^{30}Si ratio changes dramatically as we move from sub- to super-solar metallicities. ^{29}Si is produced in a broad range of conditions in T1.4Z0, with production extending above 6 GK. This small contributor to the ejected ^{29}Si is lost at higher metallicities, although this is more than compensated for by the boost in secondary production at lower peak temperatures. This same trend is seen in the S1.0 and M0.8 models, with a reduction in the production at intermediate peak temperatures accompanied by a boost in production at lower temperatures. Radiogenic ^{29}P is a significant contributor to ^{29}Si in the T1.4Z0, S1.0Z0 and M0.8Z0 models although there is no significant radiogenic contribution at metallicities above 0 from ^{29}P . At supersolar metallicities, we see a small contribution to the ejected ^{29}Si mass of the order of a few percent.

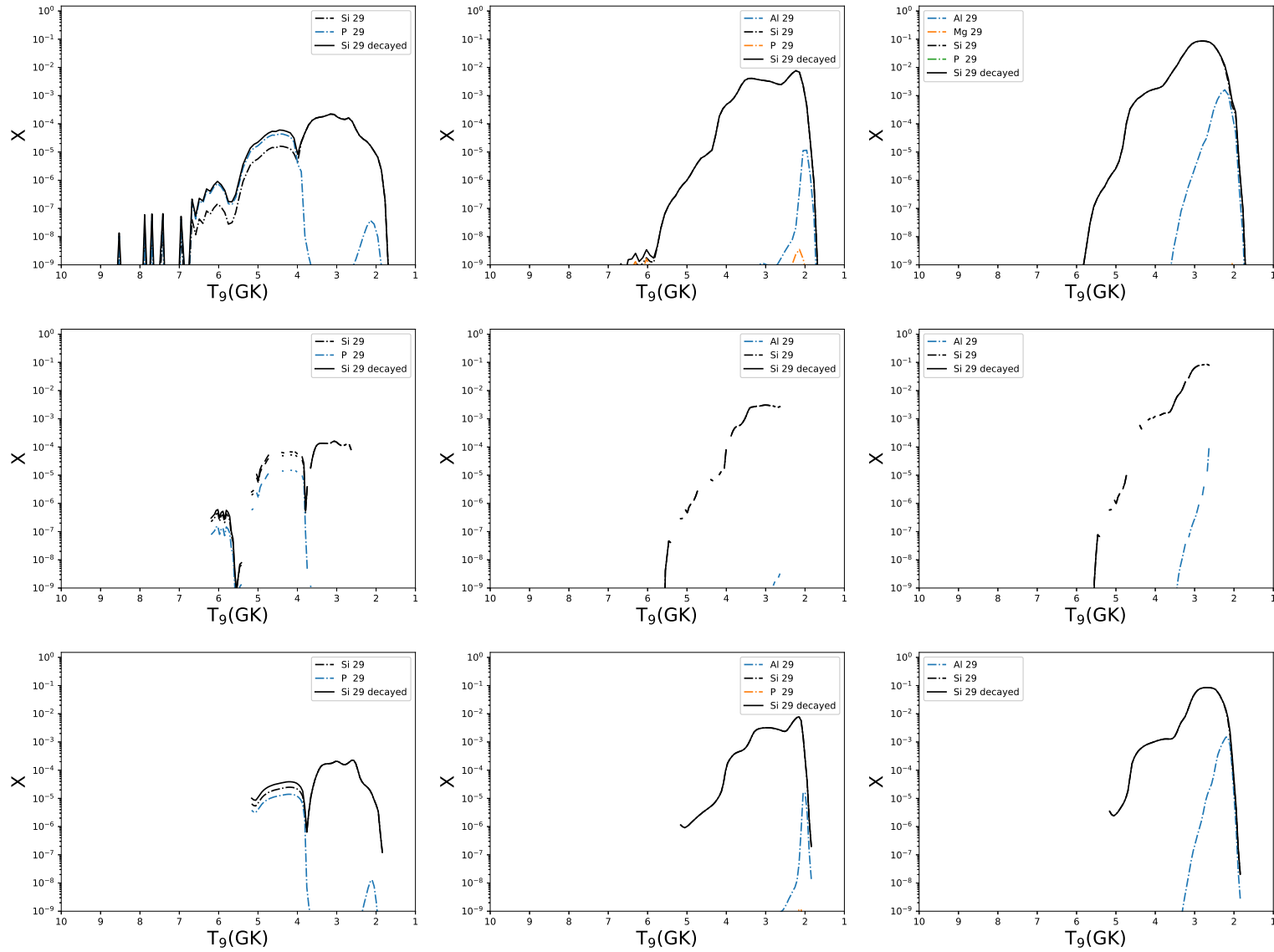


FIGURE 3.20: The abundance distributions of ^{29}Si are shown, arranged as in figure 3.5. With metallicities of $Z = 0, 0.014$ and 0.1 from left to right, and the three categories of model - T1.4, S1.0 and M0.8 - from top to bottom.

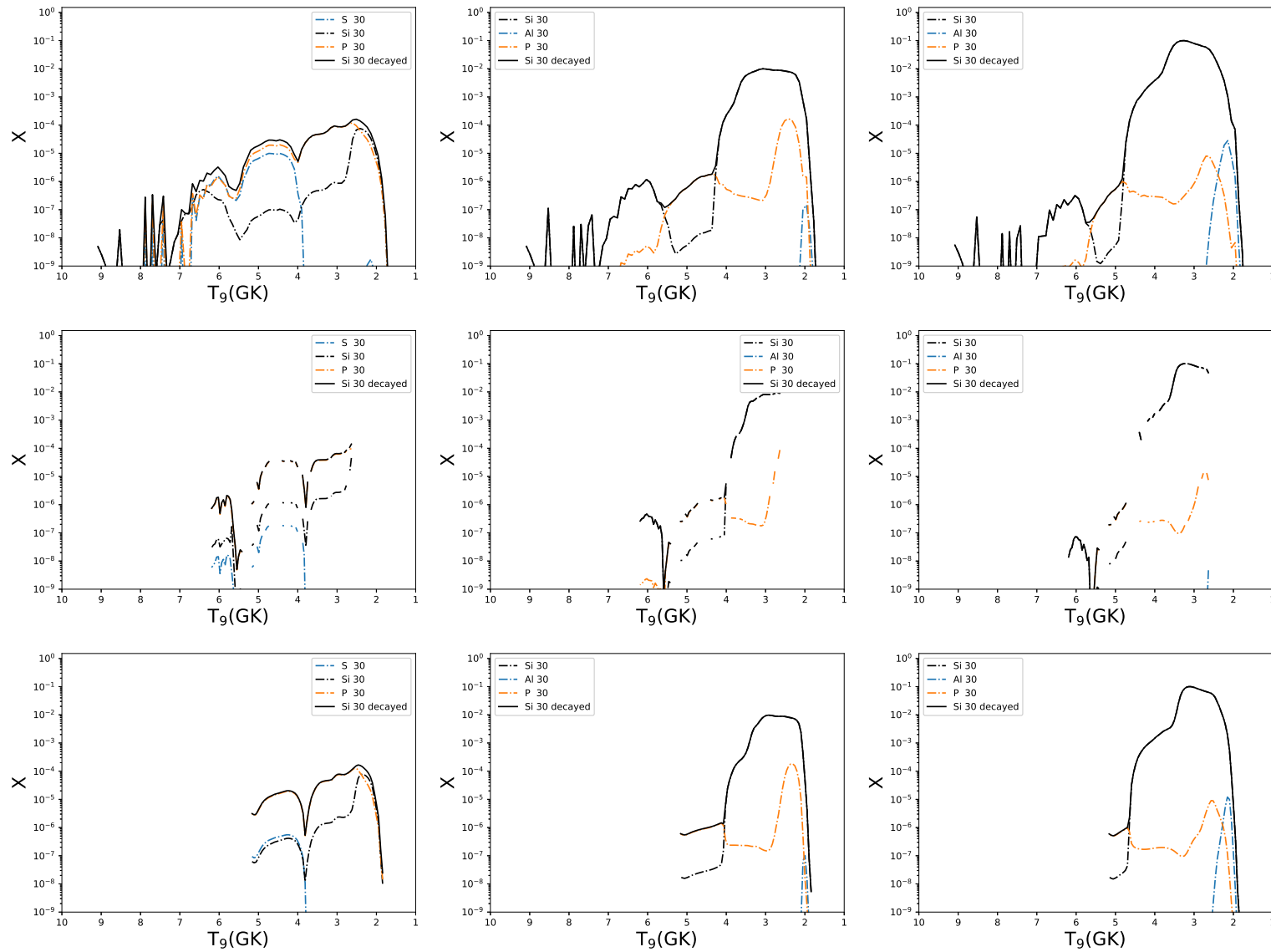


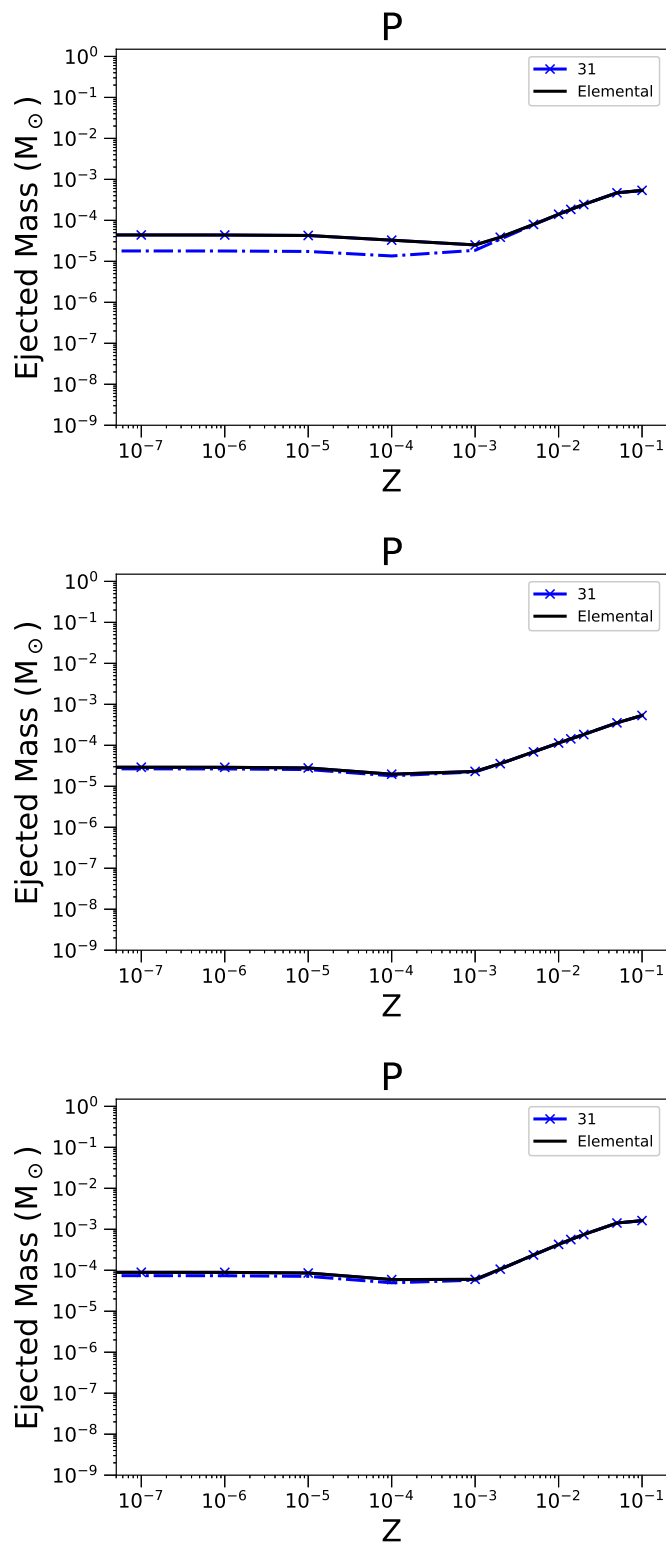
FIGURE 3.21: The abundance distributions of ^{30}Si are shown, arranged as in figure 3.5. With metallicities of $Z = 0, 0.014$ and 0.1 from left to right, and the three categories of model - T1.4, S1.0 and M0.8 - from top to bottom. Note that the contribution from ^{30}P in S1.0Z0 is very nearly 100% of the ejected ^{30}S , and is therefore difficult to observe under the decayed abundance line.

Production of ^{30}Si is more complex, especially in the model T1.4Z0. There are broad radiogenic contributions from two isotopes - ^{30}P is dominant at most peak temperatures, while there is equal production with ^{30}S at temperatures above 5 GK. At higher metallicities, the contribution from ^{30}S becomes negligible, and ^{30}Si is primarily ejected. ^{30}P also becomes negligible at higher metallicities. We see this same trend in the S1.0 and M0.8 models, where at metallicity $Z = 0$ ^{30}P dominated production of ^{30}Si , while at higher metallicities ^{30}Si is mostly ejected.

3.2.6 Phosphorus

Phosphorus is mono-isotopic and is produced in carbon and neon burning in massive stars (Woosley, Heger, and Weaver, 2002). Pignatari et al. (2016) identify explosive helium burning as a source. ^{31}P is made in roughly equal proportions in our three types of progenitor (see figure 3.22). Production at lower metallicities in the intermediate mass S1.0 models is a factor of 2 lower than the T1.4 models, and 5 compared to the M0.8 models. Primary production of phosphorus decreases slightly from $Z = 10^{-5}$ to $Z = 10^{-3}$, after which production increases across all classes of model by more than an order of magnitude.

At $Z = 0$, ^{31}P is ejected mainly as ^{31}S in the T1.4Z0 model, whilst it is directly made in the S1.0Z0 and M0.8Z0 models. As we move to the $Z = 0.014$ models, ^{31}P is directly ejected, with the three models being nearly identical in the lower peak temperature range. Contributions to the ejected mass of ^{31}P above $T_9 = 4$ GK are negligible, we may therefore ignore the high peak temperature tail of production in T1.4Z0.014. At $Z = 0.1$, we have a trace production of ^{31}Al , which is shifted between the T1.4Z0.1 and S1.0Z0.1 and M0.8Z0.1 models from a peak around 2.2 GK, to a broader peak centered at 3 GK in the lower mass models.

FIGURE 3.22: As in Figure 3.4 but for ejected mass of ^{31}P .

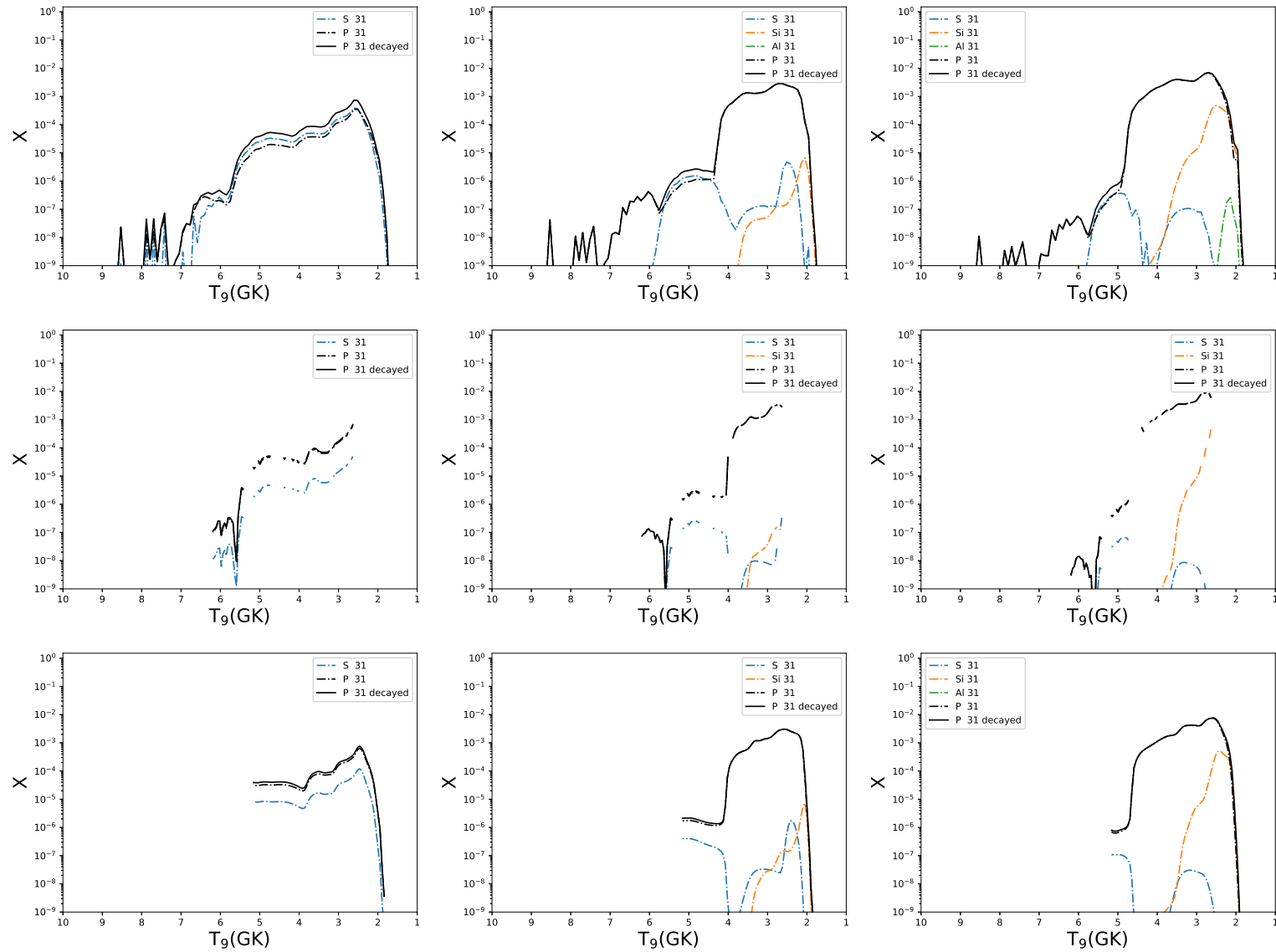


FIGURE 3.23: The abundance distributions of ^{31}P are shown, arranged as in figure 3.5. With metallicities of $Z = 0, 0.014$ and 0.1 from left to right, and the three categories of model - T1.4, S1.0 and M0.8 - from top to bottom.

3.2.7 Sulphur

Sulphur consists of 4 stable isotopes: ^{32}S , ^{33}S , ^{34}S and ^{36}S . ^{32}S is produced in explosive and hydrostatic oxygen burning as is ^{34}S . ^{33}S is produced in explosive oxygen or neon burning, all of these occur in CCSN (Woosley, Heger, and Weaver, 2002). ^{36}S , the least abundant stable isotope, is produced in AGB stars in addition to the contribution from CCSN, in either hydrostatic helium burning or carbon neon burning (Pignatari et al., 2016; Woosley, Heger, and Weaver, 2002).

From figure 3.24 the trends of each isotope of sulphur are very similar between different sets of model, with similar trends with respect to metallicity. The models differ on the absolute ejected mass of the various S isotopes by about a factor of 2, except for ^{33}S , which is more strongly produced in the M0.8 models, at some metallicities by nearly an order of magnitude.

We see in figure 3.25 that ^{32}S is ejected directly at zero metallicity for all models, with a similar profile for production below 5 GK. There is a negligible contribution to the ejected mass of ^{32}S from a high peak temperature tail in the T1.4Z0 model. At $Z = 0.014$, we begin to see the secondary production of other isotopes, namely ^{32}P and ^{32}Si although these are in trace amounts compared with the direct synthesis of ^{32}S . The same is again true of the $Z = 0.1$ models.

3.2.8 Chlorine

Chlorine consists of two stable isotopes: ^{35}Cl and ^{37}Cl . ^{35}Cl is produced during explosive oxygen and neon burning, with a small contribution from neutrino interactions Pignatari et al., 2016; Woosley, Heger, and Weaver, 2002 during a CCSN. The majority of ^{37}Cl is made in explosive oxygen or neon burning. SNIa are not expected to contribute significantly to the abundances

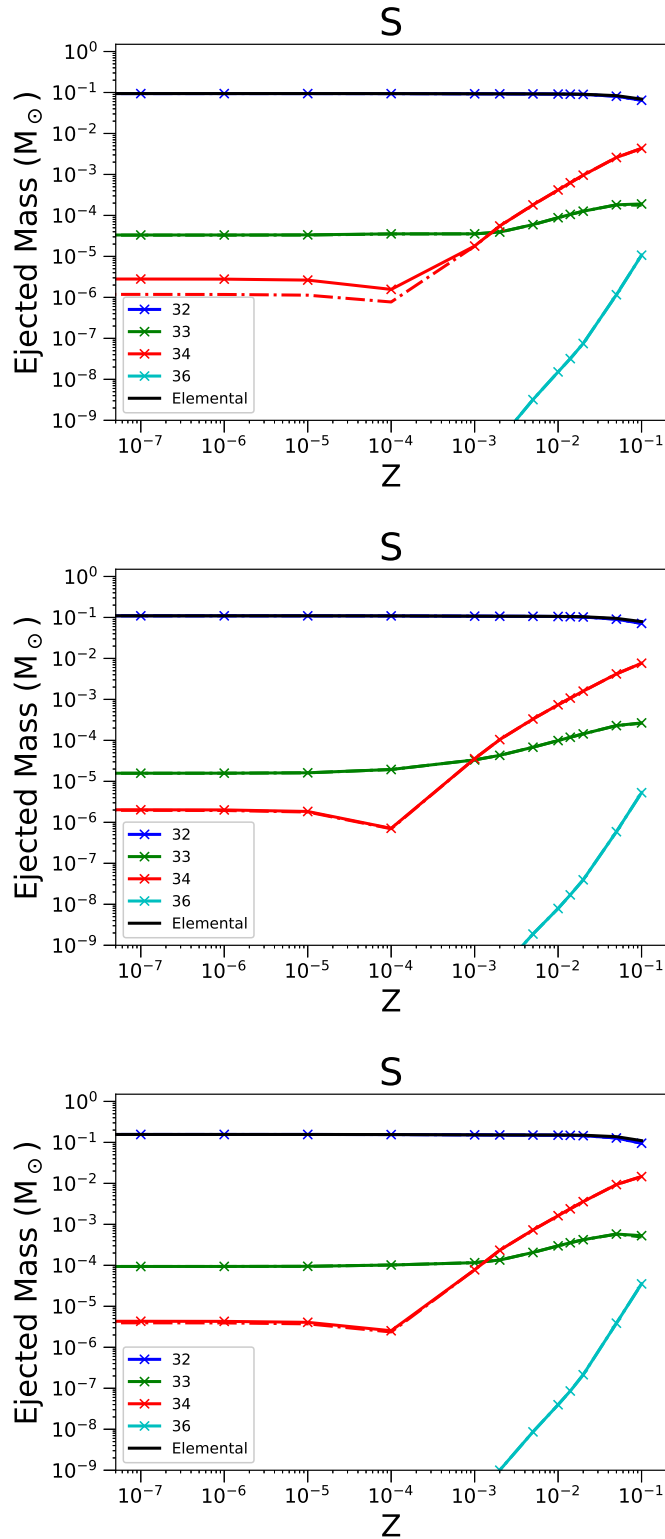


FIGURE 3.24: As in Figure 3.4 but for ejected mass of S, and its stable isotopes ^{32}S , ^{33}S , ^{34}S and ^{36}S .

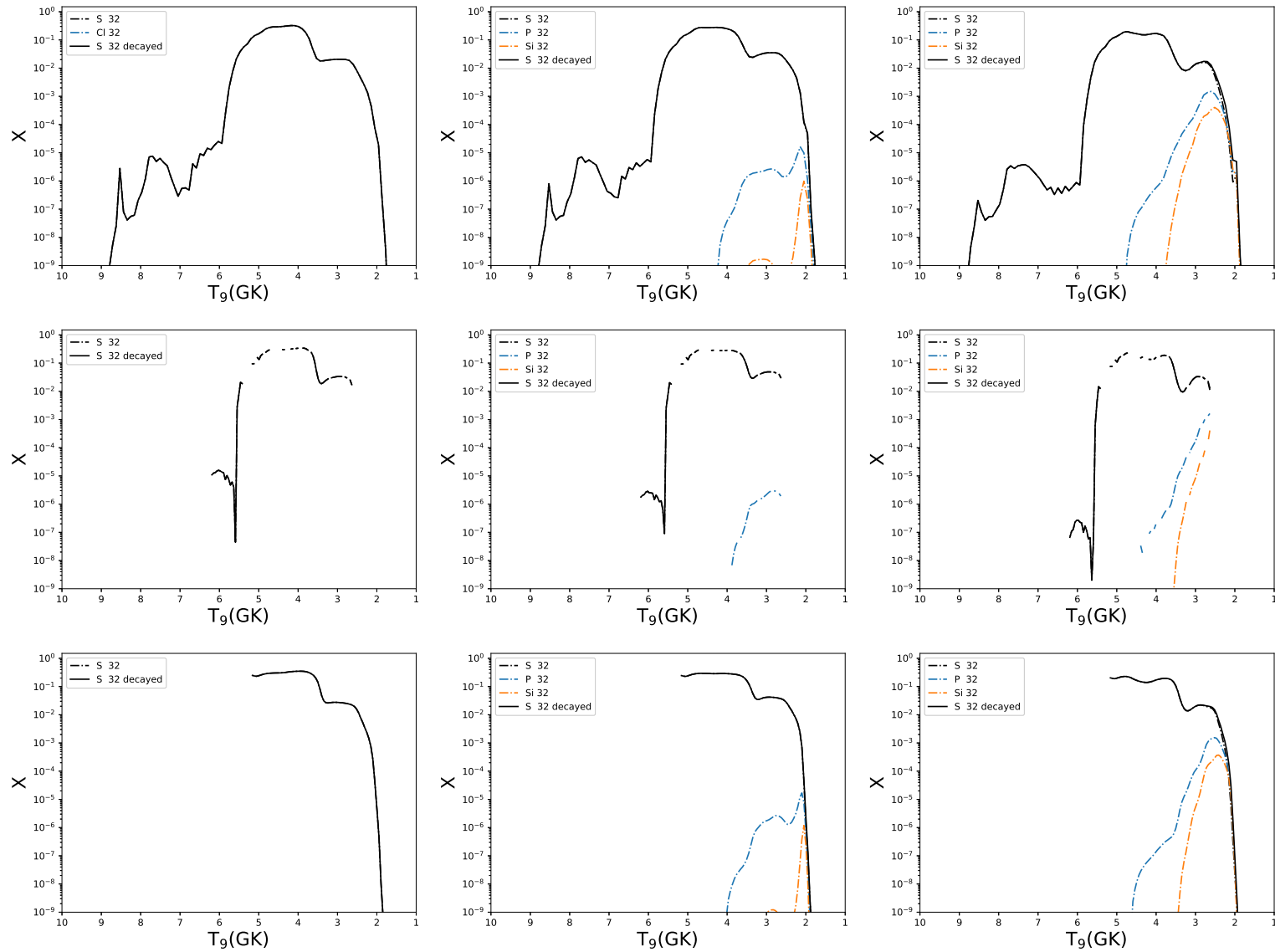


FIGURE 3.25: The abundance distributions of ^{32}S are shown, arranged as in figure 3.5. With metallicities of $Z = 0, 0.014$ and 0.1 from left to right, and the three categories of model - T1.4, S1.0 and M0.8 - from top to bottom.

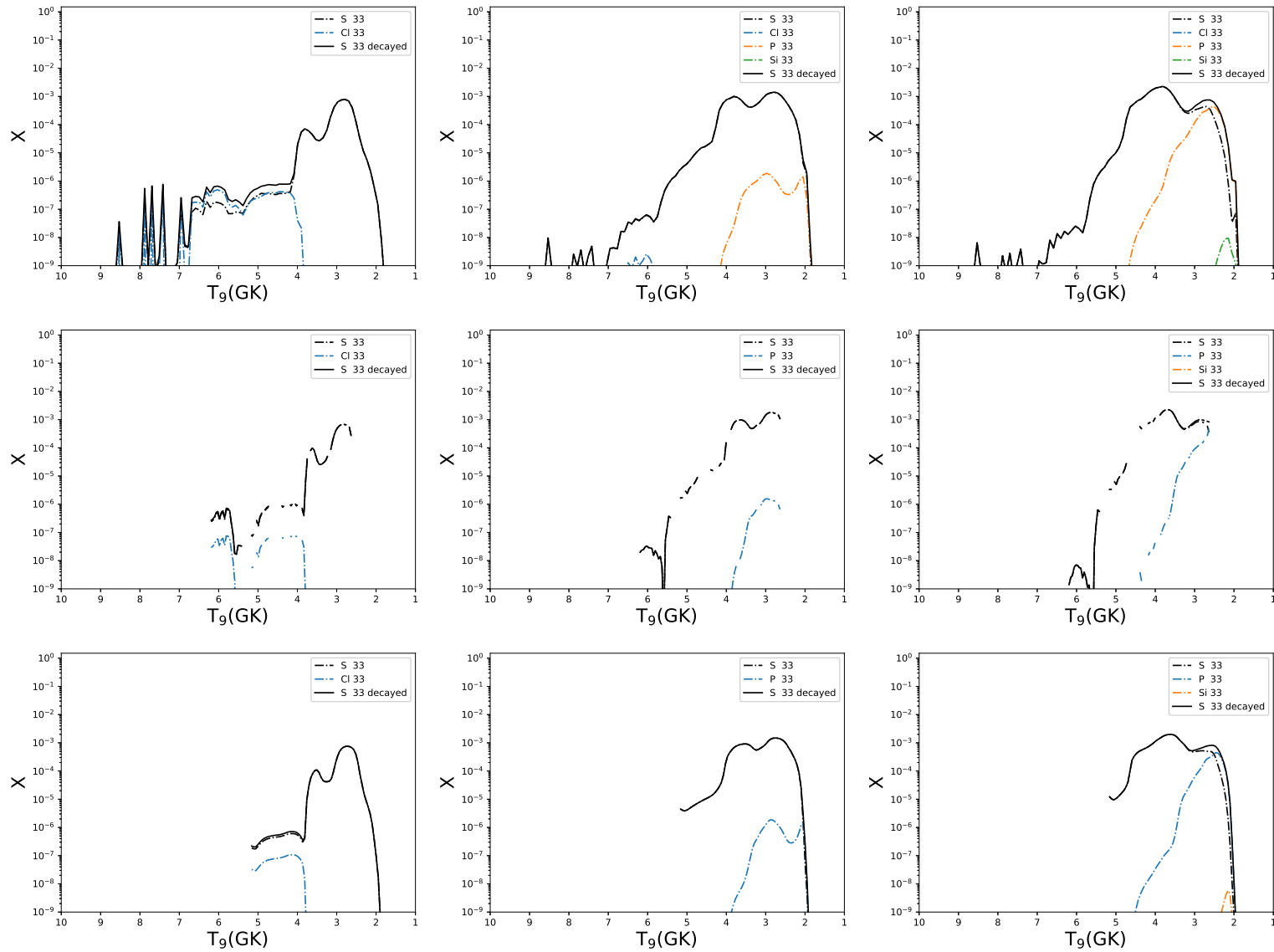


FIGURE 3.26: The abundance distributions of ^{33}S are shown, arranged as in figure 3.5. With metallicities of $Z = 0, 0.014$ and 0.1 from left to right, and the three categories of model - T1.4, S1.0 and M0.8 - from top to bottom.

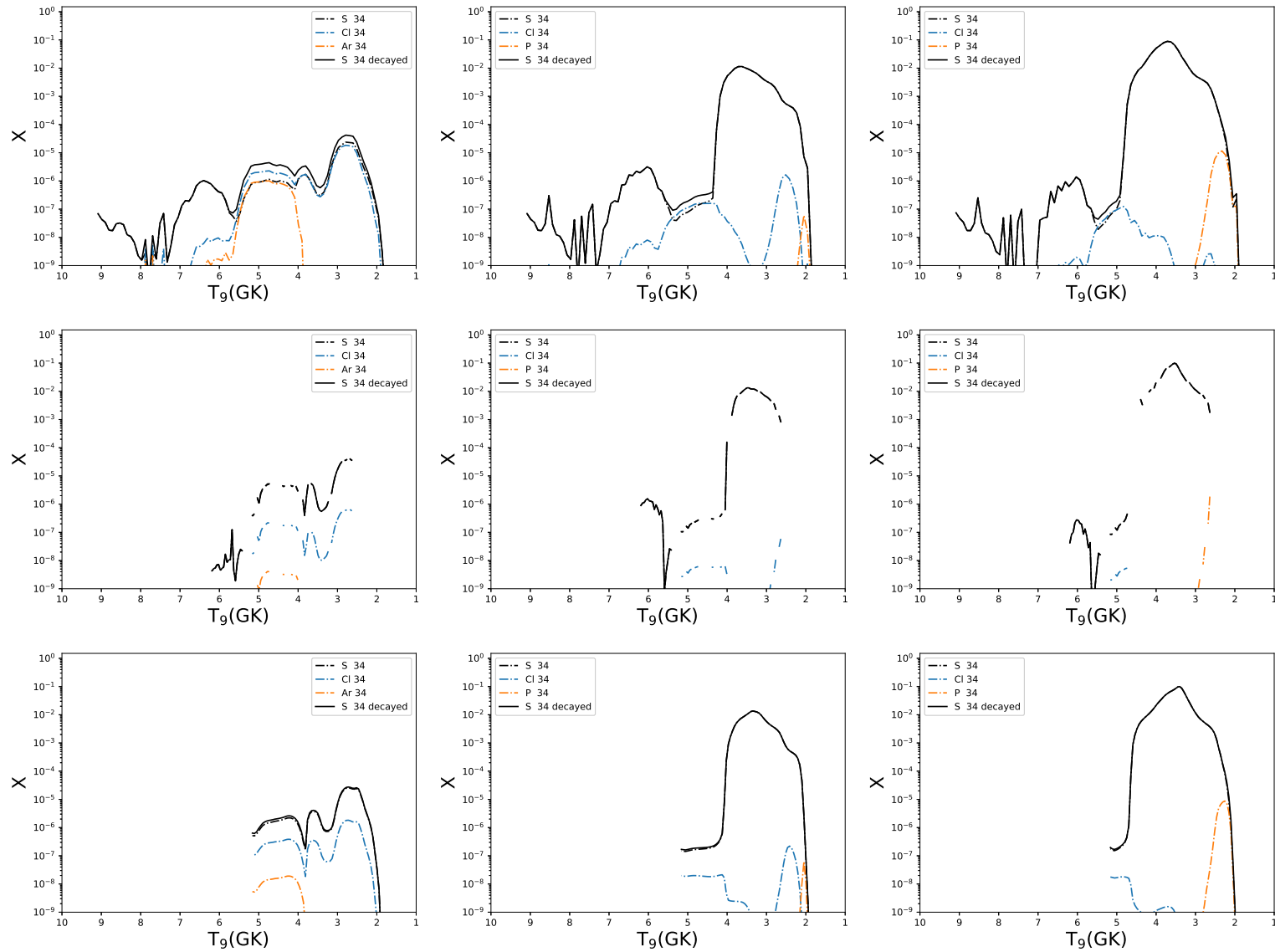


FIGURE 3.27: The abundance distributions of ^{34}S are shown, arranged as in figure 3.5. With metallicities of $Z = 0, 0.014$ and 0.1 from left to right, and the three categories of model - T1.4, S1.0 and M0.8 - from top to bottom.

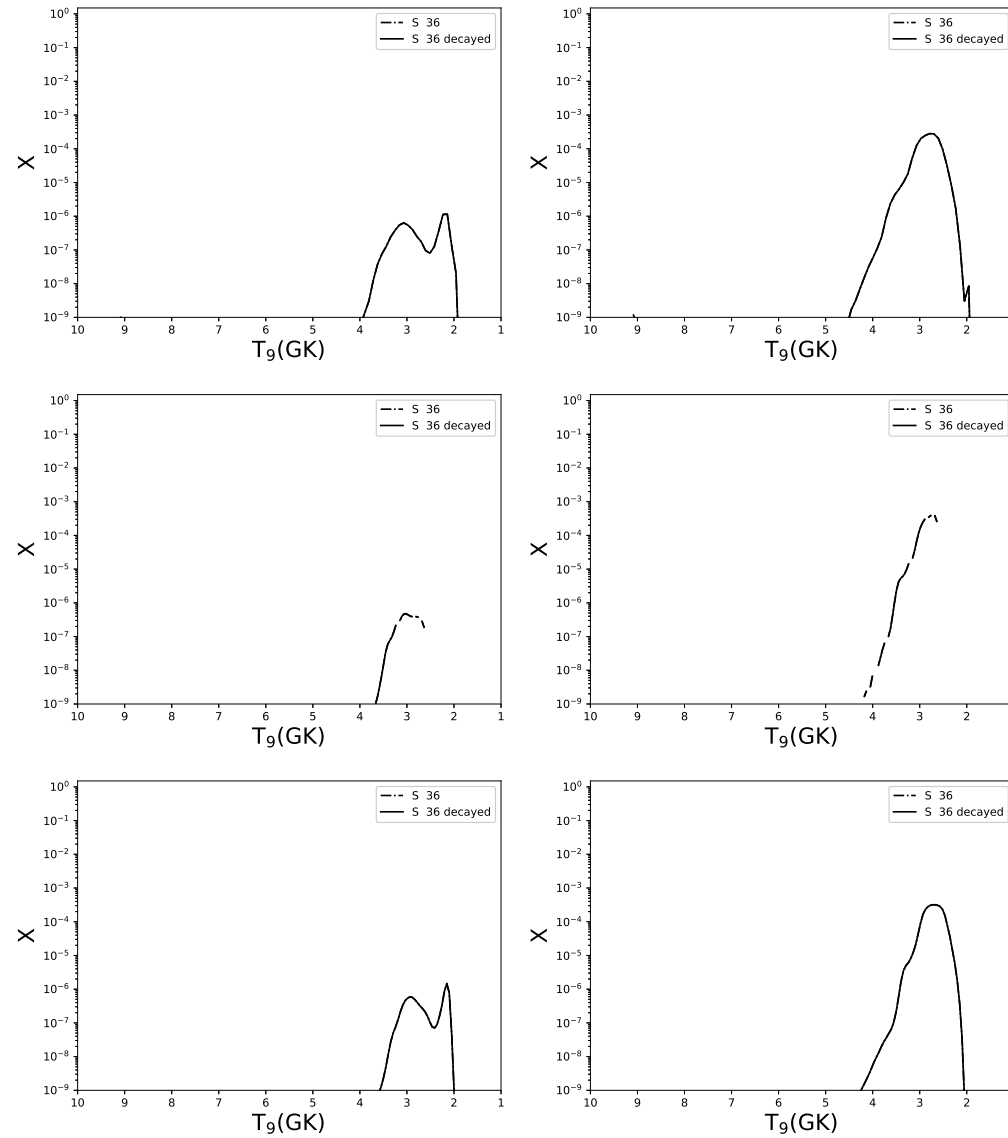


FIGURE 3.28: The abundance distributions of ^{36}S are shown, arranged as in figure 3.5. With metallicities of $Z = 0, 0.014$ and 0.1 from left to right, and the three categories of model - T1.4, S1.0 and M0.8 - from top to bottom. There is no production of ^{36}S at $Z = 0$ and so those plots have been omitted.

of chlorine in the galaxy (Kobayashi, Karakas, and Lugaro, 2020; Woosley, Heger, and Weaver, 2002).

Figure 3.29 shows the metallicity dependency of the two chlorine isotopes. The trend with metallicity is similar between all three models, with the ejected mass of elemental chlorine being a factor of 2 higher in the M0.8 models than in the T1.4 and S1.0 models at all metallicities. Significant radiogenic contributions are seen for both ^{35}Cl and ^{37}Cl at lower metallicities, however this contribution decreases for both isotopes above $Z = 10^{-4}$. Whilst there remains a large radiogenic contribution for ^{37}Cl up to $Z = 0.1$, ^{35}Cl is directly ejected at these higher metallicities.

Figure 3.30 shows that a significant proportion of ^{35}Cl in the T1.4Z0 model is ejected as radioactive ^{35}Ar . This production occurs mainly in the region from 2GK to 5.8GK. As seen in model T1.4Z0.014, this contribution decreases with metallicity. Production of ^{35}Ar is significantly reduced across the whole temperature range. On the other hand, the ^{35}S radiogenic contribution increases with metallicity. Both of these trends continue in the T1.4Z0.1 model, with ^{35}S becoming the dominant production pathway in the lower peak temperature trajectories. ^{35}Cl production is still dominated by its direct production.

We see a similar trend in the S0.8 models, however there is no significant radiogenic contribution to the ejected mass of ^{35}Cl , even in the S0.8Z0 model. The M0.8 models also follow the same trend as the low peak temperature component of the T1.4 models.

We see a double peak in production of ^{35}Cl in the $Z = 0.014$ models at lower peak temperatures - one at 2.5GK and one at 3.8GK. These correspond to the carbon and oxygen burning regions and therefore to distinct reaction pathways producing these two regions of ^{35}Cl . Production of ^{35}Cl is suppressed in the lower of these two peaks in the $Z = 0.1$ model and the higher temperature production peak is boosted. As discussed above, this peak is

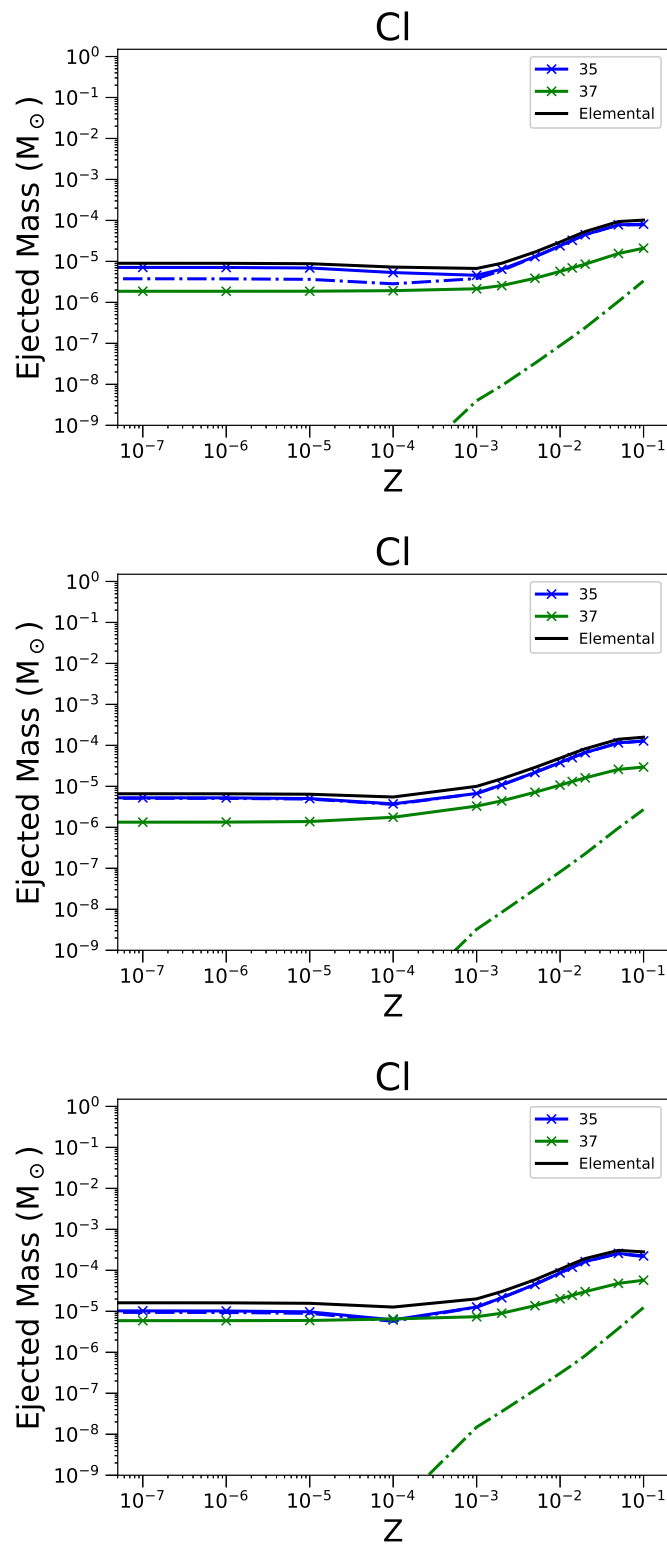


FIGURE 3.29: As in Figure 3.4 but for ejected mass of Cl, and its stable isotopes ^{35}Cl and ^{37}Cl .

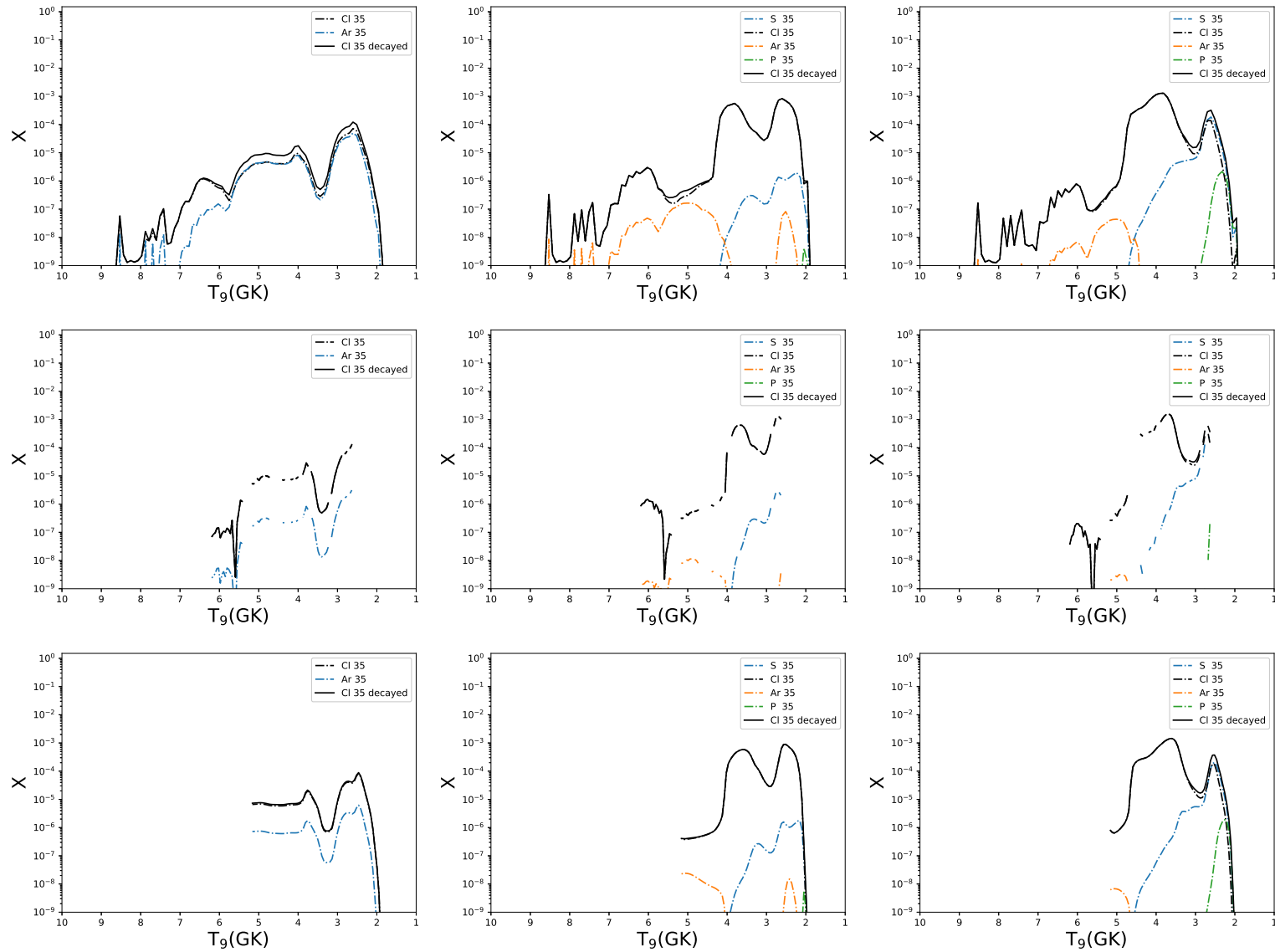


FIGURE 3.30: The abundance distributions of ^{35}Cl are shown, arranged as in figure 3.5. With metallicities of $Z = 0, 0.014$ and 0.1 from left to right, and the three categories of model - T1.4, S1.0 and M0.8 - from top to bottom.

directly ejected as ^{35}Cl , where as the peak at lower temperatures is a mixture of ^{35}Cl and radiogenic ^{35}S .

In figure 3.31 ^{37}Cl is mostly ejected as radiogenic ^{37}Ar . We see in the T1.4Z0, S1.0Z0 and M0.8Z0 models that there is almost no contribution from direct synthesis of ^{37}Cl . There is a trace contribution to the ejected mass of ^{37}Cl in the T1.4Z0 model from ^{37}K , however this is negligible. In these models again see a double peak of production in the lower temperature range, slightly shifted to higher temperatures, at 3 GK and 3.8 GK respectively, compared to ^{35}Cl . This temperature range corresponds to the onset of oxygen burning-like conditions in the SNIa in the higher temperature regime, and carbon burning like conditions for the lower band.

As we increase the initial metallicity to $Z = 0.014$, the higher temperature of these two peaks broadens, with production extending to 5 GK and more. The lower temperature peak is suppressed, as was the case for ^{35}Cl , and we see an increase in the direct synthesis of ^{37}Cl although this remains a small contribution at this metallicity. This trend is similar across all of the $Z = 0.014$ models.

As the metallicity is again increased to $Z = 0.1$, the lower temperature peak becomes dominated by the direct synthesis of ^{37}Cl . We see the higher temperature peak broadens again, extending peak production throughout the 4 to 5 GK range. We see from comparison with figure 3.29 that this gives rise to significant increase in the abundance of ^{37}Cl , similar to the processes discussed for ^{35}Cl .

3.2.9 Argon

Argon consists of 3 stable isotopes: ^{36}Ar , ^{38}Ar and ^{40}Ar . ^{36}Ar and ^{38}Ar are produced in CCSN during oxygen burning and explosive oxygen burning

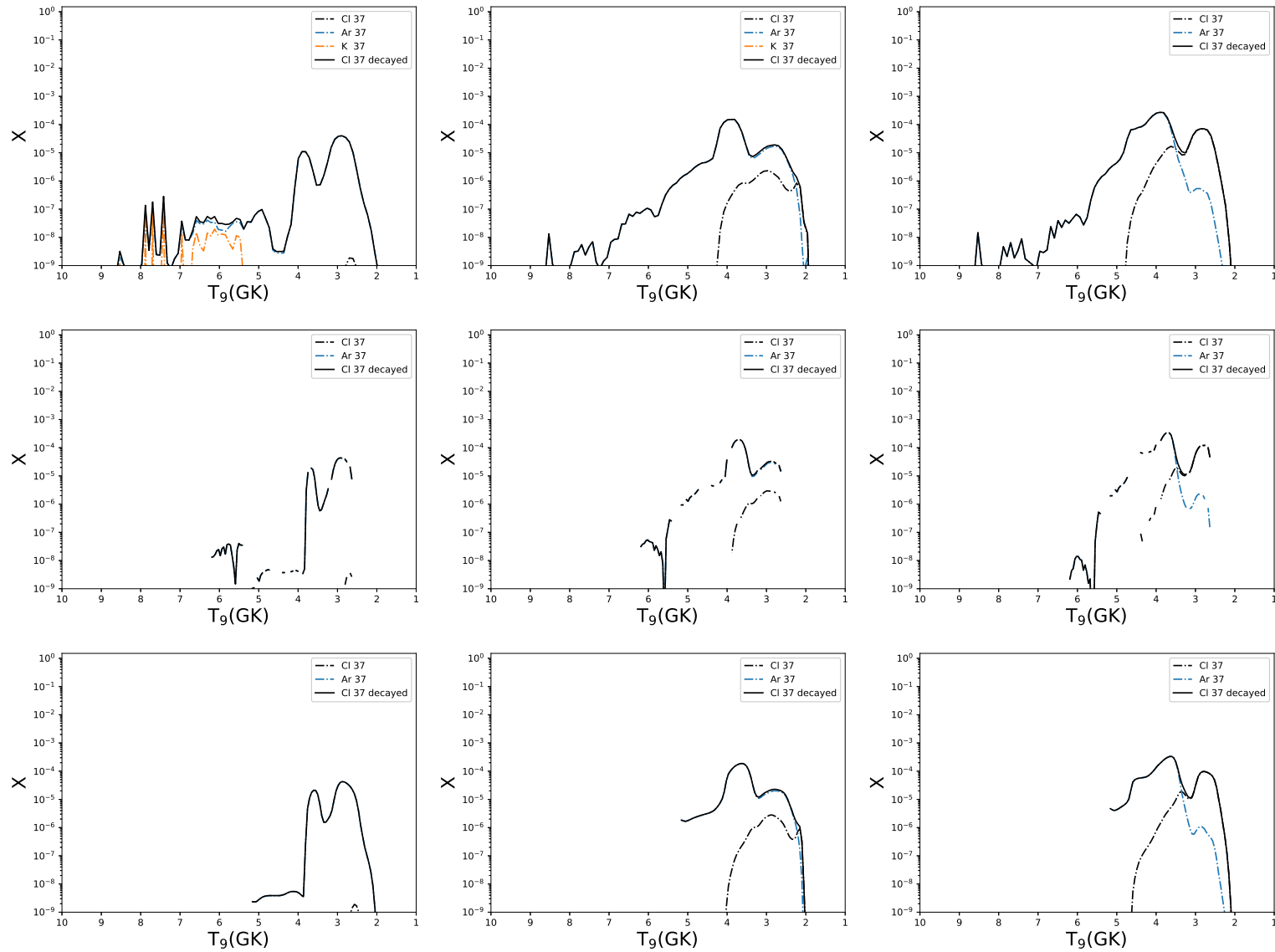


FIGURE 3.31: The abundance distributions of ^{37}Cl are shown, arranged as in figure 3.5. With metallicities of $Z = 0, 0.014$ and 0.1 from left to right, and the three categories of model - T1.4, S1.0 and M0.8 - from top to bottom.

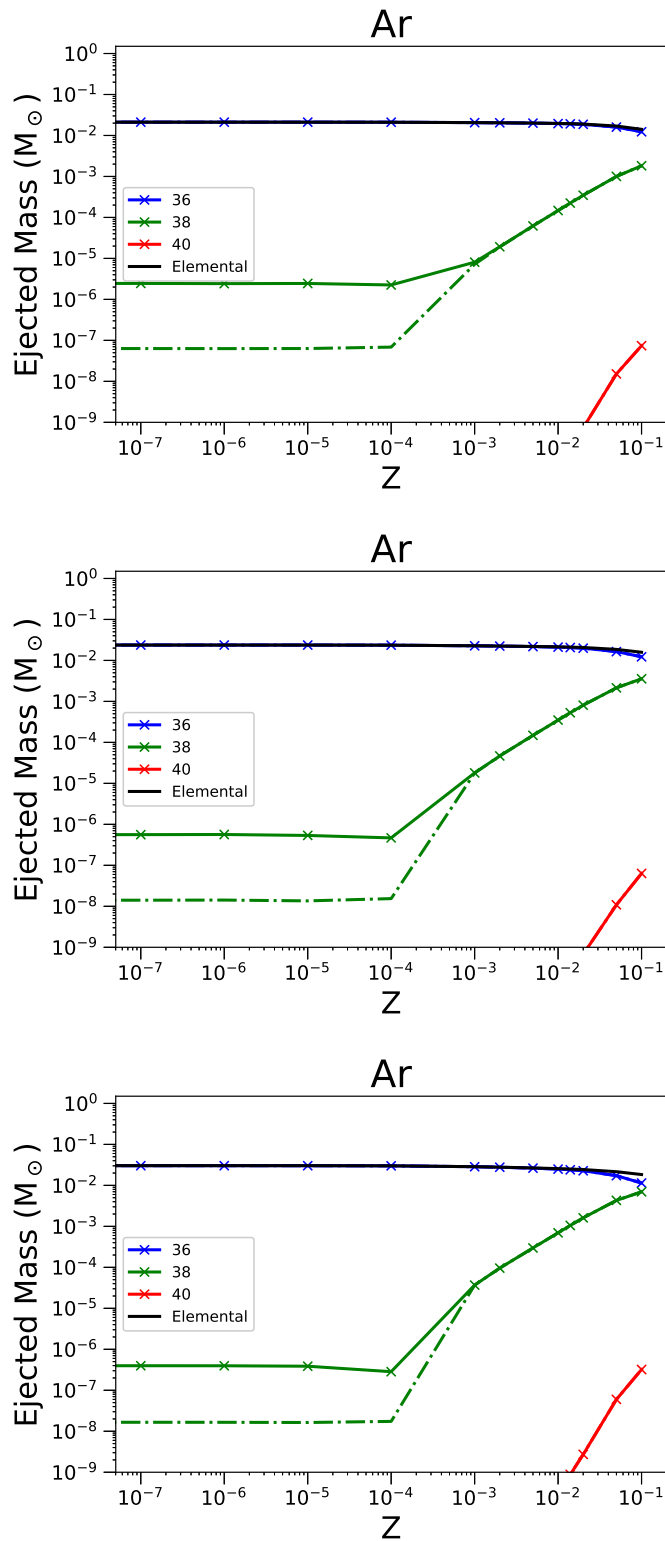


FIGURE 3.32: As in Figure 3.4 but for ejected mass of Ar, and its stable isotopes ^{36}Ar , ^{38}Ar and ^{40}Ar .

(Woosley, Heger, and Weaver, 2002). ^{40}Ar is produced either during explosive helium burning, or carbon or neon burning. Pignatari et al. (2016) note that the solar abundance of ^{40}Ar is produced by the s-process, with theoretical yields from typical s-process sources matching observations well.

In all three sets of models argon production is seen to be mostly primary, with a slight reduction in the total ejected mass at super-solar metallicities (3.32). This is due to the decrease in production of ^{36}Ar with increasing metallicity which is partially compensated for at the highest metallicities, with the increase in production of ^{38}Ar . In the case of the M0.8 models, ^{36}Ar becomes almost as abundant as ^{38}Ar . Indeed, the ratio of ^{36}Ar to ^{38}Ar at super-solar metallicities approaches unity as the mass of the progenitor decreases, whilst there is a factor of 5 difference in the T1.4Z0.1 model. Radiogenic ^{38}Ar has a primary production up to $Z = 10^{-4}$, direct production becomes the dominant channel above $Z = 10^{-3}$.

Again with ^{36}Ar all three classes of model have similar production sites and metallicity trends. Inspection of figure 3.33 shows that ^{36}Ar is primarily produced at $Z = 0$ at temperatures between 4 and 5 GK. this production is the same for all three classes of model. There is a trace amount of ^{36}Cl produced at temperatures between 2.5 and 3 GK, which sits in a secondary peak of production in ^{36}Ar . At $Z = 0.014$, production is largely the same as in the $Z = 0$ case. We see an increased production of radioactive ^{36}Cl , although this is still negligible compared to the bulk of production.

Figure 3.34 shows that ^{38}Ar is mainly made as the radiogenic product of ^{38}K at low metallicities in the T1.4 class of models. We also see a difference in the nucleosynthetic site of ^{38}Ar , as there is a large contribution to production in the higher temperature range of 5.5 - 7GK, temperatures which are not reached in the M0.8 models, and only at the lower end (around 6 GK) in the S1.0 models. ^{38}Ar has an ejected mass approximately 5x greater in the low metallicity models of T1.4 as compared with S1.0 and M0.8 due to this higher

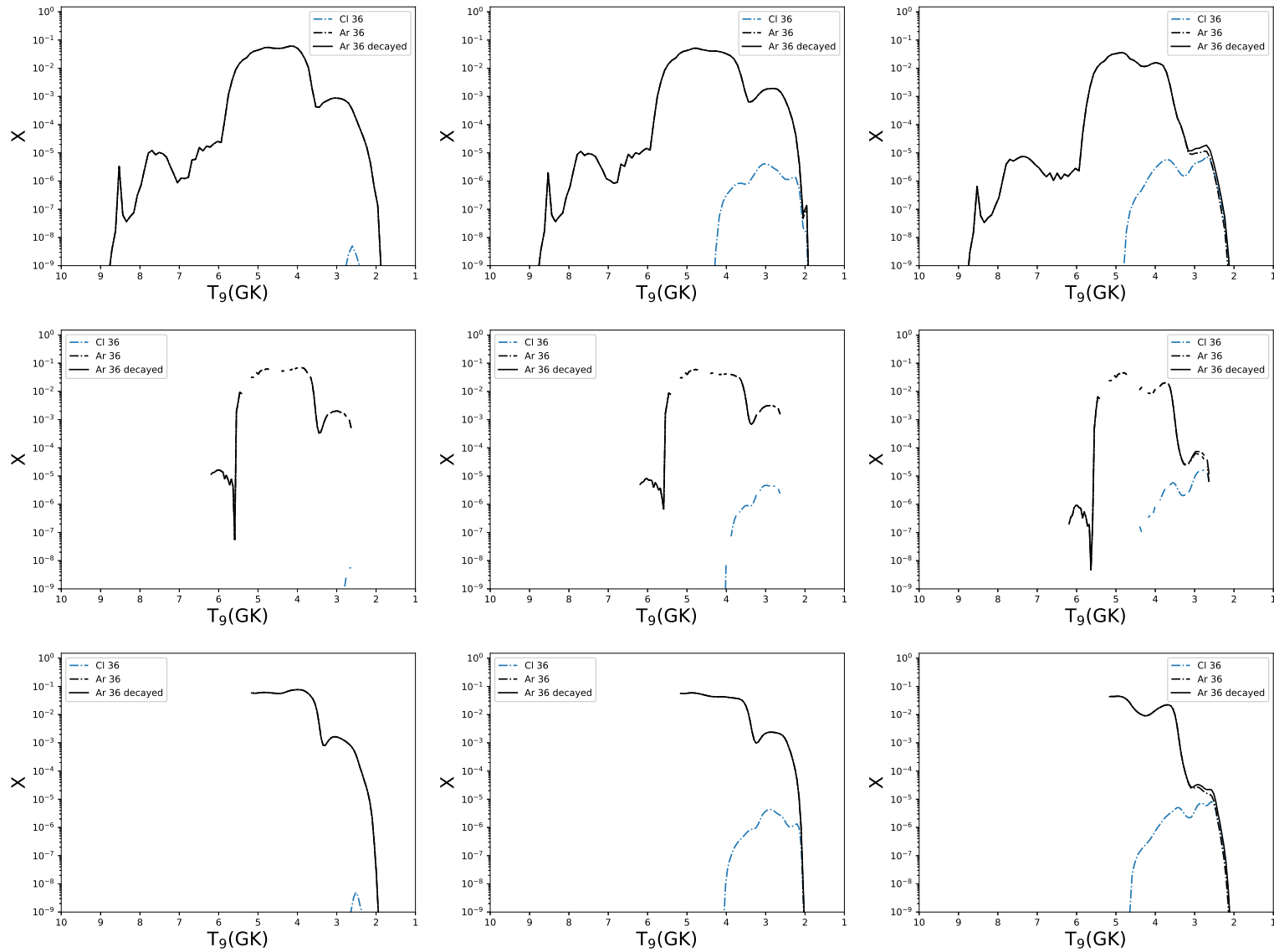


FIGURE 3.33: The abundance distributions of ^{36}Ar are shown, arranged as in figure 3.5. With metallicities of $Z = 0, 0.014$ and 0.1 from left to right, and the three categories of model - T1.4, S1.0 and M0.8 - from top to bottom.

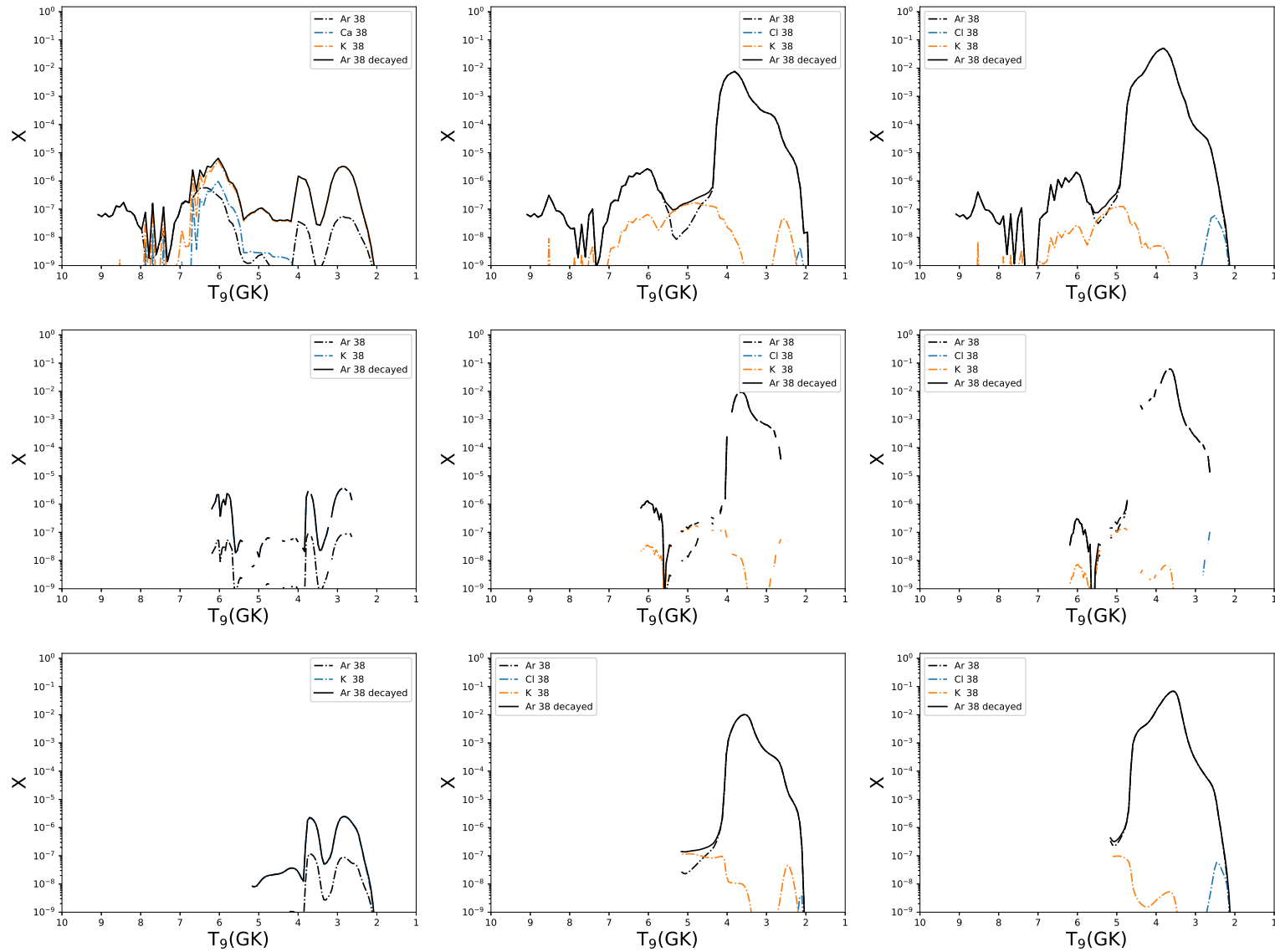


FIGURE 3.34: The abundance distributions of ^{38}Ar are shown, arranged as in figure 3.5. With metallicities of $Z = 0, 0.014$ and 0.1 from left to right, and the three categories of model - T1.4, S1.0 and M0.8 - from top to bottom.

temperature production range. We see two production peaks in the lower temperature region, consistent across the three classes of model.

^{38}Ar dominates the higher temperature region noted for the T1.4Z0 model, although this is now a negligible component to the overall ejected mass. The lower temperature region is a superposition of burning in the O and C burning layers, with the oxygen burning zone contributing the greatest proportion of ^{38}Ar . Explosive oxygen burning produces ^{38}Ar through the reaction $^{34}\text{S}(\alpha,\gamma)^{38}\text{Ar}$, ^{34}S being produced through the reaction $^{35}\text{Cl}(\gamma,p)$ as discussed in Thielemann and Arnett (1985).

In the $Z = 0.014$ models, production is dominated by the oxygen burning region. The double peak production has merged into one broad secondary peak of directly synthesised ^{38}Ar . In the $Z = 0.1$ models, production at lower temperatures is dominated by the broad secondary peak of direct nucleosynthesis of ^{38}Ar . This has increased further, and as such the higher temperature component of the T1.4Z0.1 model has an even smaller relative impact on the ejected mass.

We see from figure 3.35 that there is no high temperature component of ^{40}Ar in SNIa. we also see that ^{40}Ar production is highly dependent on initial metallicity. No models show production of ^{40}Ar at $Z = 0$, and only trace amounts of ^{40}Ar are synthesised between 2 and 3 GK in the $Z = 0.014$ models. We see a sharp rise in the production of ^{40}Ar at super-solar metallicities.

3.2.10 Potassium

Potassium consists of 2 stable isotopes: ^{39}K and ^{41}K , and a long-lived radioisotope, ^{40}K with a halflife of 1.28 Gyr. The bulk of solar potassium is ^{39}K , which is produced in explosive and hydrostatic oxygen burning in CCSN (Pignatari et al., 2016; Woosley, Heger, and Weaver, 2002). ^{41}K is also produced in explosive oxygen burning in CCSN, with a contribution from AGB

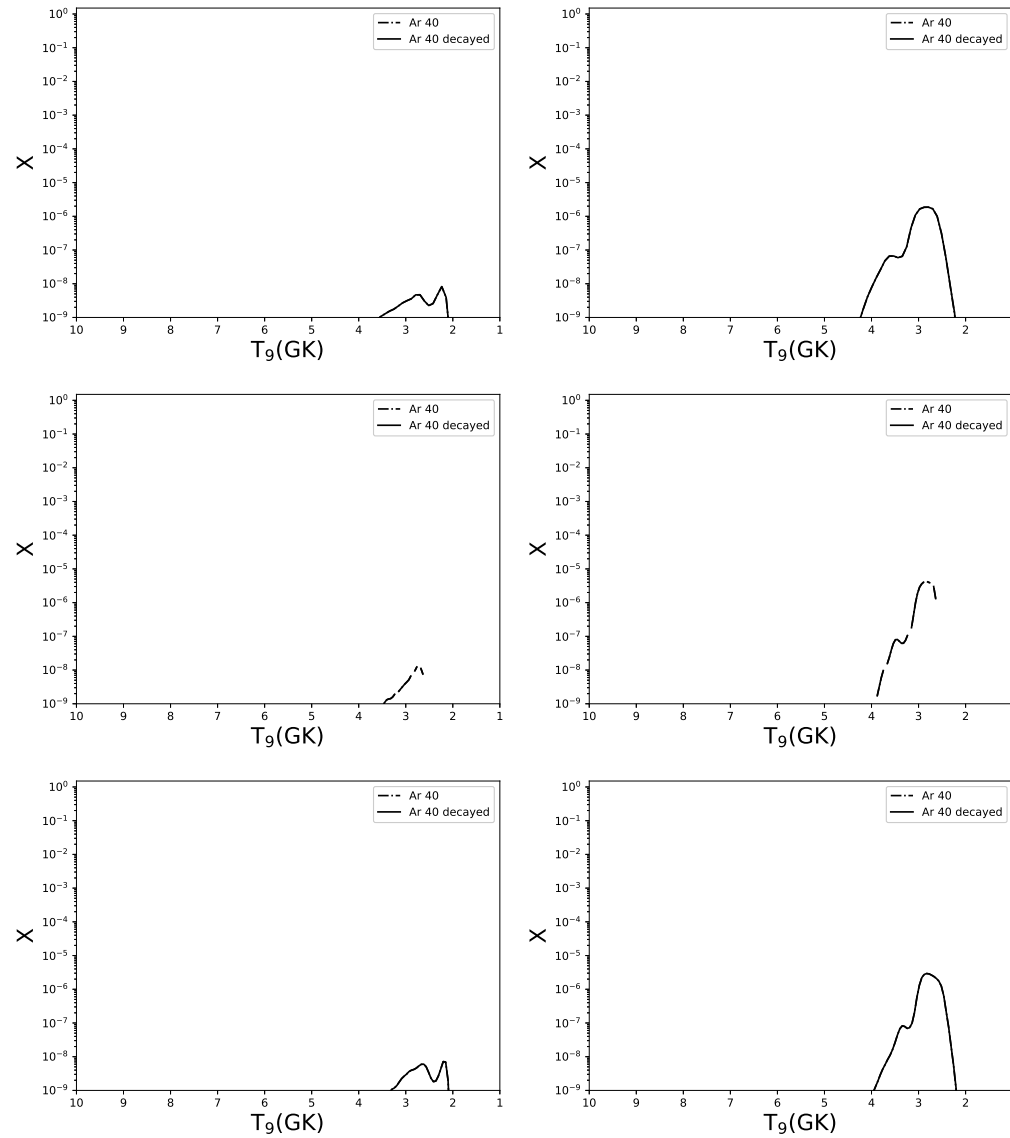


FIGURE 3.35: The abundance distributions of ^{40}Ar are shown, arranged as in figure 3.5. With metallicities of $Z = 0, 0.014$ and 0.1 from left to right, and the three categories of model - T1.4, S1.0 and M0.8 - from top to bottom.

stars. Yields of ^{40}K are around 2 orders of magnitude smaller than total potassium yields. ^{40}K have contributions from AGB, massive stars and the s-process prior to explosion through explosive helium burning (Pignatari et al., 2016). ^{40}K is relevant to the formation and evolution of rocky planets due to the heat generated from its decay (Nimmo et al., 2020). The predicted theoretical abundance of ^{40}K in the Milky Way is currently at odds with the observed abundance, with Kobayashi, Karakas, and Lugaro (2020) identifying it as being underproduced. It may be the case that SNIa contribute significantly to the observed abundances of ^{40}K , as we see a production factor in excess of one for some of our models starting at solar metallicity in the T1.4 and S1.0 models, and at sub-solar metallicity in the M0.8 model set, within a factor of ten of the production factor of, e.g. ^{28}Si . Events such as carbon oxygen shell mergers have previously been suggested as a way to boost the abundance of ^{40}K in Ritter et al. (2018)

Figure 3.36 shows the metallicity dependence of the stable potassium isotopes. ^{40}K is only produced at higher metallicities, and only in trace amounts. We also see that ^{39}K and ^{41}K have similar trends. The relative ratio of these isotopes changes more dramatically for the S1.0 and M0.8 models than for the T1.4 model. ^{41}K has a large radiogenic contribution, and a significant proportion of ^{39}K in the T1.4 models for $Z = 10^{-4}$ is also from radiogenic sources.

Nucleosynthesis in the $Z = 0$ models differs significantly between the classes of models seen in figure 3.37. While the overall production is similar within a factor of two between T1.4 and M0.8 (around 0.5) and S1.0 (around 1), T1.4Z0 has a relevant radiogenic contribution across the whole range of production from ^{39}Ca . We also note that the range of temperatures over which ^{39}K is produced is large, with similar mass fractions from 2 GK up to 7 GK (for those models with the appropriate particles to reach the respective peak temperatures). All three models show a production peak between 2

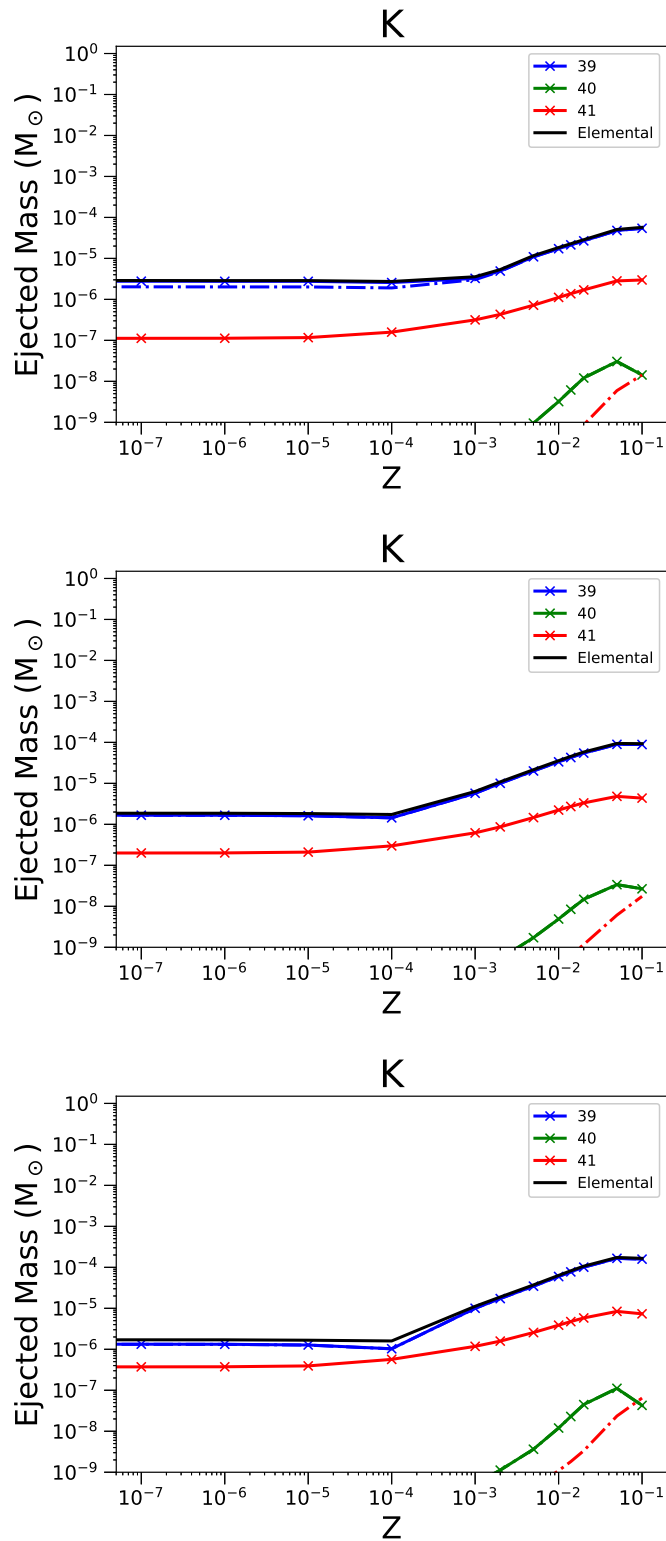


FIGURE 3.36: As in Figure 3.4 but for ejected mass of K, and its stable isotopes ^{39}K , ^{40}K and ^{41}K .

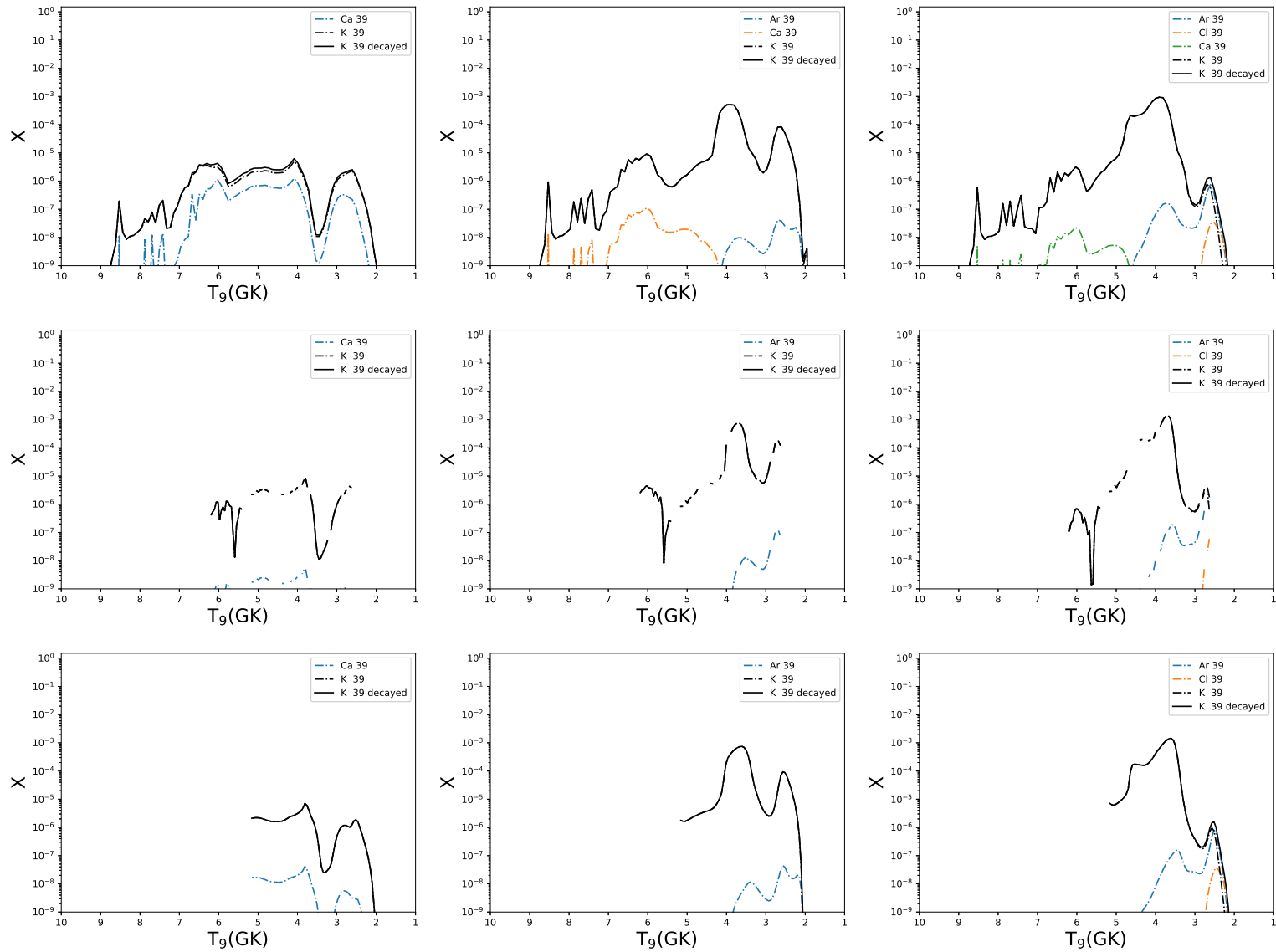


FIGURE 3.37: The abundance distributions of ^{39}K are shown, arranged as in figure 3.5. With metallicities of $Z = 0, 0.014$ and 0.1 from left to right, and the three categories of model - T1.4, S1.0 and M0.8 - from top to bottom.

and 3 GK, the T1.4Z0 model containing a significant contribution from ^{39}Ca . A narrow dip in production at around 3.5 GK then leads to a broad plateau, where production continues up to 7 GK.

The path of nucleosynthesis in these SNIa is more consistent between models at $Z = 0.014$ with production almost exclusively through direct synthesis of ^{39}K . Trace amounts of ^{39}Ar are produced in the 2-4 GK range in all classes of model, and there is a trace contribution from ^{39}Ca in the intermediate to high peak temperature range in model T1.4Z0.014.

As the initial metallicity increases to $Z = 0.1$, this trace production of ^{39}Ca is suppressed further in the T1.4Z0.1 model, there is an increase in the production of radio-isotope ^{39}Ar , and a trace amount of ^{39}Cl produced in the 2-3 GK range due to neutron captures in the carbon burning region. Production in the low peak temperature region is consistent between all models.

^{40}K shows no production at $Z = 0$ for any of the three class of models, we therefore show no plots for the $Z = 0$ column in figure 3.38. Above $Z = 0$ ^{40}K production is very similar for all of the models shown in figure 3.38. At $Z = 0.014$, we have a double peak of production - the largest between 2.5 and 3 GK, the second between 3.5 and 4 GK. We note that the position of the second peak here is slightly shifted between models, with the T1.4Z0.014 peak being at a higher temperature with a broader profile. This peak in the T1.4 model remains slightly broader in the $Z = 0.1$ models, where it is also boosted by secondary contributions to the nucleosynthesis of ^{40}K .

We see the same general trend for ^{41}K in (figure 3.39) as was observed in ^{39}K . Lower peak temperature production is consistent between all classes of model, here the primary production of nucleosynthesis is ^{41}Ca , in the $Z = 0$ models almost 100% of the ^{41}K ejected is produced as radiogenic ^{41}Ca , which is therefore obscured in these plots by the decayed abundance line. We see a double peaked feature in the cooler outer layers of the SNIa explosion, with

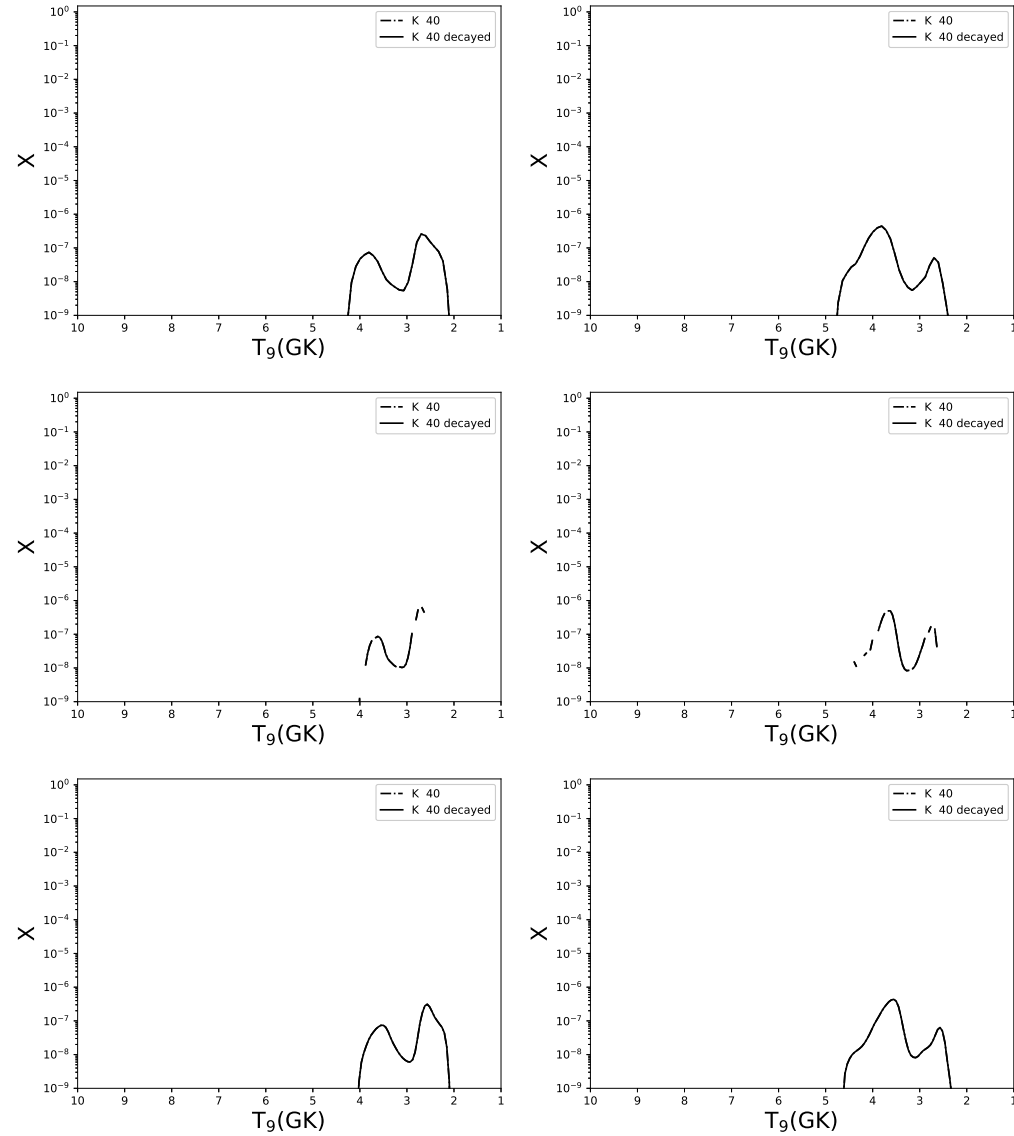


FIGURE 3.38: The abundance distributions of ^{40}K are shown, arranged as in figure 3.5. With metallicities of $Z = 0, 0.014$ and 0.1 from left to right, and the three categories of model - T1.4, S1.0 and M0.8 - from top to bottom. There are no data for the $Z = 0$ models, these panels have therefore been omitted.

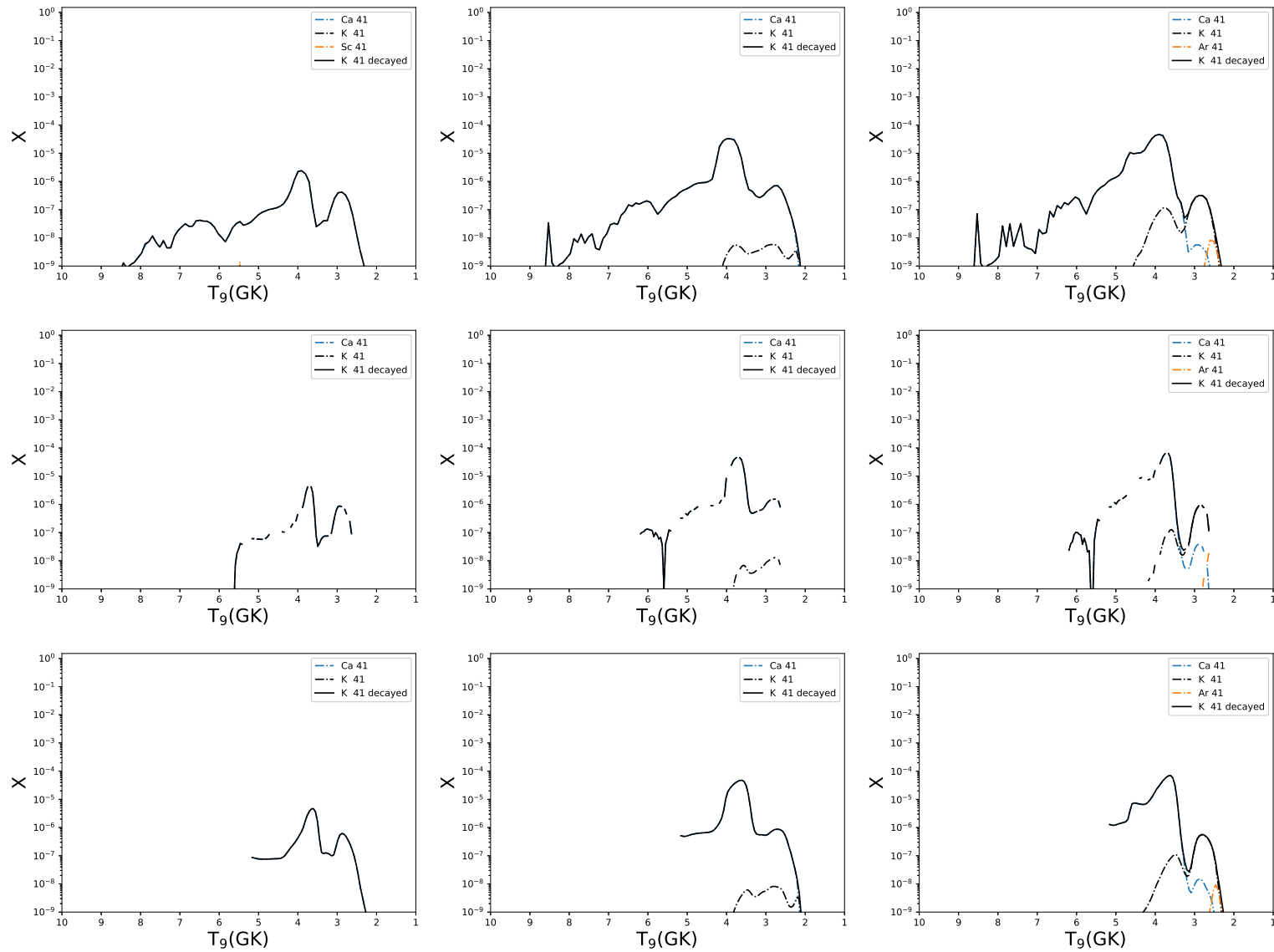


FIGURE 3.39: The abundance distributions of ^{41}K are shown, arranged as in figure 3.5. With metallicities of $Z = 0, 0.014$ and 0.1 from left to right, and the three categories of model - T1.4, S1.0 and M0.8 - from top to bottom. Radiogenic contributions from ^{41}Ca account for nearly 100% of production at low metallicities, and is therefore obscured by the decayed abundance line.

the T1.4Z0 model having a slight broadening and shifting to higher temperatures as compared with the S1.0Z0 and M0.8Z0 models. A broad high temperature production region is also present in the T1.4Z0 model, which provides a non-negligible contribution to the integrated abundance of ^{41}K on the order of a few percent.

In the $Z = 0.014$ models, the second of the low temperature peaks begins to dominate production, with a secondary boost to the production of ^{41}Ca , under explosive oxygen burning conditions. It is similar between each of the three models, the T1.4Z0.014 peak is at a slightly higher temperature and is broader. The high temperature production in the T1.4Z0.014 model is small in comparison to the production in the explosive oxygen burning layers of the ejecta. We see a trace amount of ^{41}K produced directly in the outer layers of the WD at peak temperatures between 2 and 4 GK.

In the $Z = 0.1$ models, this trace production begins to dominate in the carbon burning conditions. A trace amount of ^{41}Ar is produced in the very lowest peak temperature conditions, corresponding to the tail of carbon burning.

3.2.11 Calcium

Calcium consists of 6 stable isotopes: ^{40}Ca , ^{42}Ca , ^{43}Ca and ^{44}Ca , ^{46}Ca and ^{48}Ca . ^{40}Ca is produced in oxygen burning, and both ^{40}Ca and ^{42}Ca are produced in explosive oxygen burning during CCSN events. ^{43}Ca is produced in carbon and neon burning, and in α -rich freezeout from NSE (Woosley, Heger, and Weaver, 2002). ^{44}Ca is predicted to be produced efficiently from SNIa helium detonation or from α -rich freezeout, where it is formed as ^{44}Ti (Pignatari et al., 2016; Magkotsios et al., 2010). ^{46}Ca has a contribution from AGB stars, and is also produced in carbon and neon burning. Finally, ^{48}Ca is formed in the n-process (Pignatari et al., 2016), or in conditions in a CCSN with high

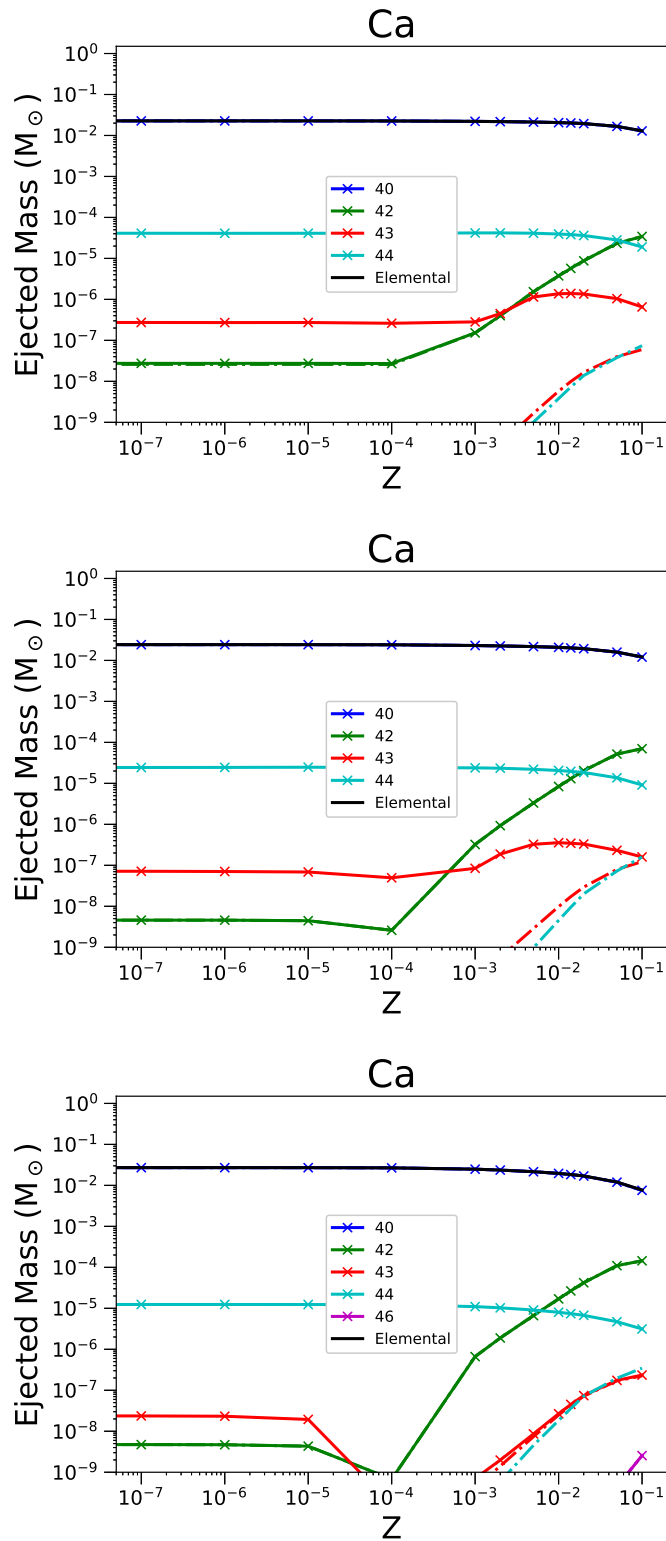


FIGURE 3.40: As in Figure 3.4 but for ejected mass of Ca, and its stable isotopes ^{40}Ca , ^{42}Ca , ^{43}Ca and ^{44}Ca .

neutron fluxes. Woosley, Heger, and Weaver, 2002 also identify ^{48}Ca as having a significant contribution from Chandrasekhar mass SNIa events.

Figure 3.40 shows how similar production is between our three classes of model, with ^{40}Ca , ^{42}Ca and ^{44}Ca having very similar trends with respect to metallicity. ^{43}Ca also has a similar trend. In the $Z = 10^{-4}$ to 10^{-2} range, production drops significantly for this isotopes in the M0.8 models, as compared with the T1.4 and S1.0 models, it is also produced directly, whereas the production in the other models is almost exclusively as radio-isotopes. Only a trace amount of ^{46}Ca is produced in any model, and only in the M0.8Z0.1 metallicity model. ^{48}Ca is not produced in any of our post-processed models.

In figure 3.41 we see that production of ^{40}Ca is fairly simple and consistent throughout the models. A broad production peak is observed in the $Z = 0$ models in the peak temperature range between 4 and 5.5 GK. As the initial metallicity is increased we see that the mass fraction of ^{40}Ca in this peak production region also decreases, resulting in the metallicity trend of ^{40}Ca observed in figure 3.40. The ejected mass of ^{40}Ca decreases from 2.27×10^{-2} to $1.29 \times 10^{-2} M_{\odot}$ for the T1.4 models, 2.43×10^{-2} to $1.21 \times 10^{-2} M_{\odot}$ in the S1.0 models and 2.71×10^{-2} to $7.55 \times 10^{-3} M_{\odot}$ in the M0.8 models. The larger effect in the M0.8 model is due to the absence of any production in NSE regions in this class of model.

Production of ^{42}Ca in T1.4Z0 is dominated by a high temperature peak in the 6-7 GK range, with smaller peaks between 4 and 4.3 GK and 8 and 9 GK. The lowest temperature peak is reproduced in the S1.0Z0 and M0.8Z0 models in the same temperature range. Direct synthesis of ^{42}Ca is the main path for all three classes of model.

Production of ^{42}Ca is significantly boosted in the T1.4Z0.014, S1.0Z0.014 and M0.8Z0.1 models, the low temperature peak observed in the $Z = 0$ models is here increased by several orders of magnitude and covers a peak temperature range from 2 to 4 GK. This temperature range covers both carbon

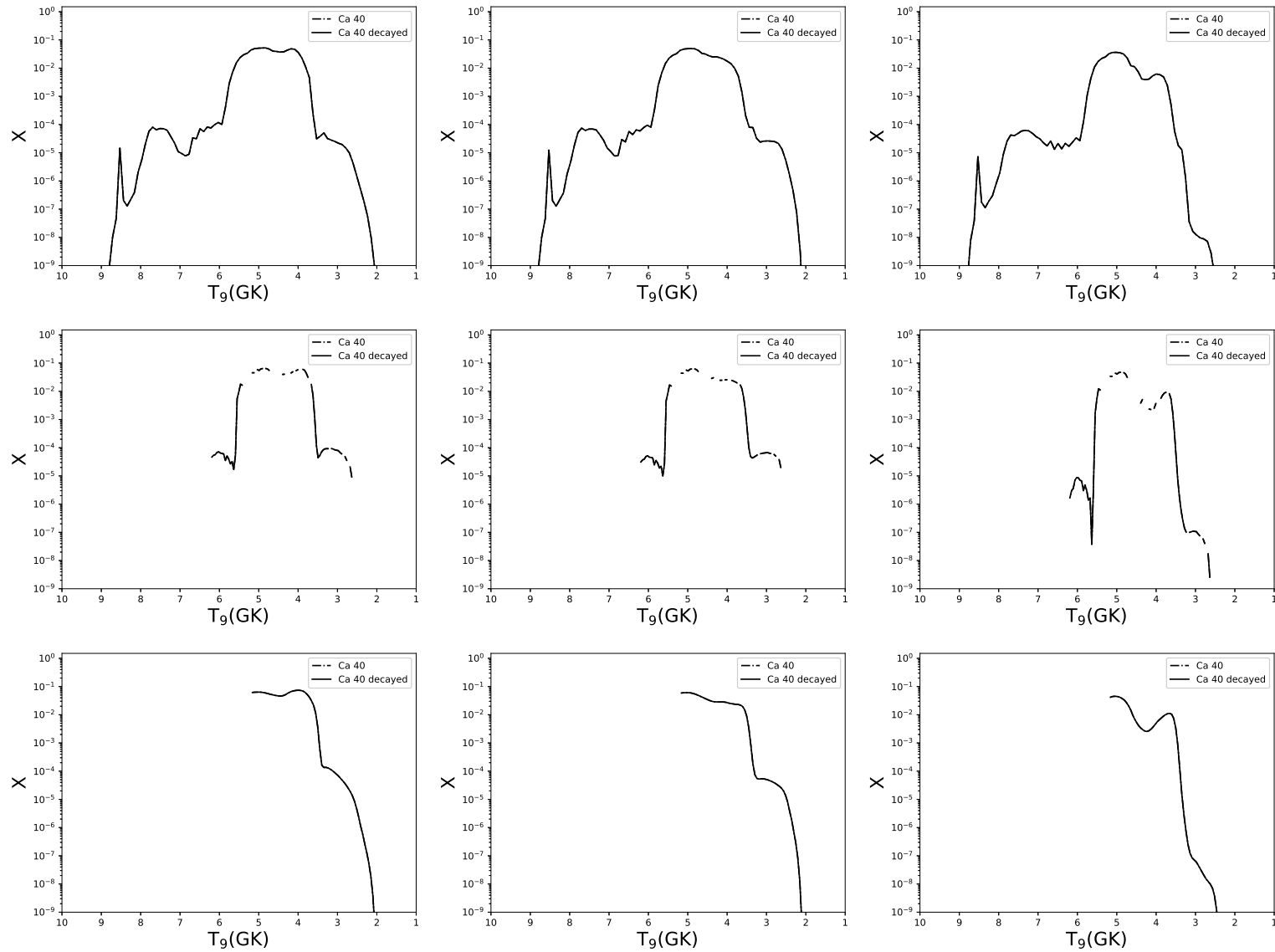


FIGURE 3.41: The abundance distributions of ^{40}Ca are shown, arranged as in figure 3.5. With metallicities of $Z = 0, 0.014$ and 0.1 from left to right, and the three categories of model - T1.4, S1.0 and M0.8 - from top to bottom.

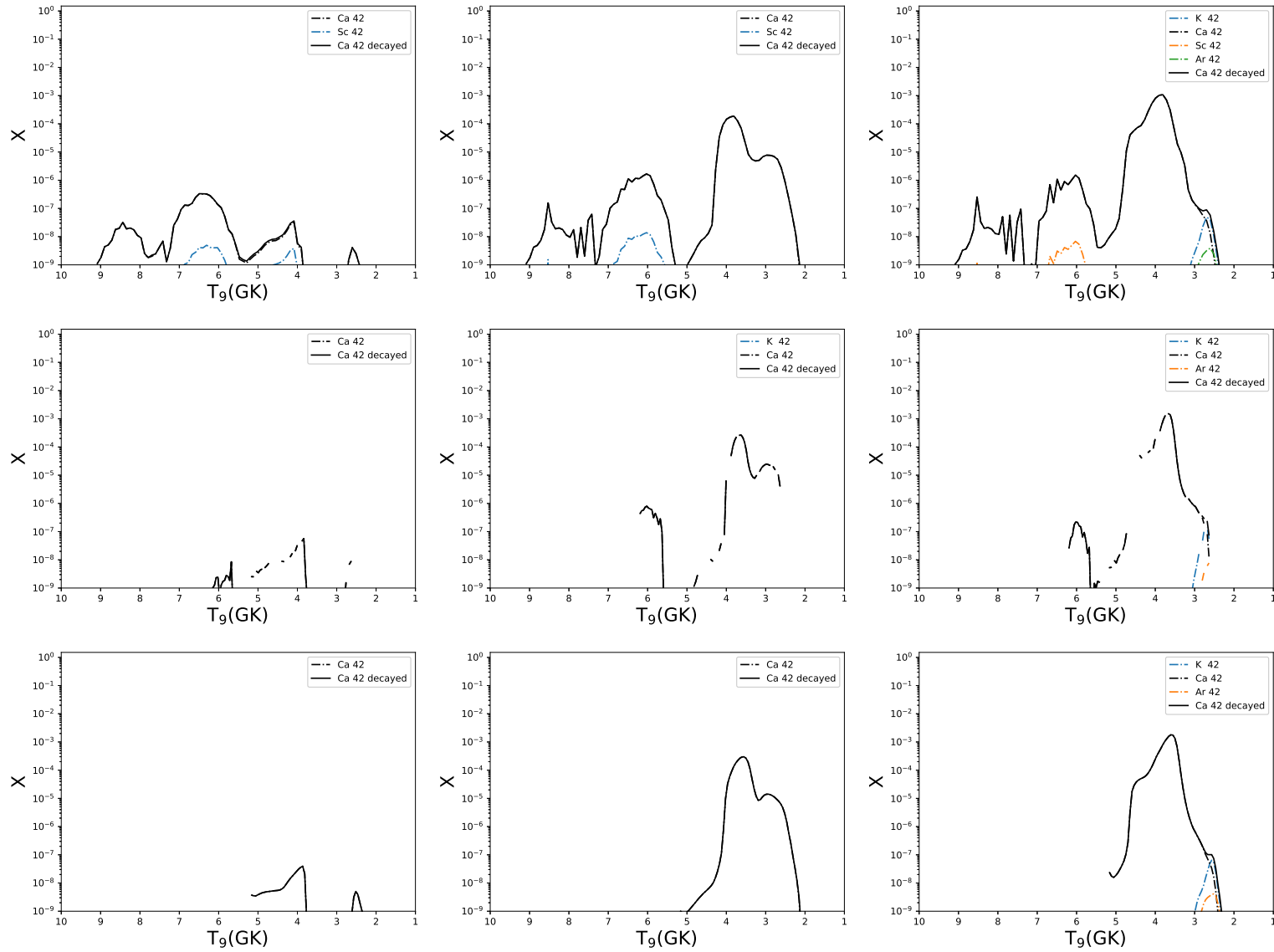


FIGURE 3.42: The abundance distributions of ^{42}Ca are shown, arranged as in figure 3.5. With metallicities of $Z = 0, 0.014$ and 0.1 from left to right, and the three categories of model - T1.4, S1.0 and M0.8 - from top to bottom.

burning and oxygen burning regions, with the largest contribution being in the 3.5 - 5 GK range, corresponding to oxygen burning. The lower temperature shoulder of production below approximately 3 GK contributes on the order of a few percent to the ejected mass of ^{42}Ca , in both regions through direct synthesis of ^{42}Ca . In T1.4Z0.014, there is also a significant boost to the production in the intermediate temperature range peak but due to the rapid growth of production in the outer layers of the SNIa explosion, this contribution is negligible.

We see a further dramatic increase in production in the $Z = 0.1$ case. T1.4Z0.1 has a small reduction in production in the 6-7 GK peak. This is compensated for by the increase in the oxygen burning region where ^{42}Ca is around 0.2% of the mass fraction of these tracer particles. This is accompanied by a decrease in production in the carbon burning like region below 3 GK. This same trend is seen in models S1.0Z0.1 and M0.8Z0.1, with trace production of ^{42}K and ^{42}Ar appearing in the very lowest peak temperature range. The peak at around Z_{\odot} for ^{42}Ca in the carbon burning region to the decline at higher metallicity is due to the effect of excess neutron captures driving production to more neutron rich isotopes.

Figure 3.43 shows the production of ^{43}Ca . Production in the T1.4Z0 is dominated by the 5.5 - 7 GK temperature range, where ^{43}Ca is produced as ^{43}Sc with a contribution on the order of 1% from ^{43}Ti . The majority of nucleosynthesis in this temperature range is primary as ^{43}Sc production does not change across metallicities; however, the radiogenic contribution does show some secondary effects. As the metallicity increases (T1.4Z0.014), we see that production below 5 GK shifts to lower peak temperatures. We now see a double peaked structure, which corresponds to the positions of the oxygen and carbon burning regions described in Iliadis (2015) between 2 and 4 GK. In these two regions, ^{43}Ca is produced directly with a small contribution from ^{43}Sc . As the initial neon mass fraction is increased further, the carbon

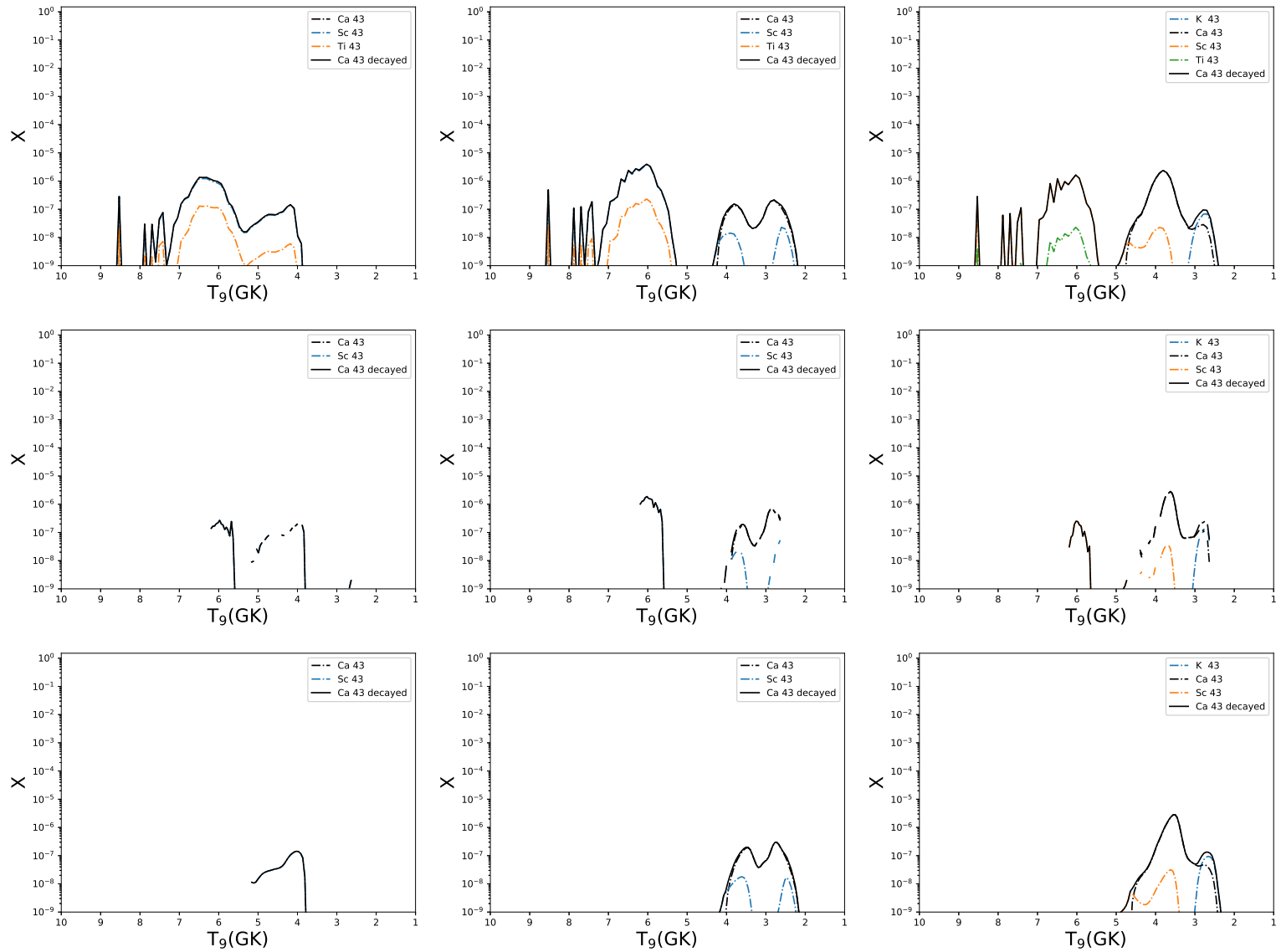


FIGURE 3.43: The abundance distributions of ^{43}Ca are shown, arranged as in figure 3.5. With metallicities of $Z = 0, 0.014$ and 0.1 from left to right, and the three categories of model - T1.4, S1.0 and M0.8 - from top to bottom.

and oxygen burning regions become less distinct, and a broad production peak is seen spanning the whole peak temperature range. A small radiogenic contribution from ^{43}Sc is observed in the 3.5 - 5 GK range, where as ^{43}Ca is mainly produced as radiogenic ^{43}K in the lower temperature carbon burning region. This shows that there is a fundamental difference in the nucleosynthesis of ^{43}Ca in these two regions and that ^{43}Ca production may be sensitive to a range of nuclear reaction rates at these lower temperatures.

In the S1.0Z0 model, the maximum peak temperature is approximately 6.2 GK. From around 5.5 to 6.2 GK we see again the production of the radioisotope ^{43}Sc . The double peaked production region between 2 and 4 GK, which corresponds to the carbon and oxygen-like burning regions is present in the S1.0Z0.014 model. We see that it is similar between to the T1.4Z0.014 case, with direct production of ^{43}Ca with a small contribution from ^{43}Sc however the carbon region production is boosted in the S1.0Z0.014 model compared with T1.4Z0.014. S1.0Z0.1 shows the same trend as the T.14 models, where the double peak of production between 2 and 4 GK broadens, with the carbon region producing radiogenic ^{43}K and the oxygen region producing ^{43}Ca directly.

The M0.8 models show the same trends in the 2 to 5 GK range as are observed in the T1.4 and S1.0 models, with the higher temperature region being absent. In the M0.8Z0.014 models, the carbon peak production of ^{43}Ca is closer to the value found in the T1.4Z0.014 model than the S1.0Z0.014 model.

^{44}Ca is produced primarily as ^{44}Ti in all of the $Z = 0$ models. In T1.4Z0, it is produced over a wide range of peak temperatures from 4 to 6.5 GK, with a negligible contribution from a peak at 2.8 GK. We see a similar distribution in the S1.0Z0 and M0.8Z0 models, with appropriate upper temperature limits as discussed for in previous sections.

T1.4Z0.014 shows a small drop in the production of ^{44}Ti at the lower end of this broad range of production, this is partially compensated for by the

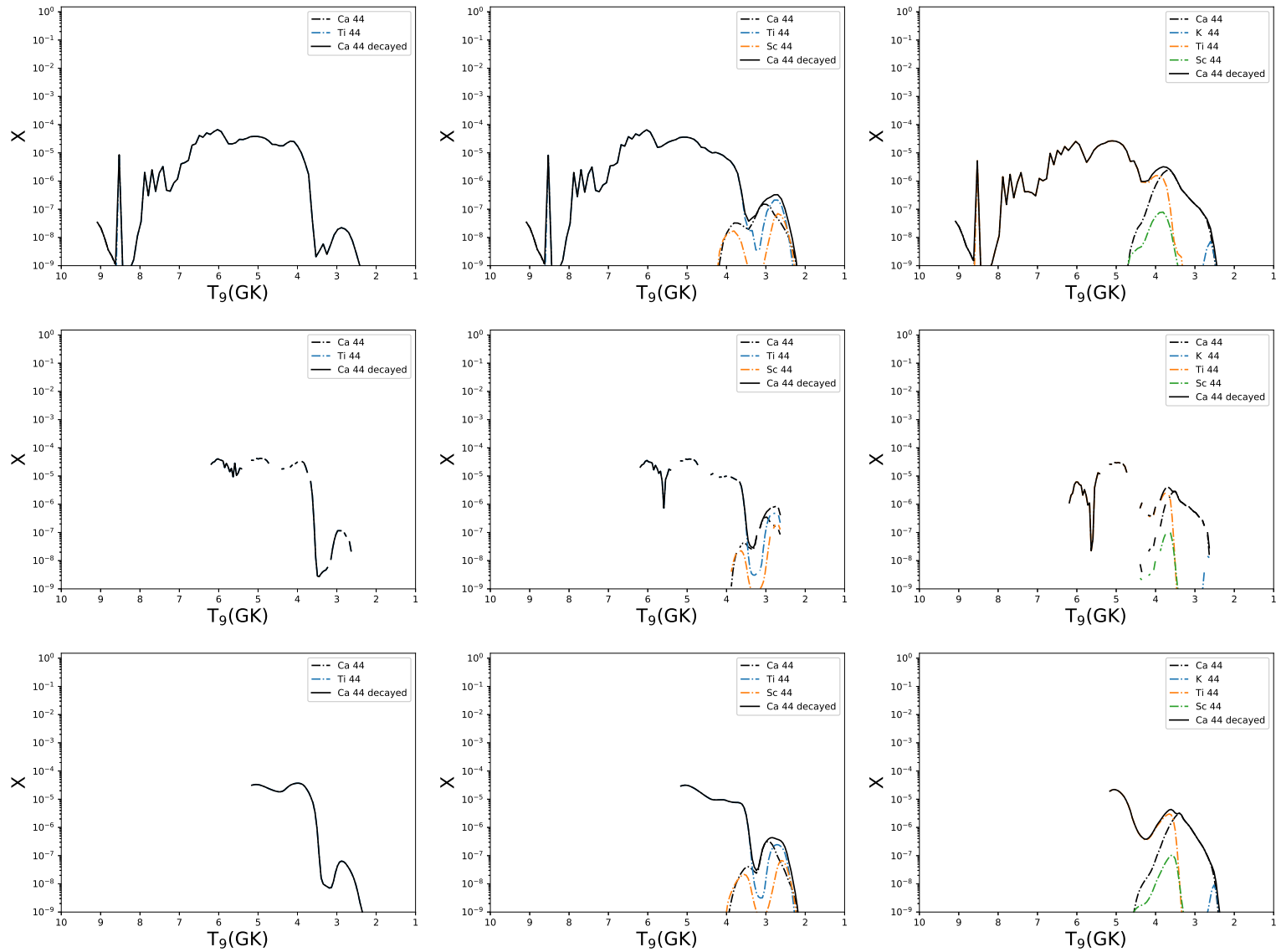


FIGURE 3.44: The abundance distributions of ^{44}Ca are shown, arranged as in figure 3.5. With metallicities of $Z = 0, 0.014$ and 0.1 from left to right, and the three categories of model - T1.4, S1.0 and M0.8 - from top to bottom.

increased secondary production in the small peak centered at 2.8 GK. Across the rest of the peak temperature range, we see contributions only from ^{44}Ca and ^{44}Ti , in this secondary peak we see production of ^{44}Sc also, although it is not the most abundant isotope in this temperature window. S1.0Z0.014 shows the same trend, as does M0.8Z0.014.

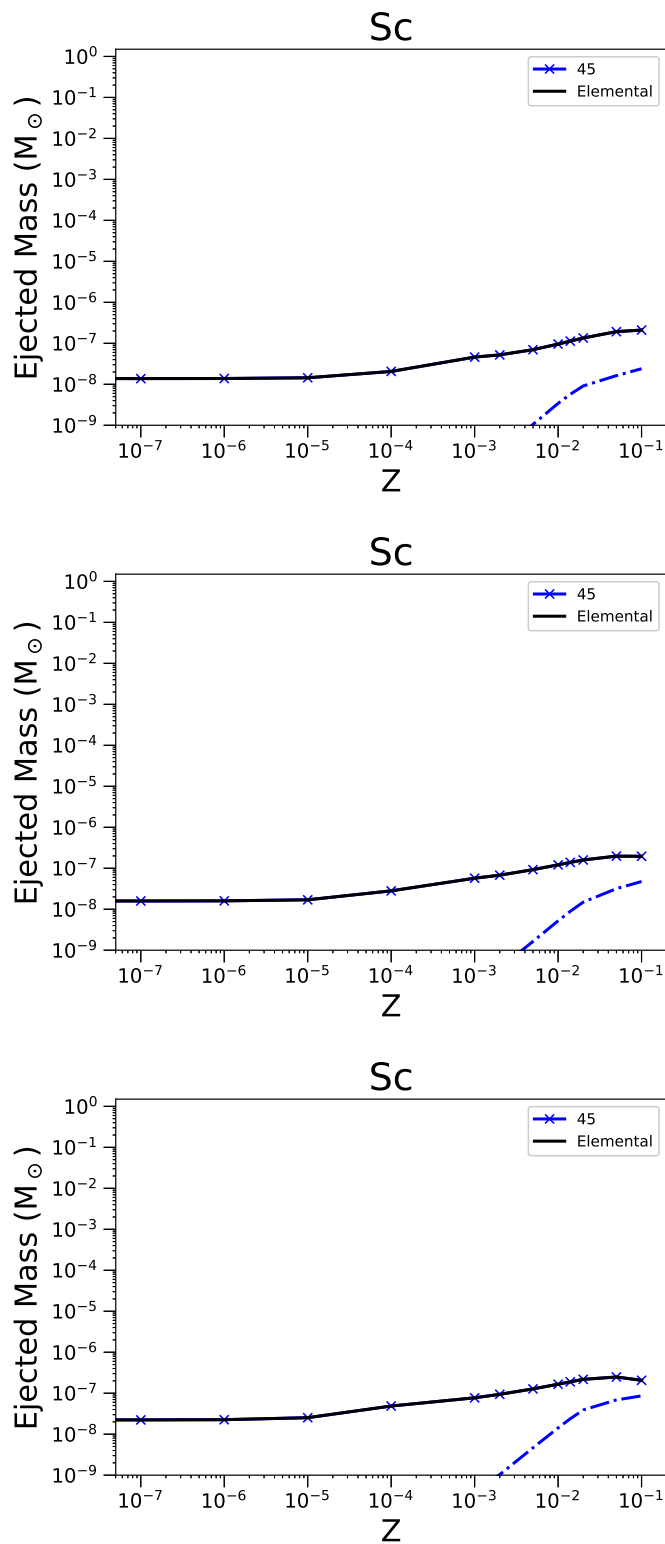
In the $Z = 0.1$ models, we see a further suppression of the ^{44}Ti production at the tail end of the broad production range, the increase in direct synthesis of ^{44}Ca compensates for this somewhat and leads to a continuation of the production range out to approximately 2.4 GK

3.2.12 Scandium

Scandium is mono-isotopic, with ^{45}Sc being produced in α -rich freeze-out, the neutrino process and carbon and neon burning in massive stars (Woosley, Heger, and Weaver, 2002). Current theoretical predictions of the GCE of scandium report it being underproduced relative to observations (Kobayashi, Karakas, and Lugaro, 2020; Kobayashi et al., 2006), although recent work including the contributions of jet-induced supernovae mitigate this somewhat. Carbon oxygen shell shell mergers also increase the amount of scandium produced in CCSN (Ritter et al., 2018) which accounts for some of this discrepancy.

Scandium shows a similar trend across all three classes of model with respect to metallicity. It is mainly produced as a radiogenic ^{45}Ti , with only M0.8Z0.1 having a direct ^{45}Sc yield of greater than 10% synthesised during the explosion.

^{45}Sc is produced over a range of peak temperatures in the T1.4Z0 model, mostly as ^{45}Ti . There is a peak in production at 4 GK and a broad region between 5 and 8 GK. Production is similar in S1.0Z0 however as the maximum peak temperature in this model is at around 6.2 GK, the broad production

FIGURE 3.45: As in Figure 3.4 but for ejected mass of ^{45}Sc .

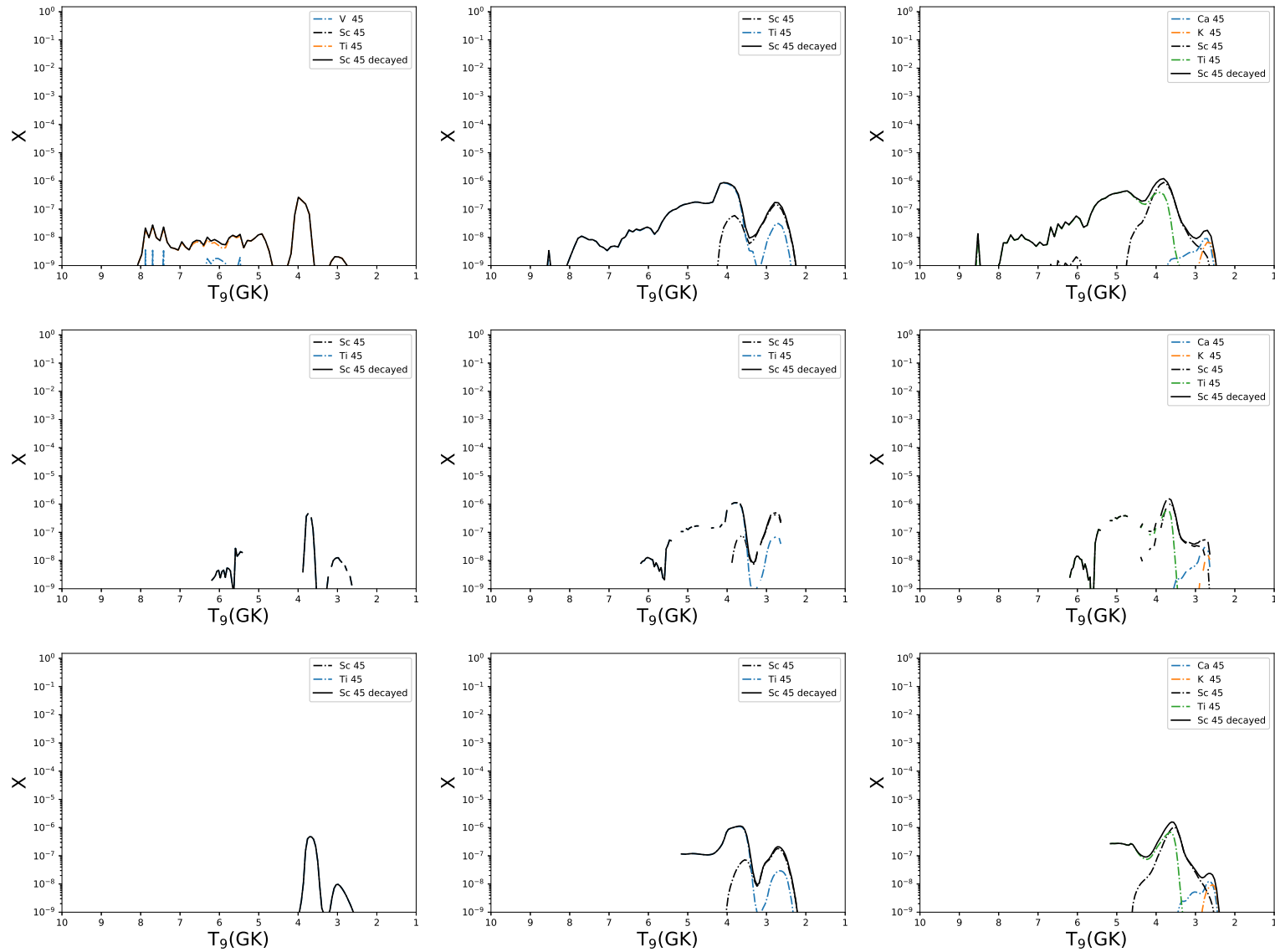


FIGURE 3.46: The abundance distributions of ^{45}Sc are shown, arranged as in figure 3.5. With metallicities of $Z = 0, 0.014$ and 0.1 from left to right, and the three categories of model - T1.4, S1.0 and M0.8 - from top to bottom.

region above 5 GK contributes proportionally less to the ejected mass of ^{45}Sc . The 4 GK peak is shifted slightly to between 3.5 and 4 GK, and is narrower. The small peak at 3 GK, which was negligible in the T1.4Z0.0 model is larger here. Production in M0.8Z0 is similar to the low temperature peak component of S1.0Z0.

In model T1.4Z0.014, production of ^{45}Sc is boosted significantly across a wide range of temperatures as compared with the $Z = 0$ case. In figure 3.46, we see a secondary component in production of both ^{45}Sc and ^{45}Ti which boosts production in the lower temperature burning region significantly. This effect is also seen in S1.0Z0.014 and M0.8Z0.014. At peak temperatures above 3.5 GK, ^{45}Sc is mostly produced as the radioisotope ^{45}Ti . At lower temperatures it is directly produced. As the metallicity increases further, a small contribution from ^{45}K in the 2.5 - 3 GK range is seen. This is also true for the S1.0 and M0.8 models.

As the initial metallicity is increased further, production at the very lowest temperatures is suppressed, with the double peaked production sites evident in the $Z = 0$ and 0.014 cases becoming a single peak.

3.2.13 Titanium

Titanium has 5 stable isotopes: ^{46}Ti , ^{47}Ti , ^{48}Ti , ^{49}Ti and ^{50}Ti . ^{46}Ti is produced in explosive oxygen burning and SNIa detonations, ^{47}Ti is produced in the same as well as in explosive silicon burning. ^{48}Ti is produced in explosive silicon burning or SNIa detonations, and ^{49}Ti in explosive silicon burning only. Finally, ^{50}Ti is produced in Chandrasekhar mass SNIa explosions and the s-process in massive stars (Woosley, Heger, and Weaver, 2002).

Figure 3.47 presents the metallicity dependence of the production of these isotopes. We see that ^{48}Ti is the most abundant isotope of titanium in all three

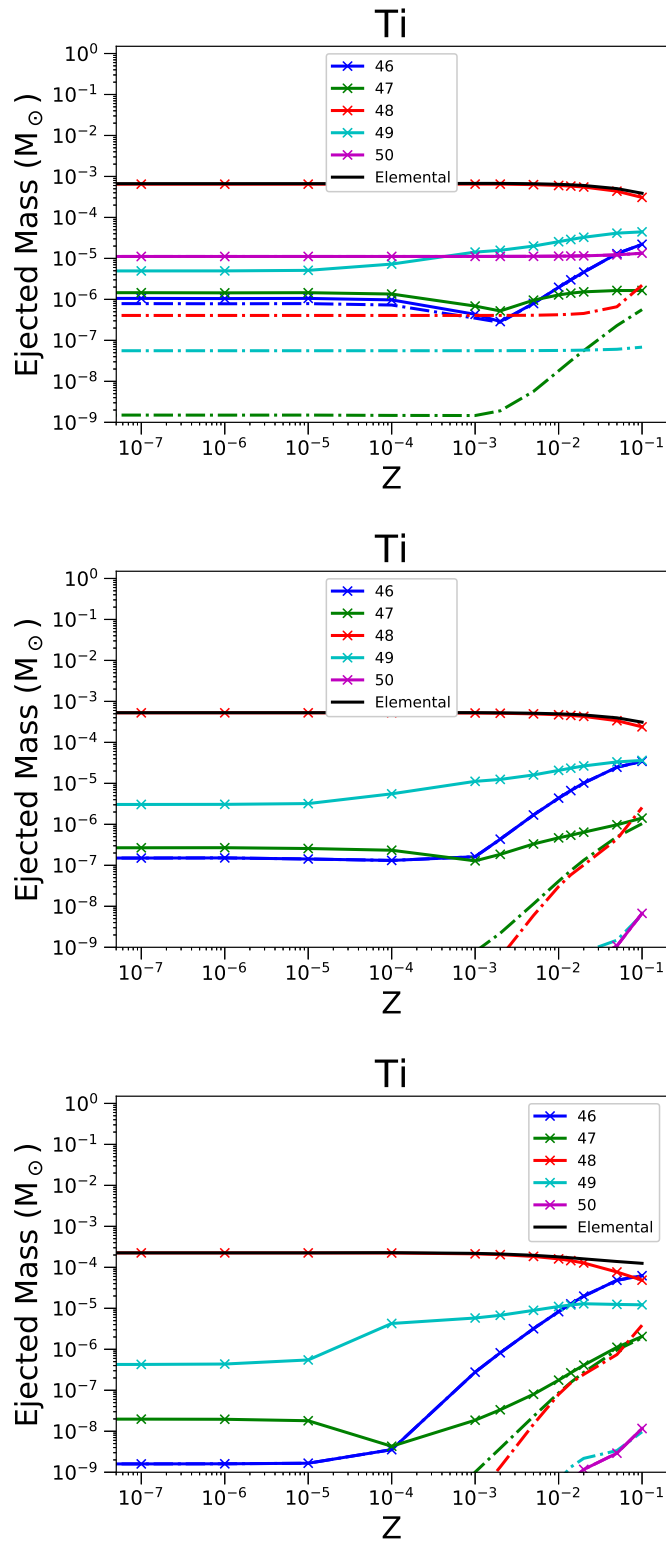


FIGURE 3.47: As in Figure 3.4 but for ejected mass of Ti, and its stable isotopes ^{46}Ti , ^{47}Ti , ^{48}Ti , ^{49}Ti and ^{50}Ti .

models for almost all metallicities. Only in the M0.8Z0.1 model does ^{46}Ti become more abundant than ^{48}Ti . ^{46}Ti production is primary at $Z < 0.00001$ and secondary above this, with the ejected mass of ^{46}Ti increasing with metallicity. ^{47}Ti has a strong secondary component in the three classes of model above $Z = 0.001$, this secondary component is through direct production of ^{47}Ti . ^{48}Ti is flat with metallicity in the T1.4 models until $Z > 0.05$ where a strong secondary contribution is seen, for the S1.0 and M0.8 models, this contribution starts at $Z = 0.001$. ^{50}Ti is abundant the T1.4 models only, with only trace amounts produced in the S1.0 and M0.8 models at $Z > 0.01$. ^{50}Ti also has a very flat dependency on the metallicity of the progenitor. These properties suggest that the $^{50}\text{Ti}/^{48}\text{Ti}$ isotopic ratio may provide a diagnostic for the determination of SNIa progenitor.

The ejected mass of elemental titanium decreases with increasing progenitor metallicity, despite the strong secondary production observed in all isotopes except for ^{48}Ti .

Figure 3.48 shows that ^{46}Ti production at $Z = 0$ is much more active in T1.4Z0 than in either of the other two models. This is due to ^{46}Ti being synthesised in intermediate to high temperatures, at 6 GK or above, which do not exist in the S1.0 and M0.8 models. There is a small peak of production at approximately 4 GK which is negligible.

We see in the $Z = 0.014$ panels that production of ^{46}Ti (through direct nucleosynthesis) is highly dependent on the initially metallicity. The small peak at 4 GK now dominates the production. The high temperature component of the T1.4 models remains unchanged.

Figure 3.49 shows the production of ^{47}Ti with respect to the peak temperatures experienced in a given tracer particle. ^{47}Ti is produced over a broad range of peak temperatures in the T1.4 models. At $Z = 0$, the production of ^{47}Ti occurs in the temperature range from 4 to 9 GK, this spans the range from explosive oxygen burning through to NSE. There is a peak between 5.5 and

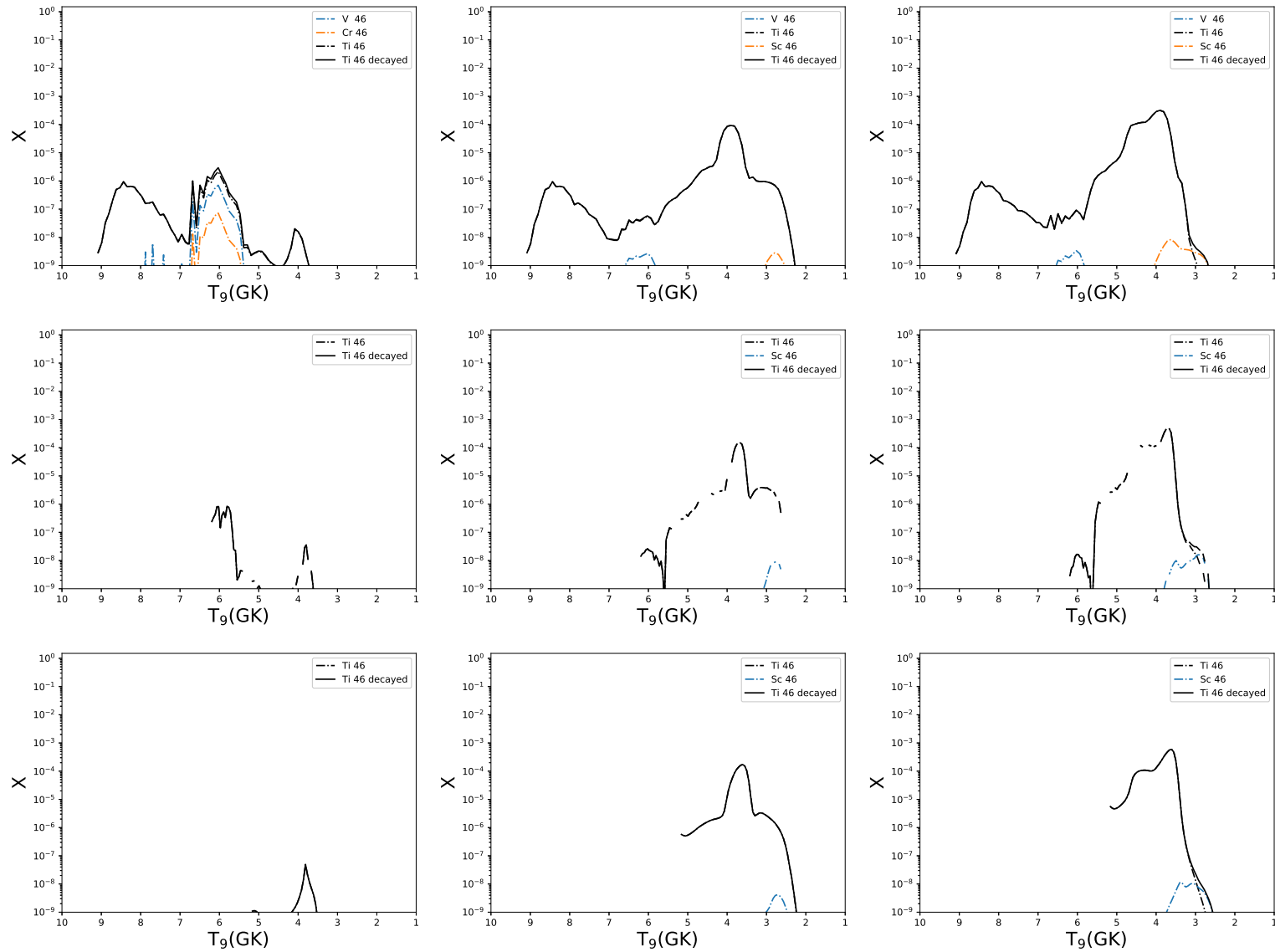


FIGURE 3.48: The abundance distributions of ^{46}Ti are shown, arranged as in figure 3.5. With metallicities of $Z = 0, 0.014$ and 0.1 from left to right, and the three categories of model - T1.4, S1.0 and M0.8 - from top to bottom.

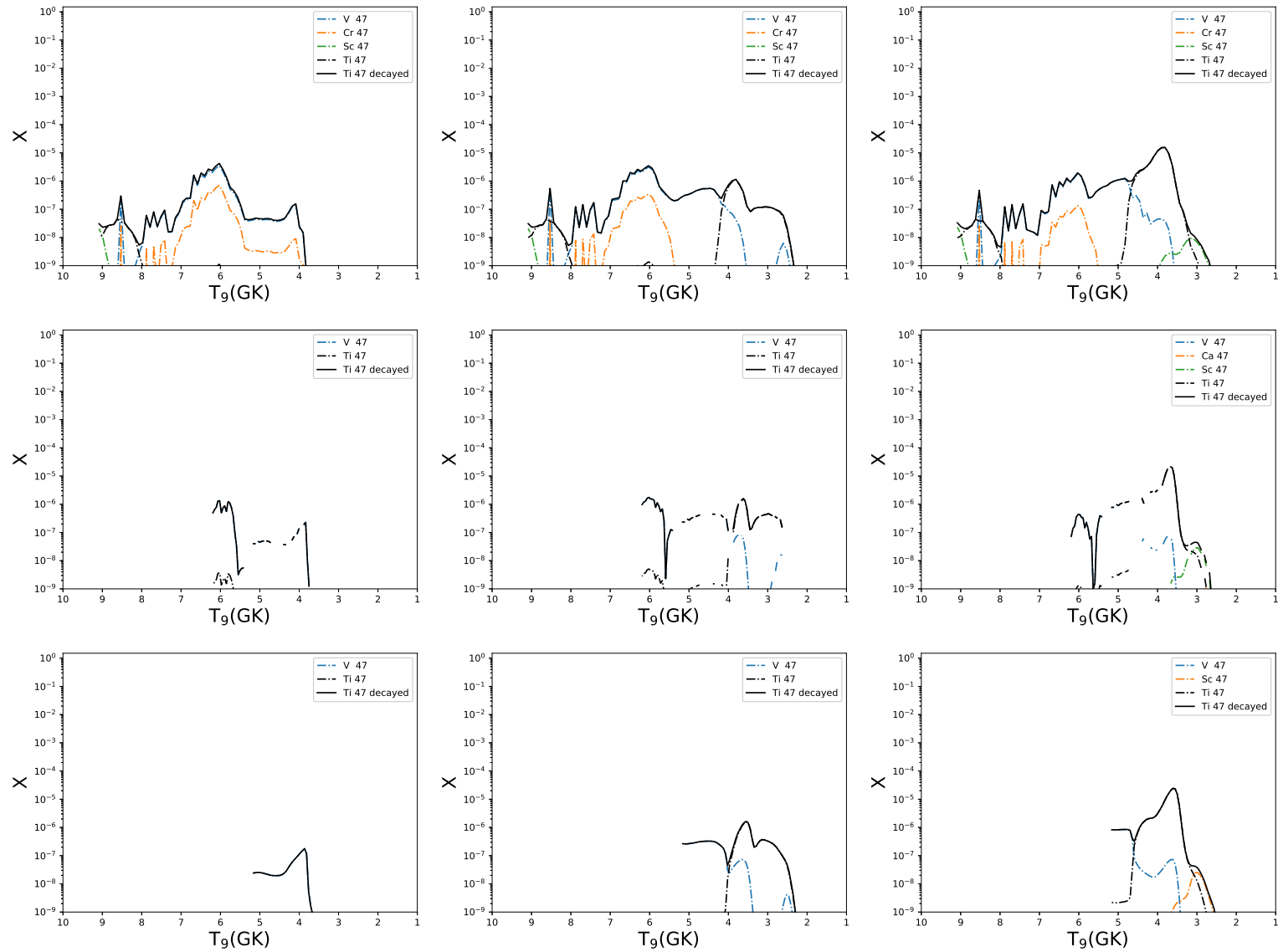


FIGURE 3.49: The abundance distributions of ^{47}Ti are shown, arranged as in figure 3.5. With metallicities of $Z = 0, 0.014$ and 0.1 from left to right, and the three categories of model - T1.4, S1.0 and M0.8 - from top to bottom.

7 GK, which contributes the majority of material. Across the whole temperature range, the radioisotope ^{47}V contributes the largest proportion of ^{47}Ti . In the peak temperature range from 8 to 9 GK, there is some contribution from ^{47}Ti however this is a small fraction of the integrated ^{47}V contribution. Above 9 GK, there is a region of ^{47}Sc production but again this is small. Moving to the T1.4Z0.014 model, production extends to lower peak temperatures, with a peak between 2.3 and 4.2 GK being formed. This temperature range corresponds to the carbon burning regions. ^{47}Ti is produced directly in this region. In T1.4Z0.1 model, we see that production of ^{47}Ti in the lower peak temperature regions has increased further. ^{47}Ti now accounts for more than 1% of the ejected Ti mass, however this is also, in part, due to a decrease in the ejected mass driven by the metallicity dependence of ^{46}Ti .

In model S1.0Z0, production is between 3.8 and 6.1 GK, with the radioisotope ^{47}V dominating production. In model S1.0Z0.014, the carbon and oxygen burning regions begin to contribute a significant proportion of the ejected mass of ^{47}Ti . It is produced directly in this region. At $Z = 0.1$, almost the whole amount of ^{47}Ti is produced as radiogenic ^{47}V , mostly in the carbon and oxygen burning regions.

As with the S1.0 models the production in the M0.8 models is strongly metallicity dependent. As there is no contribution in the M0.8 models from the >6 GK production region, the yields of ^{47}Ti for M0.8 are very sensitive to the nucleosynthesis in the carbon and oxygen burning regions. The trend is otherwise the same as for the S1.0 model, with production being through the same mechanism.

The production of ^{48}Ti is shown in figure 3.50. The trend for the T1.4 models is similar to that observed for ^{47}Ti . Production is again over a broad range of temperatures, ranging from oxygen burning at 4 GK, to the high density NSE region at > 9 GK. Above 8.2 GK, the main production pathway of ^{48}Ti is direct production. Below 8.2 GK and across the whole of the

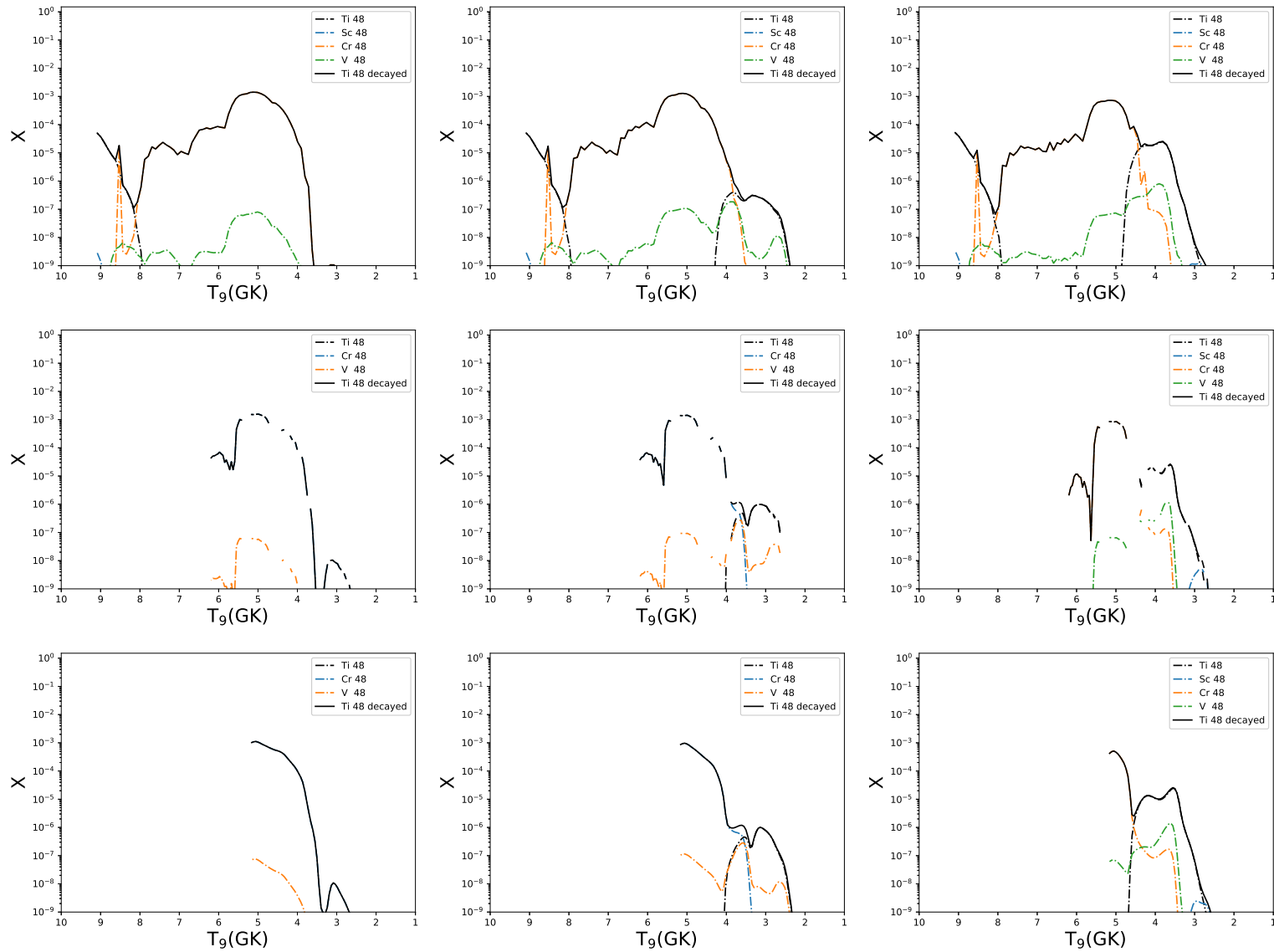


FIGURE 3.50: The abundance distributions of ^{48}Ti are shown, arranged as in figure 3.5. With metallicities of $Z = 0, 0.014$ and 0.1 from left to right, and the three categories of model - T1.4, S1.0 and M0.8 - from top to bottom.

rest of the production sites, ^{48}Ti is produced as ^{48}Cr , with a negligible contribution from ^{48}V . This is similar to the ^{47}Ti where it is produced mainly as radiogenic ^{47}V . In T1.4Z0.014, production extends into the carbon burning region between 2.3 and 3.8 GK. Here ^{48}Ti is produced directly and is strongly metallicity dependent. Production at higher temperatures remains fairly unchanged, although there must be a small decrease in production as the ejected mass of ^{48}Ti decreases slightly compared with the T1.4Z0 model - from $1.46 \times 10^{-6} M_{\odot}$ to $1.42 \times 10^{-6} M_{\odot}$. The increasing production in the cooler outer regions in the $Z = 0.1$ model more than compensate for the slight reduction in the oxygen burning and NSE regions, where we see an overall increase in the ejected mass of ^{48}Ti to $1.65 \times 10^{-6} M_{\odot}$. We see an increase in the contributions from ^{48}V in the 4 - 6 GK range however its contribution remains small. ^{48}Ti is directly produced above 8.8 GK and below 4.5 GK, and radiogenic ^{48}Cr provides the bulk of material in the 4 - 8 GK region.

In the S1.0Z0 model, production of radiogenic ^{48}Cr dominates the ^{48}Ti production. Only a trace contribution from ^{48}V is seen. The 3.5 - 6.1 GK production region is otherwise solely ^{48}Cr . Similar to the metallicity dependence in the T1.4 models, we see direct production of ^{48}Ti in the 2.8 - 3.8 GK range as we move to the S1.0Z0.014 model. ^{48}V production also increases somewhat however the dominant channel is still through ^{48}Ti . In the S1.0Z0.1 models the carbon burning production has increased further. As we see in figure 3.47 however, in neither T1.4, S1.0 or M0.8 is the increase in direct production enough to compensate for the decrease in the oxygen burning and NSE contributions with increasing metallicity.

The M0.8 models show a similar behaviour to the S1.0 set, with a proportionally larger contribution from the carbon burning ejecta.

Figure 3.51 shows the ejected abundances for ^{49}Ti in the three sets of models. In T1.4Z0, production ranges from 3.8 GK to $> 9\text{GK}$, with three peaks of production between 3.8 and 6 GK, 7 and 8 GK and above 9 GK respectively.

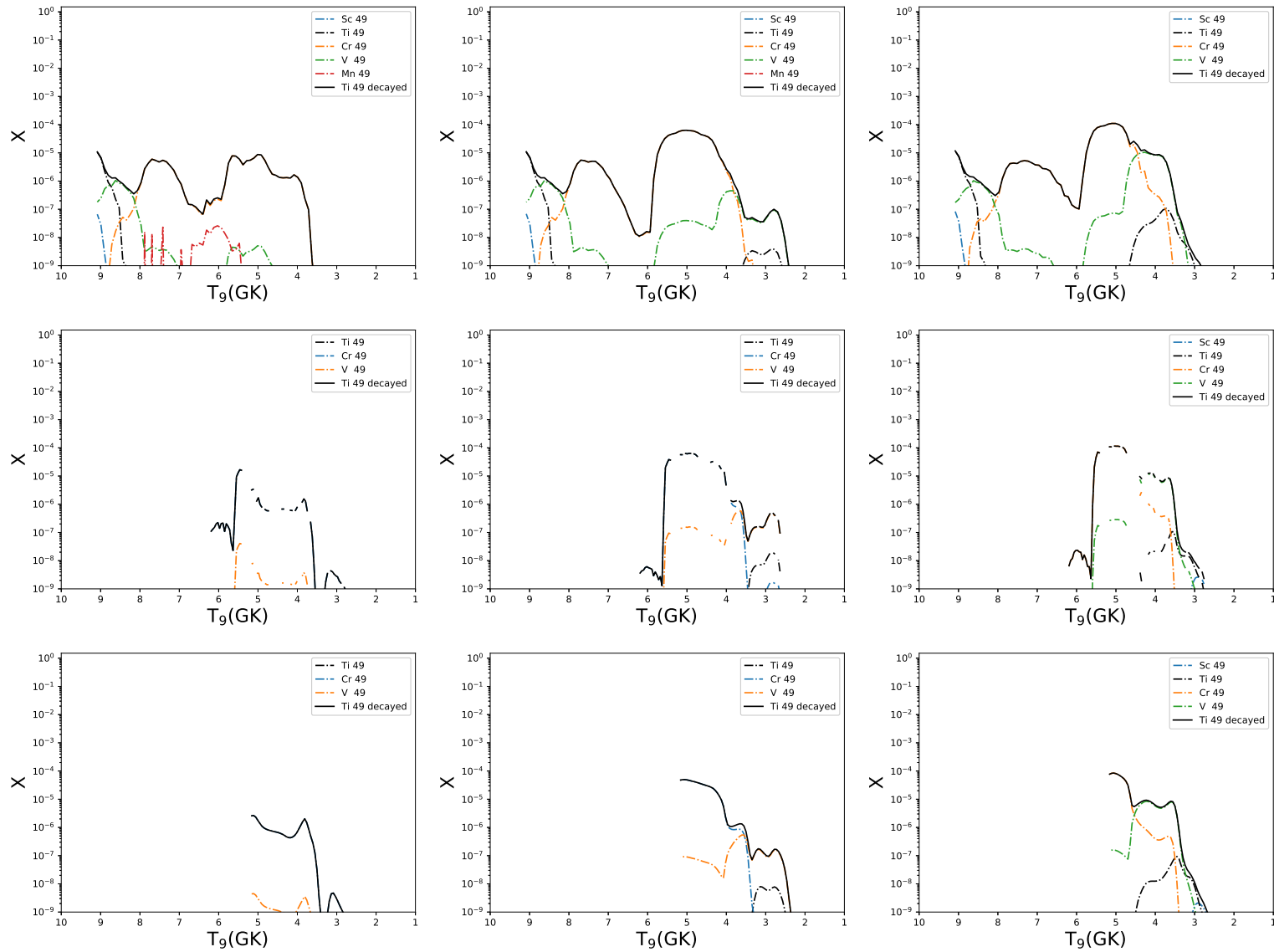


FIGURE 3.51: The abundance distributions of ^{49}Ti are shown, arranged as in figure 3.5. With metallicities of $Z = 0, 0.014$ and 0.1 from left to right, and the three categories of model - T1.4, S1.0 and M0.8 - from top to bottom.

The majority of ^{49}Ti is produced as ^{49}Cr , particularly below 8 GK where almost 100% of the ejecta is radiogenic ^{49}Cr . Only trace amounts of radiogenic ^{49}Mn and ^{49}V are present. Between 8 and 9 GK, there is a small region where production is dominated by contributions from radiogenic ^{49}V , and above 9 GK direct production of ^{49}Ti is seen. These two regions are small compared to the ^{49}Cr producing region however. In the T1.4Z0.014 model, we see a significant increase in the 4 - 6 GK region, corresponding to oxygen and silicon burning. Peak production in these particles increases by an order of magnitude between these two models. We also see an increase in the contribution from ^{49}V , where a low temperature production region in the carbon burning particles is seen between 2.3 and 3.5 GK. In the T1.4Z0.1 model, this low temperature region is depleted, due to increased neutron captures shifting material to more neutron rich isotopes. We see a further increase in the 4.5 - 6 GK region, which drives the increasing ejected mass of ^{49}Ti with initial metallicity.

The models of S1.0 and M0.8 show a similar trend to the two lower temperature peaks in T1.4. There is an initial, small increase in production in the carbon burning region, along with a larger increase in the 3.5 - 5.8 GK region in these two models. ^{49}Ti is produced as ^{49}Cr in the intermediate temperature region, and ^{49}V in the lower temperature regions. When the initial metallicity is increased further to $Z = 0.1$, then the carbon burning region is suppressed. This has a larger effect on the trend in the S1.0 and M0.8 models.

Figure 3.52 shows the production of ^{50}Ti in our three classes of model. In T1.4Z0, we see that the only contribution to ^{50}Ti is from the particles with peak temperature $T > 8$ GK. As such, neither the S1.0 or M0.8 model can produce ^{50}Ti at $Z = 0$. As the metallicity is increased, we see a small production of ^{50}Ti in the oxygen burning region, between 3 and 3.5 GK. This is reproduced in S1.0Z0.014 and M0.8Z0.014, where production is slightly larger than in the T1.4 model. In all cases however, the lower temperature component is

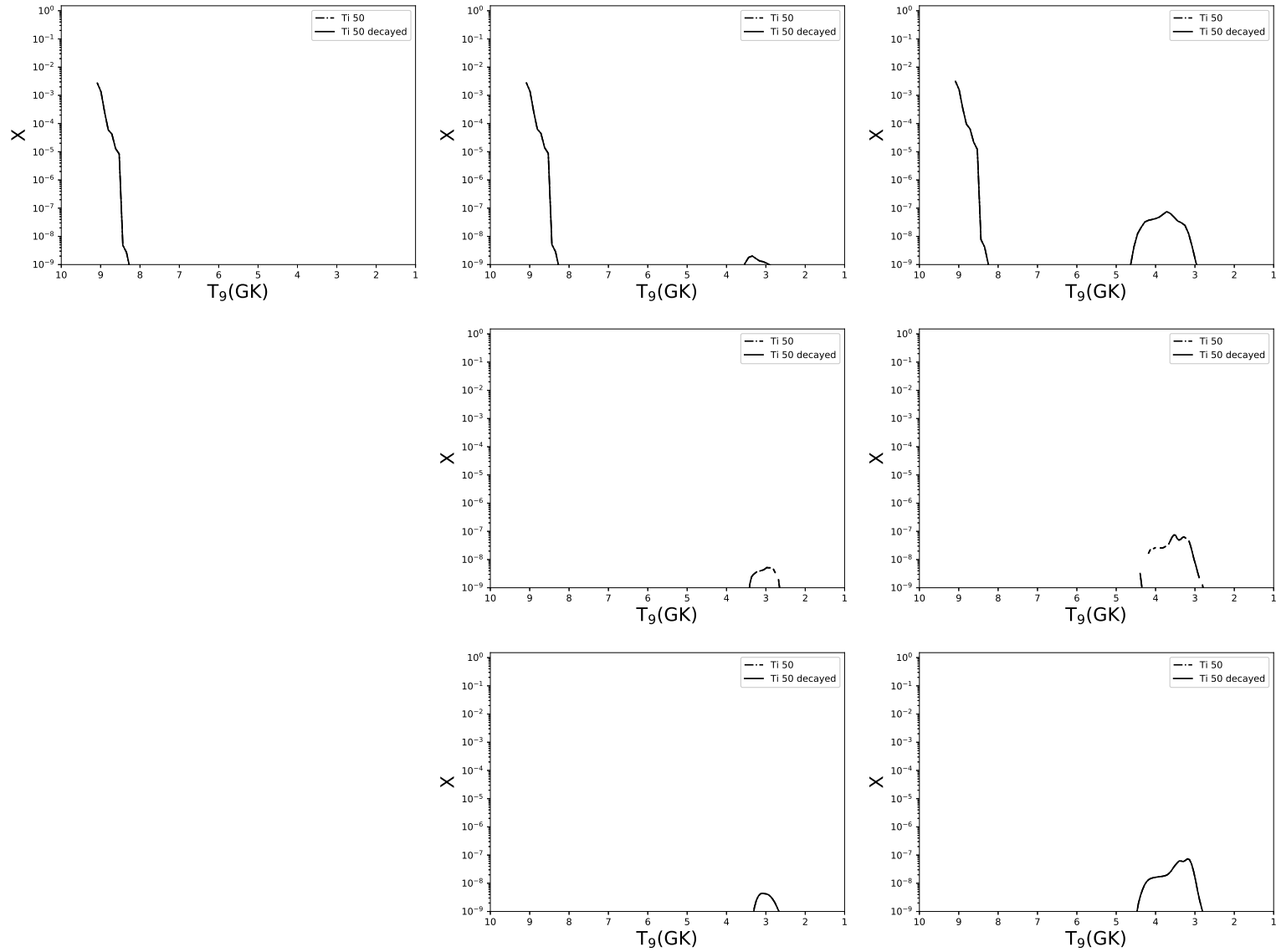


FIGURE 3.52: The abundance distributions of ^{50}Ti are shown, arranged as in figure 3.5. With metallicities of $Z = 0, 0.014$ and 0.1 from left to right, and the three categories of model - T1.4, S1.0 and M0.8 - from top to bottom.

small, and has a negligible impact on the abundances of ^{50}Ti in T1.4. As the metallicity is increased to $Z = 0.1$, we see a very slight increase in the ejected mass of ^{50}Ti , from $1.12 \times 10^{-5} M_{\odot}$ in the $Z = 0$ case to $1.34 \times 10^{-5} M_{\odot}$ in the $Z = 0.1$ case. There is a larger proportional increase in the S1.0 and M0.8 models however the maximum ejected mass of ^{50}Ti in either of these models is of the order a few $\times 10^{-8} M_{\odot}$ and so it is only ejected as a trace isotope.

3.2.14 Vanadium

Vanadium has two isotopes which are considered stable (one with a half-life of 10^{17} Yrs): ^{50}V and ^{51}V . ^{50}V is made in a variety of conditions in massive stars - carbon and neon burning, and explosive oxygen and neon burning. ^{51}V is made also in massive stars in explosive oxygen and silicon burning, as well as the neutrino process, α -rich freeze-out and SNIa detonation models (Woosley, Heger, and Weaver, 2002).

We see in figure 3.53 that vanadium has a similar trend with metallicity through our three classes of model. There is a factor of 10 between production between the T1.4 and M0.8, and a dip in production in M0.8 at $Z = 10^{-4}$ which is not observed in the other models, however the broad trend of a strong secondary component is the same across the models. We do see that trace amounts of ^{50}V are produced at all metallicities in the T1.4 models, with a weak secondary component, where as in the S1.0 and M0.8 models, this secondary component has a much stronger dependency on metallicity.

In figure 3.54 we show the production of ^{50}V . There is no production of ^{50}V in the lower mass models at zero metallicity, and that a secondary component arises in the 2.5-4 GK range at solar metallicity. This oxygen burning region shifts to hotter peak temperature particles as metallicity continues to increase. In the T1.4 models, we see that the primary component from the hottest particles ($T > 8$ GK). This is due to the Y_e of these particles being

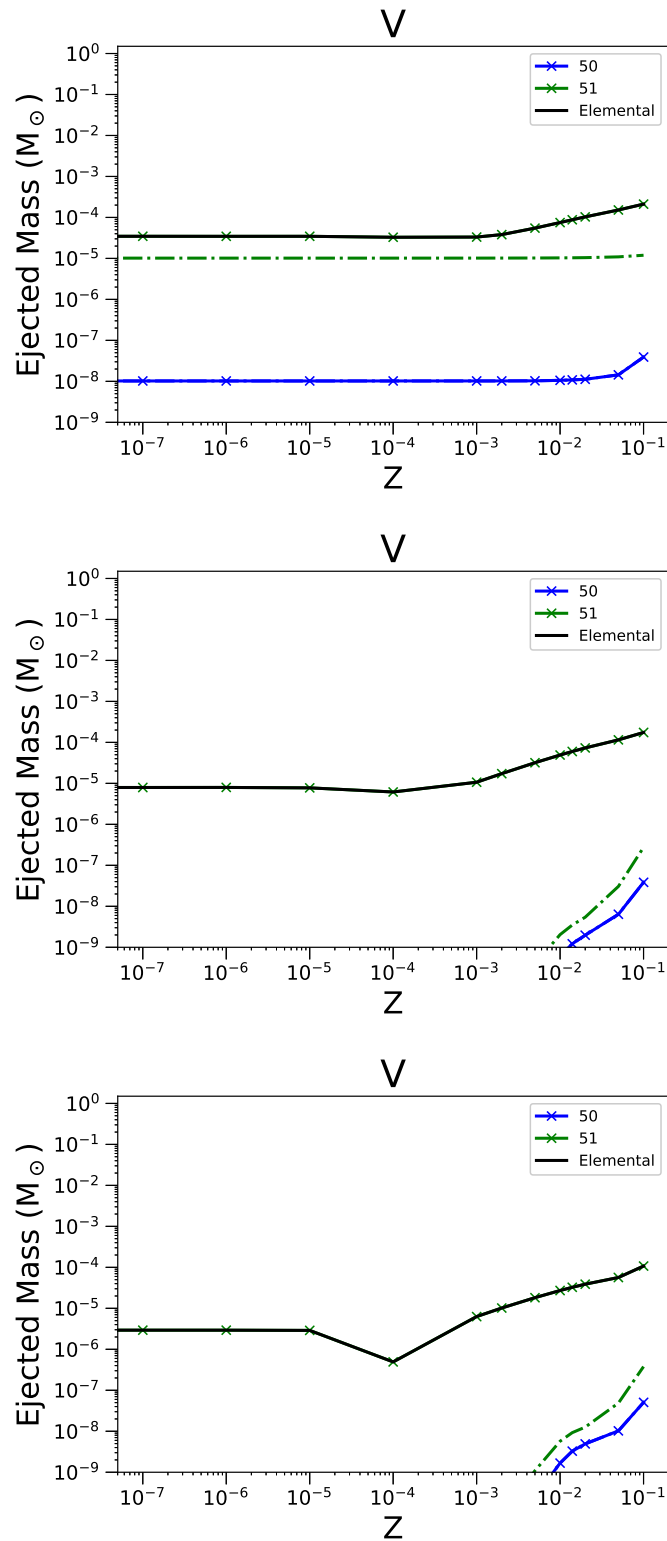


FIGURE 3.53: As in Figure 3.4 but for ejected mass of V, and its stable isotopes ^{50}V and ^{51}V .

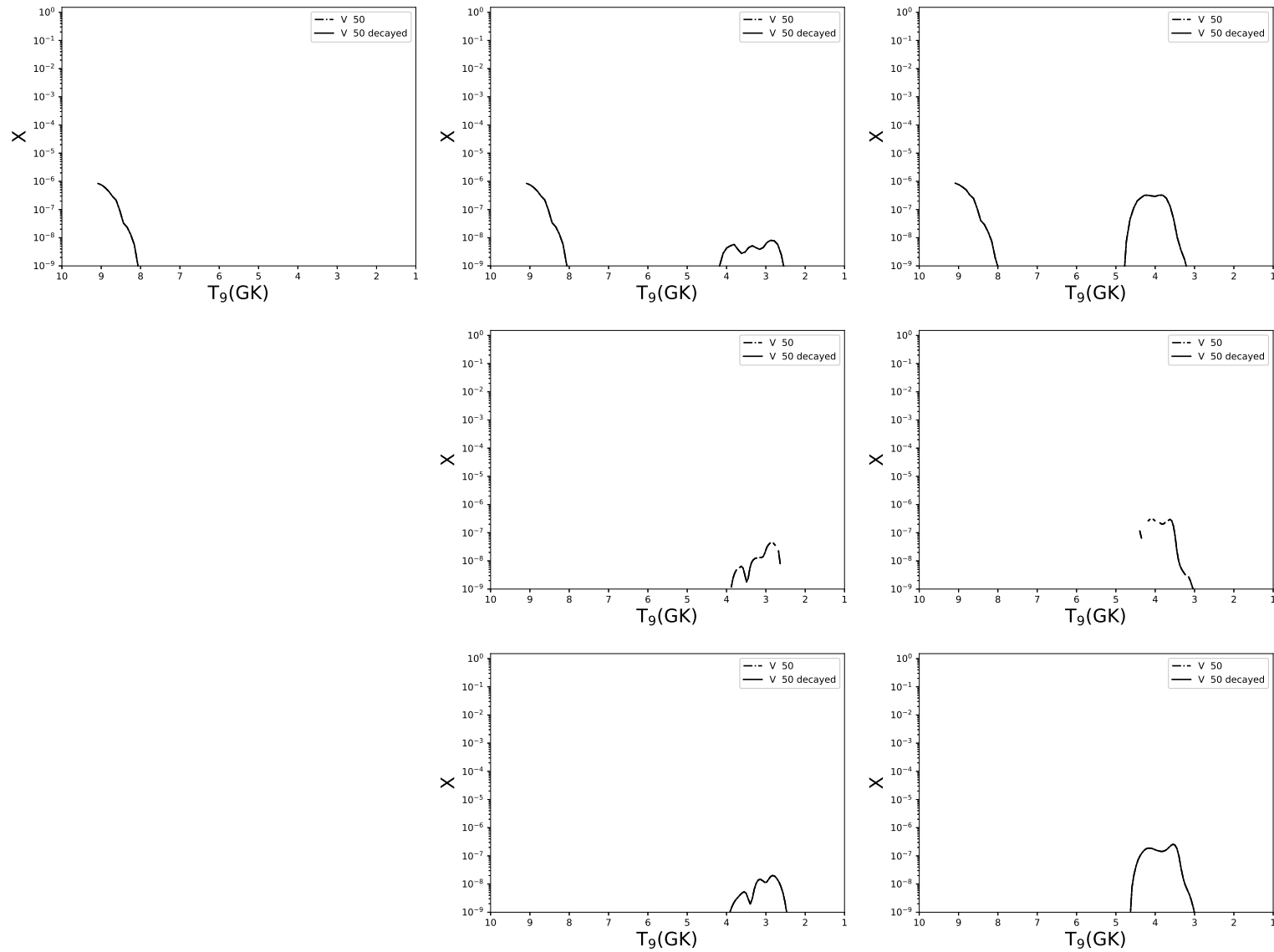


FIGURE 3.54: The abundance distributions of ^{50}V are shown, arranged as in figure 3.5. With metallicities of $Z = 0, 0.014$ and 0.1 from left to right, and the three categories of model - T1.4, S1.0 and M0.8 - from top to bottom.

governed by electron captures in the high density, high temperature regime. This sets a Y_e that is independent from the initial electron fraction. A similar secondary production trend as seen in S1.0Z0.014 and S1.0Z0.1 can be seen between T1.4Z0.014 and T1.4Z0.1 in the ejecta of the external layers.

Production of ^{51}V is significantly more complex than ^{50}V , particularly in the T1.4 models. In model T1.4Z0, the highest peak temperature particles (above 9 GK) have direct synthesis of ^{51}V . As we move to lower peak temperatures, ^{51}Cr becomes the largest contributor. This extends only over a narrow temperature range from approximately 7.8 to 8.5 GK, below which synthesis of ^{51}V is mostly as ^{51}Mn . We see a trace contribution from ^{51}Fe in this model, but it is small in comparison to the other contributing isotopes. As the metallicity increases in model T1.4Z0.014, the high temperature contribution to the isotopic abundance of ^{51}V remains the same. We see the low temperature contribution from ^{51}Cr increase, boosting production of ^{51}V slightly. From comparison with figure 3.53, we can see that this increase in radiogenic contribution has a significant impact on the ejected mass of ^{51}V , and consequently on the ejected mass of elemental vanadium. Secondary production is boosted still further in model T1.4Z0.1, where the low temperature secondary tail begins to dominate the ejecta.

The synthesis of ^{51}Mn is the main route for production in model S1.0Z0, with a trace contribution from radioactive ^{51}Cr . This production occurs over a broad range of temperatures, but is much less abundant than in the T1.4 cases.

In models S1.0Z0.014, the production of ^{51}Cr at lower temperatures begins to contribute significantly to the overall ejected mass of ^{51}V . This trend increases as we move to model S1.0Z0.1, where the contributions from ^{51}Mn and ^{51}Cr become comparable. The contribution from ^{51}Mn occurs above peak temperatures greater than 4.5 GK and ^{51}Cr below this.

Production in the M0.8 models follows a similar trend to the S1.0 models.

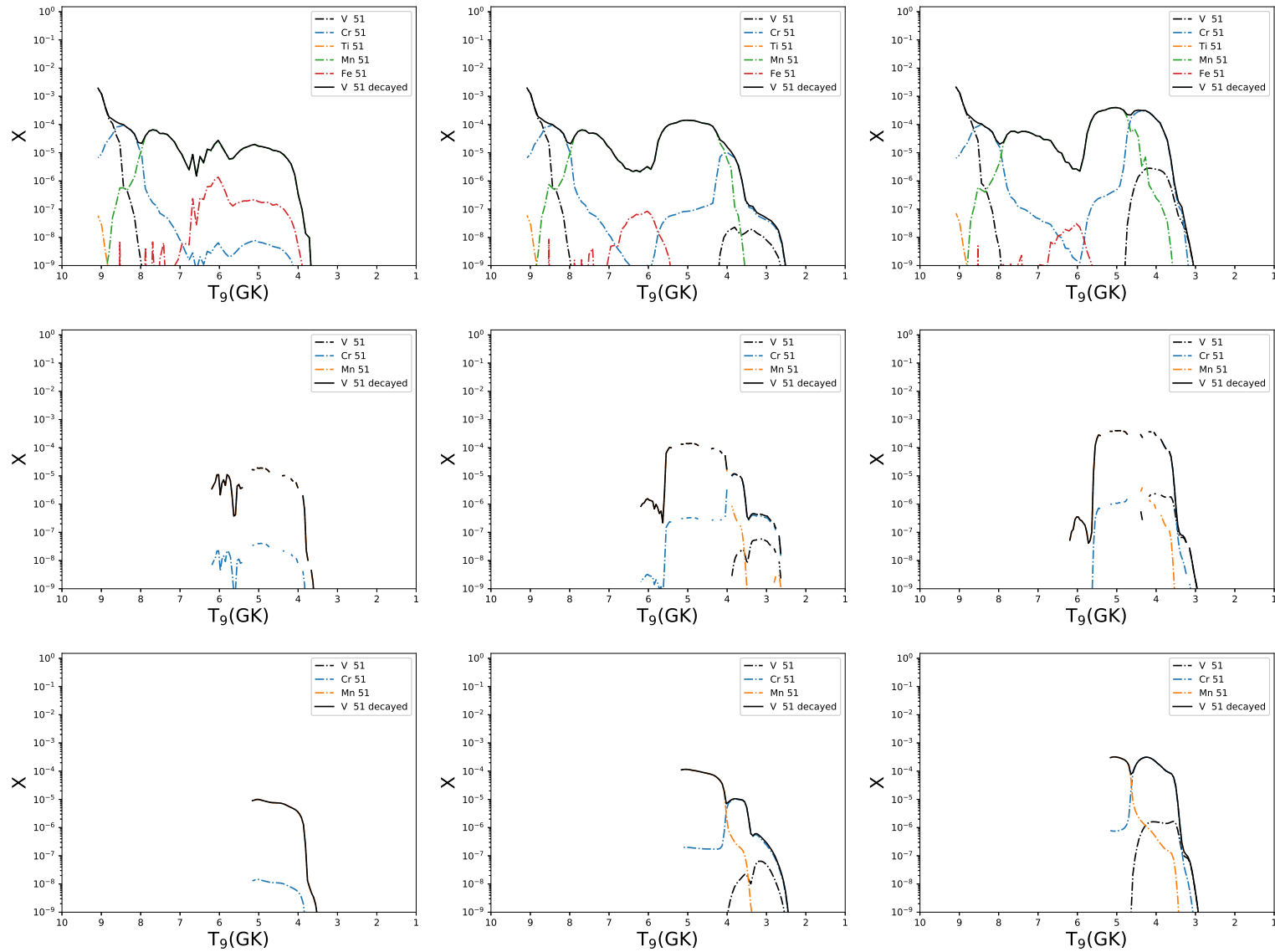


FIGURE 3.55: The abundance distributions of ^{51}V are shown, arranged as in figure 3.5. With metallicities of $Z = 0, 0.014$ and 0.1 from left to right, and the three categories of model - T1.4, S1.0 and M0.8 - from top to bottom.

M0.8Z0.1 shows a much larger ^{51}Cr to ^{51}Mn production due to the smaller number of particles at higher peak temperatures, and the lower maximum peak temperature in this model.

3.2.15 Chromium

Chromium has 4 stable isotopes: ^{50}Cr , which has a half-life of 1.3×10^{18} years and which we therefore can treat as stable, ^{52}Cr , ^{53}Cr and ^{54}Cr . ^{52}Cr is the most abundant Cr isotope in the Sun (83.789% of the solar Cr), while ^{54}Cr has the lowest abundance (2.365% of the solar Cr) (Asplund et al., 2009; Lodders, 2003).

In Figure 3.56, we show the integrated Cr yields for the element and its isotopes, for the T1.4, S1.0 and M0.8 sets. Cr production is dominated by ^{52}Cr for all metallicities in the T1.4 and S1.0 sets. At metallicities higher than solar, in the M0.8Z0.1 models ^{50}Cr and ^{53}Cr production increases enough as the metallicity of the progenitor increases to affect the Cr abundance budget, causing an increase of the total ejected mass. With the exception of this pattern, Cr production appears to be primary in all models, following the ^{52}Cr behavior. Here, primary denotes that material which is synthesised directly in the explosion during freeze-out, whereas secondary is material which is synthesised from the seeds of other nuclei (ultimately in this work originating with the initial abundance of ^{22}Ne)

On the other hand, the relative production of different Cr isotopes changes significantly with metallicity and using different model sets. ^{50}Cr is the only isotope that is always produced directly. ^{54}Cr is mostly ejected as itself in T1.4 models, while for other the sets it is mostly radiogenic. ^{52}Cr and ^{53}Cr are produced by radiogenic contribution in the Chandrasekhar mass explosion models, primarily from ^{52}Fe and ^{53}Fe respectively. There is a significant

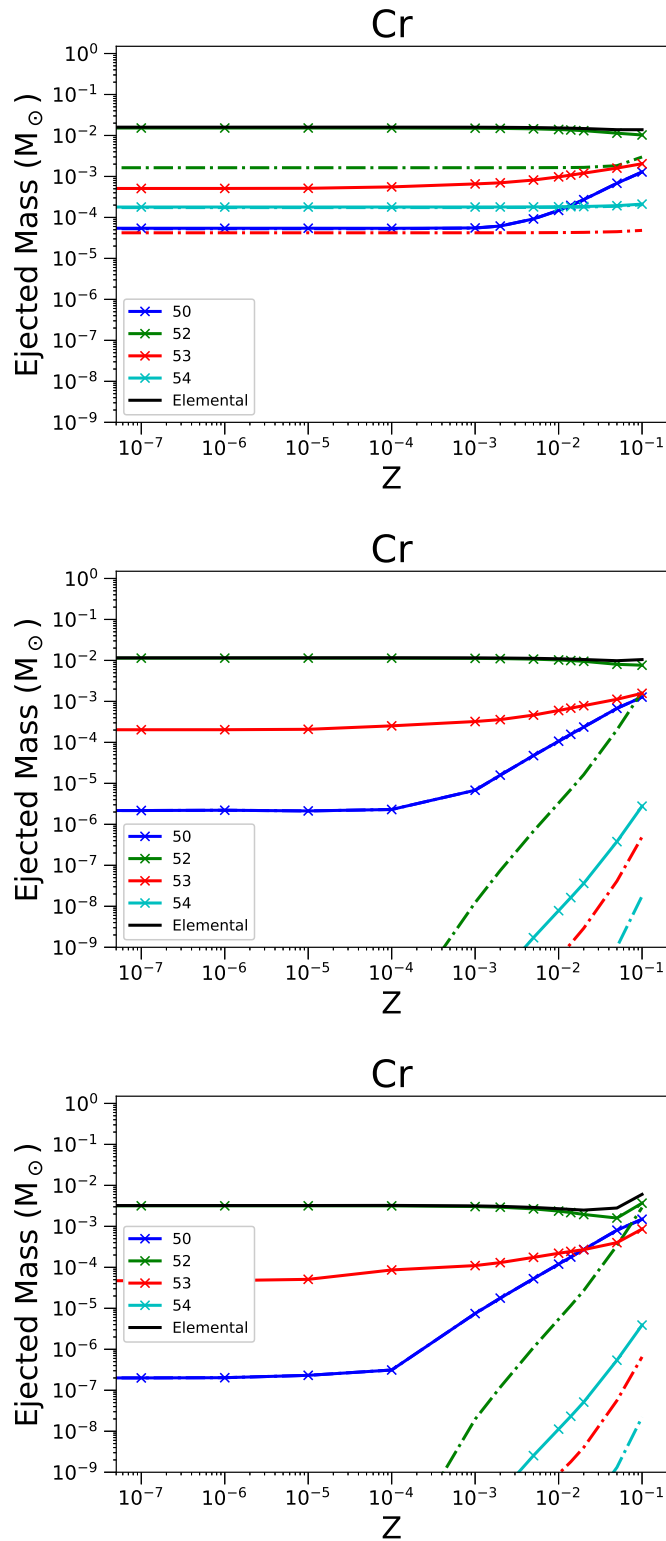


FIGURE 3.56: As in Figure 3.4 but for ejected mass of Cr, and its stable isotopes ^{50}Cr , ^{52}Cr , ^{53}Cr and ^{54}Cr .

contribution from ^{53}Mn , particularly at higher initial ^{22}Ne mass fractions, indicating a strong secondary production. Production of ^{52}Cr is more mixed in the lower mass explosions, with competing contributions from ^{52}Cr and ^{52}Fe , along with negligible ^{52}Mn . ^{53}Mn becomes a significant contributor to the abundance of ^{53}Cr at higher metallicities, becoming comparable to the contribution from ^{53}Fe . Non radiogenic contributions to ^{53}Cr are negligible. For all sets, the yield of ^{50}Cr rises with increasing metallicity of the WD progenitor above a threshold value of $Z = 10^{-4}$. ^{53}Cr shows a much weaker rise. ^{54}Cr is mostly primary for T1.4 models, while its (much weaker) production is secondary for other sets.

In the T1.4 set, the ^{50}Cr yields are dominated by two production peaks, at 7-9 GK and 3-5 GK temperature, respectively (Figure 3.57). The first peak is primary, while the low temperature peak is secondary, rising with increasing metallicity. Only the T1.4Z0 model shows a relevant radiogenic contribution by ^{50}Mn at lower temperatures, but the production is dominated by the first peak. S1.0 and M0.8 sets only carry the secondary peak, explaining their smaller ^{50}Cr production at low metallicities compared to T1.4. On the other hand, for all sets the strong secondary component in ^{50}Cr causes this isotope to form up to about 10% of all Cr ejecta (M0.8Z0.1 model).

The ^{52}Cr abundance pattern is significantly more complex than ^{50}Cr , revealing a larger number of production channels (Figure 3.58). For the T1.4 set, primary ^{52}Cr is directly produced in the hottest ejecta, with SN shock temperatures above 8 GK. Two additional peaks, from the eventual decay of ^{52}Fe occur at around 7 GK and 5 GK. These are insensitive to the initial metallicity of the model, and contribute the majority of ^{52}Cr . Finally, we obtain a secondary production of ^{52}Cr at about 4 GK in the T1.4Z0.014 and T1.4Z0.1 models. Small amounts of ^{52}Mn are also produced in all models. The Sxx and Mxx models all show the primary ^{52}Fe production, and the secondary ^{52}Cr channel at lower temperatures.

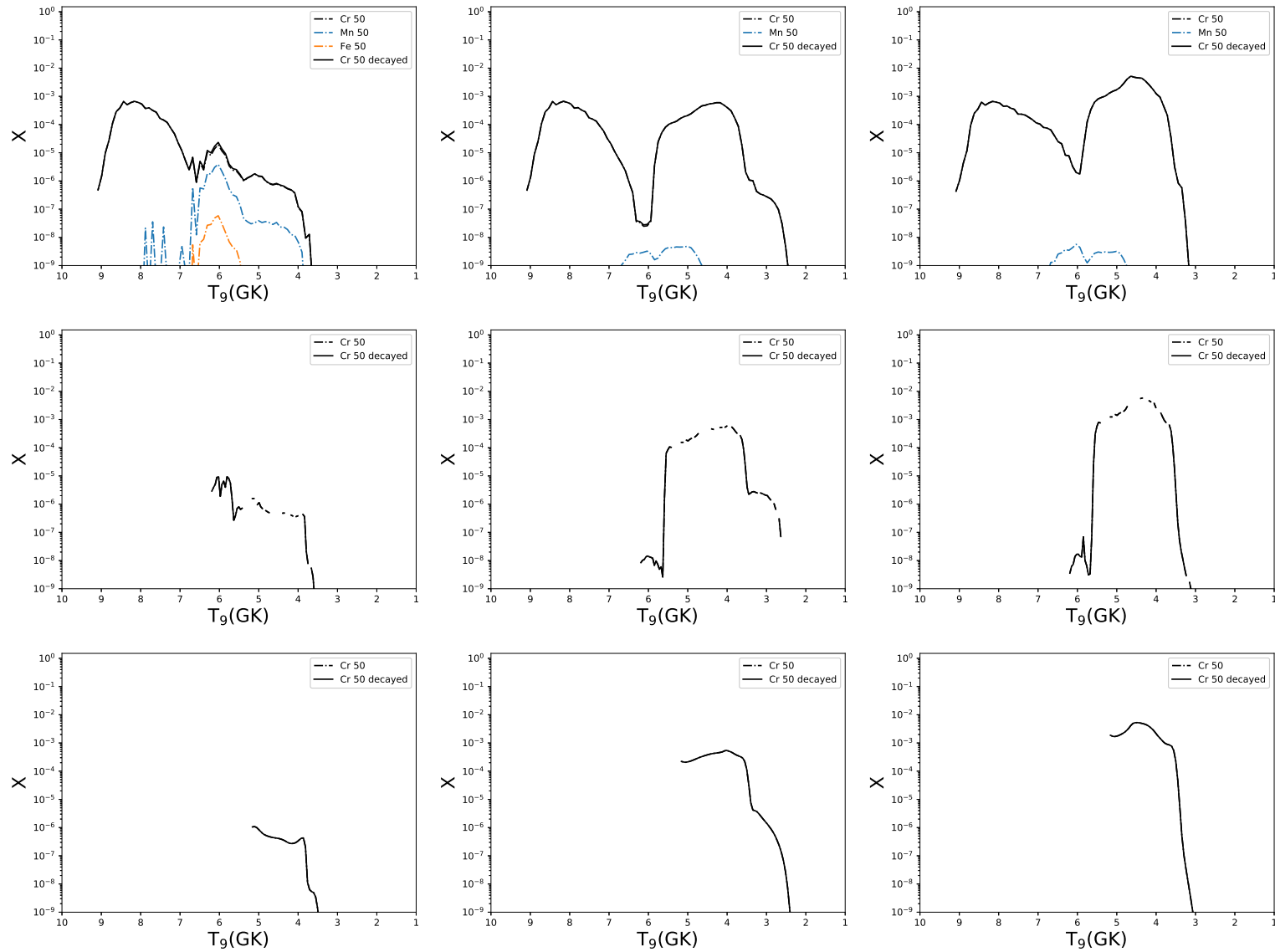


FIGURE 3.57: The abundance distributions of ^{50}Cr are shown, arranged as in figure 3.5. With metallicities of $Z = 0, 0.014$ and 0.1 from left to right, and the three categories of model - T1.4, S1.0 and M0.8 - from top to bottom.

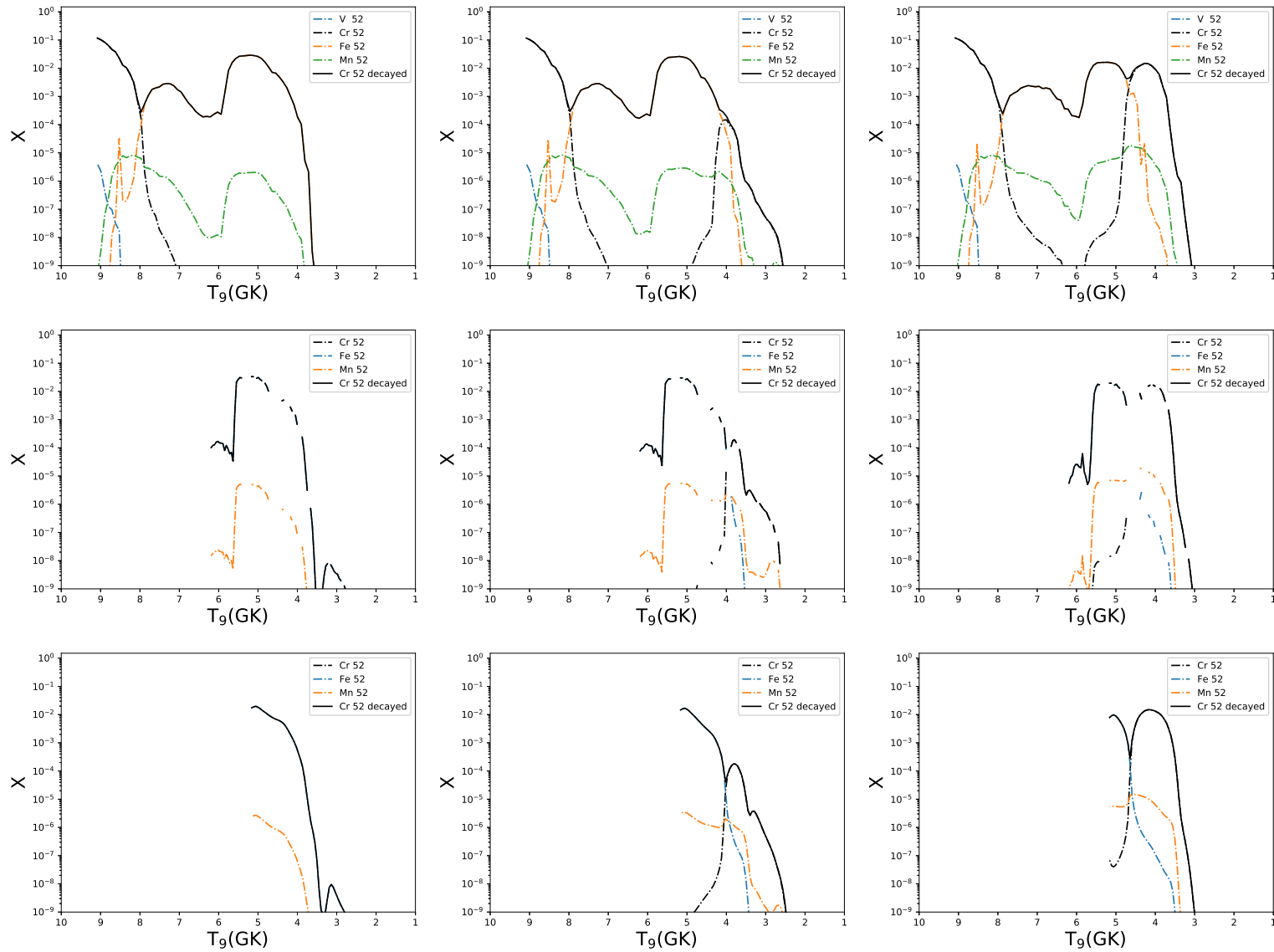


FIGURE 3.58: The abundance distributions of ^{52}Cr are shown, arranged as in figure 3.5. With metallicities of $Z = 0, 0.014$ and 0.1 from left to right, and the three categories of model - T1.4, S1.0 and M0.8 - from top to bottom.

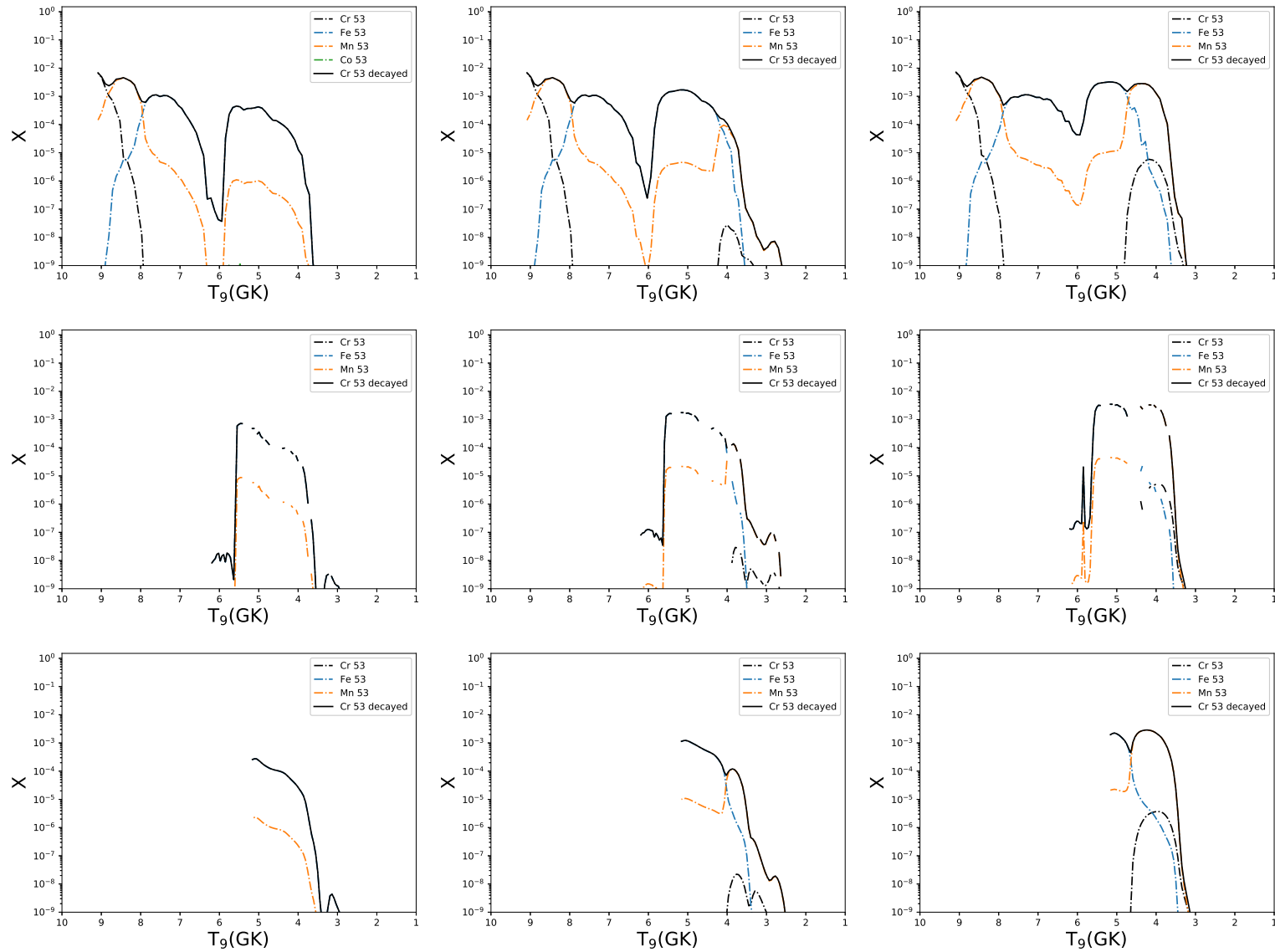


FIGURE 3.59: The abundance distributions of ^{53}Cr are shown, arranged as in figure 3.5. With metallicities of $Z = 0, 0.014$ and 0.1 from left to right, and the three categories of model - T1.4, S1.0 and M0.8 - from top to bottom.

In Figure 3.59, for the T1.4 set, ^{53}Cr is produced directly above 9 GK in the innermost ejecta. For 8-9 GK the production is dominated by a primary peak of radiogenic ^{53}Mn . Two additional ^{53}Mn channels appear at lower temperatures, with the colder production peak in oxygen burning conditions becoming particularly relevant at super-solar metallicities, again demonstrating that it is a secondary production channel. Two broad primary peaks at 7-8 GK and about 5 GK are due to the radiogenic contribution from ^{53}Fe . ^{53}Fe continues to be the primary radiogenic source of ^{53}Cr in the S1.0 and M0.8 sets. In agreement with T1.4 models, a secondary production of ^{53}Mn and ^{53}Cr is obtained at 3-4 GK.

In Figure 3.60, ^{54}Cr is produced directly at temperatures above 8 GK, while a secondary production peak is present at about 4 GK from the radiogenic decay of ^{54}Mn .

3.2.16 Manganese

Mn is mono-isotopic, with only ^{55}Mn being stable. It is formed in explosive silicon burning, the neutrino process and in SNIa (Woosley, Heger, and Weaver, 2002). Most of the solar manganese is produced in SNIa (Kobayashi, Karakas, and Lugaro, 2020), it has also been proposed as a key tracer for differentiating the mass of SNIa progenitor (Eitner et al., 2020). Figure 3.61 shows the ejected mass of Mn from our three models with respect to metallicity, indicating a large radiogenic contribution across the range of Z investigated.

Figure 3.62 shows the radiogenic contributions from the different models. In the low metallicity sub Chandrasekhar mass models, most production of Mn is as ^{55}Co , with a negligible contribution from ^{55}Fe . This contribution increases as the secondary ^{55}Fe component begins to dominate at lower temperatures, between 3 and 4 GK in explosive oxygen burning conditions.

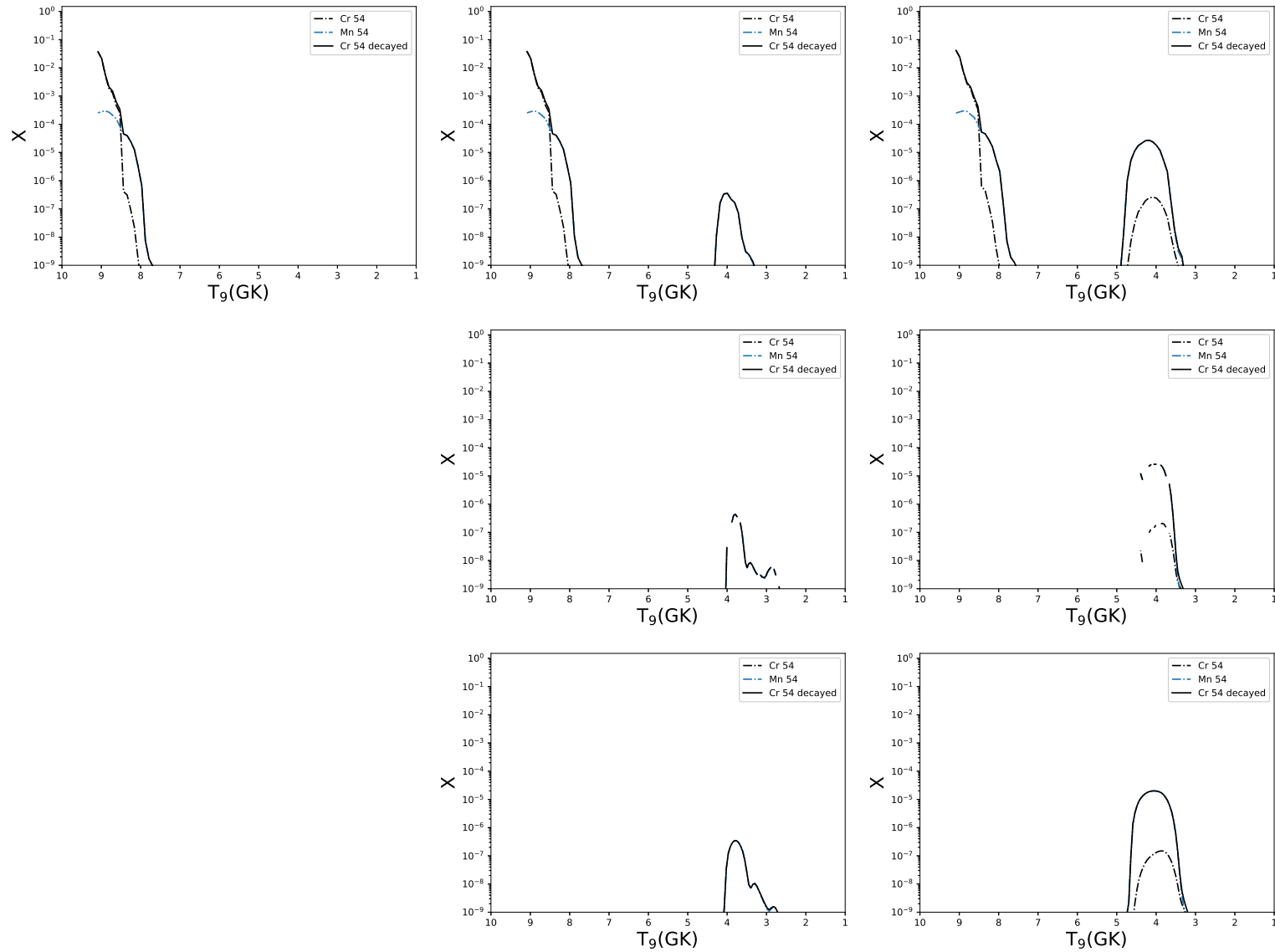
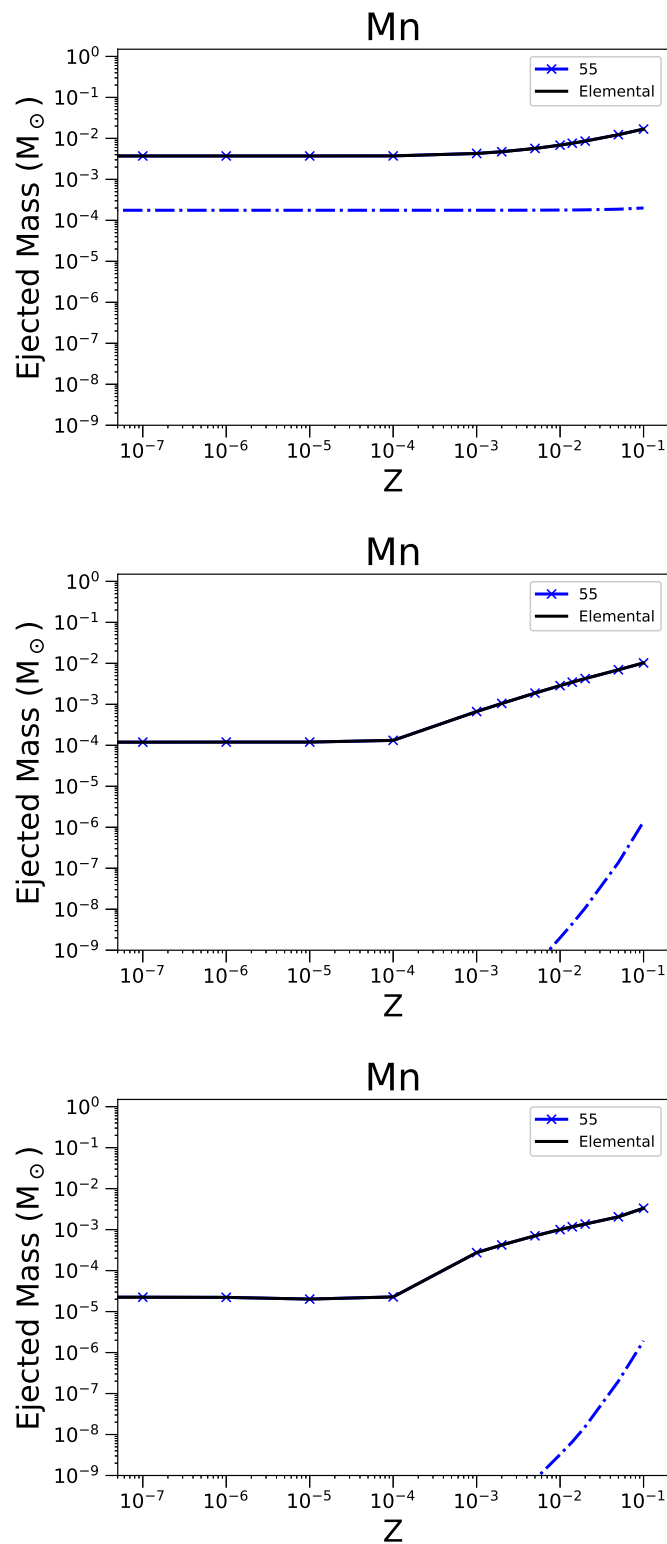


FIGURE 3.60: The abundance distributions of ^{54}Cr are shown, arranged as in figure 3.5. With metallicities of $Z = 0, 0.014$ and 0.1 from left to right, and the three categories of model - T1.4, S1.0 and M0.8 - from top to bottom.

FIGURE 3.61: As in Figure 3.4 but for ejected mass of ^{55}Mn .

Production of ^{55}Co is also boosted by this secondary component in both the S1.0 and M0.8 models. In the T1.4 models, we see that the production of ^{55}Fe is again boosted at higher metallicities, with a small primary secondary peak of ^{55}Mn contributing at lower temperatures in in these models. This peak has a negligible impact on the total production of Mn. We see that the trace amount of ^{55}Ni produced at intermediate temperatures in this model is suppressed with increasing initial ^{22}Ne abundance while ^{55}Fe production is boosted throughout the model. ^{55}Cr production is comparable to the radiogenic ^{55}Fe contribution, in contrast with the lower mass models where it is the dominant radiogenic contribution. Unfortunately, the half-life of ^{55}Cr is 3.5 minutes, much too short to be able to observe in the expanding ejecta of a Type Ia explosion.

Manganese production is predicted to be sensitive to the mass of the progenitor model. Truran, Arnett, and Cameron (1967) identifies Mn as being mainly produced as ^{55}Co , consistent with the production presented in figure 3.62. ^{55}Mn production in the most extreme conditions is dependent on a normal, low α , freeze out from NSE (Seitenzahl et al., 2013a; Thielemann, Nomoto, and Yokoi, 1986)

Seitenzahl et al. (2013a) states ^{55}Co is the largest contributor to manganese yields at densities above $2 \times 10^8 \text{ g cm}^{-3}$. In the T1.4 Chandrasekhar mass models, these densities cover the full range of peak temperatures (although not all of the particles have a density above this threshold density). ^{55}Co is the dominant source of ^{55}Mn in the T1.4Z0 model, and remains the largest contributor to ejected ^{55}Mn mass however the relative contribution from ^{55}Fe increases with increasing metallicity and at $Z = 0.1$ contributes on the order of 10% of the ejected ^{55}Mn mass. There is also a contribution from direct synthesis of ^{55}Mn in the highest temperature regions, however this is small - of the order 1% of total ejected mass of ^{55}Mn in the T1.4Z0 model.

^{55}Co is destroyed at lower densities through the reaction $^{55}\text{Co}(p, \gamma)^{56}\text{Ni}$

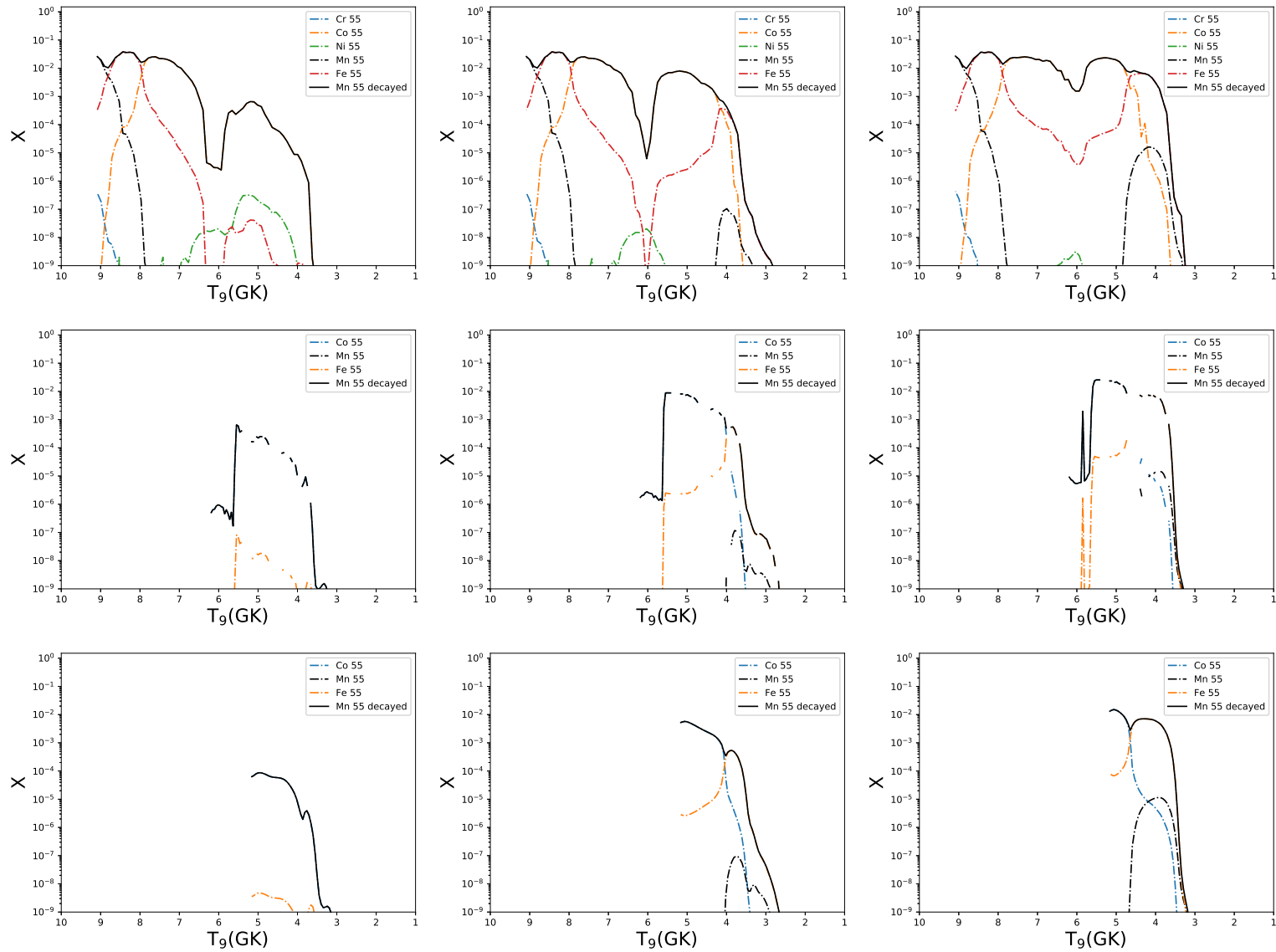


FIGURE 3.62: The abundance distributions of ^{55}Mn are shown, arranged as in figure 3.5. With metallicities of $Z = 0, 0.014$ and 0.1 from left to right, and the three categories of model - T1.4, S1.0 and M0.8 - from top to bottom.

(Seitenzahl et al., 2013a) which we see in the differences (particularly at low metallicities) between M0.8 and the higher mass models. At $Z = 0$, the T1.4 model ejects $3.72 \times 10^{-3} M_{\odot}$ of ^{55}Mn , the S1.0 model $1.19 \times 10^{-4} M_{\odot}$ and the M0.8 model $2.24 \times 10^{-5} M_{\odot}$.

Kobayashi, Leung, and Nomoto (2020) identify a positive correlation for the production of Mn with respect to initial metallicity, similar to the results presented here. They see a decrease in the ejected mass of Mn with increasing progenitor mass for sub-Chandrasekhar mass models, in Chandrasekhar mass models in Seitenzahl et al. (2013b) and this work Mn production increases with metallicity. The reaction $^{52}\text{Fe}(\alpha, p)^{55}\text{Co}$ is identified as the main production channel for the bulk of ^{55}Mn (Seitenzahl et al., 2013b). The production of Mn with respect to Fe in SNIa has been extensively studied, and has been the subject of a number of GCE investigations (Seitenzahl et al., 2013a; Kobayashi et al., 2006; Eitner et al., 2020) as both Mn and Fe in the Milky Way are produced primarily in SNIa (Matteucci et al., 2009). This $[\text{Mn}/\text{Fe}]$ has been used in many publications to investigate the ratio of Chandrasekhar to sub-Chandrasekhar SNIa progenitor.

Eitner et al. (2020) consider the fraction of sub-Chandrasekhar mass SNIa to be as high as 75%, due to the large $[\text{Mn}/\text{Fe}]$ ratios possible in these low mass models.

3.2.17 Iron

Iron has 4 stable isotopes: ^{54}Fe , ^{56}Fe , ^{57}Fe and ^{58}Fe . $^{54,56,57}\text{Fe}$ are all produced in explosive silicon burning or in SNIa explosions. ^{58}Fe is produced in Chandrasekhar mass SNIa explosions in NSE or in the helium burning s-process (Woosley, Heger, and Weaver, 2002). Around 70% of Fe in the universe is produced in SNIa explosions (Matteucci and Greggio, 1986). Kobayashi, Leung, and Nomoto (2020) find that up to 25% of SNIa progenitors may be

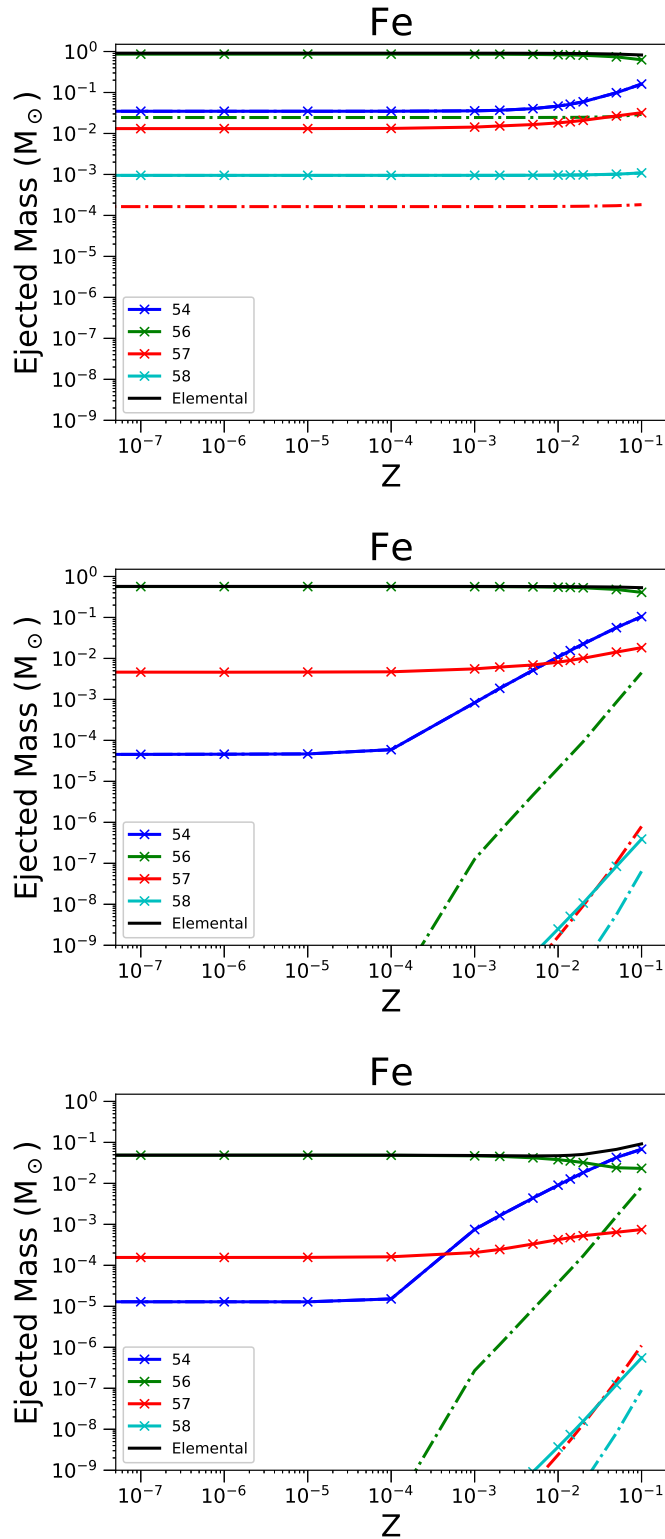


FIGURE 3.63: As in Figure 3.4 but for ejected mass of Fe, and its stable isotopes ^{54}Fe , ^{56}Fe , ^{57}Fe and ^{58}Fe .

sub-Chandrasekhar mass WDs, while Seitenzahl et al. (2013a) find a value close to 50%.

^{54}Fe , in all conditions, is produced directly. In figure 3.63 the ejected mass of the stable Fe isotopes is given, along with their radiogenic contributions, as a function of initial metallicity. There is a small decrease in the abundance of elemental Fe ejected from the T1.4 and S1.0 models due to a reduction in the ejected mass of ^{56}Fe with increasing initial metallicity. This is compensated for partially by an increase in the abundances of ^{54}Fe in these two models, which occurs sharply at $Z=0.0001$ in the S1.0 and M0.8 models, and more gradually at super-solar metallicities in the Chandrasekhar mass model. The increase of over two orders of magnitude in the abundance of ^{54}Fe is significant, particularly as this only becomes a significant contributor to the overall abundance of Fe in models other than T1.4 at super-solar metallicities.

Figure 3.64 shows the production of ^{56}Fe in our models with respect to peak temperature. ^{56}Fe is one of the largest components of the ejecta of all three models. While M0.8 has a smaller contribution than the others, most metallicities still have mass fractions of ^{56}Fe above 10%. In T1.4 we can see that production is dominated by contributions from ^{56}Ni , with a non-negligible contribution from direct synthesis of ^{56}Fe at higher metallicities. This is more than offset by the reduction in production at intermediate peak temperatures from the $Z = 0.014$ and $Z = 0.1$ metallicity models. We also see this reduction in ^{56}Fe in the S1.0 and M0.8 models, most clearly illustrated in figure 3.65. We see that ^{56}Fe is produced directly at temperatures above 8 GK, which is insensitive to metallicity effects. There is a more pronounced effect on the overall abundance of ^{56}Fe vs metallicity in the $0.8M_{\odot}$ model, however iron production actually increases for M0.8 at higher metallicities, due to a significant contribution from ^{54}Fe .

^{57}Fe has a large radiogenic contribution across all models. We see that ^{57}Fe produced directly during the explosion accounts for 1% of the mass

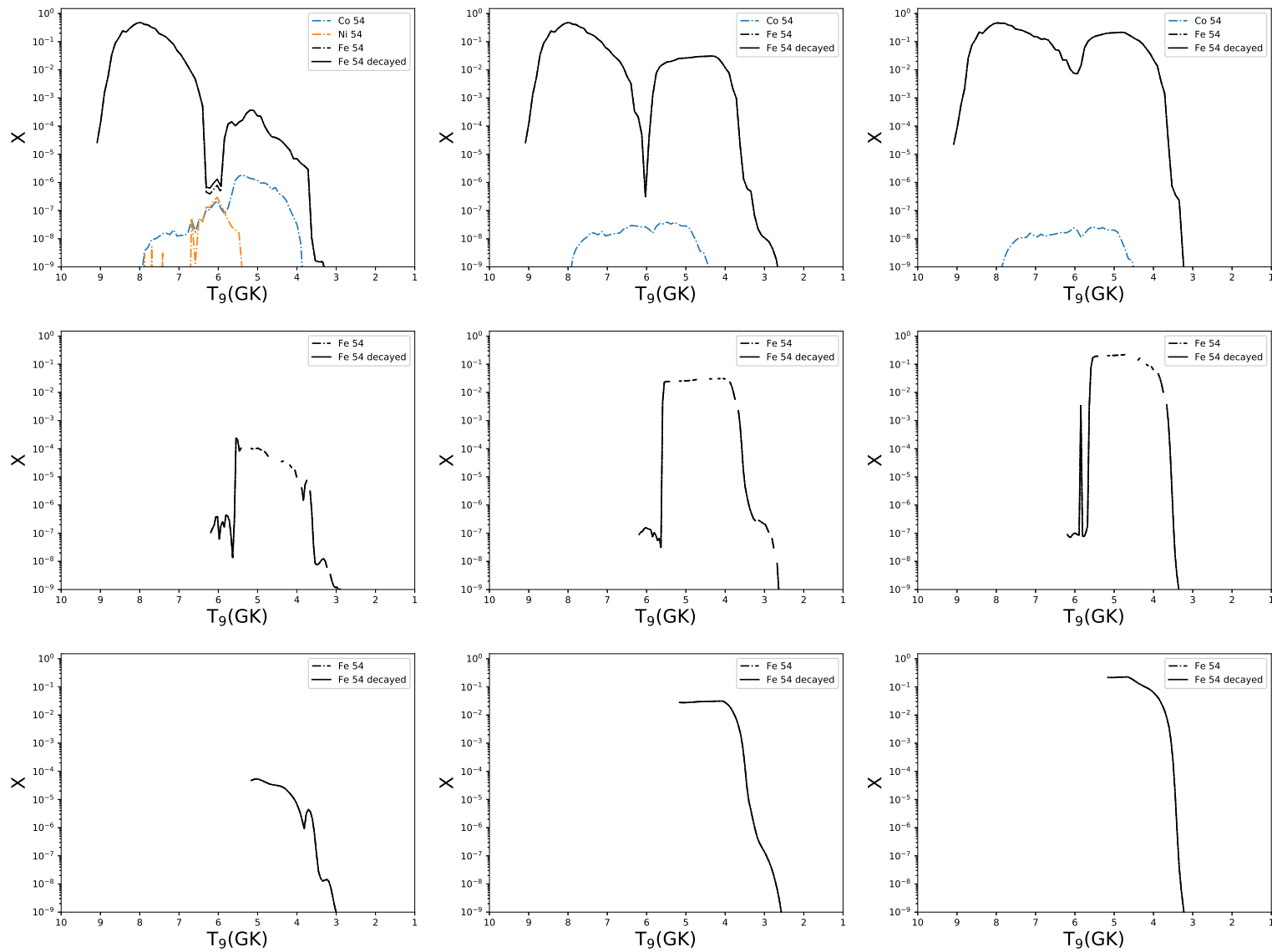


FIGURE 3.64: The abundance distributions of ^{54}Fe are shown, arranged as in figure 3.5. With metallicities of $Z = 0, 0.014$ and 0.1 from left to right, and the three categories of model - T1.4, S1.0 and M0.8 - from top to bottom.

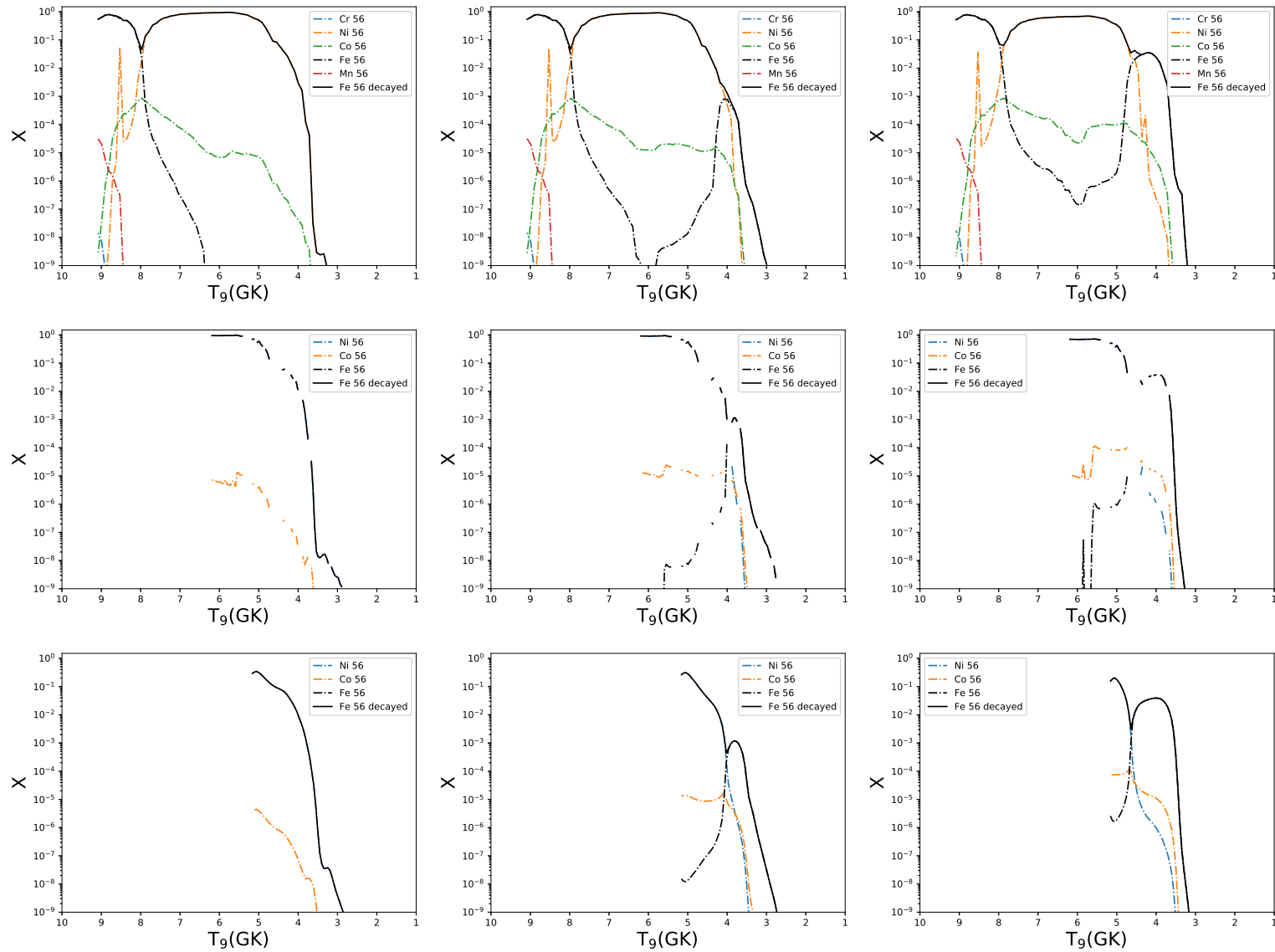


FIGURE 3.65: The abundance distributions of ^{56}Fe are shown, arranged as in figure 3.5. With metallicities of $Z = 0, 0.014$ and 0.1 from left to right, and the three categories of model - T1.4, S1.0 and M0.8 - from top to bottom.

of ^{57}Fe in the T1.4 models, where as it contributes almost nothing to the ejected mass in the sub Chandrasekhar models, where almost all production is through radiogenic contributions. These radiogenic contributions come mainly from ^{57}Ni and ^{57}Co , particularly in the lower mass models. There is a small contribution to ^{57}Fe abundance from ^{57}Mn and ^{57}Cu in T1.4 which is negligible, and ^{57}Cu production is still smaller at non-zero metallicity. Primary production of ^{57}Fe does occur in models at higher metallicity, in the low temperature end. This constitutes a small fraction of the total ejected mass of ^{57}Fe . ^{57}Co production is boosted at higher metallicities, driving the increasing trend in all models in figure 3.63.

^{58}Fe is an interesting isotope, as only trace abundances of it are ever produced in the sub-Chandrasekhar models, whilst production in T1.4 models is both consistent over a range of metallicities (with a weak increase in production at super-solar) and with an ejected mass in the order of $0.001 M_{\odot}$. Production at lower temperatures as initial metallicity increases is very similar between our three classes of model, with radiogenic ^{58}Co contributing to most of ^{58}Fe ejecta. At the highest temperature peaks in the T1.4 models (>8.5 GK) direct nucleosynthesis of ^{58}Fe dominates, below this there is a band of production where ^{58}Co is the most abundant isotope in this isobar. The relatively simple nucleosynthesis pathways of ^{58}Fe , where the majority is produced in the most extreme conditions, is a tracer for the progenitors of SNIa explosions.

Timmes, Brown, and Truran (2003) have investigated the impact of metallicity on Fe production in SNIa. They find a linear dependence on metallicity, with a decrease in production as initial metallicity increases for metallicity close to solar or higher. Between 0.1 and 10x solar metallicity, a variation of 25% in the production of Fe through its radioactive progenitor ^{56}Ni is observed. Models T1.4 and S1.0 have similar trends with metallicity, in agreement with the results of Timmes, Brown, and Truran (2003), showing a linear

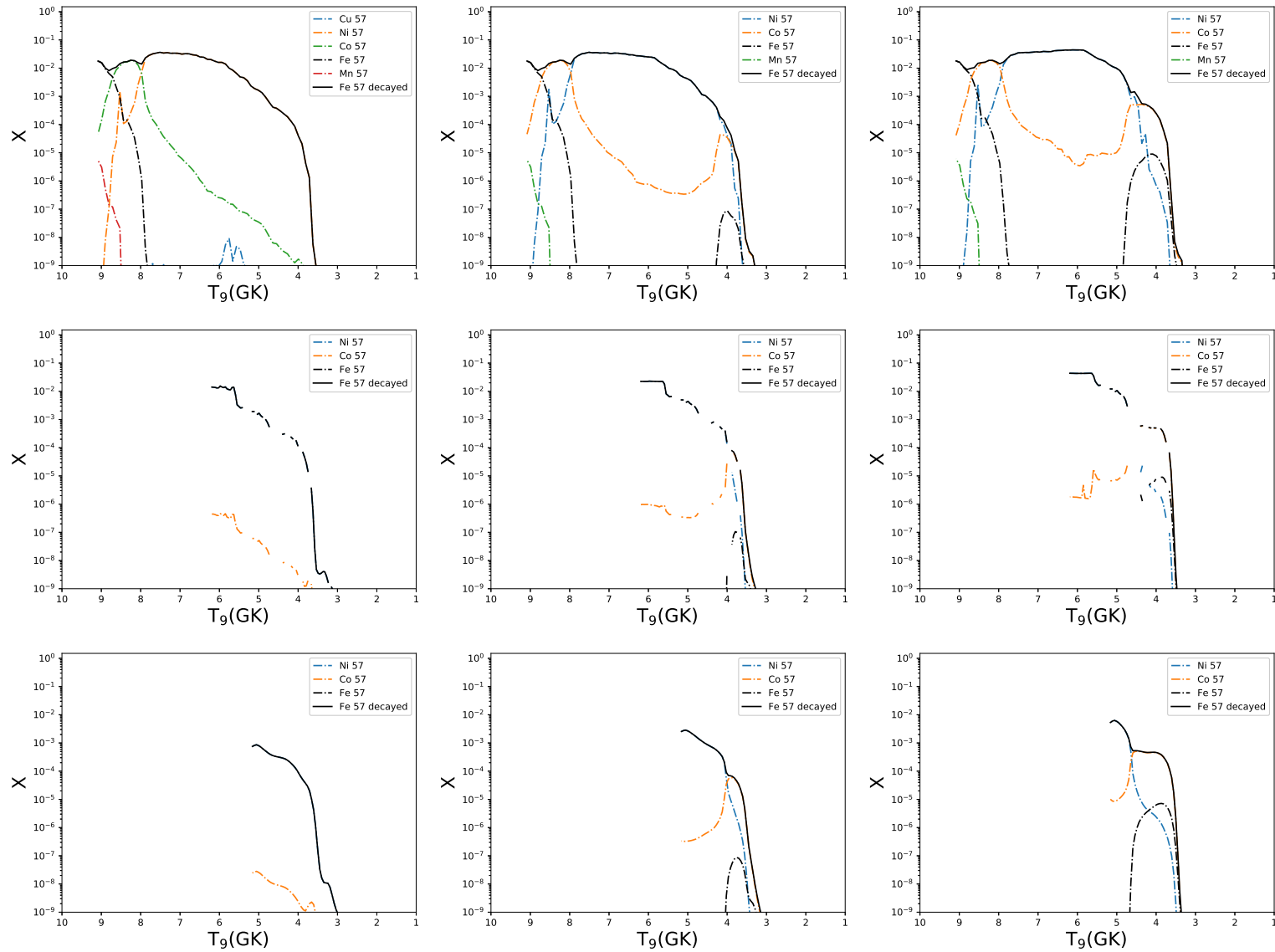


FIGURE 3.66: The abundance distributions of ^{57}Fe are shown, arranged as in figure 3.5. With metallicities of $Z = 0, 0.014$ and 0.1 from left to right, and the three categories of model - T1.4, S1.0 and M0.8 - from top to bottom.

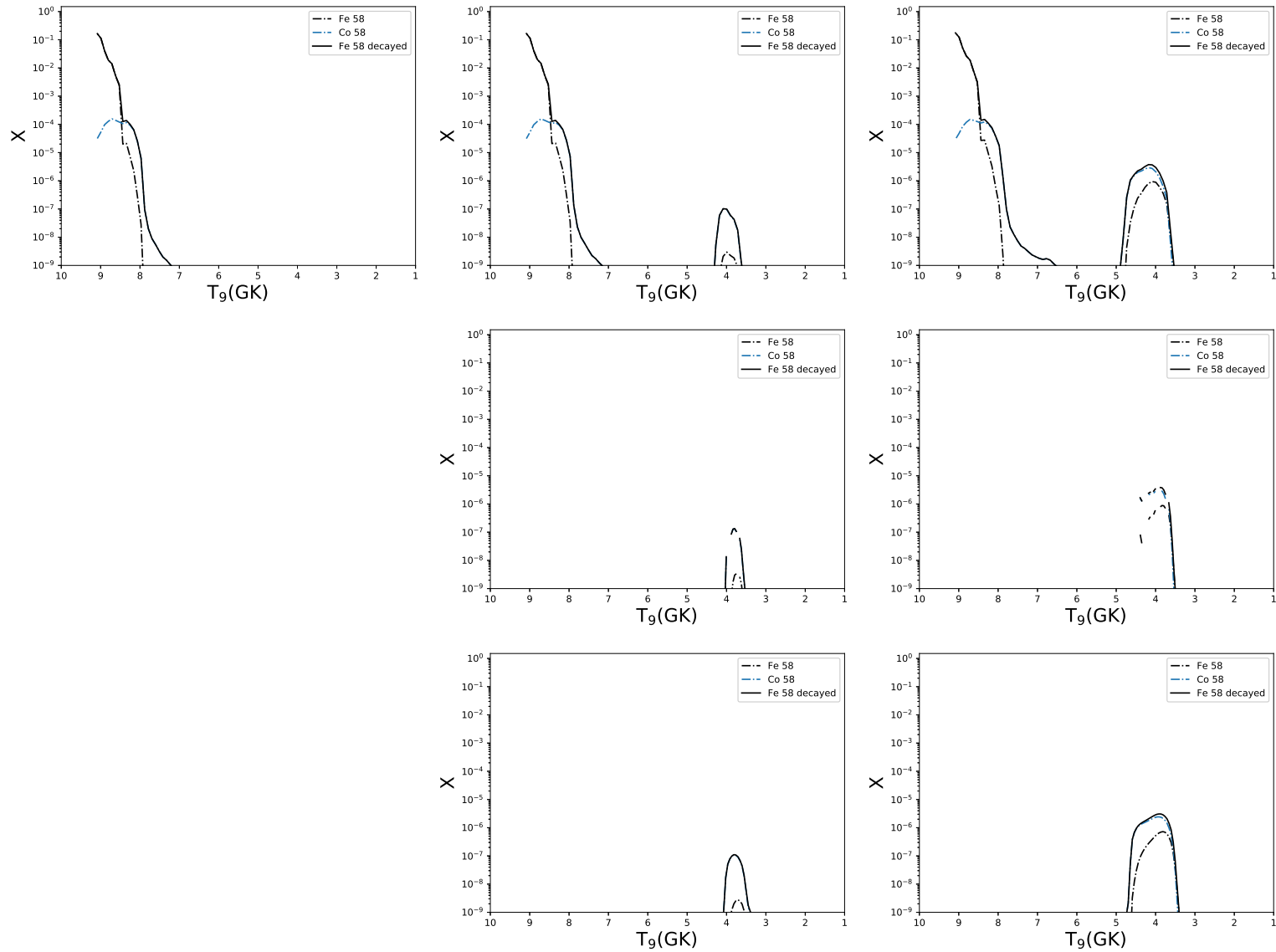


FIGURE 3.67: The abundance distributions of ^{58}Fe are shown, arranged as in figure 3.5. With metallicities of $Z = 0, 0.014$ and 0.1 from left to right, and the three categories of model - T1.4, S1.0 and M0.8 - from top to bottom.

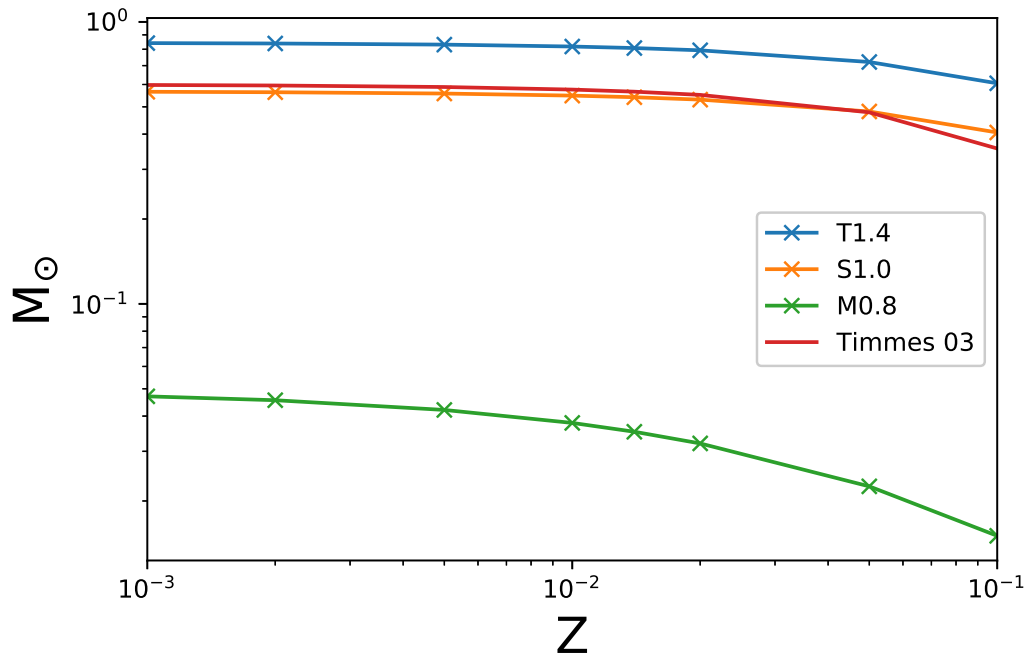
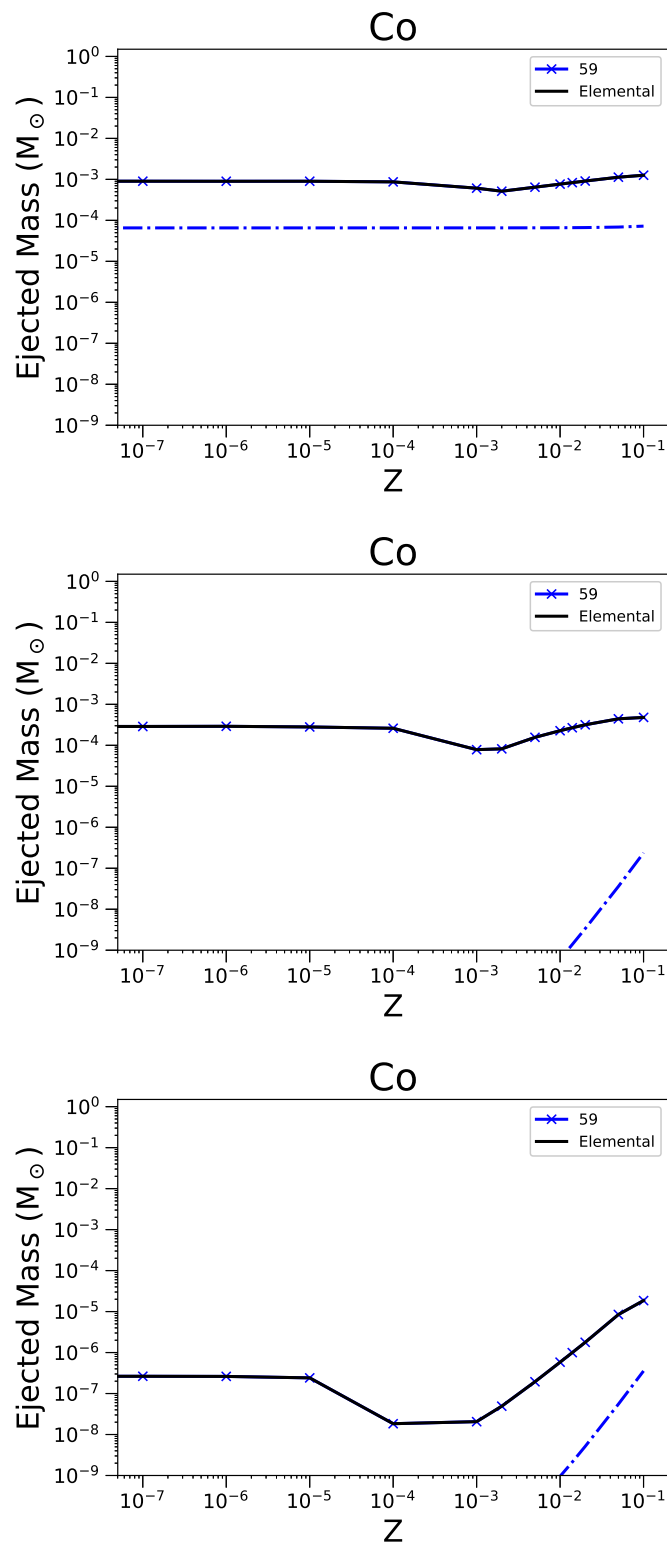


FIGURE 3.68: Ejected mass of ^{56}Ni as a function of initial metallicity.

decrease in production over the range of metallicities investigated here. This decrease in the production of Fe is approximately 25% across this metallicity range. The M0.8 model however does not show the same linear dependence as the higher mass models. We instead see a decrease in the ejected mass of ^{56}Ni to around 30% of the initial ejected mass at $Z = 0$.

In figure 3.68 I compare the results of my models with Timmes, Brown, and Truran (2003). S1.0 matches the Chandrasekhar mass SNIa model of Timmes, Brown, and Truran (2003) most closely. This is because the T1.4 model is 2 dimensional, as discussed in Townsley et al. (2016), which decreases the neutronisation in the innermost $0.2 M_{\odot}$ of the WD progenitor, resulting in the destruction of this stable iron group material as compared to a 1 dimensional model.

FIGURE 3.69: As in Figure 3.4 but for ejected mass of ^{59}Co .

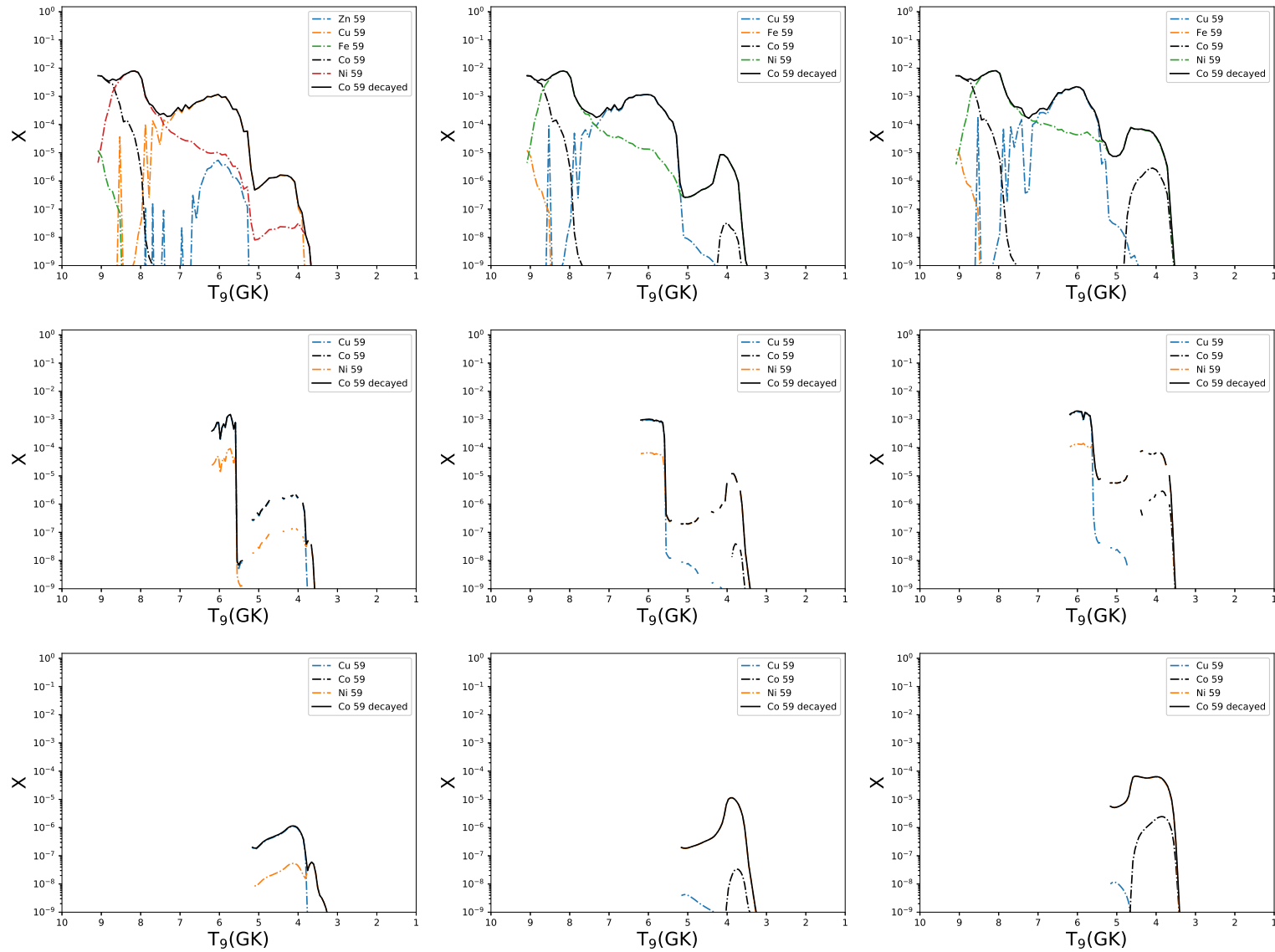


FIGURE 3.70: The abundance distributions of ^{59}Co are shown, arranged as in figure 3.5. With metallicities of $Z = 0, 0.014$ and 0.1 from left to right, and the three categories of model - T1.4, S1.0 and M0.8 - from top to bottom.

3.2.18 Cobalt

^{59}Co is the only stable isotope of cobalt. It is produced in a variety of stellar environments - the helium burning s-process, α -rich freeze-out, the neutrino process and SNIa explosions (Woosley, Heger, and Weaver, 2002).

^{59}Co has significant contributions from radiogenic sources across all models (figure 3.69). We see that for the case of S1.0 and M0.8, there is a strong secondary effect in both the direct and radiogenic synthesis of ^{59}Co , starting at $Z = 0.001$. In the models T1.4, there is no strong dependency on metallicity. The production of cobalt shows an increasing efficiency with an increase in the mass of the SNIa progenitor. M0.8 models show the strongest metallicity dependence, with an increase in production of almost 3 orders of magnitude between the model at $Z = 0.001$ and the maximum at $Z = 0.1$.

In figure 3.70, we show that the radiogenic contribution to ^{59}Co is dominated from ^{59}Ni (at peak temperatures between 7.5 and 8.5 GK) and ^{59}Cu (at intermediate and lower peak temperatures). ^{59}Cu is produced directly at $T > 8.5$ GK. This radiogenic production of cobalt is insensitive to metallicity effects at temperatures above 5 GK. The ^{59}Ni ejecta is uniform across T1.4 models at temperatures exceeding 7 GK, and the increase at around $T = 4$ GK in models T1.40.014 and T1.4Z0.1 is small compared to contributions from deeper layers. Production of ^{59}Cu in the intermediate peak temperature range is broadly insensitive to increasing metallicity, and as this contributes a large proportion of the ^{59}Co production in this model, the production of Co is also therefore insensitive. The trace production of ^{59}Zn observed in model T1.4Z0 is suppressed at metallicities above $Z = 0$. Production of ^{59}Ni is significantly increased in the lower temperature region at higher metallicities, contributing to a slight increase in Co yields with increasing metallicity.

Production in the S1.0 models has two components - a large, narrow peak for $T > 5.5$ GK, and a broader shallower peak between 3.5 and 5.5 GK. In

the S1.0Z0 model, both of these Co peaks are dominated by radiogenic ^{59}Cu . As initial metallicity rises, the production of ^{59}Cu is suppressed in the lower temperature peak, and the secondary component of ^{59}Ni is boosted. In model S1.0Z0.1, production of ^{59}Ni is boosted to the extent that it is comparable with the total contribution of ^{59}Cu .

In the S0.8 models, ^{59}Co production is severely reduced as compared with the previous sets of models. S0.8Z0 has a small peak between 3.2 and 5 GK, where the main contributor to ejected cobalt mass is from radioactive ^{59}Cu . As seen in the S1.0 models, production of ^{59}Cu is suppressed at higher metallicities, leading to ^{59}Ni dominating the production, here with a small contributing abundance of ^{59}Co which is directly made. The direct production of ^{59}Co is boosted still further moving to higher metallicities; however, the contribution from ^{59}Co is still small compared to ^{59}Ni .

3.2.19 Nickel

Nickel is composed of 5 stable isotopes: ^{58}Ni , ^{60}Ni , ^{61}Ni , ^{62}Ni and ^{64}Ni . The isotopes $^{(58,60,61,62)}\text{Ni}$ are produced during α -rich freeze-out from NSE (Woosley, Heger, and Weaver, 2002), with the dominant source of $^{(58,60)}\text{Ni}$ being SNIa (Pignatari et al., 2016). ^{58}Ni is the largest contributor to ejected elemental nickel from CCSN (Jerkstrand et al., 2015). Isotopes $^{(60,61,62,64)}\text{Ni}$ also have contributions from the s-process during helium burning (Woosley, Heger, and Weaver, 2002). Only ^{61}Ni is identified as having a large contribution from SNIa events in Woosley, Heger, and Weaver (2002), (Pignatari et al., 2016) identify $^{(61,62,64)}\text{Ni}$ as having some contribution from AGB stars. Kobayashi, Karakas, and Lugaro (2020) find that the evolution of $[\text{Ni}/\text{Fe}]$ vs $[\text{Fe}/\text{H}]$ for elemental nickel is reproduced well with only contributions from CCSN and SNIa events, with other sources having a negligible impact.

Figure 3.71 shows the metallicity dependence of the ejected elemental

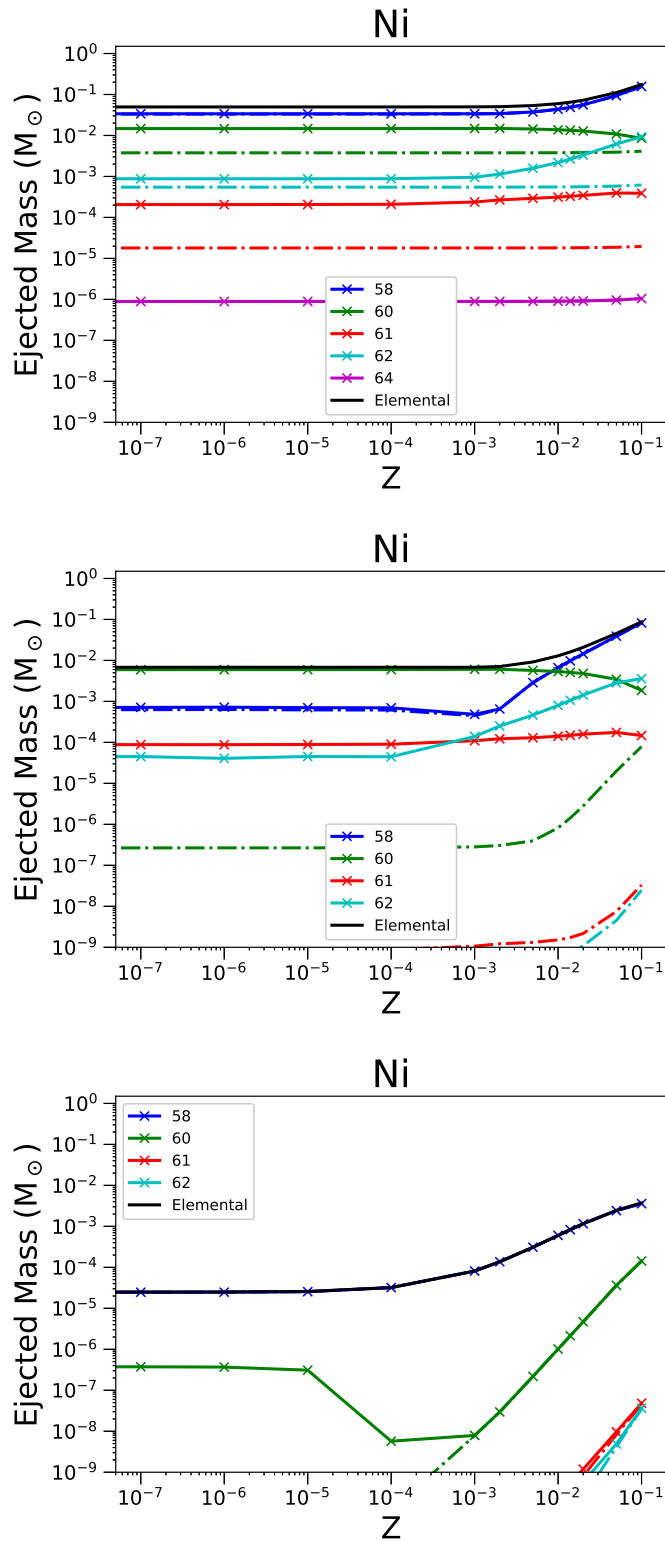


FIGURE 3.71: As in Figure 3.4 but for ejected mass of Ni, and its stable isotopes ^{58}Ni , ^{60}Ni , ^{61}Ni , ^{62}Ni and ^{64}Ni .

nickel and the stable isotopes, with radiogenic contributions. In the T1.4 models, there is an increase in the ejected mass of elemental nickel at around Z_{\odot} from around $5 \times 10^{-2} M_{\odot}$ to over $0.1 M_{\odot}$ at $Z = 0.1$, driven by an increase in the production of ^{58}Ni . In S1.0, we see a similar increase from a lower initial mass of approximately $6 \times 10^{-3} M_{\odot}$ to nearly $0.1 M_{\odot}$. In these models however the major contributor at low metallicities is ^{60}Ni , which is suppressed above $Z = 10^{-3}$, although this is compensated for by the increase in production of ^{58}Ni which becomes the dominant isotope and drives the metallicity dependence of elemental nickel. In M0.8, we see an increase in the abundance of ^{58}Ni from 2.5×10^{-5} at $Z = 0$ to 3.6×10^{-3} at $Z = 0.1$.

In all models, we see an increase in the ejected mass of ^{58}Ni with increasing metallicity, due to contributions from lower temperature regions of the SNIa explosion. Figure 3.72 shows the mass fraction of ^{58}Ni with respect to peak temperature in each particle. We see that the NSE regions of the T1.4 models are largely insensitive to the changing metallicity. Although there is a decrease in the radiogenic contributions from ^{58}Cu , these are negligible at most peak temperatures, except in the T1.4Z0 model where a non-negligible contribution in the 5-6 GK range from ^{58}Co is seen. Even so, this will have no impact on the total ejected yields. Because of the large contributions from NSE conditions, the proportional change in the abundance of ^{58}Ni is less in the T1.4 model than for the S1.0 and M0.8 models, where we see a change in the ejected mass of ^{58}Ni of over an order of magnitude (this is also due to the lower starting abundance). Production of ^{58}Ni extends to the top of the oxygen burning region at approximately 3.5 GK, it is between 4 and 5 GK at which we see the increase in ^{58}Ni production at higher metallicities in all models.

Figure 3.73 shows that the metallicity dependence of ^{60}Ni production is similar between models T1.4 and S1.0, where the ejected mass of ^{60}Ni decreases with increasing metallicity above approximately $Z = 10^{-2}$ for the T1.4

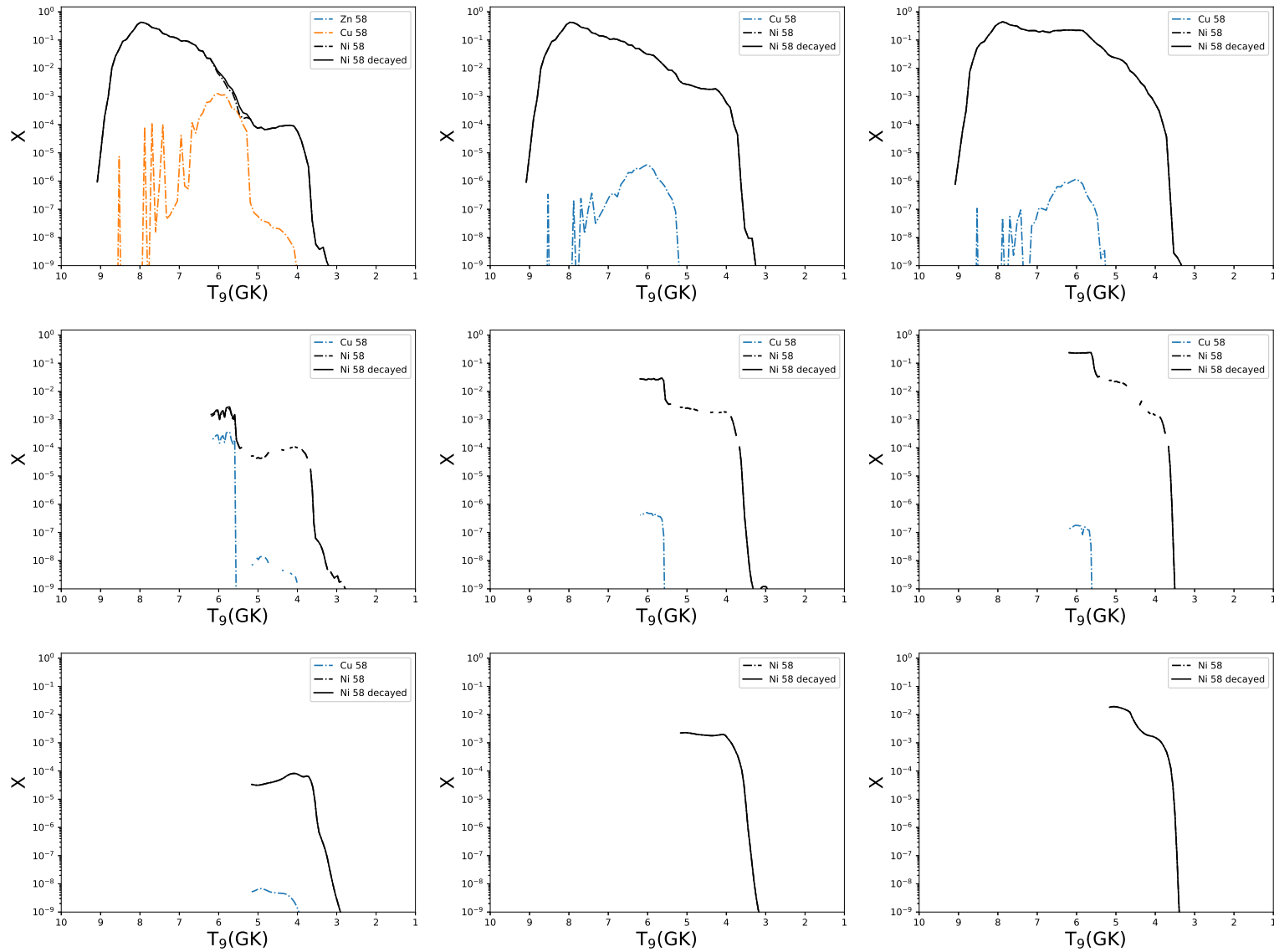


FIGURE 3.72: The abundance distributions of ^{58}Ni are shown, arranged as in figure 3.5. With metallicities of $Z = 0, 0.014$ and 0.1 from left to right, and the three categories of model - T1.4, S1.0 and M0.8 - from top to bottom.

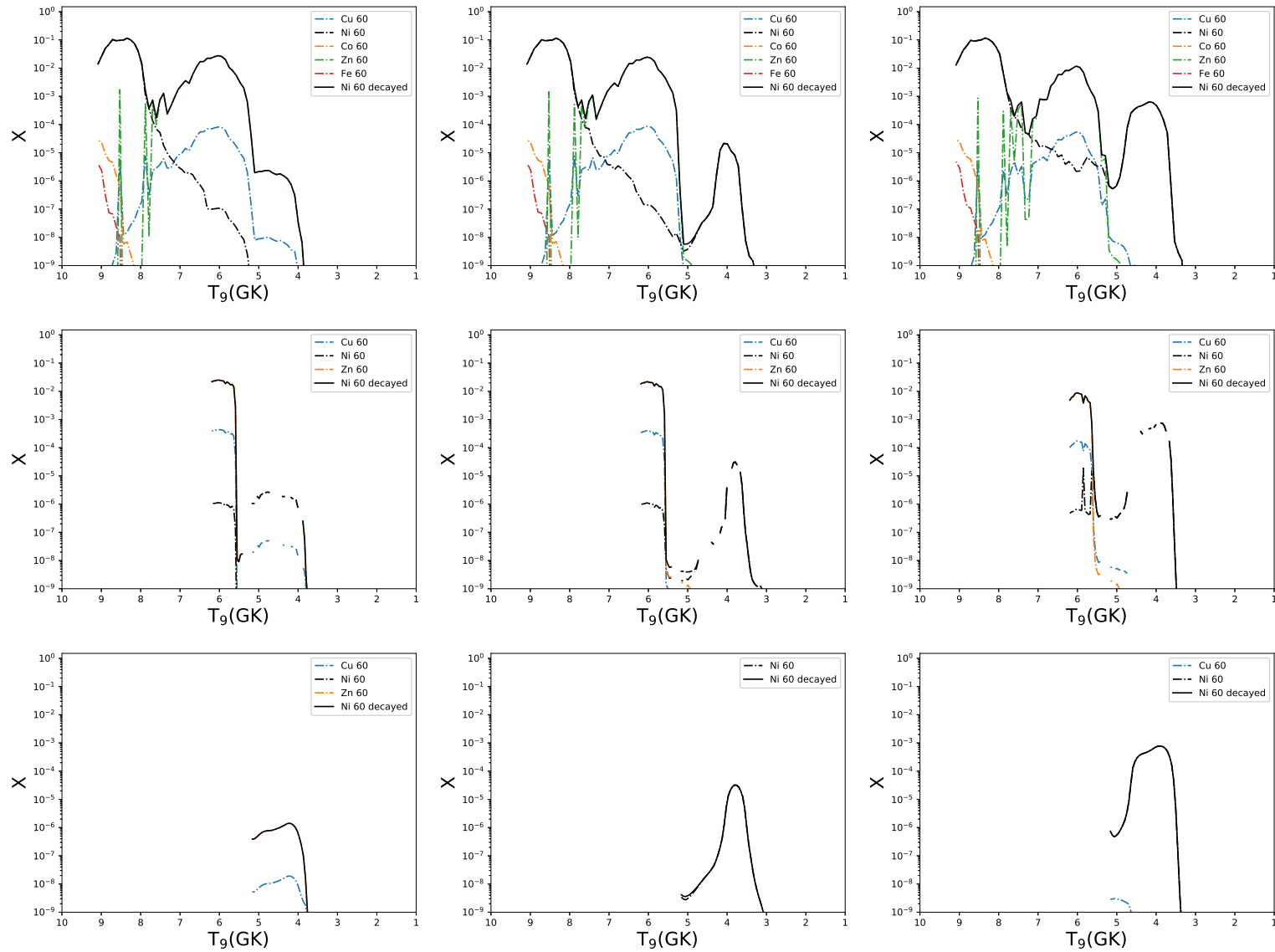


FIGURE 3.73: The abundance distributions of ^{60}Ni are shown, arranged as in figure 3.5. With metallicities of $Z = 0, 0.014$ and 0.1 from left to right, and the three categories of model - T1.4, S1.0 and M0.8 - from top to bottom.

models and $Z = 2 \times 10^{-3}$ for the S1.0 models. We see three areas of production in the T1.4Z0 model - one above 8 GK, one between 5 and 7 GK and a smaller peak between 4 and 5 GK, in the 8-9 GK region production is dominated through direct synthesis of ^{60}Ni , due to the high density conditions in the central region. In the 5-6 GK peak, most ^{60}Ni is synthesised as ^{60}Zn . We see that this contribution decreases with increasing metallicity, driving the shallow decline of ejected ^{60}Ni . In the T1.4Z0.014 model, we see that the low temperature peak has been boosted significantly, with direct production of ^{60}Ni , this peak also extends further down to around 3.5 GK, corresponding with the lower edge of the oxygen burning region. This trend continues in T1.4Z0.1, where there is a significant boost to the ^{60}Ni production in the oxygen burning region. In model S1.0, the highest temperature peak is missing, as no particles experience these conditions. We therefore see a much stronger metallicity dependence on the ^{60}Ni for this model, with the total ejected mass of ^{60}Ni decreasing as the metallicity increases. This is due to the same effects driving the decrease in the T1.4 models - namely a drop in production of ^{60}Zn in the intermediate peak temperature region, but as there is not a large contribution from $T > 6$ GK regions in the S1.0 models, there is proportionally a much larger effect. While the low temperature oxygen burning region does increase significantly, it does not compensate for the lost material in the intermediate region. We see in figure 3.71 that this effect causes ^{58}Ni to become the dominant isotope in the S1.0 models at metallicities above $Z = 4 \times 10^{-3}$.

In the M0.8 models we initially see the same trend of suppression of ^{60}Zn production leading to a decrease in the ^{60}Ni ejected mass however, since both the high temperature and most of the intermediate temperature region are absent in the M0.8 model, the $Z = 0$ mass of ^{60}Ni is already low. When production moves to lower temperatures therefore, with ^{60}Ni being synthesised directly, the ejected abundance of ^{60}Ni increases compared to the $Z = 0$ value.

Shifts in the isotopic distribution of the iron group cannot be attributed

to any one particular reaction, as the models are in NSE. In the oxygen burning region however, neutron capture reactions with the increased Y_e of the system lead to the increase in production of ^{60}Ni .

In figure 3.74 we see that production of ^{61}Ni is dominated by the intermediate and high temperature regions. In the T1.4 model sets, the ejected mass of ^{60}Ni changes from $2.06 \times 10^{-4} M_{\odot}$ at $Z = 0$ to $3.89 \times 10^{-4} M_{\odot}$ at $Z = 0.1$. This is consistent with the results for other isotopes mainly produced in the high temperature regions, where the changing initial Y_e has a marginal impact in the NSE conditions. The increase in production in the peak temperature region between 3.5 and 5 GK may be sufficient to account for the observed increase in ejected mass, however a very small increase in the higher temperature regions cannot be excluded. In the high temperature region, ^{61}Ni is directly produced, in the intermediate peak temperature region ^{61}Zn is the major contributor to ejected ^{61}Ni mass (and this dominates the production overall). In the low temperature region, ^{61}Ni is produced directly.

Similarly for the S1.0 models, there is a small increase in the ejected mass of ^{61}Ni between S1.0Z0 ($8.81 \times 10^{-5} M_{\odot}$) and S1.0Z0.1 ($1.47 \times 10^{-4} M_{\odot}$). Production in the intermediate peak temperature region is insensitive to an increase in the initial ^{22}Ne mass fraction, with ^{61}Ni being synthesised as ^{61}Zn , as in the T.14 models. The low temperature region is directly produced as ^{61}Ni , and contributes only on the order of 0.1-1% of the ejected mass of ^{61}Ni in this model. With the high temperature region missing, the total ejected mass of ^{61}Ni compared with the T1.4 models is a factor of two lower.

In the M0.8 models, both the intermediate and high temperature peaks are missing, so only the relatively small contribution from the oxygen burning region is seen, and only in non-negligible amounts above $Z = 2 \times 10^{-2}$. We see that in the case of ^{61}Ni , the intermediate peak of production is slightly higher than e.g. $^{56,57}\text{Fe}$, leading to there being no contribution from the higher temperature regions of this class of model.

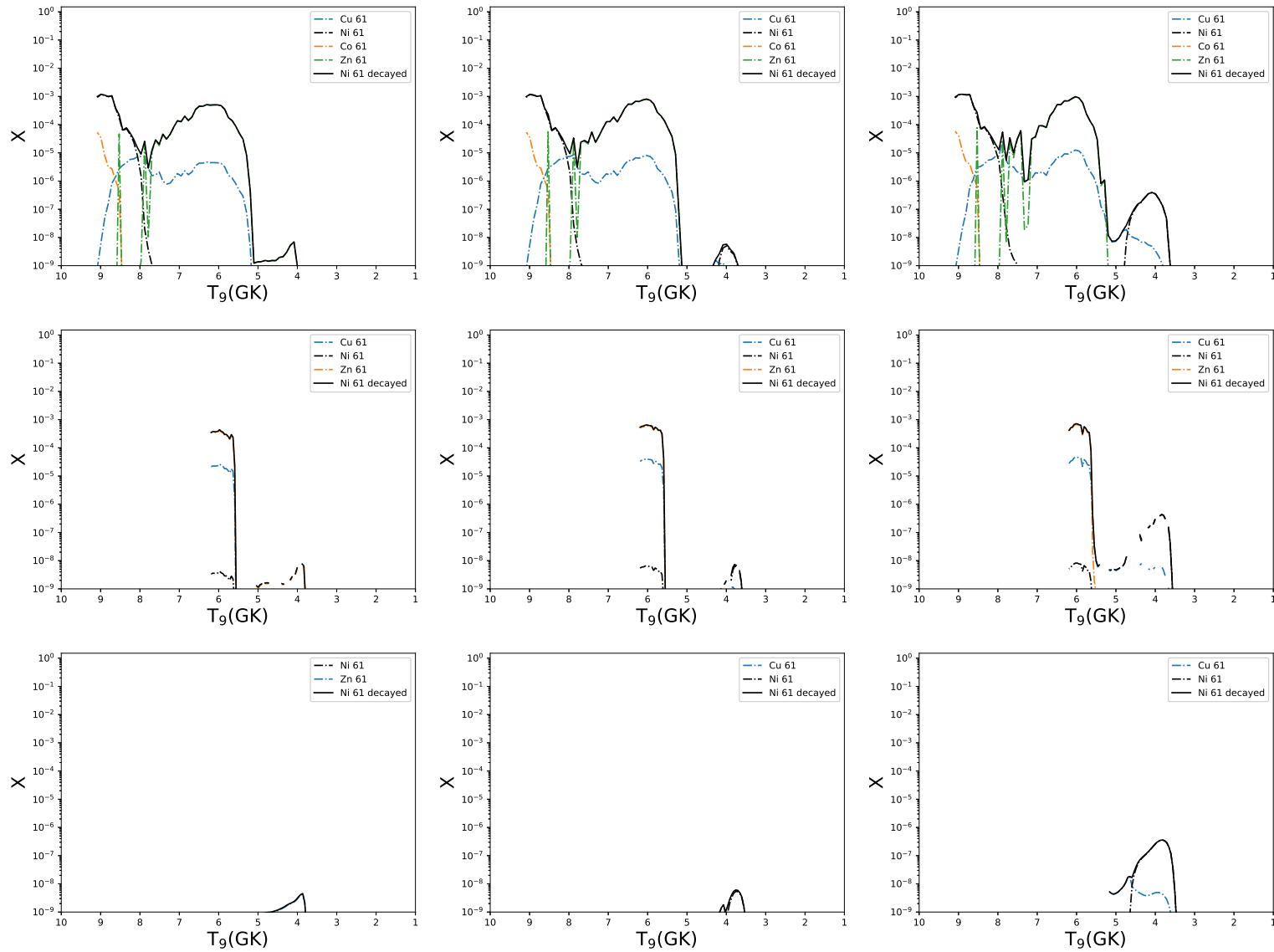


FIGURE 3.74: The abundance distributions of ^{61}Ni are shown, arranged as in figure 3.5. With metallicities of $Z = 0, 0.014$ and 0.1 from left to right, and the three categories of model - T1.4, S1.0 and M0.8 - from top to bottom.

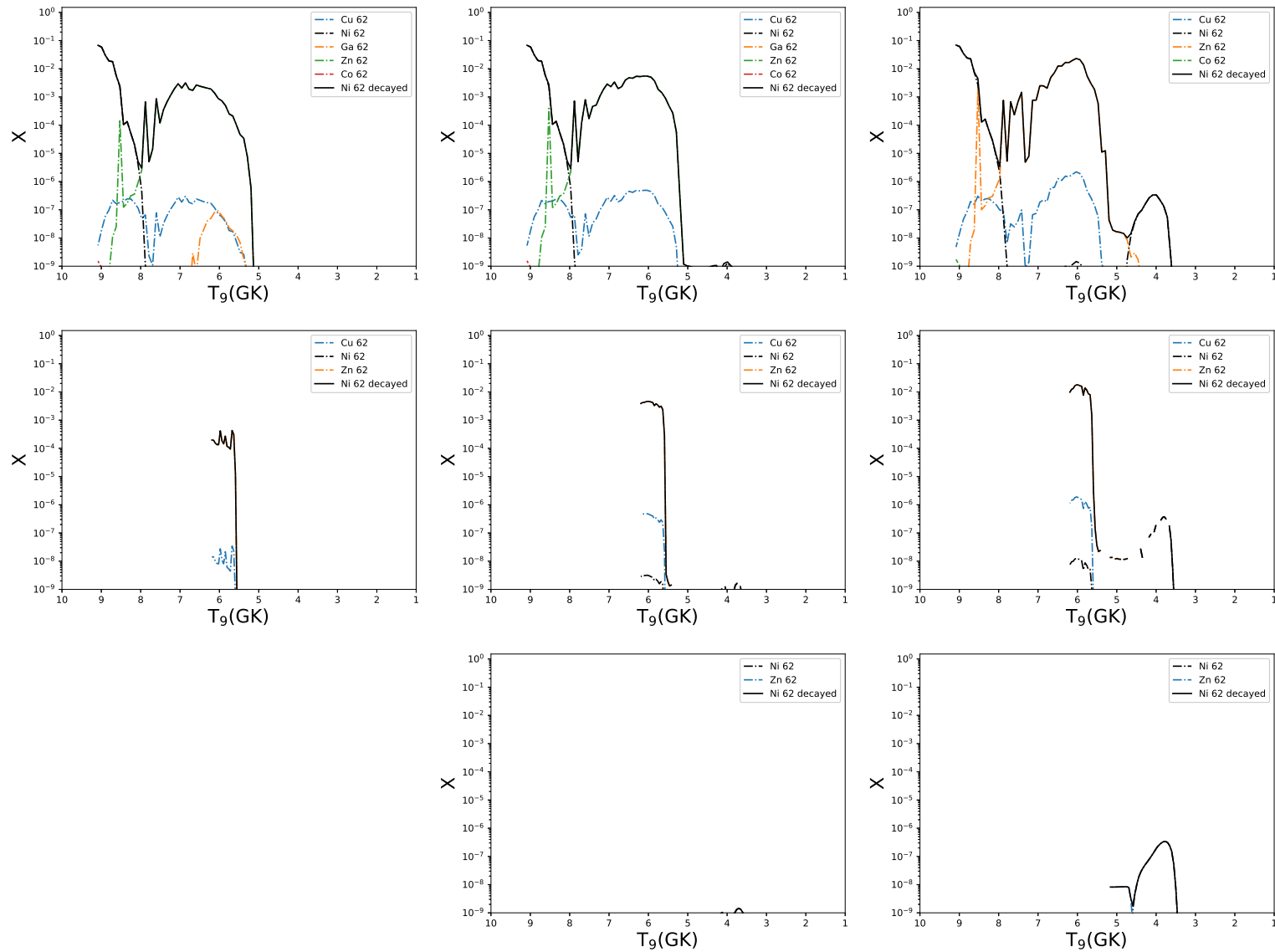


FIGURE 3.75: The abundance distributions of ^{62}Ni are shown, arranged as in figure 3.5. With metallicities of $Z = 0, 0.014$ and 0.1 from left to right, and the three categories of model - T1.4, S1.0 and M0.8 - from top to bottom. Model M0.8Z0 produces no ^{62}Ni , and so the subplot for this model is omitted.

Figure 3.75 shows the production of ^{62}Ni . The trend in production is very similar to that for ^{61}Ni , with a large contribution from the high and intermediate peak temperature regions. In the T1.4 models, we see that production of ^{62}Ni in the 8-9 GK region is larger than the production of ^{61}Ni in that same region. This is due to the increased density which causes production to shift to more neutron rich isotopes in the central region. Production is through direct synthesis of ^{62}Ni .

The intermediate peak temperature region from around 5 to 7 GK is very similar to the ^{61}Ni production region in the T1.4 models, with the mass fraction of ^{62}Ni being around 0.1%. ^{62}Zn is the major contributor to abundances in this region as direct production ceases at 8 GK. Production in this region is sensitive to the initial metallicity, increasing from the initial approximately 0.2% by mass fraction in T1.4Z0 to around 3% in model T1.4Z0.1. We also see a small contribution in the oxygen burning region through direct production of ^{62}Ni , although this has a negligible effect on the ejected mass.

In the S1.0 series of models, we again see an increase in the production at intermediate peak temperatures. As the highest temperatures in this model are at approximately 6 GK, we see only the lower end of this production region, which significantly reduces the ejected mass of ^{62}Ni from these models. There is again a small contribution at around 3.5 GK but this is negligible.

In the models M0.8, there is no production at $Z = 0$, and only a marginal production at $Z = Z_{\odot}$. The 6 GK region is completely absent from this model and so the production through formation of ^{62}Zn is not possible. We therefore only have the small secondary contribution in the lower temperature region, as seen for the T1.4 and S1.0 models.

Figure 3.76 shows the production of ^{64}Ni in the T1.4 models. Production is confined to the high peak temperature region above 8 GK, and as such the effect of initial metallicity is suppressed, as weak interactions in the core of the WD change the Y_e of the interior. There is a very mild dependence

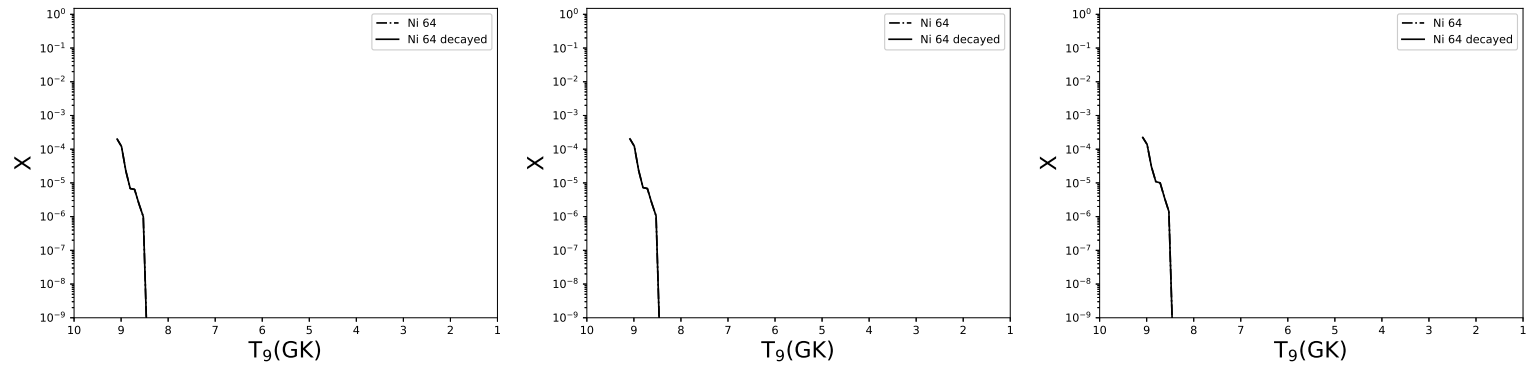


FIGURE 3.76: The abundance distributions of ^{64}Ni . Only models T1.4Z0, T1.4Z0.014 and T1.4Z0.1 produce ^{64}Ni . Only the T1.4 models show production of ^{64}Ni , as such the other models have been omitted.

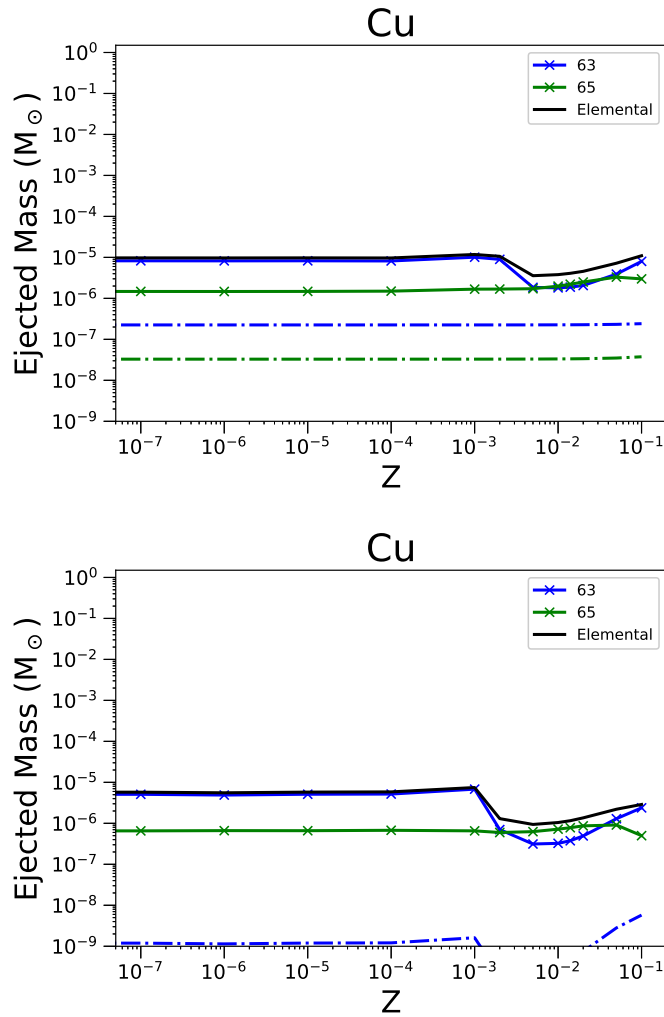


FIGURE 3.77: As in Figure 3.4 but for ejected mass of Cu, and its stable isotopes ^{63}Cu and ^{65}Cu . The M0.8 models are excluded as copper is not produced efficiently in these low.

on initial metallicity however, with the ejected mass of ^{64}Ni changing from $8.89 \times 10^{-7} M_{\odot}$ at $Z = 0$ to $1.05 \times 10^{-6} M_{\odot}$ at $Z = 0.1$. ^{64}Ni is directly produced in this region, with no radiogenic component.

3.2.20 Copper

Copper has two stable isotopes: ^{63}Cu and ^{65}Cu . ^{63}Cu is produced in the helium burning s-process, carbon, and neon burning in massive stars and ^{65}Cu is mainly produced in the s-process in massive stars (Woosley, Heger, and Weaver, 2002). SNIa do not produce copper efficiently.

In figure 3.77 both ^{63}Cu and ^{65}Cu show a large radiogenic contributions to their abundances in both the T1.4 and S1.0 models. These models also have a similar distribution with respect to metallicity. At approximately $Z = 2 \times 10^{-3}$ and 10^{-3} for T1.4 and S1.0 respectively, the production of ^{63}Cu is reduced dramatically. At super-solar metallicities, ^{63}Cu production increases again for the region around $Z = Z_{\odot}$ we see that ^{65}Cu becomes the most abundant copper isotope in the ejecta.

Figure 3.78 illustrates the complicated nucleosynthesis of ^{63}Cu , particularly in the T1.4 models. In T1.4Z0, there is a contribution from ^{63}Ni at the most extreme temperature peaks, which becomes negligible for $T < 8.5$ GK. In this region, we next see the direct synthesis of ^{63}Cu . This is quickly replaced, from $T = 8$ GK to the coolest temperature at which ^{63}Cu is produced at around 5.2 GK by radiogenic contributions from ^{63}Ga and ^{63}Zn . The change in production between ^{63}Ga and ^{63}Zn is more ordered in the T1.4Z0.014 model: the lower temperature production below 6.5 GK is dominated by ^{63}Ga , between 6.5 and 8 GK ^{63}Zn has the largest radiogenic contribution. In T1.4Z0.1, production of ^{63}Zn is boosted across the whole temperature range from 5.2 to 8 GK, ^{63}Ga production is reduced in this same range. The innermost ejecta stays consistent with lower metallicities.

Production in the S1.0 models follows a similar, non-linear trend with metallicity, whereby ^{63}Ga and ^{63}Zn exchange positions as the most abundant isotope. In model S1.0Z0, ^{63}Ga is the most abundant. In the S1.0Z0.014 model, there is a reduction in the overall ejected mass of ^{63}Cu , as the reduction in ^{63}Ga is not fully compensated for by the increase in the abundance of ^{63}Zn . Total ejected mass is then similar again in S1.0Z0.1, as ^{63}Zn continues to increase with metallicity.

Figure 3.79 shows the production of ^{65}Cu in the T1.4 and S1.0 models. There is no low temperature contribution to the ejected mass of ^{65}Cu at any metallicity. Production in the T1.4Z0 model is largely in the temperature

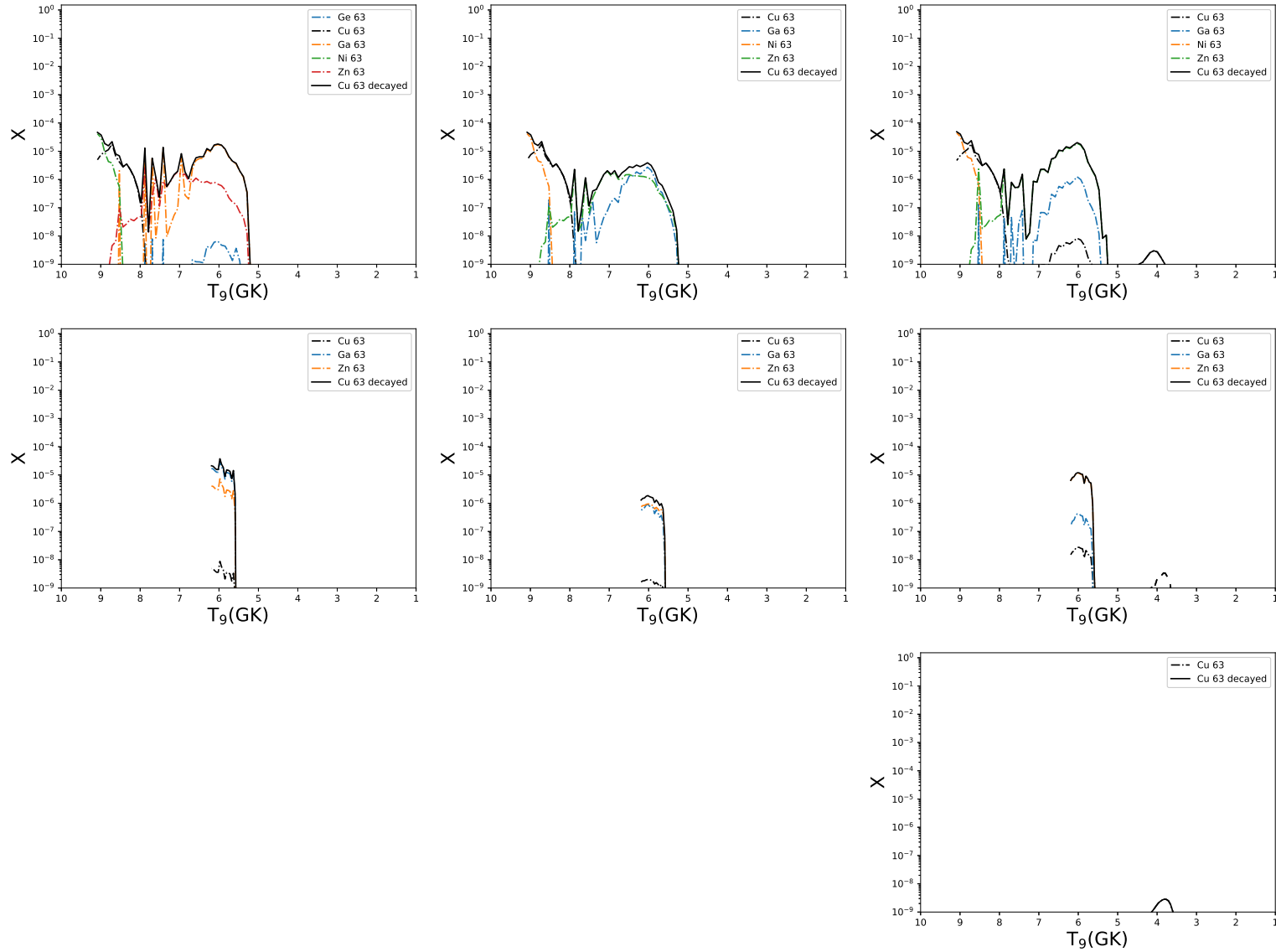


FIGURE 3.78: The abundance distributions of ^{63}Cu are shown, arranged as in figure 3.5. With metallicities of $Z = 0, 0.014$ and 0.1 from left to right, and the three categories of model - T1.4, S1.0 and M0.8 - from top to bottom. The models M0.8Z0 and M0.8Z0.014 do not produce ^{63}Cu and are therefore omitted.

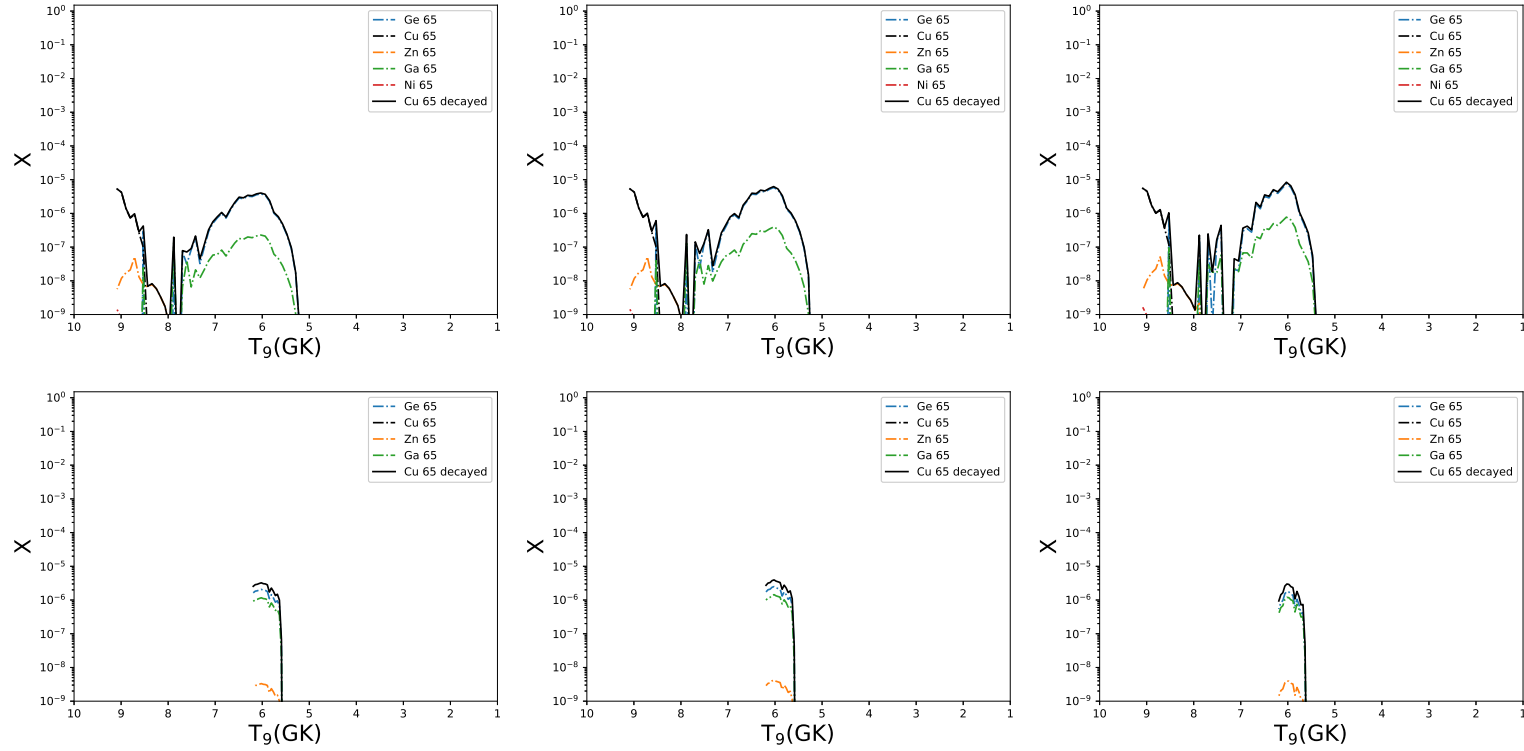


FIGURE 3.79: The abundance distributions of ^{65}Cu are shown, arranged as in figure 3.5. With metallicities of $Z = 0, 0.014$ and 0.1 from left to right, and the three categories of model - T1.4, S1.0 and M0.8 - from top to bottom. There is no production of ^{65}Cu in the M0.8 models, these are therefore omitted.

range 5.2 - 7.8 GK, where ^{65}Cu is produced as the radioisotope ^{65}Ge . In the high temperature peak above 8 GK, ^{65}Cu is produced directly. There is a shallow trend with respect to metallicity in the ejected mass of ^{65}Cu in the T1.4 models, from 1.47 to $2.99 \times 10^{-6} M_{\odot}$. Production becomes more tightly centered around 6 GK but with a larger contribution from this narrower range of temperatures, especially at the higher end of the intermediate peak temperature range.

Because this peak temperature range is missing in the S1.0 models, we see that the ^{65}Cu production peaks at around solar metallicity. As the increase in the temperature in the lower end of the intermediate production region becomes larger, the slight increase in production at those temperatures is not enough to compensate for the loss of production sites. In all three models shown for S1.0, ^{65}Cu is produced as a combination of ^{65}Ge and ^{65}Ga .

3.2.21 Zinc

Zinc has 5 stable isotopes: ^{64}Zn , ^{66}Zn , ^{67}Zn , ^{68}Zn and ^{70}Zn . None of the models investigated here produce ^{70}Zn , as such, we will not discuss this isotope further. ^{64}Zn is produced in neutrino driven winds (Woosley, Heger, and Weaver, 2002) - where neutrino interactions in dense stellar environments with large neutrino fluxes cause neutrino captures. It is also formed in the helium burning s-process in massive stars, and α -rich freeze-out from NSE. ^{66}Zn is likewise produced in the helium burning s-process and α -rich freeze-out, however Woosley, Heger, and Weaver (2002) also identify ^{66}Zn as having a significant contribution from Chandrasekhar mass SNIa explosions. ^{68}Zn is produced only in massive stars through the helium burning s-process (Woosley, Heger, and Weaver, 2002).

Zinc production in the models T1.4 and S1.0 is very similar (figure 3.80, with similar trends for all of the isotopes produced aside from a scaling factor

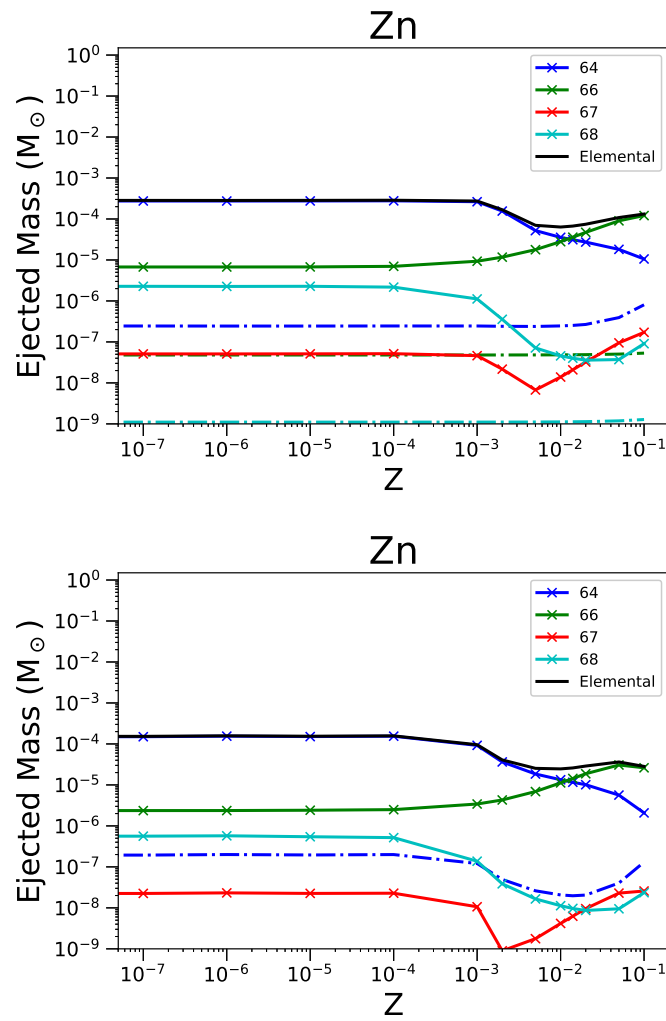


FIGURE 3.80: As in Figure 3.4 but for ejected mass of Zn, and its stable isotopes ^{64}Zn , ^{66}Zn , ^{67}Zn and ^{68}Zn . There is no production of zinc in the M0.8 models and therefore the plot is omitted.

between models for these isotopes. The elemental trend of Zn production decreases at around $Z = 0.001$ by approximately a factor of 5, following the trend of ^{64}Zn . At the same time ^{66}Zn production increases becoming the most abundant isotope at higher metallicities.

Production of ^{64}Zn in fig 3.81 shows that production in all T1.4 models is dominated by the radio-isotope ^{64}Ge . The contribution of ^{64}Ga to the ejected abundance is never large, although it increases at higher metallicities as the intermediate peak temperature range production of ^{64}Ge shrinks.

We see that production in the S1.0 models is also primarily through synthesis of ^{64}Ge . We clearly see the decrease in the overall production of ^{64}Zn with the reduction in ^{64}Ge and ^{64}Ga produced at between peak temperatures of 5.5-6 GK. We also observe the rise in direct production of ^{64}Zn , although the absolute abundance is only on the order of 5% in the S1.0Z0.1 model.

The production of ^{66}Zn is largely centered in the intermediate peak temperature range starting at approximately 5.2 GK and continuing to 8 GK. ^{66}Zn is produced as ^{66}Ge in the T1.4Z0 model, with trace amounts of other isotopes. Production is nearly identical in the T1.4Z0.014 model, with only a slight increase in the production of ^{66}Ga (already with very low abundance). The range of peak temperatures suitable for production is less broad in the T1.4Z0.1 model, with production at the upper limit of the production region becoming less efficient.

Production in all three S1.0 models is very similar, with a slight increase in the amount of ^{66}Zn ejected caused by an increase in the radiogenic contribution of ^{66}Ge . Trace amounts of ^{66}Ga do not affect the overall yields.

^{67}Zn has a similar trend as for ^{66}Zn (figure 3.83). In model T1.4Z0 we see a comparable contribution to the ejected mass of ^{67}Zn from both ^{67}Ge and ^{67}As . As the initial metallicity increases, both of these contributions become secondary to the increased production of ^{67}Ge , culminating in T1.4Z0.1, where only trace amounts of ^{67}Ge and ^{67}Cu contribute to the abundance of

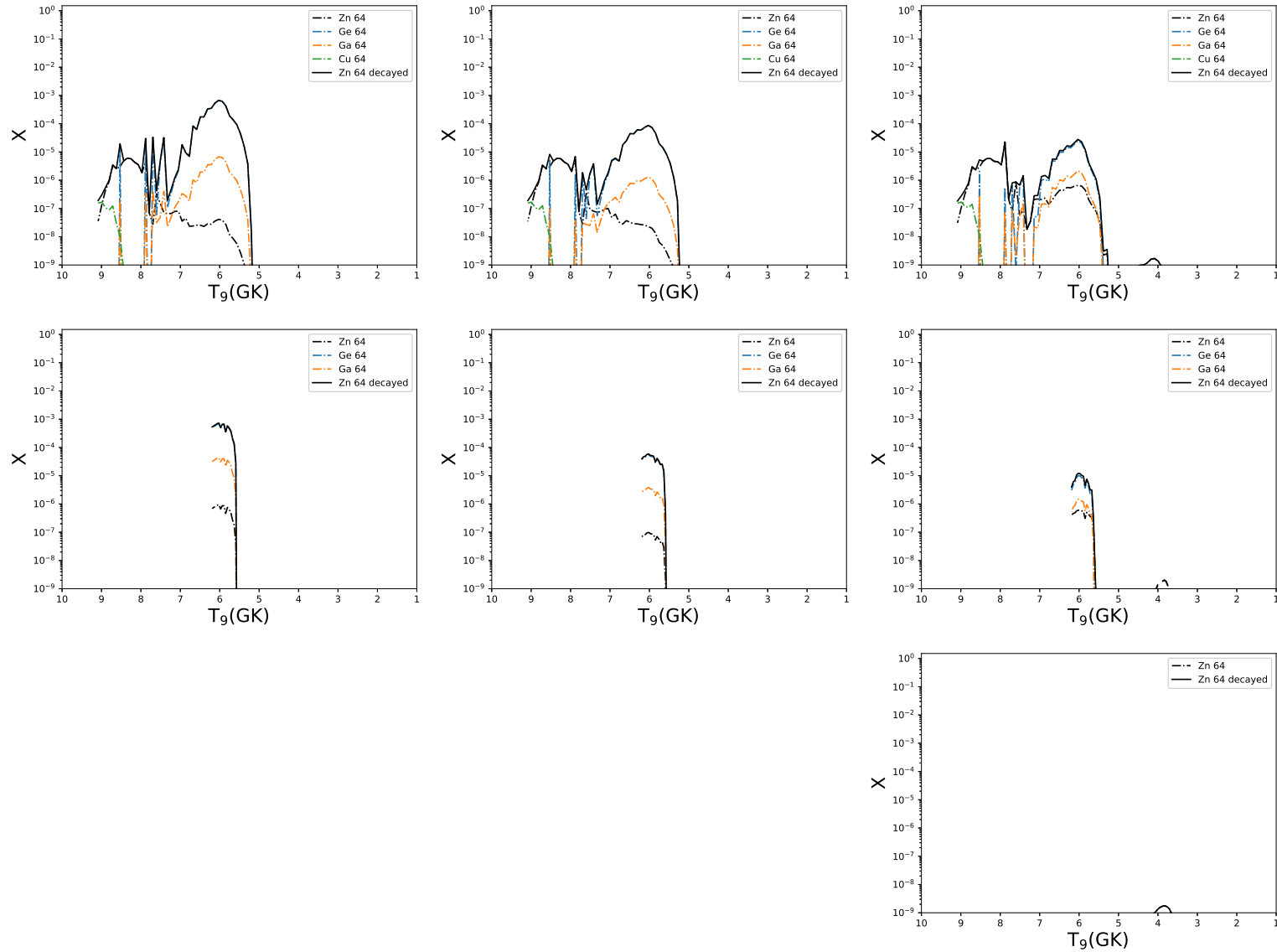


FIGURE 3.81: The abundance distributions of ^{64}Zn are shown, arranged as in figure 3.5. With metallicities of $Z = 0, 0.014$ and 0.1 from left to right, and the three categories of model - T1.4, S1.0 and M0.8 - from top to bottom. from the M0.8 models, only M0.8Z0.1 has even a trace production of ^{64}Zn . Because of this, we omitted the M0.8 plots at lower metallicities.

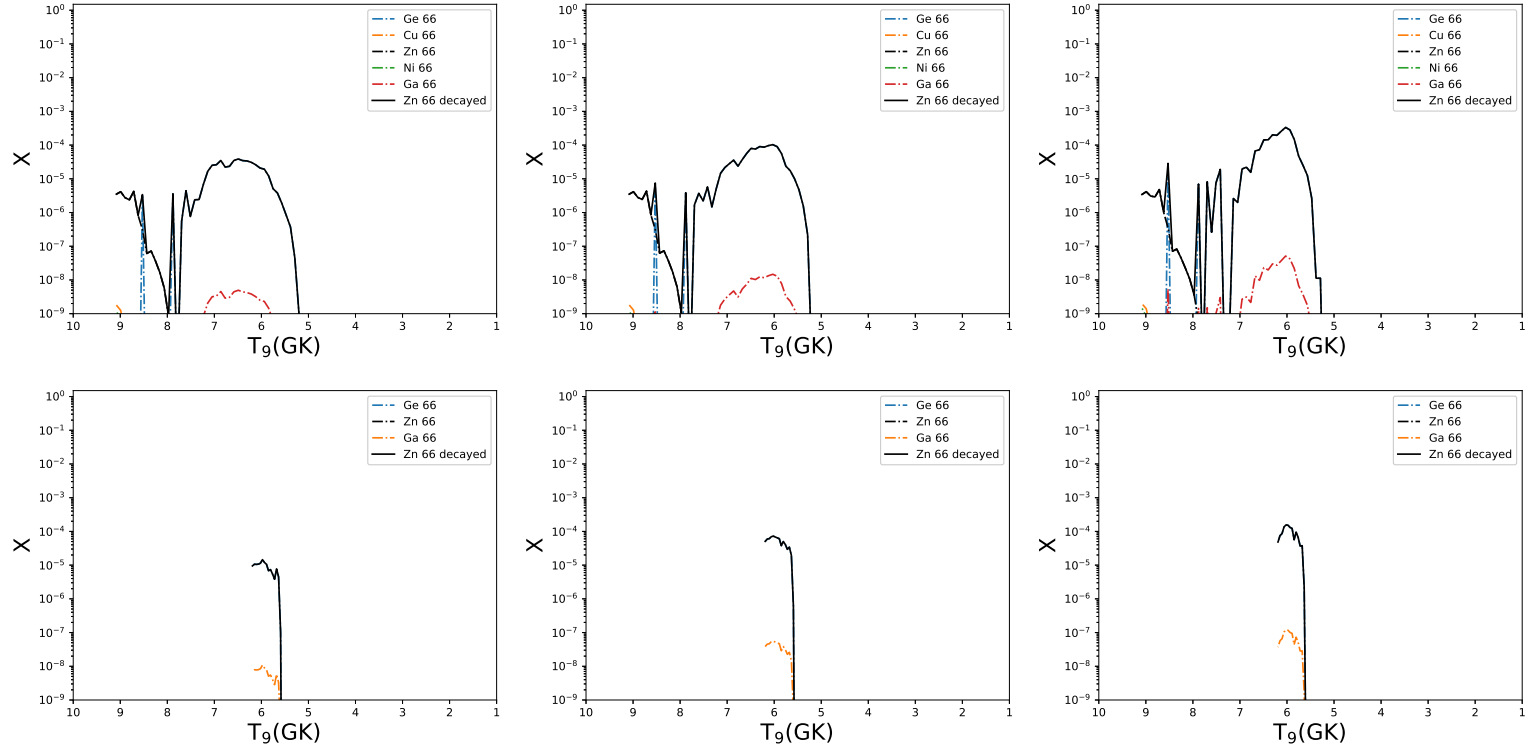


FIGURE 3.82: The abundance distributions of ^{66}Zn are shown, arranged as in figure 3.5. With metallicities of $Z = 0, 0.014$ and 0.1 from left to right, and the three categories of model - T1.4, S1.0 and M0.8 - from top to bottom. M0.8 models do not produce ^{66}Zn and are therefore omitted.

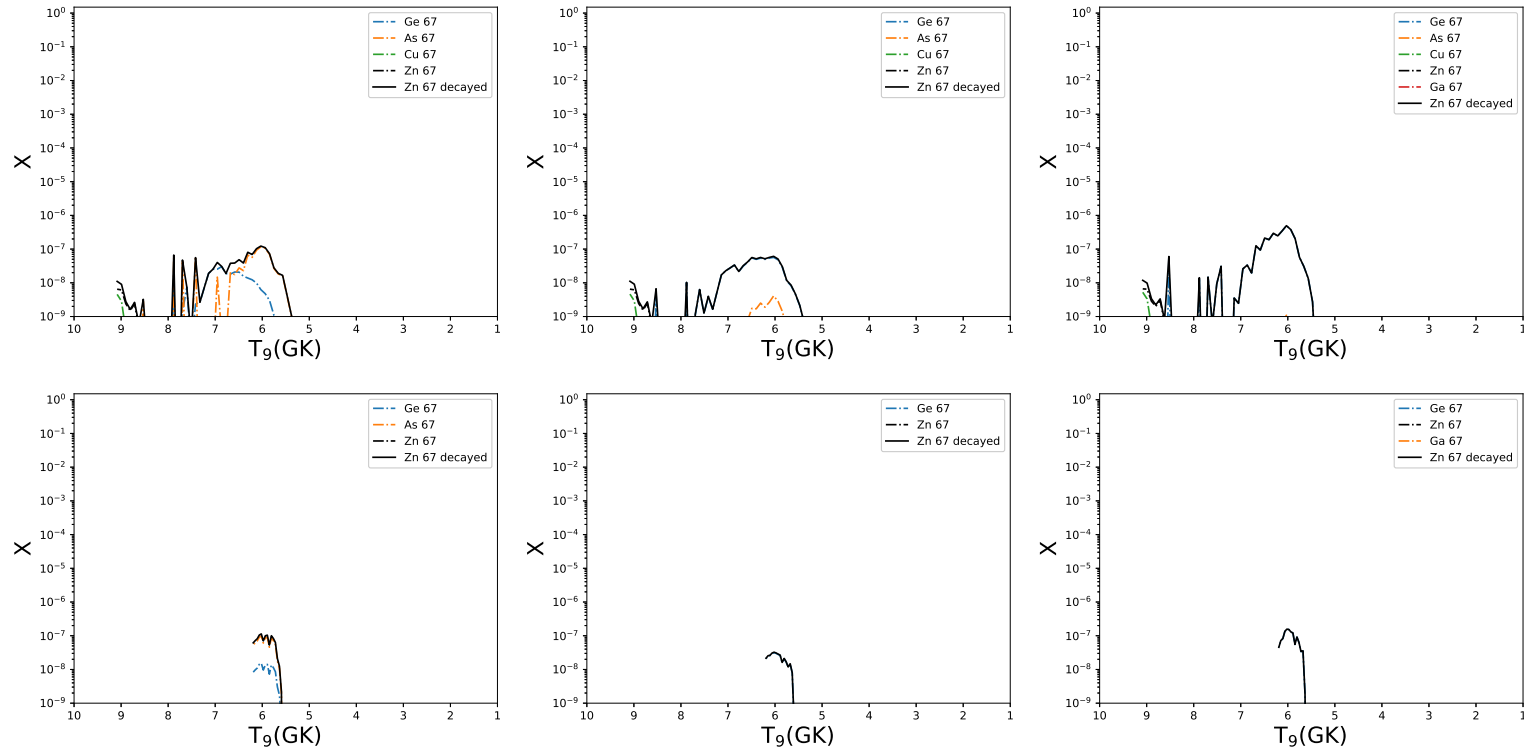


FIGURE 3.83: The abundance distributions of ^{67}Zn are shown, arranged as in figure 3.5. With metallicities of $Z = 0, 0.014$ and 0.1 from left to right, and the three categories of model - T1.4, S1.0 and M0.8 - from top to bottom. The M0.8 models do not produce ^{67}Zn and are therefore omitted.

^{67}Zn .

Production of ^{68}Zn , again occurs mainly at intermediate peak temperatures from 5.2 to 7 GK. In the model T1.4Z0, we see that there is a small contribution to ^{68}Zn from ^{68}As , with the bulk of material being synthesised as ^{68}Se . ^{68}Se production is reduced as the metallicity increases, leading to an overall decrease in the ejected mass of ^{68}Zn and an increase in the ^{68}Ge to ^{68}Se ratio. In model T1.4Z0.1, ^{68}Se is no longer the most abundant isotope, ^{68}Ge has become more favorable to produce.

In the S1.0 models, we again note that the nucleosynthesis is similar, with ^{68}Se being the most abundant isotope in the S1.0Z0 models, a decrease in the production of ^{68}Se as the initial metallicity increases, and then production becoming more reliant on ^{68}Ge , with ^{68}Se as a trace isotope only at $Z = 0.1$.

3.2.22 Germanium

Germanium consists of five stable isotopes - ^{70}Ge , ^{72}Ge , ^{73}Ge , ^{74}Ge and ^{76}Ge . Only ^{70}Ge and ^{72}Ge are produced in any of our models and so we will restrict our discussion to these isotopes. ^{70}Ge is and s only species, produced in the pre-explosive massive stars of CCSN (Pignatari et al., 2016).

Figure 3.85 shows the production of germanium in the various categories of model with respect to metallicity. While the M0.8 models do not produce Ge, both the T1.4 and S1.0 models do produce trace amounts. ^{72}Ge contributes less than 1% to elemental germanium in the T1.4 models, and less still to the S1.0 models. It is also not overproduced with respect to solar abundances and as such we will not discuss ^{72}Ge further. We see that ^{70}Ge has a fairly strong secondary component, with an increase in ejected mass of over an order of magnitude. This trend continues smoothly for the T1.4 models, however for the S1.0 models at $Z = 0.1$ we see a decrease in the total ejected mass.

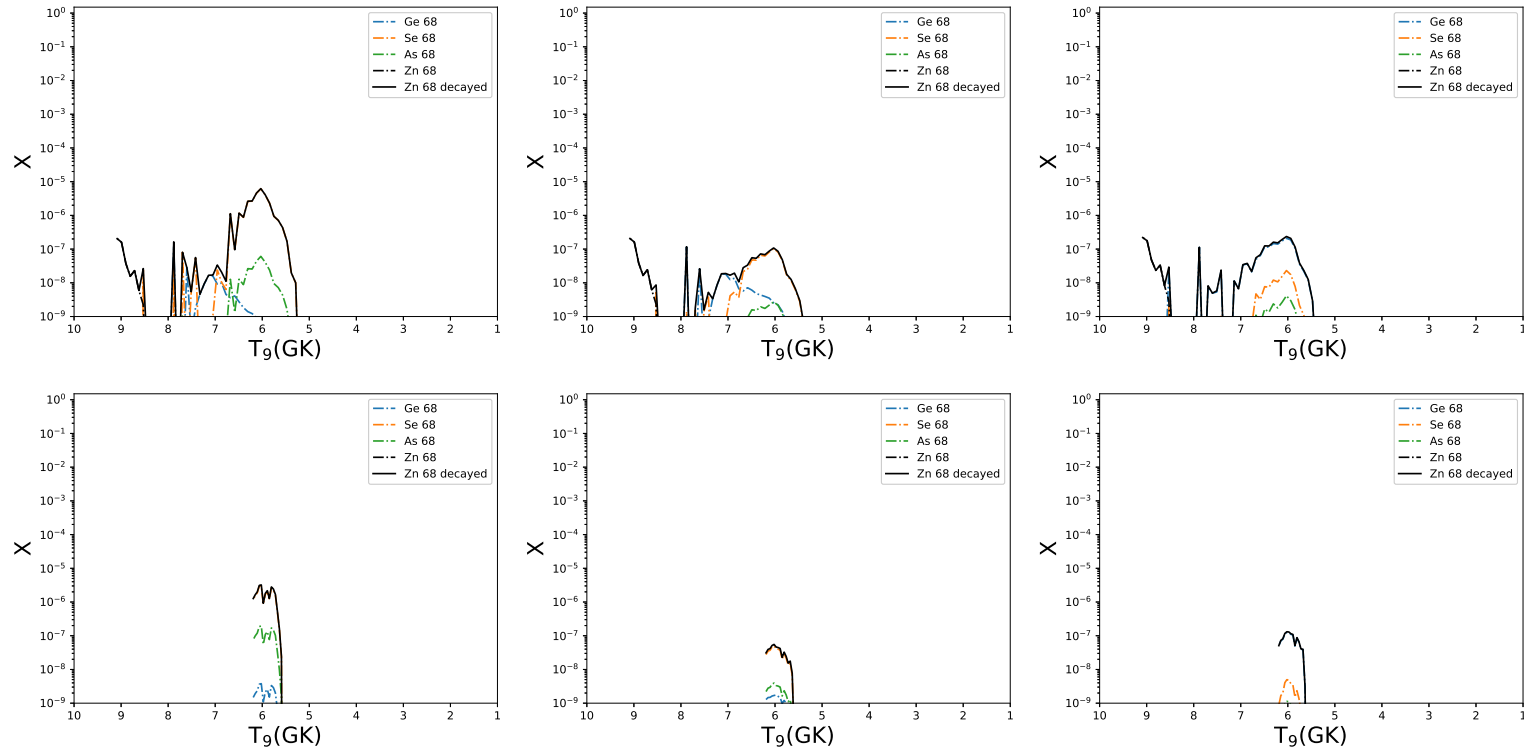


FIGURE 3.84: The abundance distributions of ^{68}Zn are shown, arranged as in figure 3.5. With metallicities of $Z = 0, 0.014$ and 0.1 from left to right, and the three categories of model - T1.4, S1.0 and M0.8 - from top to bottom. The M0.8 models do not produce ^{67}Zn and are therefore omitted.

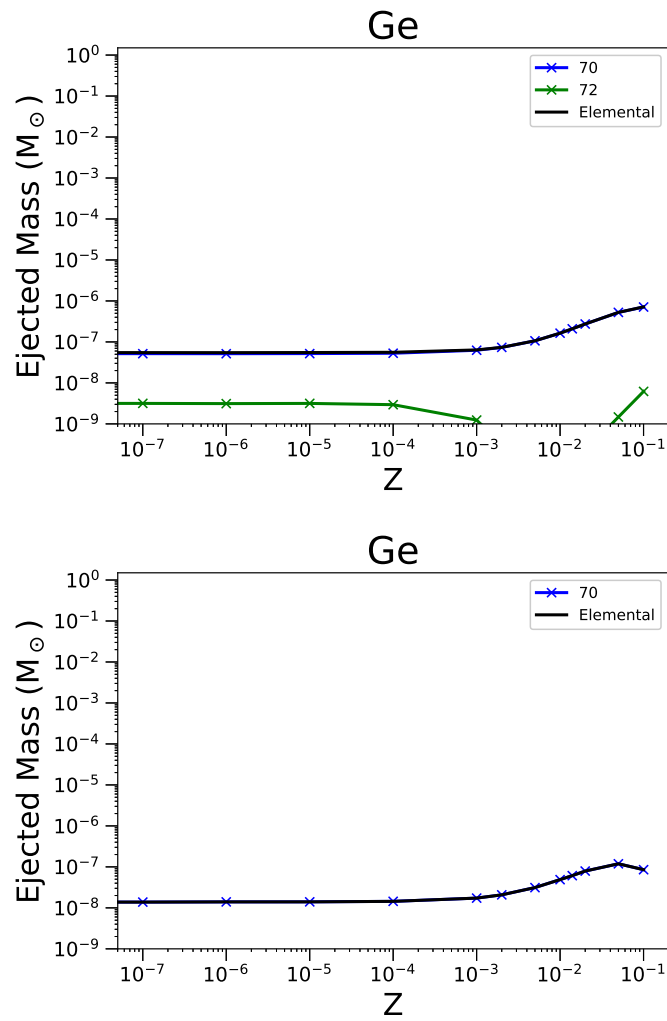


FIGURE 3.85: As in Figure 3.4 but for ejected mass of Ge, and its stable isotopes ^{70}Ge and ^{72}Ge . The M0.8 models do not produce Ge and so that figure has been omitted.

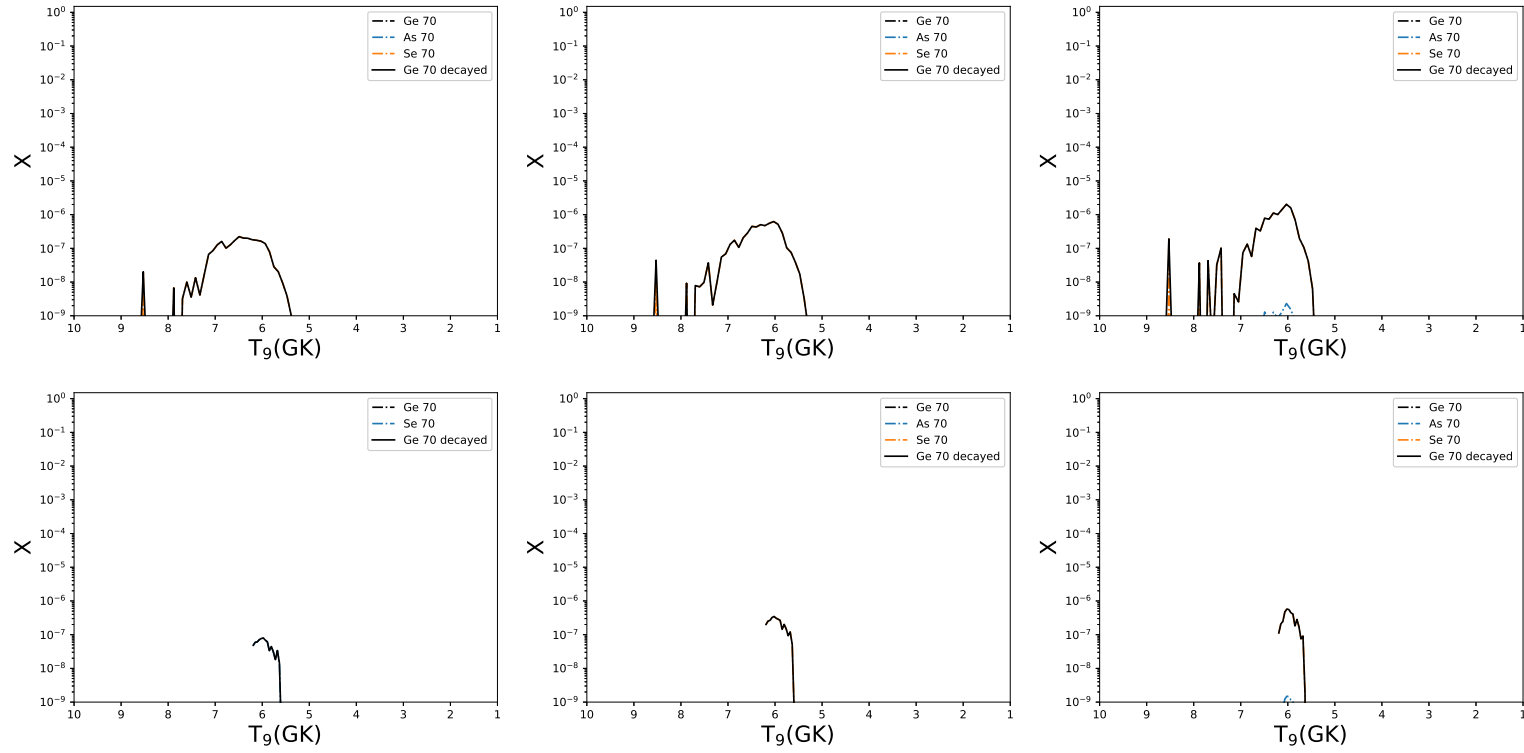


FIGURE 3.86: The abundance distributions of ^{70}Ge are shown, arranged as in figure 3.5. With metallicities of $Z = 0, 0.014$ and 0.1 from left to right, and the three categories of model - T1.4, S1.0 and M0.8 - from top to bottom.

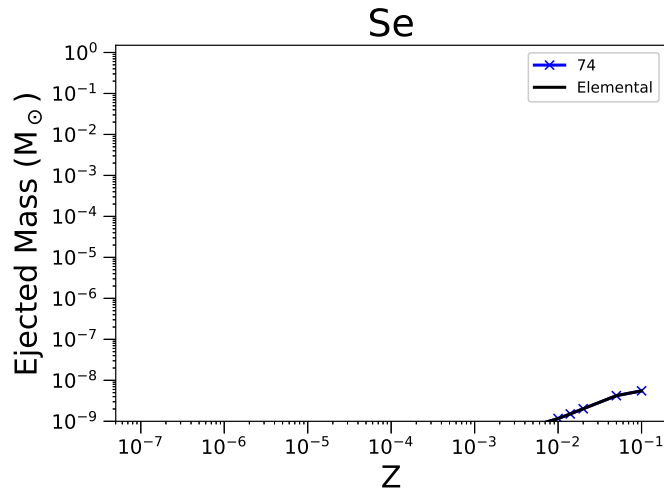


FIGURE 3.87: The ejected mass for the element Se and its stable isotopes is shown for the model set T1.4. The elemental yields take into account the radiogenic contribution. For isotopes, decayed and undecayed abundances are shown (continuous lines with crosses and dot-dashed lines with empty circles, respectively). There is no production in either of the other two categories of model.

In figure 3.86, the production of ^{70}Ge in the T1.4 models is broadly consistent through all metallicities, with a slight increase in production at temperatures close to 6 GK as the initial metallicity increases. We see that production in the S1.0 models is similar, for the peak temperatures it shares with T1.4.

3.2.23 Selenium

Although only produced in trace amounts in high metallicity Chandrasekhar mass models, these models do show an overproduction of ^{74}Se .

As we can see in figure 3.88, production of ^{74}Se is limited in Type Ia SN. It is almost completely absent in sub-Chandrasekhar mass models, and at low metallicities the contribution to the ejecta is negligible. Even in models T1.40.014 and T1.40.01, the abundance of ^{74}Se is small however the increase in production between these models does mean that there is an overproduction of ^{74}Se in Chandrasekhar mass Type IaSN at high initial metallicity.

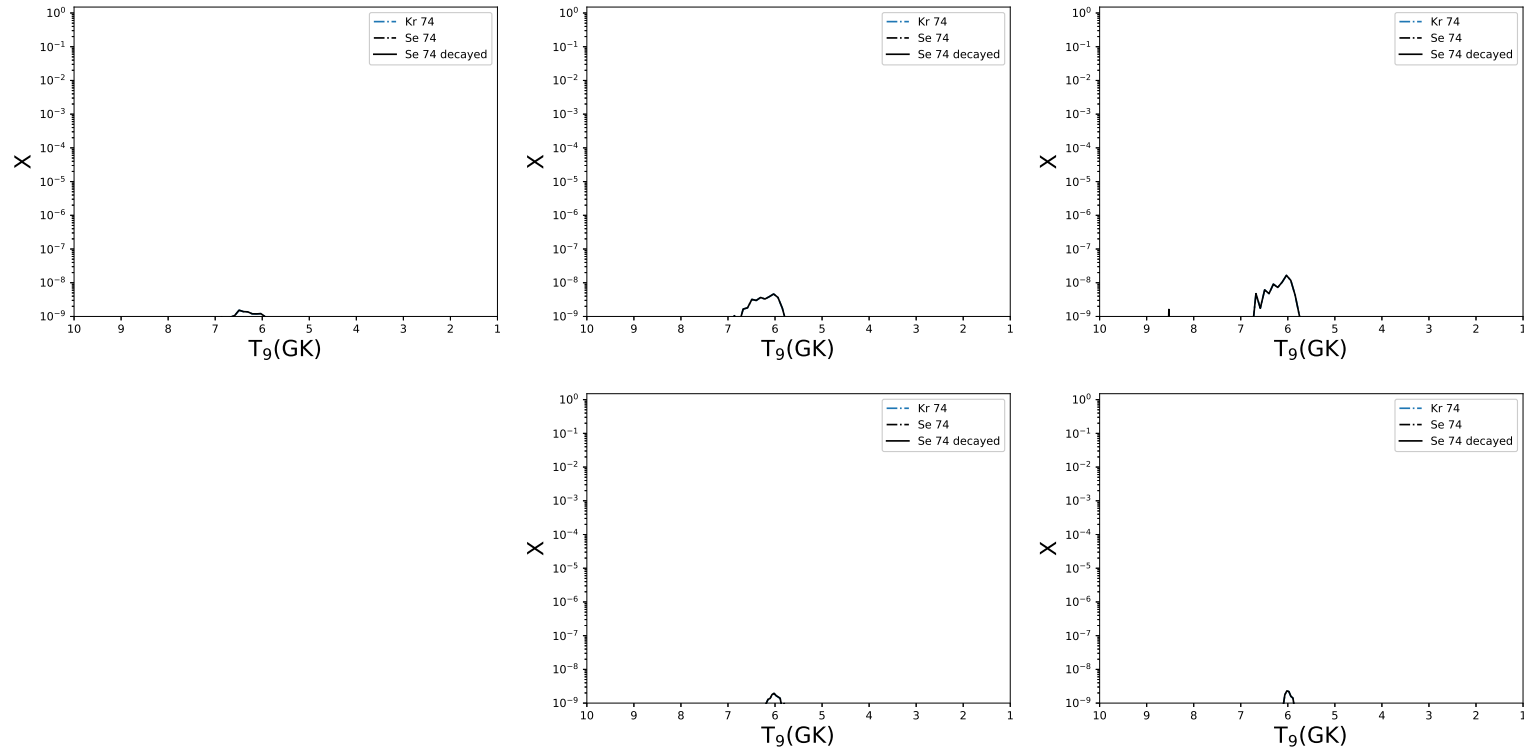


FIGURE 3.88: The abundance distributions of ^{74}Se are shown, arranged as in figure 3.5. With metallicities of $Z = 0, 0.014$ and 0.1 from left to right, and the three categories of model - T1.4, S1.0 and M0.8 - from top to bottom.

3.2.24 All Yields Comparison

Finally, figure 3.89 shows the \log_{10} of the ejected mass of each isotope in each of the three SNIa models. Metallicity is given on the y-axis, with the T1.4, S1.0 and M0.8 models shown in the top, middle and bottom panels respectively. It can be seen that production is broadly consistent between these three classes of model, with α -chain and iron group isotopes contributing the largest fraction of the ejected mass. We also see clearly the effect of initial metallicity in, for example ^{54}Cr and ^{58}Fe . Production of ^{64}Ni is exclusive to the T1.4 model.

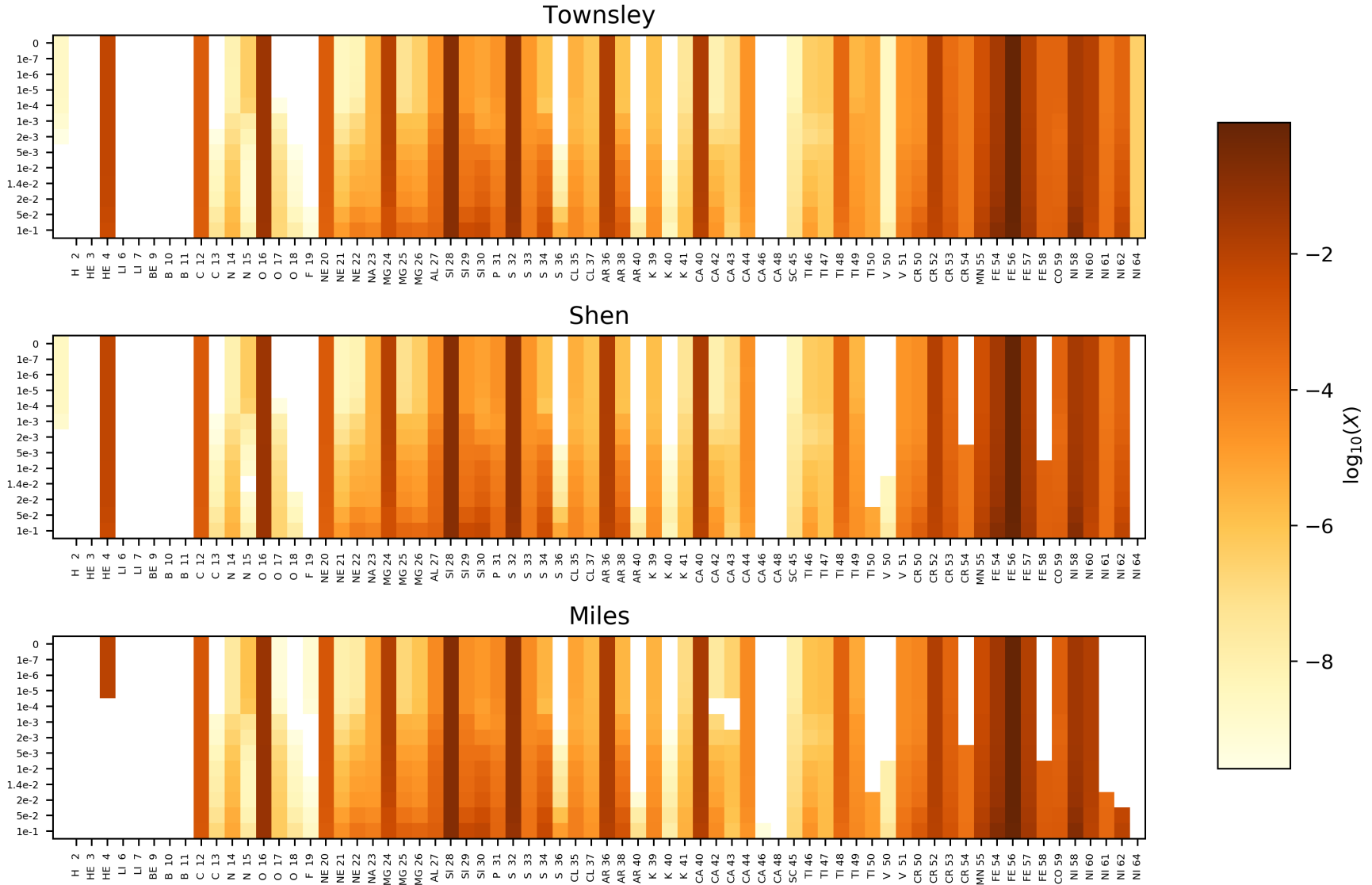


FIGURE 3.89: This plot shows the ejected mass of each stable isotope for all three models, at all metallicities. Stable isotopes with significant metallicity trends are easily identified.

Chapter 4

Literature Yields Comparison

“The pay’s not great, but the work is hard.”

Bernard Black, Black Books

In this section the results of the nucleosynthesis calculations are compared with those of Townsley et al. (2016), Shen et al. (2018) and Miles et al., 2019, in order to verify our results and highlight differences between the nuclear physics setup of our post-processed models and the published results of T1.4, S1.0 and M0.8. Agreement is good between the published works and these models, and we therefore only discuss those abundances which vary by more than a factor of 2. The appropriate metallicity model is used in each case that best matches the benchmark conditions. We then compare these values with other available yields in the literature, namely Nomoto and Leung (2018) and Seitzzahl et al. (2013b) (T1.4), Sim et al. (2010) (S1.0, M0.8) and Gronow et al. (2020) (M0.8).

4.1 Comparison with T1.4Z0.014

In figure 4.1 we compare the T1.4Z0.02 yields of our post-processing work with the results of Townsley et al. (2016). The differences between the post-processed yields and those from Townsley et al., 2016 can be attributed, in

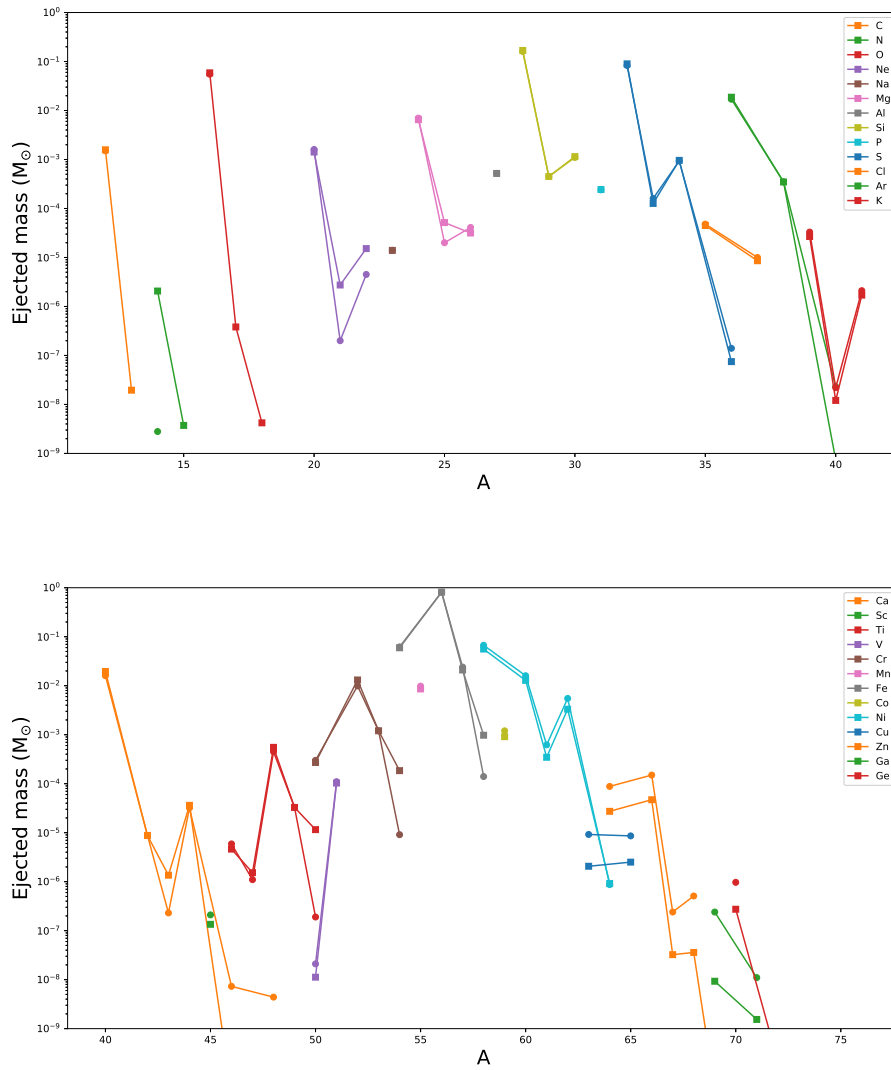


FIGURE 4.1: Decayed isotopic yields from Townsley et al. (2016) are compared with this work (T1.4Z0.02). Townsley et al. (2016) yields are denoted by circle markers.

part, to the different treatment of initial metallicity between the two models. We initialise each tracer particle with a uniform abundance of ^{22}Ne . In the calculations of Townsley et al. (2016), the particles have been post-processed with metals added as scaled solar abundances. CNO material is included in the model as ^{22}Ne . This allows for unburnt seed nuclei in the outer layers to contribute to the overall ejected masses of some heavier isotopes, which are not produced during the SNIa explosion. Comparison with figures (for example) 3.81 and 3.86 show that production of these elements is confined to a peak in the range of peak temperatures 5-9 GK. Regions which reach only 3-4 GK are not hot enough to destroy the initial abundances of these isotopes. The ejected yields therefore become sensitive to the pre-supernova nucleosynthesis, particularly in the outer layers of the WD. Battino et al. (2020) find efficient production of p-nuclei at or above solar abundances. It is unlikely that the true composition of the external layers matches precisely a scaled solar distribution of abundances, or the simplified treatment of a constant mass fraction of ^{22}Ne . Variations in abundances of products from the explosion, however, generally lie within a factor of two, with Cu, Zn, and Ge being a factor of 4-5 under-produced as compared with the published values. Ga is significantly lower due to a slightly increased production in the most abundant iron group isotopes.

Figure 4.2 shows the published elemental yields of Townsley et al. (2016) compared with our post-processed results. Inspection of the isotopic distribution in figure 4.2 shows that production in the post-processed model follows that of the published model closely for a large number of isotopes. The area of significant difference is at the upper end of the iron group, where production in the published model is larger by an order of magnitude for isotopes of Cu, Zn, and Ga. Other contributing factors include the choice of reaction rate libraries, which is particularly impactful in the lower temperature region as rates are not in equilibrium here.

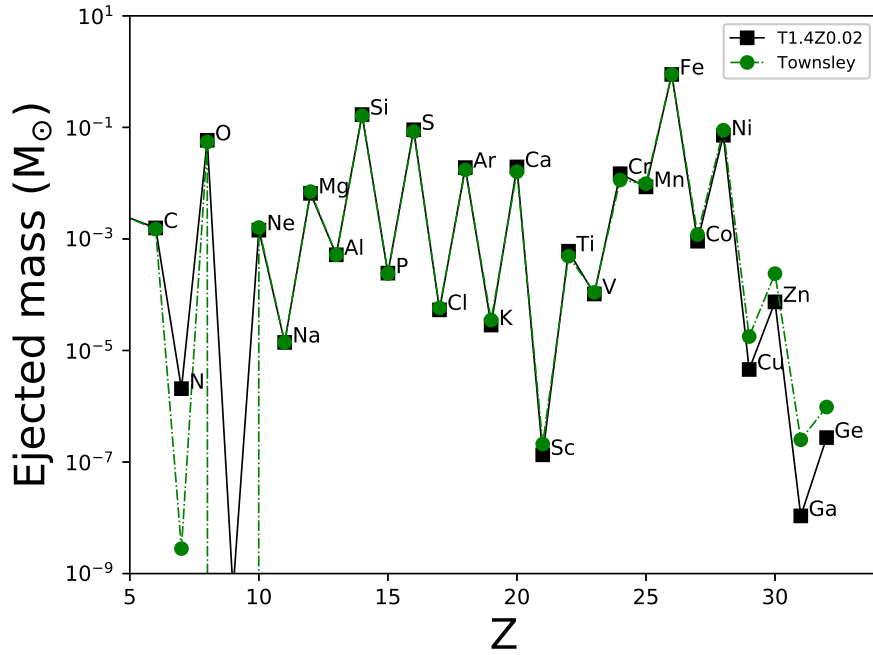


FIGURE 4.2: Published elemental yields of Townsley et al. (2016) (square markers) are compared with T1.4Z0.02 (green circles).

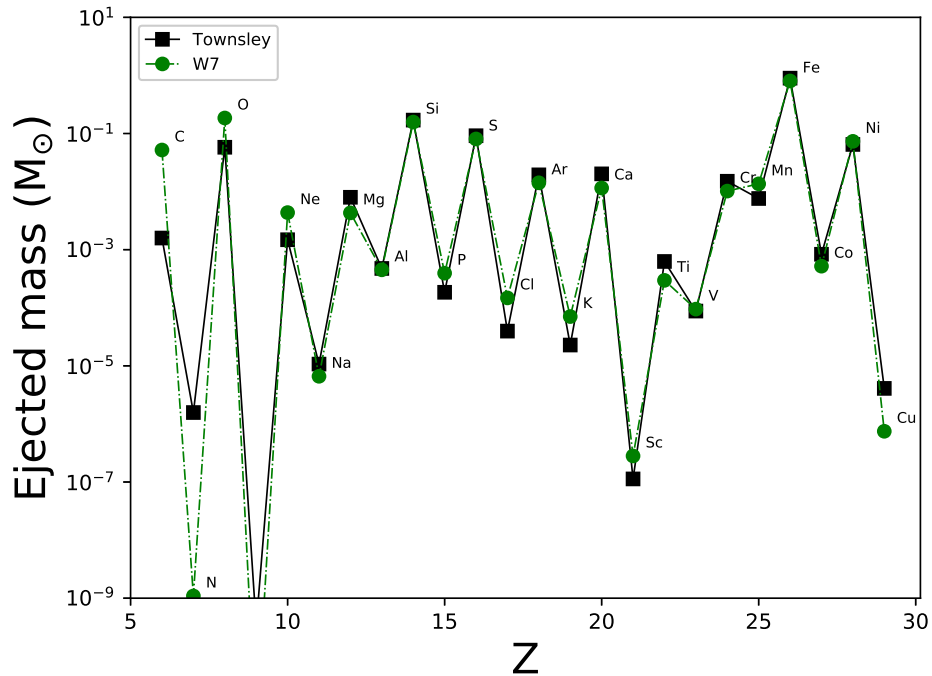


FIGURE 4.3: W7 decayed elemental abundances from Nomoto and Leung (2018) represented by the green line with circle markers, compared with T1.4Z0.014 (black line, square markers).

The elemental abundances of T1.4Z0.02 are presented in figure 4.3 compared with the results of the W7 models of Nomoto and Leung (2018), which used the same 1D structure of the original W7 model with improved nuclear physics. While there are some differences in the ejected masses of Cu, Mn, Ti and the intermediate mass elements K, Cl, and P, we see that they are generally in good agreement, with ejected decayed abundances within a factor of a few compared to the results of the T1.4Z0.014 model. For the most abundant isotopes, e.g. ^{28}Si , ^{32}S , ^{56}Fe etc. the agreement is very good. There is, however, a systematic under-production of the intermediate mass, odd Z elements, as compared with the W7 model. We also see that W7 over-produces Mn as compared with our post-processed results, by a factor of 2, as well as a slightly reduced abundance of Fe leading to a larger [Mn/Fe]. The treatment of the metallicity component of SNIa is the same in the Nomoto and Leung (2018) case as we have implemented, i.e. the inclusion of a mass fraction of ^{22}Ne in place of scaled solar abundances. We have compared models with the same initial metallicity, using the solar metallicity abundances from this work.

Nomoto and Leung (2018) identify the relative insensitivity of the Chandrasekhar mass SNIa yields to initial metallicity, due to the synthesis of neutron rich isotopes in the hot NSE region. The sensitivity of the outer layers of the WD on the initial metallicity is important, however, as we see a significant metallicity dependence in the intermediate mass elemental yields as discussed at length in chapter 3.

Figure 4.4 shows the same comparison between T1.4Z0.014 and Seitenzahl et al. (2013b). Our post-processed [Mn/Fe] ratio is much closer to the value reported in Seitenzahl et al. (2013b). We see here again the underproduction of P, Cl, and K as compared with the reference models, along with an overproduction of Cu of a factor of approximately 5, and Zn of over an order of magnitude.

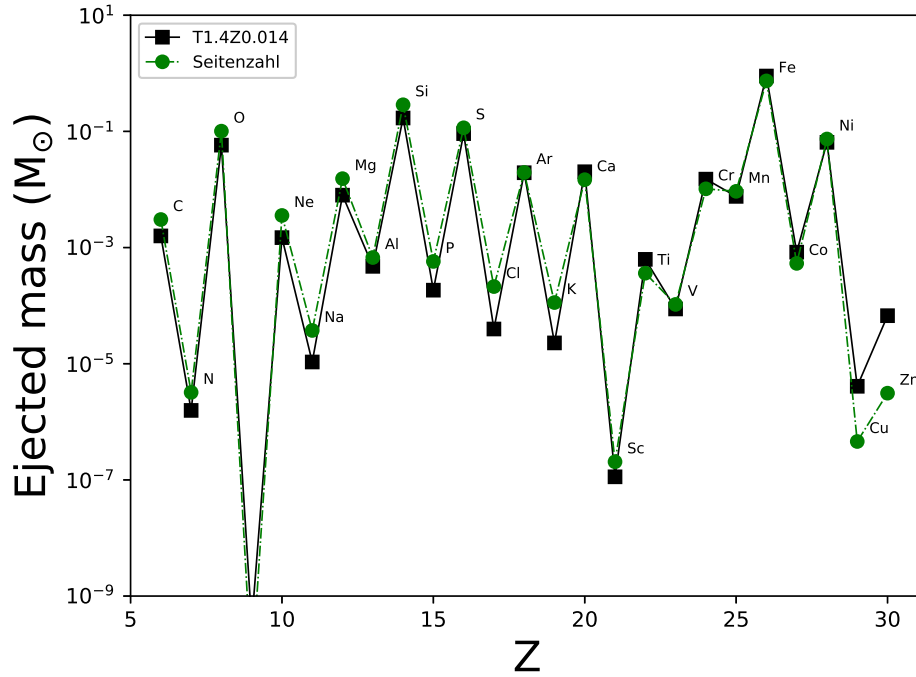


FIGURE 4.4: Seitenzahl et al. (2013b) ejected elemental abundances (green circles) compared with T1.4Z0.014 (black squares).

Note that neither W7 nor Seitenzahl et al. (2013b) produces the trace abundances of Ga and Ge reported in Townsley et al. (2016). The network of Seitenzahl et al. (2013b) contains 384 isotopes, and so is at least as complete as the Townsley et al. (2016) network. This discrepancy is therefore a consequence of the hydrodynamical modeling or the nuclear physics inputs. Zn has a significant ejected mass and is produced in non-negligible amounts; however, Ga is over 2 orders of magnitude less abundant than Zn, and is unlikely to have a large effect on the abundances of the iron group through leakage of material above the networks in W7 and Seitenzahl et al. (2013b).

The [Cr/Mn] ratio for our post-processed models is closer to the value of Seitenzahl et al. (2013b) than to that of the W7 results. Without further study, it is not possible to conclude whether this is due to the hydrodynamical modeling or the differences in reaction networks. More complete burning

throughout the T1.4Z0.014 model is indicated by the significantly reduced abundances of C and O.

4.2 Comparison with S1.0Z0.014

Figures 4.5 and 4.6 show the isotopic distribution of the $Z = 0.014$ metallicity run S1.0Z0.014 compared with the literature value published in Shen et al. (2018). While there are differences in the isotopic abundances shown in figure 4.5 - ^{21}Ne is under-produced by three orders of magnitude compared with the Townsley et al. (2016) model, ^{24}Mg by a factor of 5 and Cu and Zn isotopes by a factor of 2-3 - we see that the fit to all other isotopes is very close. The comparison of elemental yields is also good, as seen in figure 4.6. As SNIa are not significant contributors to the GCE of Cu or Zn, the impact of these differences is negligible.

The mass grid for the models of Sim et al. (2010) is much finer than that of our current study. Initial WD masses of 1.15, 1.06, 0.97 and 0.88 are provided, with an initial composition of pure C/O, as well as a C/O/Ne model for the $1.06M_{\odot}$. Our closest model in this investigation is S1.0, with a total integrated mass of $1 M_{\odot}$, which we will compare with the $0.97 M_{\odot}$ of Sim et al., 2010.

Comparing the post-processed S1.0Z0 data with that of the Sim et al. (2010) $0.97M_{\odot}$ model (figure 4.7), we see there are some significant differences in the abundances of some elements. The ejected masses of Si, S, Cl, Ar, K, Ca, Sc, Ti, V, Cr, Mn and Fe are within a factor of 2 for these two runs, Fe being the most abundant ejected element. Ne, Na, Mg and Al are within a factor of 5 whilst Co, Ni, Cu and Zn differ by more than a factor of 10. Many of the iron group elements are under-produced in the Sim et al. (2010) models as compared with S1.0Z0.1. Data for the detailed nucleosynthetic yields of the Sim models was taken from the HESMA archive. The difference in the ejecta may be due to a number of parameters - the nuclear network or

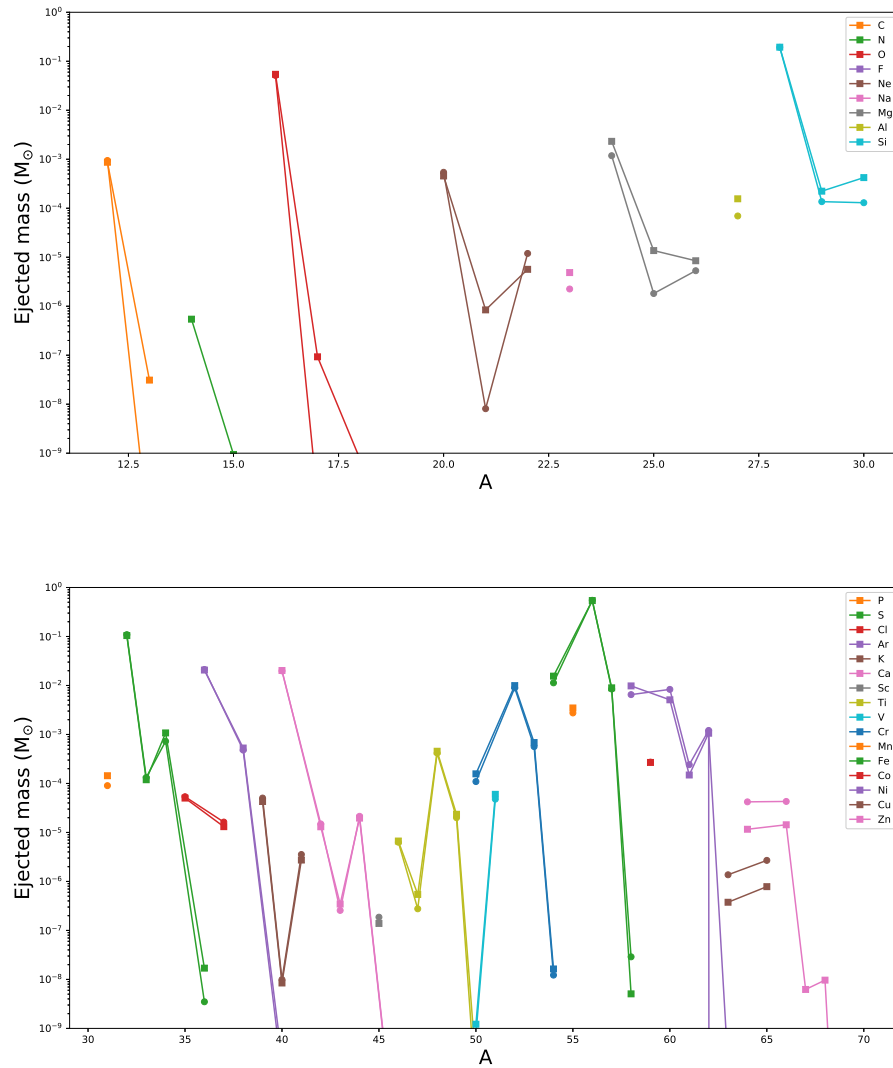


FIGURE 4.5: Isotopic yields for models S1.0Z0.014 and Shen et al., 2018 (published and post-processed yields). Published yields are denoted by circle markers, the S1.0Z0.014 by square markers.

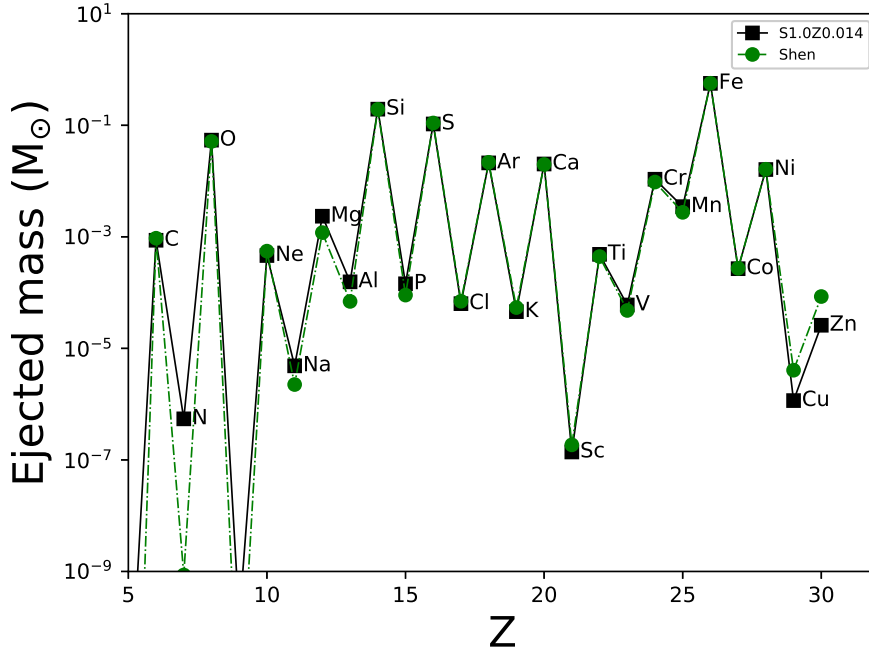


FIGURE 4.6: (Shen et al., 2018) yields (black squares) compared with S1.0Z0.014 (green circles). Decayed ejected elemental abundances are shown for both models.

the treatment of the explosion, to name two. It is not the goal of this present work to identify all of the possible causes of differences between these models, however - only to highlight that significant variation is present in the ejected masses of these elements.

The models of Sim et al. (2010) are axisymmetric, one-dimensional (due to the initial spherical symmetry being preserved throughout the explosion) pure detonation models with central detonations.

Further comparison for the 1.0 M_{\odot} against model Leung and Nomoto (2020) 1.05 M_{\odot} SNIa are shown in figure 4.8. This model more closely resembles S1.0Z0.014, being a double detonation. C, N, O, F, Si, S, Ar, V, Cr, Fe and Co are all within a factor of 2 between the two models. The iron group distribution matches more closely, although the production of Mn and V in the Shen et al. (2018) post-processed model is decreased by a factor of around 10. The detonation mechanism therefore significantly influences the distribution

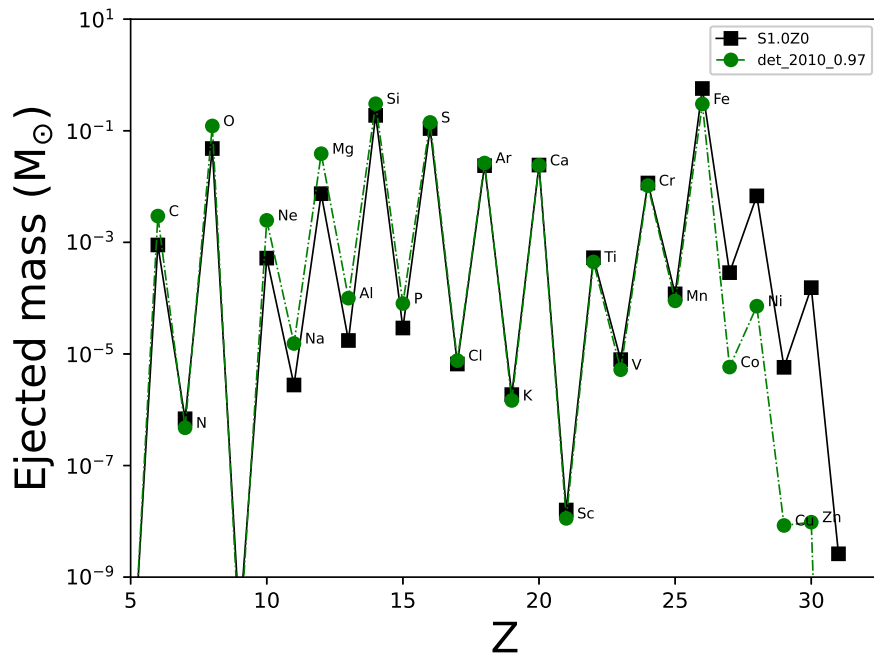


FIGURE 4.7: Yields S1.0Z0 (black squares) compared with the $0.97 M_{\odot}$ (green circles) model of Sim et al. (2010).

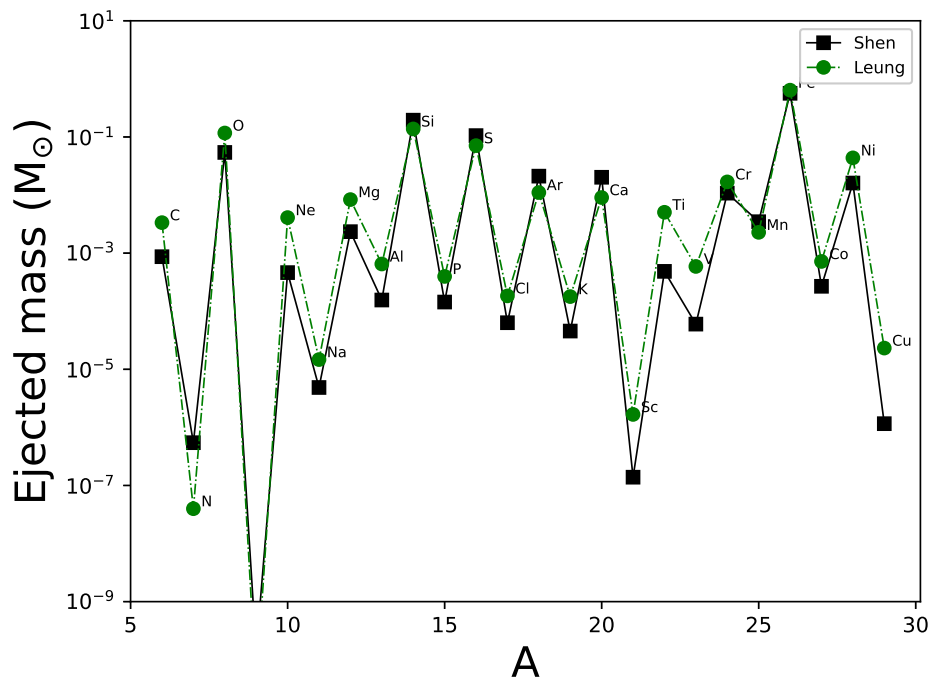


FIGURE 4.8: Shen ejected elemental abundances compared with Leung and Nomoto (2020)

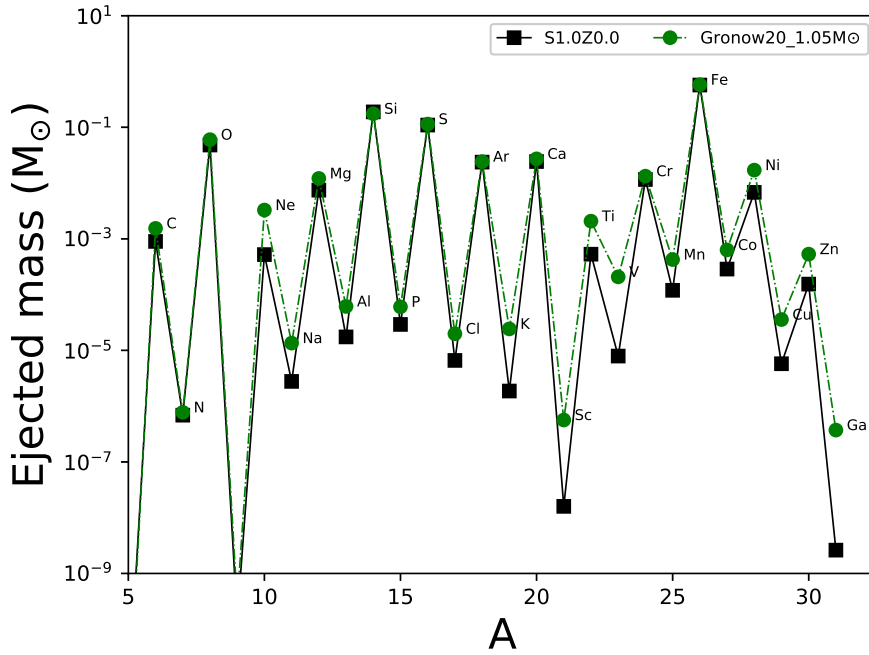


FIGURE 4.9: S1.0Z0.0 ejected elemental abundances compared with Gronow et al. (2020) data.

and ejected yields of the SNIa explosion, both in the iron group region and the intermediate mass elements.

Comparison (Gronow et al., 2020) in figure 4.9 shows good agreement between the S1.0Z0 model and the selected $1.05 M_{\odot}$ model. While there are some differences in the heavier regions of the iron group and in vanadium, the trends match closely.

We also compare with the work of Leung and Nomoto (2020), using their benchmark model. Significant differences in the abundances of Ti and V are observed, with this post-processed work being a factor of 5 under-produced compared to Leung and Nomoto (2020). A factor of 2 overproduction of the much more abundant Ca accounts for many of the differences. We again see higher production of even Z intermediate mass elements, and a reduction in the ejected mass of odd Z intermediate mass elements as compared with Leung and Nomoto (2020).

4.3 M0.8 Comparison

The work of Miles et al. (2019) consists of a white dwarf of $0.8 M_{\odot}$ with a central density of $1.05 \times 10^7 \text{ g cm}^{-3}$, also centrally detonated. Figures 4.10 and 4.11 show the isotopic and elemental ejected yields of the M0.8Z0.014 model compared with the results of Miles et al. (2019). 4.10 shows that there is good agreement between the two models, with discrepancies generally less than a factor of two. The only exceptions to this are for ^{21}Ne and ^{25}Mg in the intermediate mass range, and ^{58}Fe , ^{59}Co and the neutron-rich nickel isotopes, where we see a drop in production, as well as in Cu and Zn which are not produced in the M0.8Z0.014 yields. The reduction in more neutron-rich products is a result of the weak interaction rates used where as the discrepancy in the production of the heavier nickel isotopes is likely due to unburnt nickel in this low mass model. Figure 4.11 shows the good agreement with Miles et al. (2019), in all but the highest Z elements.

Comparison with the results of Sim et al. (2010) reveals more complete burning in the M0.8Z0.014 model. The slight reduction in the abundance of C and O results in some non-negligible differences in the intermediate and iron-group regions; however, the yields are similar to within a factor of 3 in all circumstances.

Our $0.8 M_{\odot}$ is predicted to be undetectable observationally due to the small mass of ^{56}Ni produced. Sim et al. (2010) show that their lowest mass progenitor is the limit of observable production of ^{56}Ni - ejecting a total mass of $0.07 M_{\odot}$. Their $0.81 M_{\odot}$ model, ejecting a total of $0.01 M_{\odot}$ of ^{56}Ni , is not described in their paper due to the absence of a possible observational counterpart. Our $0.8 M_{\odot}$ at zero metallicity produces $0.048 M_{\odot}$ of ^{56}Ni , close to the observable limit of the $0.88 M_{\odot}$ model.

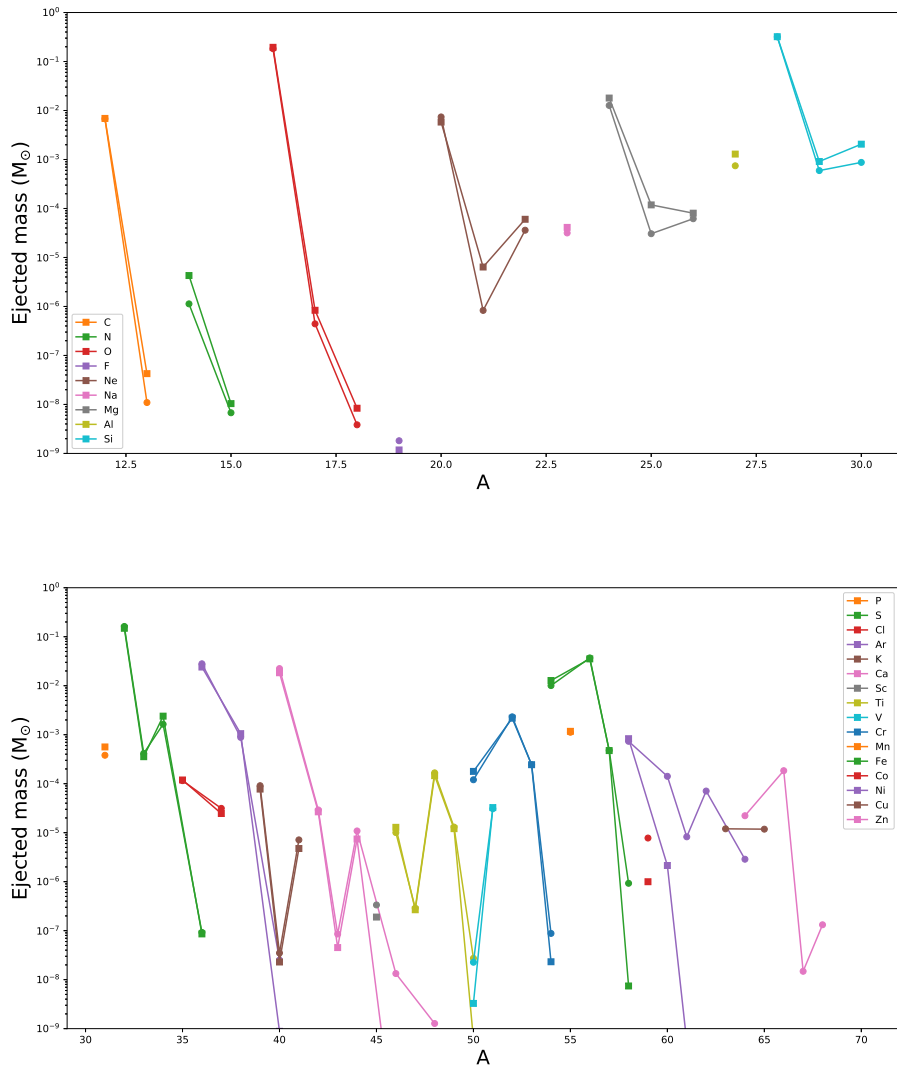


FIGURE 4.10: Isotopic abundances of Miles et al. (2019) (circle markers) compared with post-processed model M0.8Z0.014 (squares).

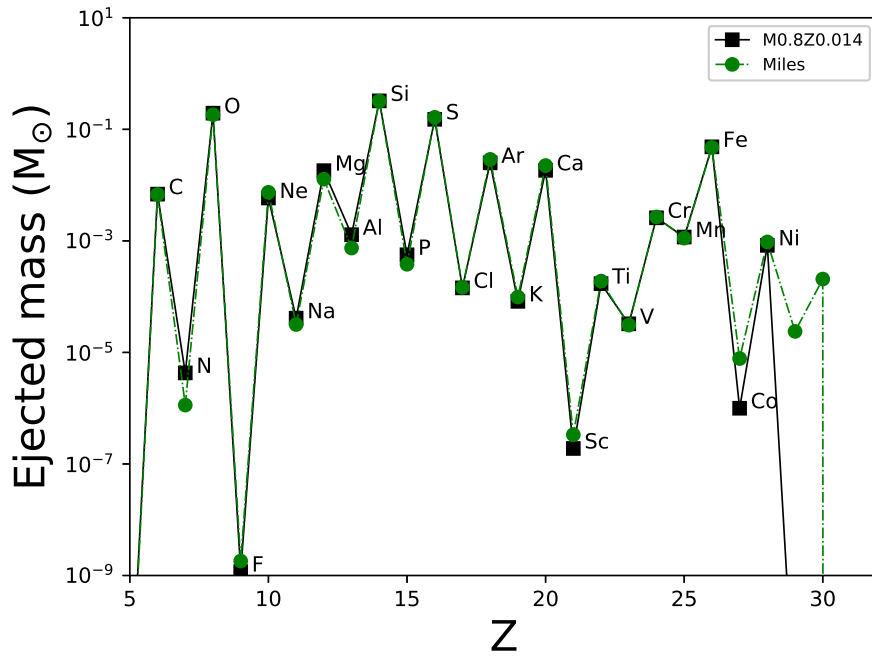


FIGURE 4.11: M0.8 ejected elemental abundances compared with this post-processing work.

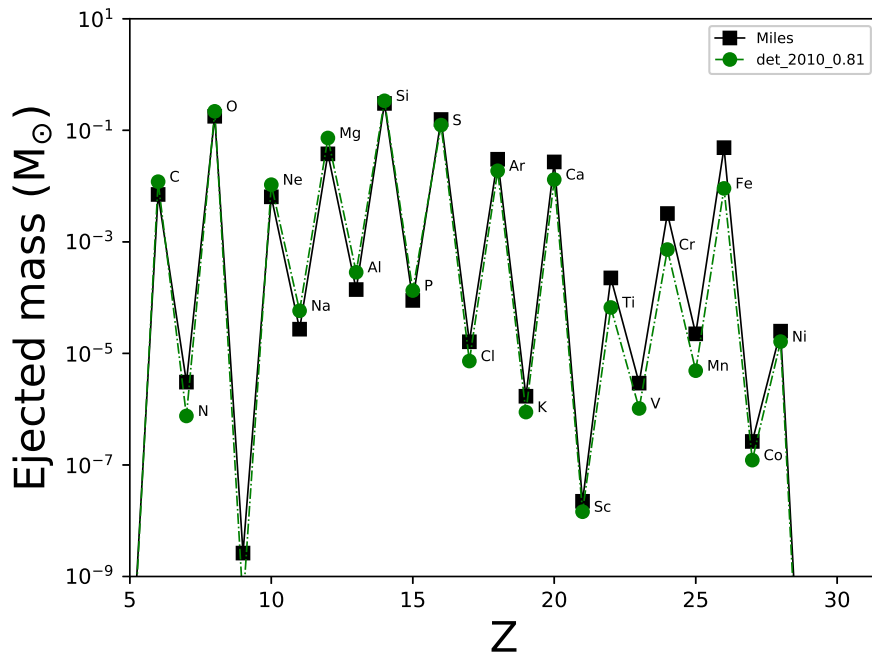


FIGURE 4.12: Our post-processed ejected elemental masses for model M0.8Z0 compared with the 0.81 M_{\odot} model of Sim et al. (2010). Both models have an initial ^{22}Ne mass fraction of 0.

4.4 Summary

This chapter has served two main purposes - firstly, it verifies the results of this post processing against the published yields of the parent models. In this way it has been shown that the results are consistent with those models, with some key differences arising from the choice of nuclear reaction network and initial abundances. This informs future investigations into the nuclear physics uncertainties of SNIa. Secondly, it gives a reference for the position of these yields as measured against the wider literature. Again we see that these models follow closely the yields of other groups, speaking to the relative insensitivity of SNIa yields to hydrodynamical modeling parameters (although clearly there are some effects which differentiate these models). Another outcome of this chapter is to highlight the degeneracy seen in the elemental abundances of different models, and the need for, if at all practical, isotopic tracers of SNIa progenitor parameters.

Chapter 5

Diagnostics of SNIa

Nucleosynthesis

"It's the only bang you're ever gonna get, sweetheart!"

Bernadette, *The Adventures of Priscilla, Queen of the Desert*

5.1 Elemental and Isotopic Ratios

The relative production of elements and isotopes allows us to probe the relative contributions from different burning sites within the ejecta of SNIa explosions. In this section, we discuss a list of the elemental and isotopic ratios for the T1.4, S1.0 and M0.8 models which show the most significant difference in production. These abundance ratios may be used as diagnostics to assess the relative contributions of different SNIa progenitors to the solar abundances, in those cases where the relative GCE contribution of SNIa are relevant compared to other stellar sources. In particular, the comparison with solar abundances of isotopic yields is crucial, and the determination of the proportion of that solar material which originates from SNIa is also necessary to constrain these results.

We also discuss isotopic ratios relevant to pre-solar grain investigations (e.g. Zinner, 2014). These data are collected through mass spectrometry of presolar grains recovered from meteorites as described in chapter 1. Although presently there is no specific type of presolar grain unambiguously identified as being produced in SNIa, it cannot be excluded that some grains may have condensed in SNIa ejecta. In order to do this, the same isotopic plots as above were made for Si, S, Ca, Ti, Cr, Fe and Ni. A selection of these plots is presented in this chapter.

This next section presents the results for elemental ratios, focusing on the analysis of elements which are efficiently produced in a SNIa explosion and which have a measurable impact on GCE.

5.1.1 Three-Element Plots

In figure 5.1, the elemental ratio of S/Fe is shown vs Si/Fe for the T1.4, S1.0 and M0.8 models in blue, orange and green respectively, along with the results of Seitenzahl et al. (2013b) and Sim et al. (2010). The Seitenzahl et al. (2013b) models have been chosen as they closely match the physics of the T1.4 models, the same is true of the Sim et al. (2010) and the S1.0 models. We do not show all of the models from these publications, only those with initial metallicity comparable with the work presented here.

In figure 5.1 we see a strong inverse correlation between the progenitor mass and the production of S and Si in SNIa explosions. This is due to the less complete burning experienced in lower mass models, where a large proportion of the final products of the explosion are in the intermediate mass element range. We see a strong dependency on the metallicity of the progenitor, especially at super-solar metallicities.

The [S/Fe] and [Si/Fe] ratios both show a factor of 3 difference between

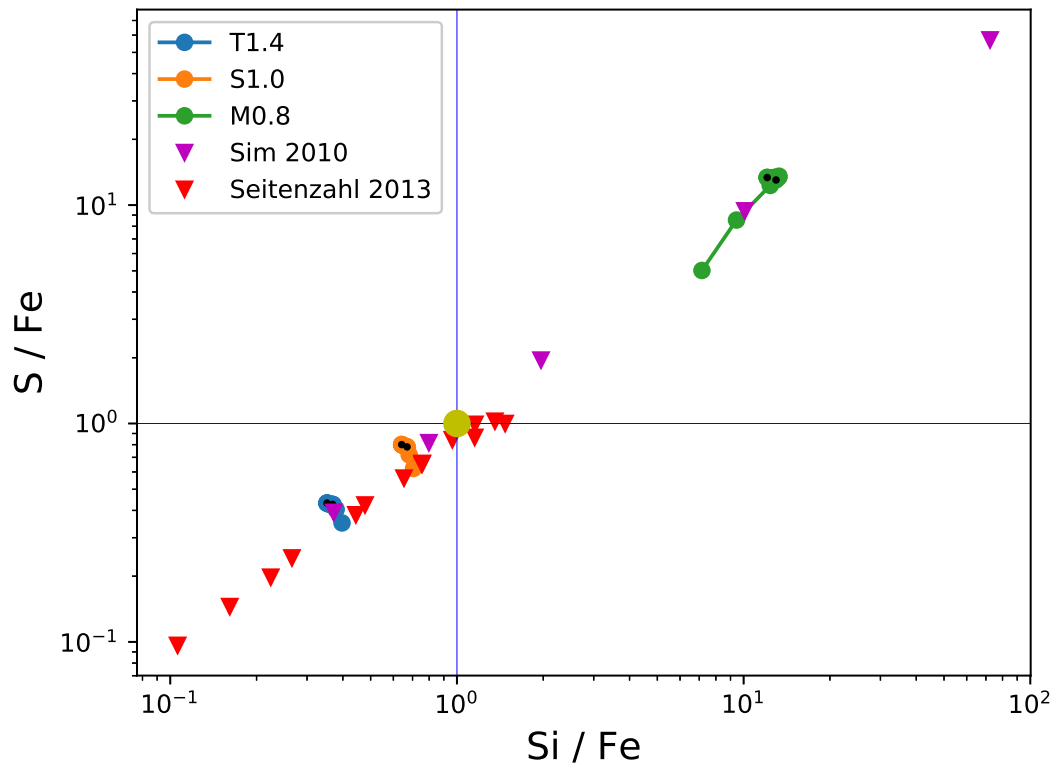


FIGURE 5.1: Elemental ratio plot $[\text{Si}/\text{Fe}]$ and $[\text{S}/\text{Fe}]$. The blue circle line corresponds to the T1.4 model, the orange to the S1.0 and the green to the M0.8. Black circles on the datapoints indicated the position of the $Z = 0$ and $Z = 0.014$ to show the metallicity trends within a model. For comparison, the models of Sim et al. (2010) (purple triangles) and Seitenzahl et al. (2013b) (red triangles). Ratios are shown normalised to the solar values, shown by the large yellow circle.

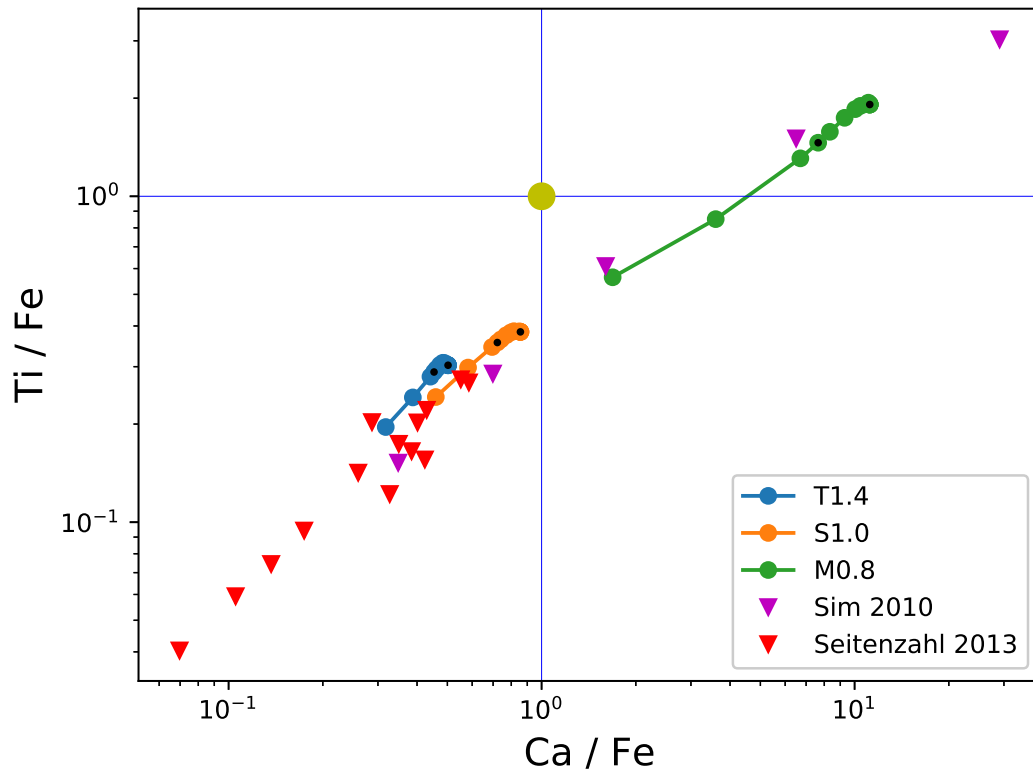


FIGURE 5.2: As figure 5.1, but for the ratios $[\text{Ti}/\text{Fe}]$ and $[\text{Ca}/\text{Fe}]$.

the T1.4 and S1.0 models, with a very low scatter in the values across metallicities. This is due to the production of Fe being confined to the high density, high temperature inner regions of these models, ensuring that the effect of the initial composition of the WD is diminished due to the electron capture rates in these dense regions. S and Si are also insensitive to the initial metallicity in these models, as they are produced in the explosive Si-burning like region which enters NSE. In the lower mass M0.8 model, these extreme conditions are not encountered and, not only does the ratio $[\text{Si}/\text{Fe}]$ increase dramatically because of the smaller iron producing region as a proportion of the total model, the scatter is larger due to the cooler and less dense burning conditions.

This metallicity dependence is more pronounced in the Ca/Fe ratio shown in 5.2. Here we do not see a clear distinction between the T1.4 and S1.0 models, although there is some separation in $[\text{Ca}/\text{Fe}]$ and to a lesser extent

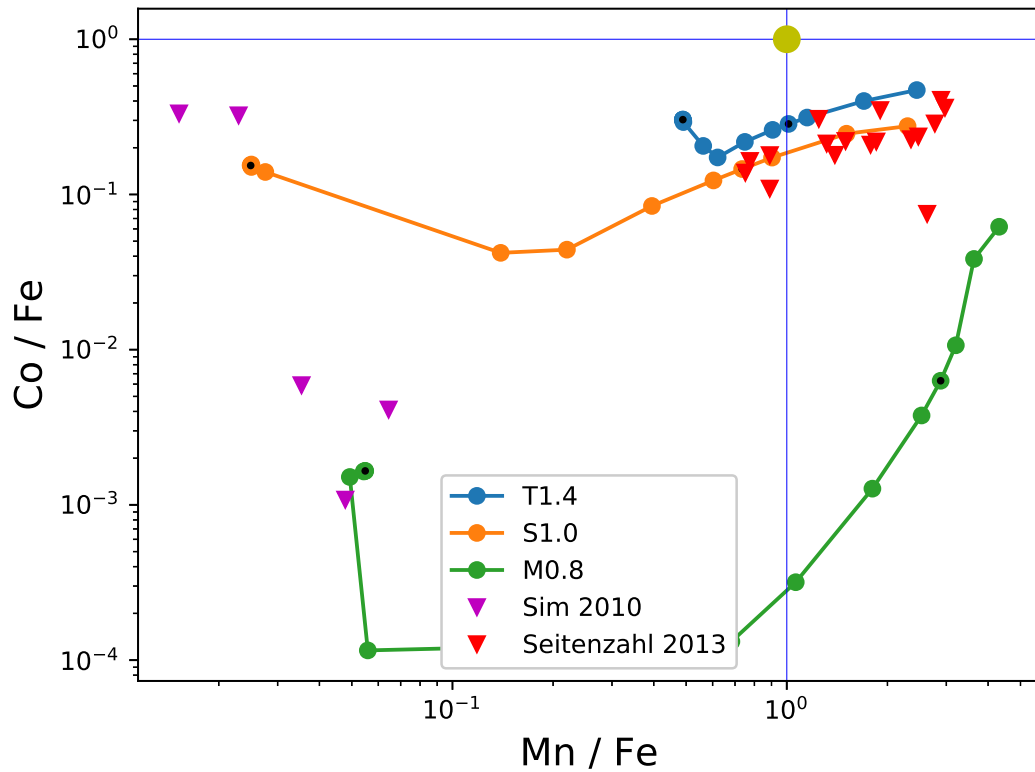


FIGURE 5.3: As figure 5.1, but for the ratios $[\text{Mn}/\text{Fe}]$ and $[\text{Co}/\text{Fe}]$.

$[\text{Ti}/\text{Fe}]$ in the $Z > Z_{\odot}$ models. The relatively shallow metallicity dependence observed for elemental Ca in chapter 3 for models T1.4 and S1.0 result in a factor of 4 spread in the Ca/Fe ratio, almost all of which occurs at super-solar metallicities. M0.8 shows a stronger metallicity dependence in its calcium yields, and therefore has a larger spread of a factor of around 8. The Ca/Fe and Ti/Fe elemental ratios are not sufficient to distinguish models of $1 M_{\odot}$ and Chandrasekhar mass models, even with a strong constraint on the metallicity.

Figure 5.3 shows the three element plots for Mn/Fe and Co/Fe. We see that there is a large spread in Mn/Fe for the $Z = 0$ case, with nearly an order of magnitude between the T1.4 Z_0 and M0.8 Z_0 models, and more for the S1.0 Z_0 . This is consistent with the work of e.g. Seitzzahl et al. (2013a), Eitner et al. (2020), Kobayashi, Leung, and Nomoto (2020). When the initial metallicity is increased, we see that the Mn/Fe ratio changes significantly. This is due

to the strong secondary production of ^{55}Mn in the oxygen burning region of the SNIa ejecta, which leads to a strong metallicity dependence in all classes of model, but particularly in the lower mass models, as these do not contain the ^{55}Mn rich inner layers of the T1.4 set. As shown in chapter 3, there is an increase in the S1.0 and M0.8 models of over 2 orders of magnitude, starting at $Z = 0.0001$. This leads to the three classes of model having similar Mn/Fe ratios at solar metallicities, with the S1.0Z0.014 model being around a factor of 2 lower and the M0.8Z0.014 model being a factor of 3 higher. Initial composition is therefore key in determining the Mn/Fe ratio of a given SNIa explosion and its possible progenitor. Ejected masses of ^{55}Mn for the three models at solar metallicity are: $7.61 \times 10^{-3} M_{\odot}$ for T1.4Z0.014, $3.48 \times 10^{-3} M_{\odot}$ for S1.0Z0.014 and $1.17 \times 10^{-3} M_{\odot}$ for M0.8Z0.014, and so the absolute yield of Chandrasekhar mass models is larger in all cases, however the Mn/Fe ratio may differ depending on initial metallicity.

Elemental ratios for the three models are generally within an order of magnitude of the solar value. Significantly larger shifts are observed in the isotopic ratio plots.

5.1.2 Isotopic Plots

In this section we present a selection from the 100 largest production factor ratio shifts between our models T1.4Z0.014 and S1.0Z0.014. These two models were selected as the T1.4 is the example of a Chandrasekhar mass model investigated in this work, and the S1.0 model as it has a larger production of the iron group isotopes. We use the models at solar metallicity, as the ejected abundances for most isotopes do not vary significantly below this value, and super-solar metallicity progenitor systems are expected to be less numerous.

The production factor ratio shift is calculated by first producing all possible combinations of X_i/X_j vs Y_k/Y_l for unique i, j, k and l , where X_i is the production factor of isotope i . This is done for both T1.4Z0.014 and S1.0Z0.014, after which the difference in production factors is found between models. We find the shift between each pair of unique 4-isotope ratios, r , where r is given by the equation:

$$r = (\Delta X^2 + \Delta Y^2)^{1/2}$$

where ΔX and ΔY are the shift in the value of X_i/X_j or Y_k/Y_l between the T1.4Z0.014 or S0.014 models and the solar X_i/X_j .

We select for the maximum shift to identify those isotopes most sensitive to the changing model parameters. A selection of 5 isotopic ratios are shown in table 5.1. These are the those isotopes with a significant GCE contribution from SNIa and the largest shift between the T1.4 and S1.0 models.

TABLE 5.1: Table showing largest isotopic ratio shifts with pros and cons of each.

Ratio	Strengths	Limitations
$^{44}\text{Ca} / ^{40}\text{Ca}$	No strong reliance on metallicity	Small dynamic range
$^{50}\text{Ti} / ^{48}\text{Ti}$	Large difference between models at all metallicities; T1.4 close to solar	Strong dep. on metallicity in S1.0, M0.8
$^{54}\text{Cr} / ^{52}\text{Cr}$	Large difference between models at all metallicities; T1.4 close to solar	Strong dep. on metallicity in S1.0, M0.8
$^{58}\text{Fe} / ^{56}\text{Fe}$	Large difference between models at all metallicities; T1.4 close to solar	Strong dep. on metallicity in S1.0, M0.8
$^{64}\text{Ni} / ^{58}\text{Ni}$	Large difference between models at all metallicities	Low abundances

This is only a small number of the combinations investigated. Reduction of the parameter space through eliminating those isotopes without large solar contributions from SNIa increases the predictive power of this technique.

This has been achieved by selecting only those isotopes which are produced above a threshold value in all models ($10^{-9} M_{\odot}$ ejected) and excluding isotopes known to have little to no contribution from SNIa events (C,N,O material excluding e.g. ^{16}O , ^{19}F , ^{40}Ar).

From these plots, we can identify three main criteria for the presence of a ‘good’ diagnostic tool for the progenitors of SNIa:

1. Significant production in the high density, high temperature region of the T1.4 model set.
2. A large absolute production of that isotope
3. Low production in the intermediate peak temperature region in the S1.0 and M0.8 models

We exclude C, N and O isotopes (other than ^{16}O) from our analysis as the contribution from SNIa to the abundances of these isotopes is known to be small (Woosley, Heger, and Weaver, 2002). ^{16}O is included as a tracer for unburnt regions of the star. We also exclude elements with $Z < 6$ and $Z > 33$, as these are the limits of production in the SNIa explosions as seen in chapter 3. In addition to this, we use an algorithmic approach to select those isotopes which cause the largest shift between the T1.4Z0.014 and S1.0Z0.014 values, by taking the logarithmic difference from the solar value (i.e. the largest shift in production factor between these two models normalised to solar).

We note, due to the large shift in isotopic ratios for many of these models, particularly in the S1.0 and M0.8 sets, a more careful implementation of the initial metallicity is likely to be needed to capture the detailed nucleosynthesis in these events. It is encouraging, however, to observe that many of the potential isotopic shifts distinguishing the models are insensitive to the initial metallicity conditions. Whilst the scatter in data is large, the data from various models often does not overlap in any way.

We compare our results with models from Sim et al. (2010) at $Z = 0$ and Seitzzahl et al. (2013b) at $Z = Z_{\odot}$.

5.1.3 Local Isotopic Ratios

In isotopic presolar grain analysis, isotopic ratios are a key tool in determining the properties of the stars which formed the grains. Unlike isotopic abundances across different elements, the chemistry of the isotopes is the same, and chemical fractionation is not relevant. This simplifies analysis and removes potential sources of uncertainty.

Certain elements are more appropriate for isotopic grain analysis because of chemical properties. To this end, we have selected a number of elements where data are available from isotopic grain analysis. These are: Si, S, Ca, Ti, Cr, Ni and Fe. These have also been selected because of their large abundances in SNIa ejecta. We look here at the isotopic abundance ratios for these 7 elements, normalising to the most abundant isotope for each. Currently, there are no grains unambiguously identified as originating in SNIa ejecta. Also, due to the formation mechanism of presolar grains, it is not clear if they are able to form directly from the ejecta or if mixing with other material may occur before they condense.

In figure 5.4 the three-isotope plot of Si isotopes is shown. The models are practically indistinguishable for these isotopes; however, the strong metallicity dependence of these ratios may provide a reference for determining the initial composition of the progenitor, especially given the strong dependence in both $^{29}\text{Si}/^{28}\text{Si}$ and $^{30}\text{Si}/^{28}\text{Si}$.

Figure 5.5 shows the local isotopic ratio for $^{34}\text{S}/^{32}\text{Si}$ vs $^{33}\text{Si}/^{32}\text{Si}$. We see that this presents a poor diagnostic as the ratios across all metallicities are very close, particularly between T1.4 and S1.0. There is some spread at low metallicity in the low- Z models, but as the Chandrasekhar mass model lies

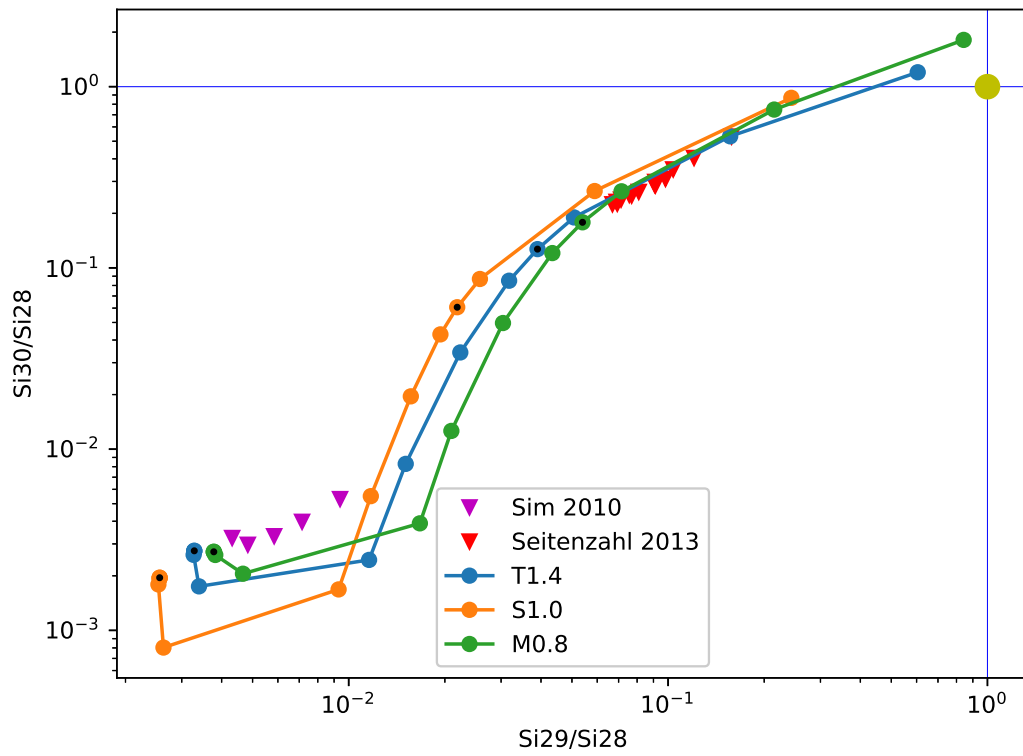


FIGURE 5.4: Isotopic ratios $[\text{Si}^{29}/\text{Si}^{28}]$ with respect to $[\text{Si}^{30}/\text{Si}^{28}]$, normalised to solar values.

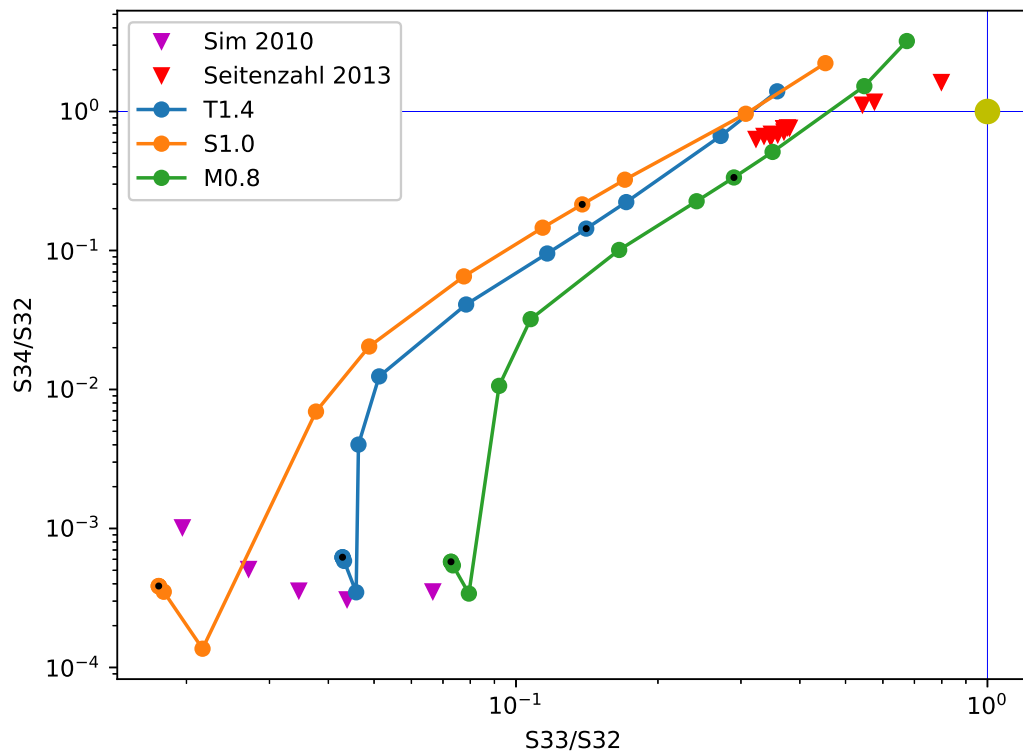


FIGURE 5.5: Local isotopic ratio diagnostic plot for ^{34}S

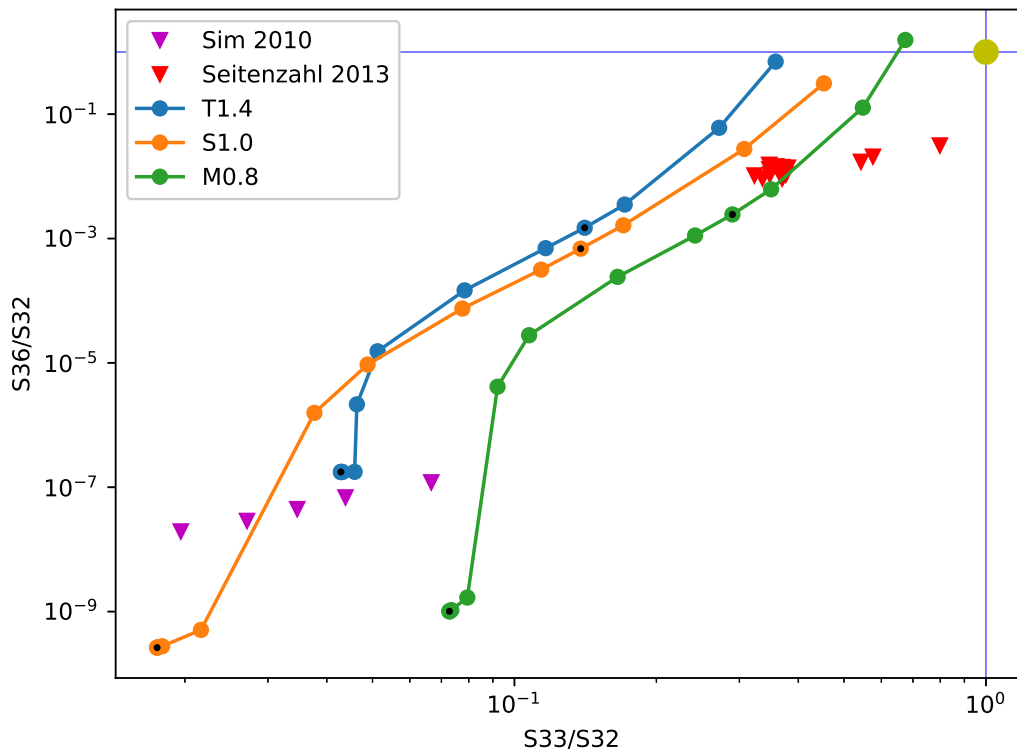
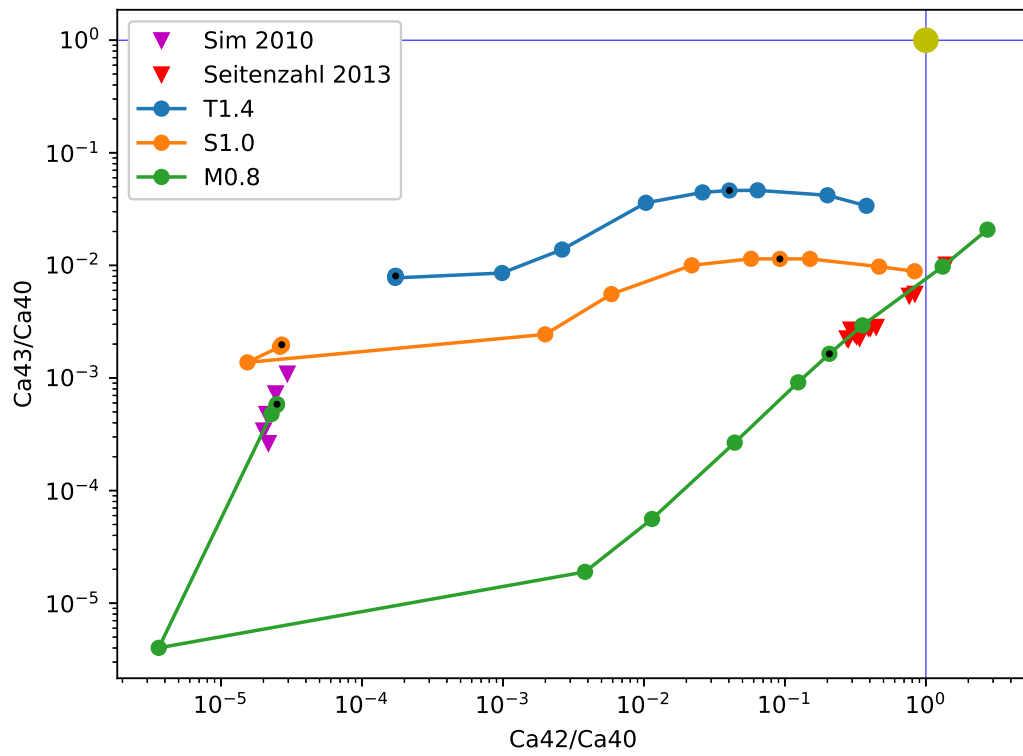
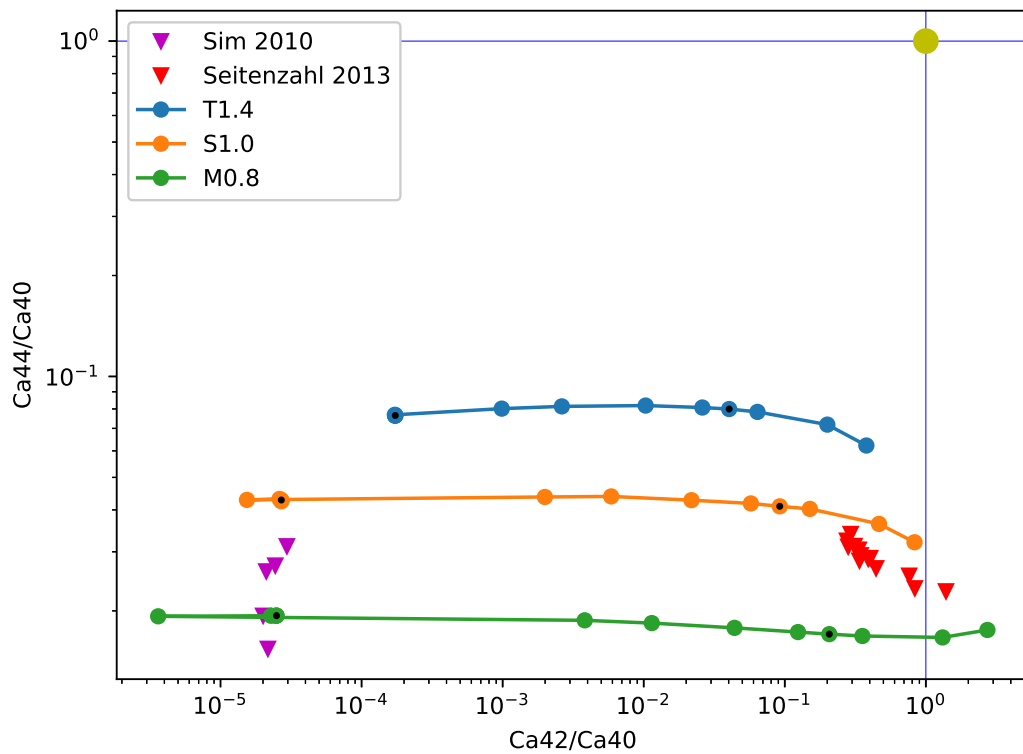


FIGURE 5.6: Local isotopic ratio diagnostic plot for ^{36}S

between the sub-Chandrasekhar mass models, this is also of little practical use. We see a similar distribution in figure 5.6. We can conclude that as S yields are similar between the three classes of model, they cannot be used to identify the SNIa progenitor.

^{43}Ca is a potential tracer of the progenitor mass of SNIa explosions. Figure 5.8 shows a consistently higher $^{43}\text{Ca}/^{40}\text{Ca}$ ratio for the T1.4 model compared to the sub-Chandrasekhar mass models. This is complicated, however, by the metallicity dependence of the yields, as a solar metallicity S1.0 model could be mistaken for a sub solar T1.4 model. The same plot for ^{44}Ca shows good separation between the three models (figure 5.8.) however as the ratio of $^{44}\text{Ca}/^{40}\text{Ca}$ is small compared to solar the contribution from SNIa to the ^{44}Ca budget of the sun is small. It is therefore difficult to disentangle the contribution of SNIa from other sources, each of which will have its own uncertainties and suite of possible literature yields. This is a difficulty in the

FIGURE 5.7: Local isotopic ratio diagnostic plot for ^{43}Ca FIGURE 5.8: Local isotopic ratio diagnostic plot for ^{44}Ca

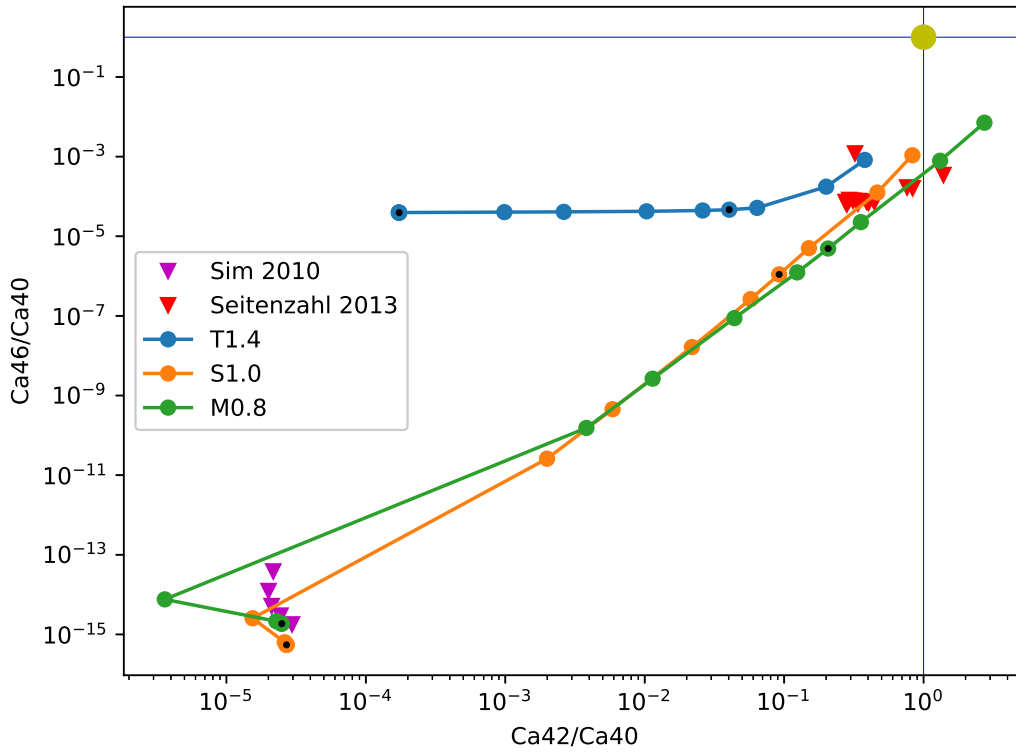


FIGURE 5.9: Local isotopic ratio diagnostic plot for ^{46}Ca

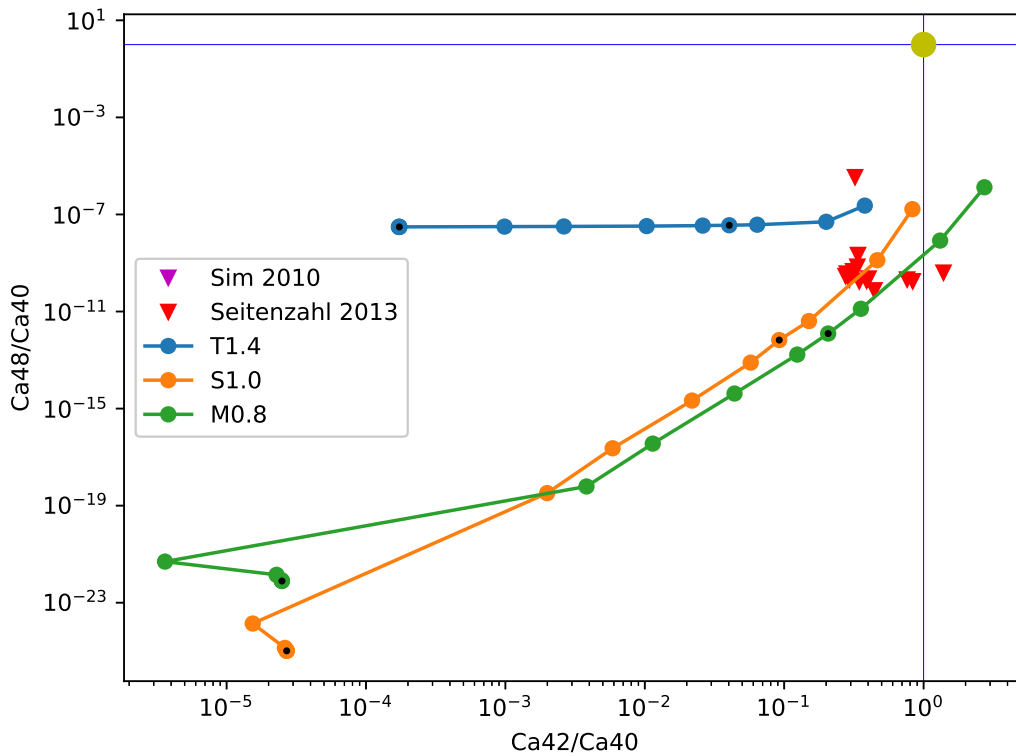


FIGURE 5.10: Local isotopic ratio diagnostic plot for ^{48}Ca

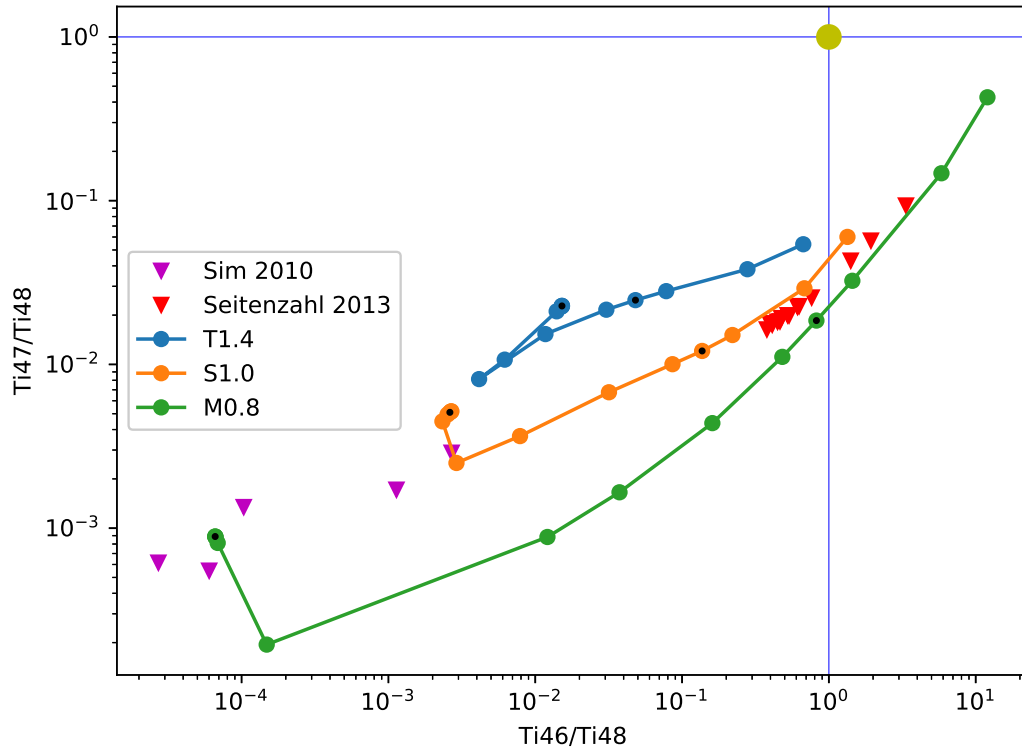


FIGURE 5.11: Local isotopic ratio diagnostic plot for ^{47}Ti

^{44}Ca , and in any diagnostic where at least one of the models investigated is not close to the solar value. Even in the case where one model is close to solar, it is possible that a large contribution from other sources could mask any information on the progenitors of SNIa. In this case, single source pre-solar grains are the only viable option for probing a particular isotopic ratio, provided that such grains exist.

Figures 5.9 and 5.10 are very similar, and both present a potential useful ratio. We note the very large difference at low metallicity between the sub and Chandrasekhar models. Only in the super-solar models we see a significant narrowing of the spread of data. Even so, there is still a significant and measurable difference between the models for both isotopes, at least up to $Z = Z_{\odot}$.

We see some separation in the ratios for $^{47}\text{Ti}/^{48}\text{Ti}$, approximately a factor of 5 at most metallicities in figure 5.11. There is very large range in $^{46}\text{Ti}/^{48}\text{Ti}$

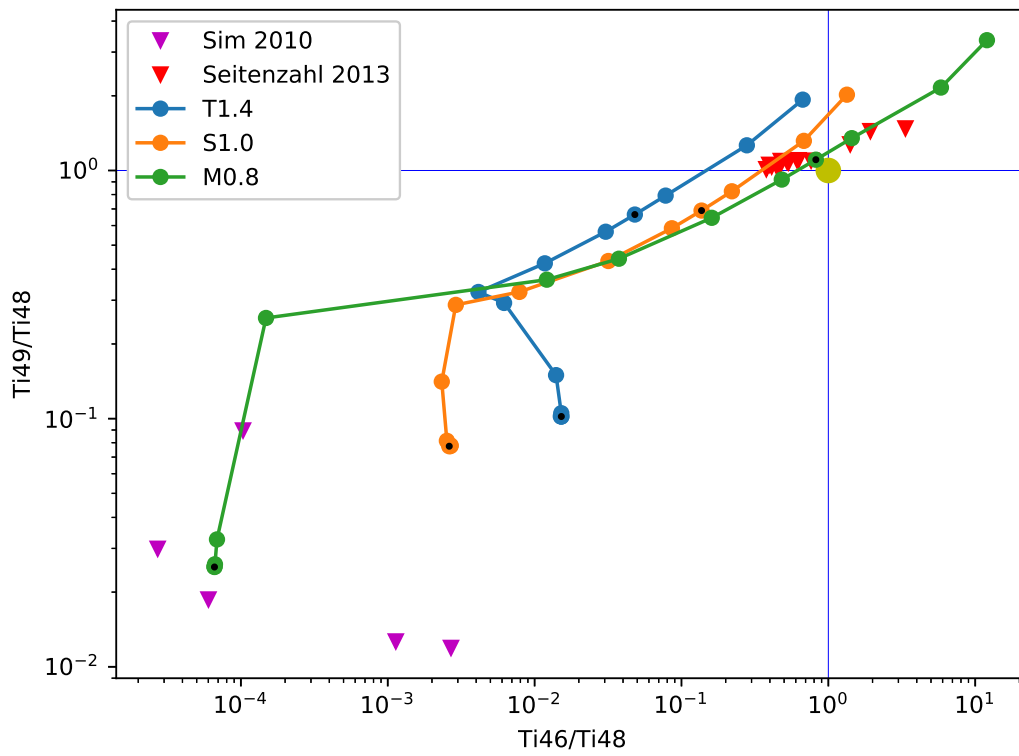


FIGURE 5.12: Local isotopic ratio diagnostic plot for ^{49}Ti

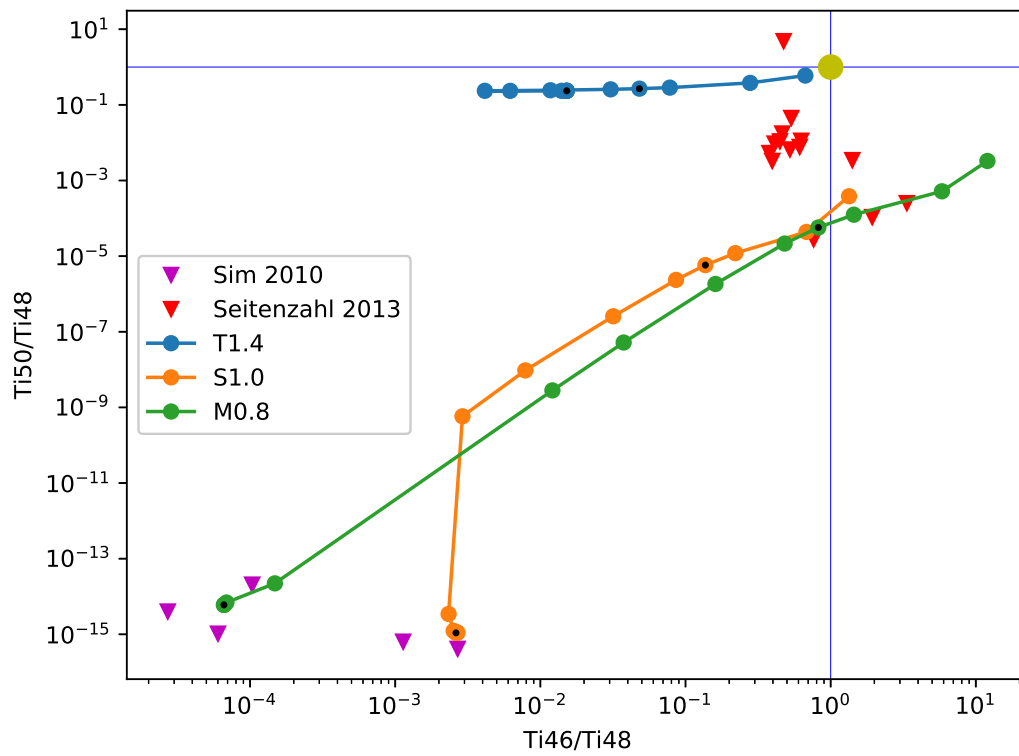


FIGURE 5.13: Local isotopic ratio diagnostic plot for ^{50}Ti

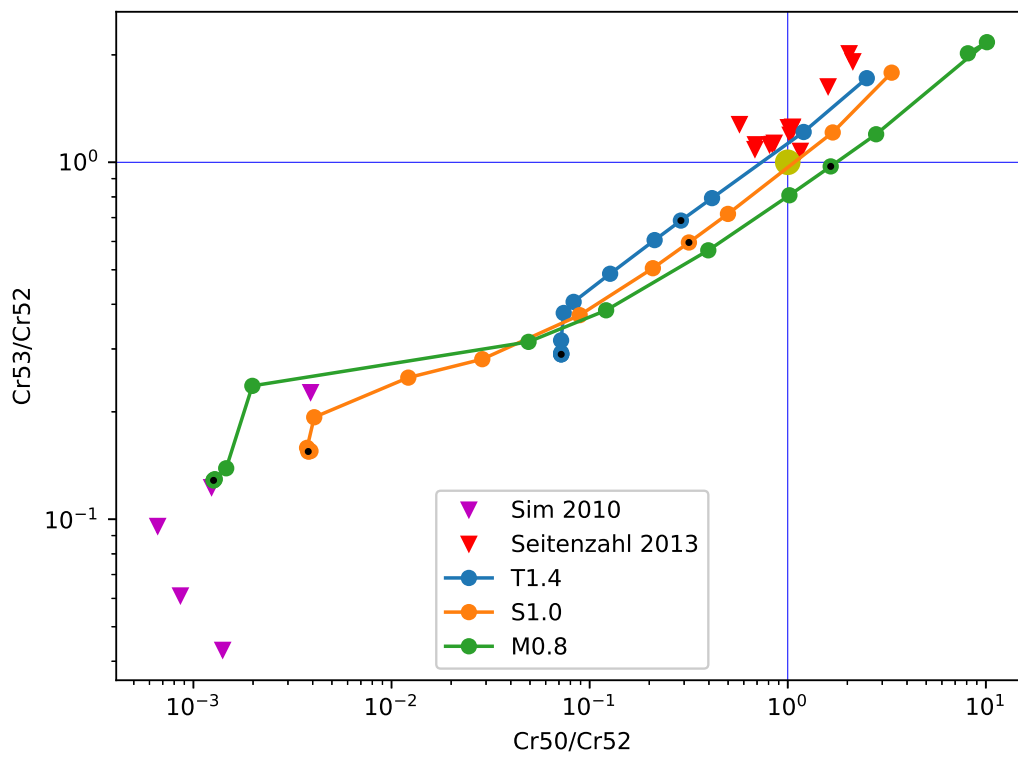
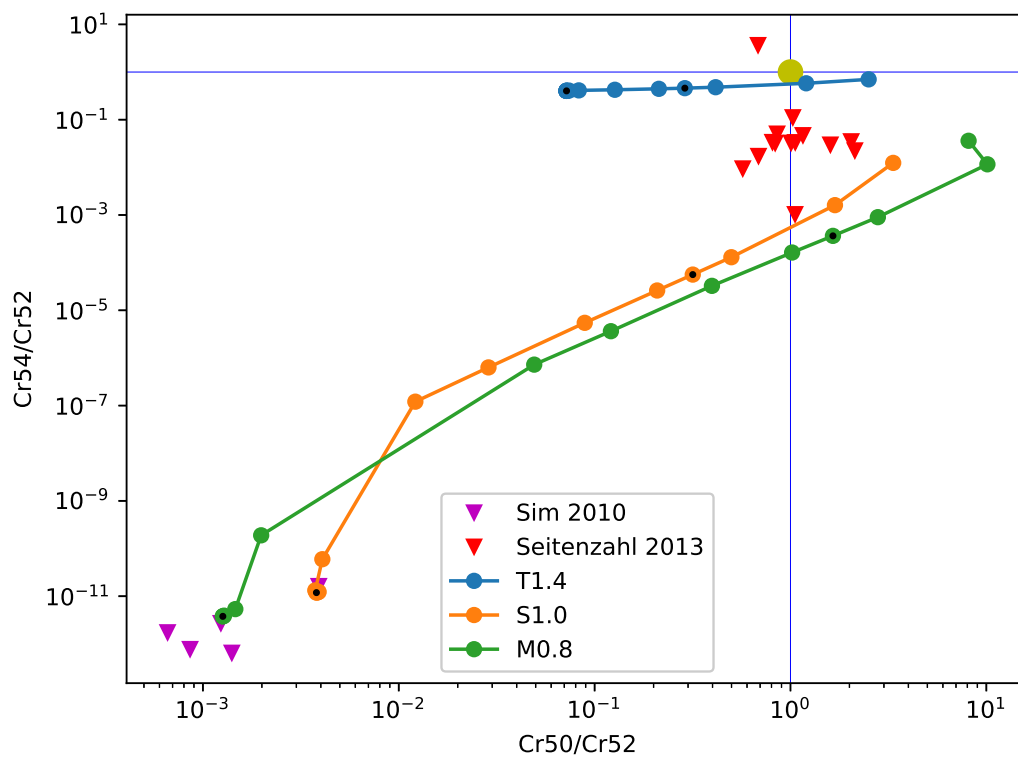
for the M0.8 models, with a smaller spread for S1.0. $^{46}\text{Ti}/^{48}\text{Ti}$ is therefore a poor tracer of the progenitor mass. $^{47}\text{Ti}/^{48}\text{Ti}$ is useful, particularly at lower metallicities.

^{49}Ti (figure 5.12) is of little to no use as a diagnostic tool. $^{50}\text{Ti}/^{48}\text{Ti}$ presents one of the best diagnostic ratios so far, with figure 5.13 showing a large difference between the sub- and Chandrasekhar mass models. This is unsurprising given the previous 4 isotope plots we have shown; however, it is encouraging to see that the local ratios for ^{50}Ti are also very distinct for the different progenitor masses.

A further consideration in using isotopic ratios as a tracer of the progenitor mass which is not addressed in this work is the contribution from the accreted helium shell in the sub-Chandrasekhar mass models. As noted in, e.g., Polin, Nugent, and Kasen (2021), there is significant production of radioactive isotopes in the helium ashes which can be observed in the late time lightcurve of SNIa. ^{48}Ti is the product of one such decay, from radioactive ^{48}Cr and ^{48}V . While Townsley et al. (2019) find that there is only a small production of ^{48}Cr in their thin shell simulations, the mass of the helium shell in those runs is on the order of $0.01 M_{\odot}$, in simulations with larger helium shell masses production can be significant. This would improve the predictive power of some of the ratios presented here, as the spread between the T1.4 and S0.8 models would be increased by the increased production of ^{48}Ti .

Figures 5.14 and 5.15 show the isotopic ratios for Cr. Both $^{53}\text{Cr}/^{52}\text{Cr}$ and $^{50}\text{Cr}/^{52}\text{Cr}$ are poor tracers of progenitor mass, as there is no clear separation between models. At metallicity $Z = 0$, there is some distinction in $^{50}\text{Cr}/^{52}\text{Cr}$ however this is highly sensitive to the initial composition and the S1.0 and M0.8 models quickly become indistinguishable from the T1.4 set.

$^{54}\text{Cr}/^{52}\text{Cr}$ appears to be a strong constraint on progenitor mass, however. Although there is a strong metallicity dependence in the S1.0 and M0.8 models, T1.4 is consistently around the solar value for $^{54}\text{Cr}/^{52}\text{Cr}$. We see the

FIGURE 5.14: Local isotopic ratio diagnostic plot for ^{53}Cr FIGURE 5.15: Local isotopic ratio diagnostic plot for ^{54}Cr

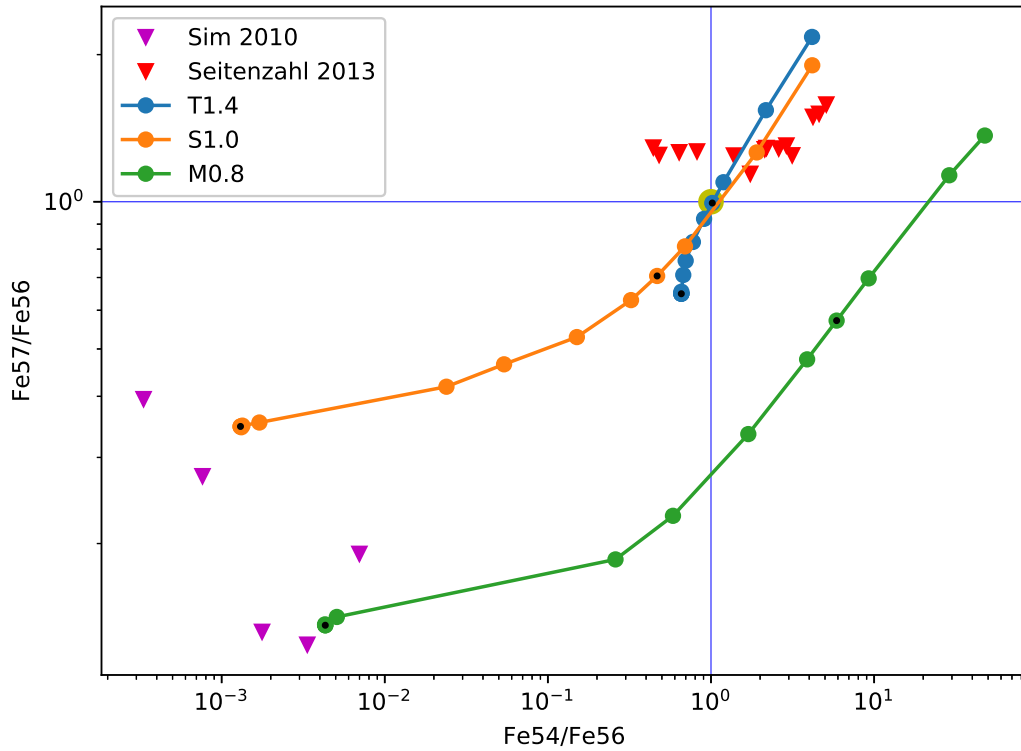


FIGURE 5.16: Local isotopic ratio diagnostic plot for ^{57}Fe

models of Seitenzahl et al. (2013b) lie intermediate between our post processed S1.0 and T1.4 results, with their N100H model being slightly super solar and a closer fit to T1.4 than the others they present.

As with the titanium ratios, ^{52}Cr can be produced in significant amounts in the helium shell as radioactive ^{52}Fe . This is not included in this work and would increase the separation between the sub- and Chandrasekhar mass models.

Figures 5.16 and 5.17 show the local isotopic ratios for the stable iron isotopes. In figure 5.16 we see that the T1.4 and S1.0 models are quite close for most of the metallicity range investigated. While at $Z = 0$, there is a clear distinction between T1.4Z0 and the two sub-Chandrasekhar models. While there is some overlap in the $^{54}\text{Fe}/^{56}\text{Fe}$ ratio between the Chandrasekhar and sub-Chandrasekhar models, this occurs only at super solar metallicity. These progenitors will constitute a small fraction of the total SNIa progenitors and

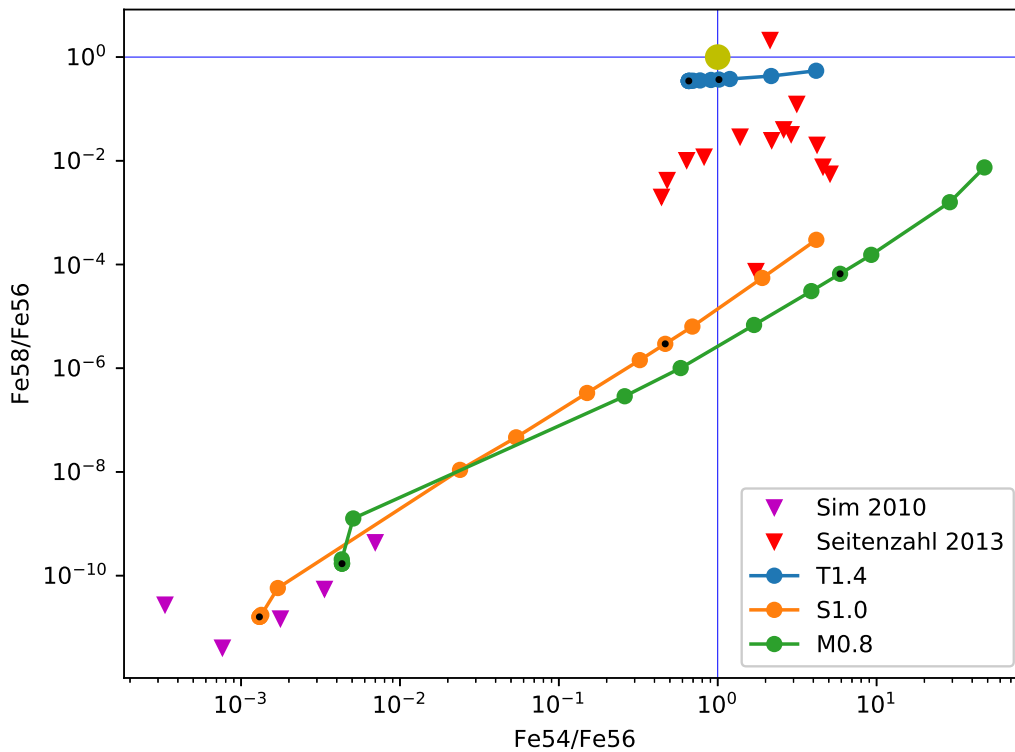


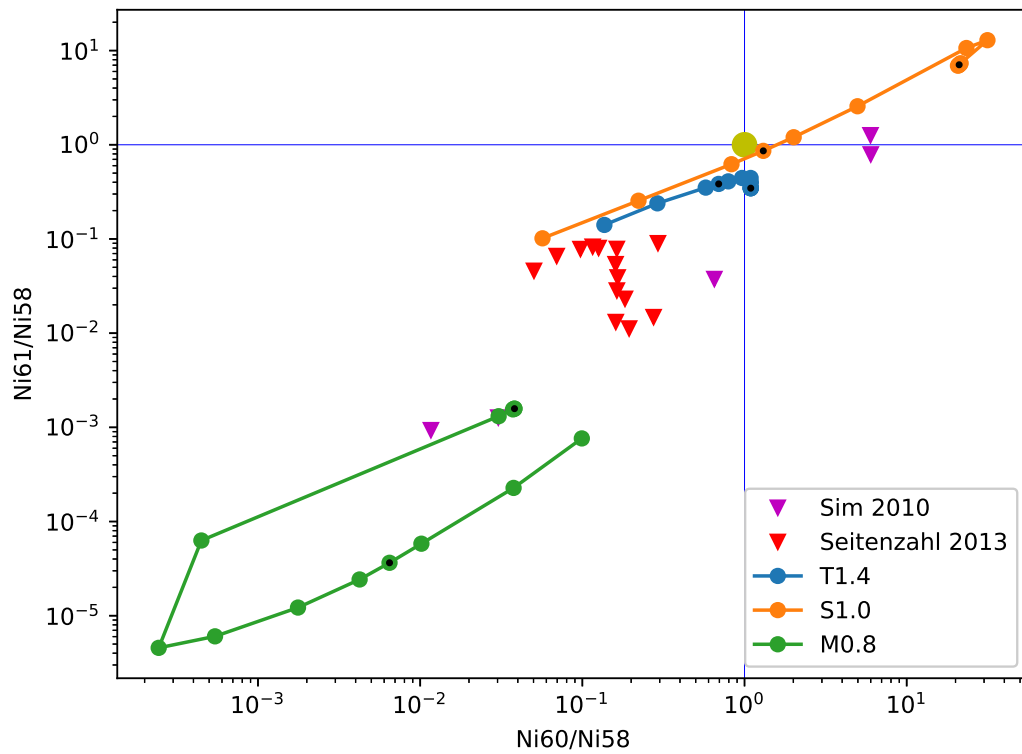
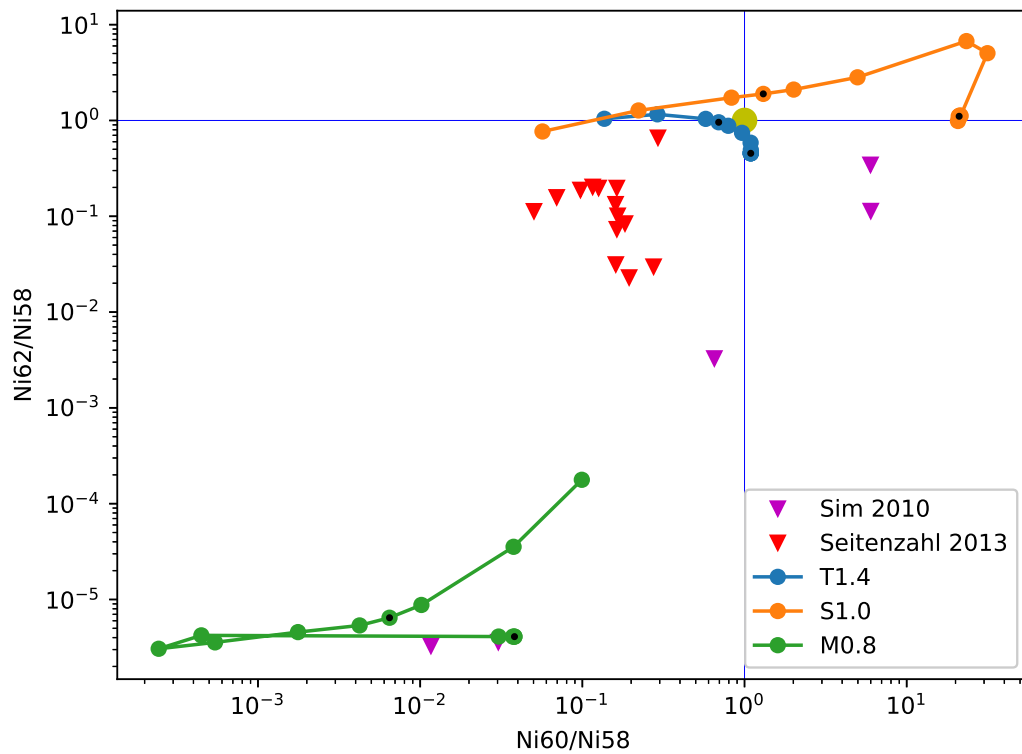
FIGURE 5.17: Local isotopic ratio diagnostic plot for ^{58}Fe

therefore the $^{54}\text{Fe}/^{56}\text{Fe}$ ratio may be seen as a tool in distinguishing the progenitor mass. As ^{54}Fe has the potential to be observed in late time SNIa spectra, this presents a way of determining the isotopic distribution of the ejecta of the observed SN.

Without an independent verification of the initial metallicity of the SNIa explosion, neither $^{57}\text{Fe}/^{56}\text{Fe}$ nor $^{54}\text{Fe}/^{56}\text{Fe}$ is a useful diagnostic.

The $^{58}\text{Fe}/^{56}\text{Fe}$ ratio, however, is a good tracer of progenitor mass, with a large separation between the sub- and Chandrasekhar-mass models across all metallicities. With over two orders of magnitude difference, the $^{58}\text{Fe}/^{56}\text{Fe}$ is a useful diagnostic tool for the initial progenitor mass and the T1.4 results are insensitive to initial metallicity.

In figures 5.18, 5.19 and 5.20 the local ratios for Ni are shown. Figure 5.18 shows the $^{61}\text{Ni}/^{58}\text{Ni}$ vs $^{60}\text{Ni}/^{58}\text{Ni}$ ratio which is unsuitable as a tracer of progenitor mass when a range of metallicities is considered. In the $Z = 0$

FIGURE 5.18: Local isotopic ratio diagnostic plot for ^{61}Ni FIGURE 5.19: Local isotopic ratio diagnostic plot for ^{62}Ni

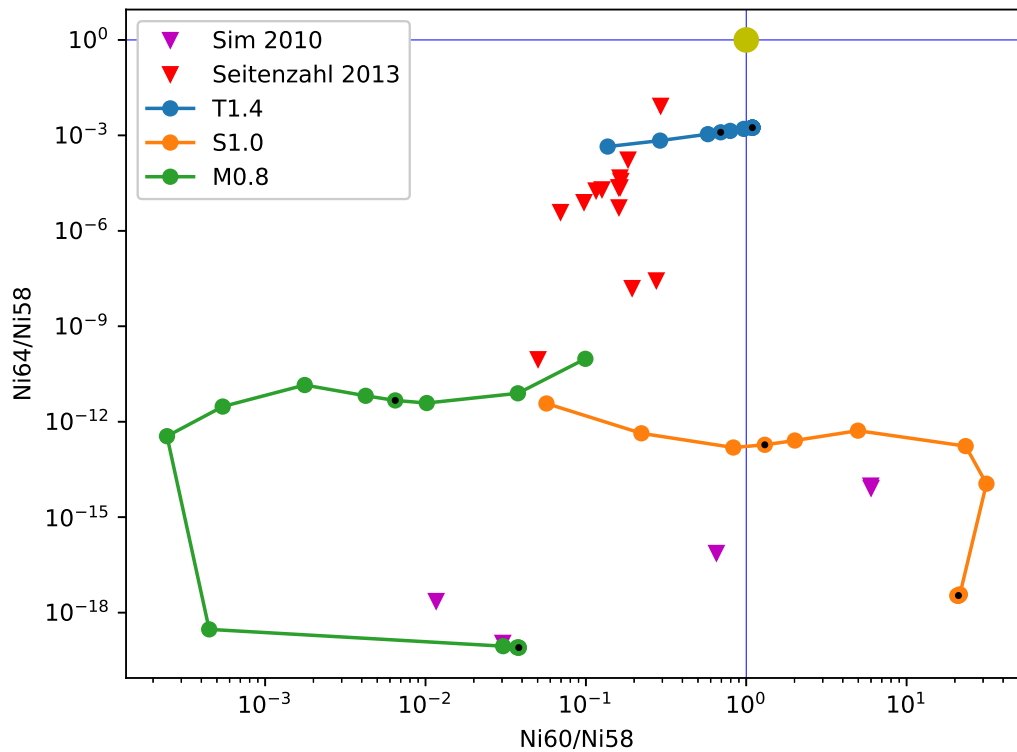


FIGURE 5.20: Local isotopic ratio diagnostic plot for ^{64}Ni

models, there is a clear distribution of models, with S1.0 being super-solar in $^{60}\text{Ni}/^{58}\text{Ni}$, T1.4 being nearly solar and M0.8 being sub-solar. Due to the strong metallicity dependence of ^{60}Ni in the S1.0 and M0.8 models, where we see an increase of two orders of magnitude in production, compared to the factor of 3 reduction in the T1.4 models, the lower mass progenitors change the $^{60}\text{Ni}/^{58}\text{Ni}$ ratio dramatically. This causes the T1.4 and S1.0 models to overlap significantly at $Z > Z_{\odot}$. A similar trend is seen in the $^{60}\text{Ni}/^{58}\text{Ni}$ ratio at super-solar metallicities. Again, for figure 5.19, the $^{62}\text{Ni}/^{58}\text{Ni}$ ratio is unsuitable for determining the progenitor mass. In this example the difficulties span the whole metallicity range of the models investigated.

Figure 5.20 shows the $^{64}\text{Ni}/^{58}\text{Ni}$ ratio for our three classes of model. In this plot we see that there is a large difference in the sub- and Chandrasekhar mass models with respect to this ratio however the T1.4 model is over three

orders of magnitude lower than the solar value. This cannot therefore contribute significantly to solar abundances of ^{64}Ni .

In summary, the local isotopic ratios which may provide information on the progenitor mass, regardless of initial metallicity, are: $^{44}\text{Ca}/^{40}\text{Ca}$; $^{50}\text{Ti}/^{48}\text{Ti}$; $^{54}\text{Cr}/^{52}\text{Cr}$; $^{58}\text{Fe}/^{56}\text{Fe}$ and $^{64}\text{Ni}/^{58}\text{Ni}$. Other isotopes may be possible tracers if the initial metallicity can be constrained. Inclusion of the helium ashes in a model with a thick accreted helium layer may cause an increase in the abundance of ^{44}Ca in the sub-Chandrasekhar models as ^{44}Ca is produced in this helium layer, however further studies including this accreted layer are necessary to confirm this.

The key isotopes with the largest difference between the T1.4Z0.014 and S1.0Z0.014 models are now presented.

^{36}Ar Vs ^{50}Ti

The ^{36}Ar Vs ^{50}Ti production factor ratio shows a large separation between the Chandrasekhar and sub-Chandrasekhar mass models (T1.4, S1.0 and M0.8) (5.21) of over 7 orders of magnitude. This is largely due to the 5 order of magnitude difference in the production of ^{50}Ti between the models T1.4Z0.014, S1.0Z0.014 and M0.8Z0.014 - ^{36}Ar is here only a reference point and does not highlight any particular physical difference between the models. This large difference in production arises due to the absence of the high density, high temperature inner regions of the S1.0 model. In S1.0 and M0.8 only secondary production of ^{50}Ti is observed, in the low temperature outer regions. We see in figure 5.21 that the secondary production of ^{50}Ti has a significant effect on the isotopic ratio ^{36}Ar Vs ^{50}Ti , as the production of ^{50}Ti is highly metallicity dependent in the sub-Chandrasekhar mass models. The scatter in the ratios associated with T1.4 are much smaller, as the bulk of ^{50}Ti in these is primary. The models of Seitenzahl et al. (2013b) lie intermediate between the sub and Chandrasekhar mass models, whereas the models of Sim et al. (2010) are to

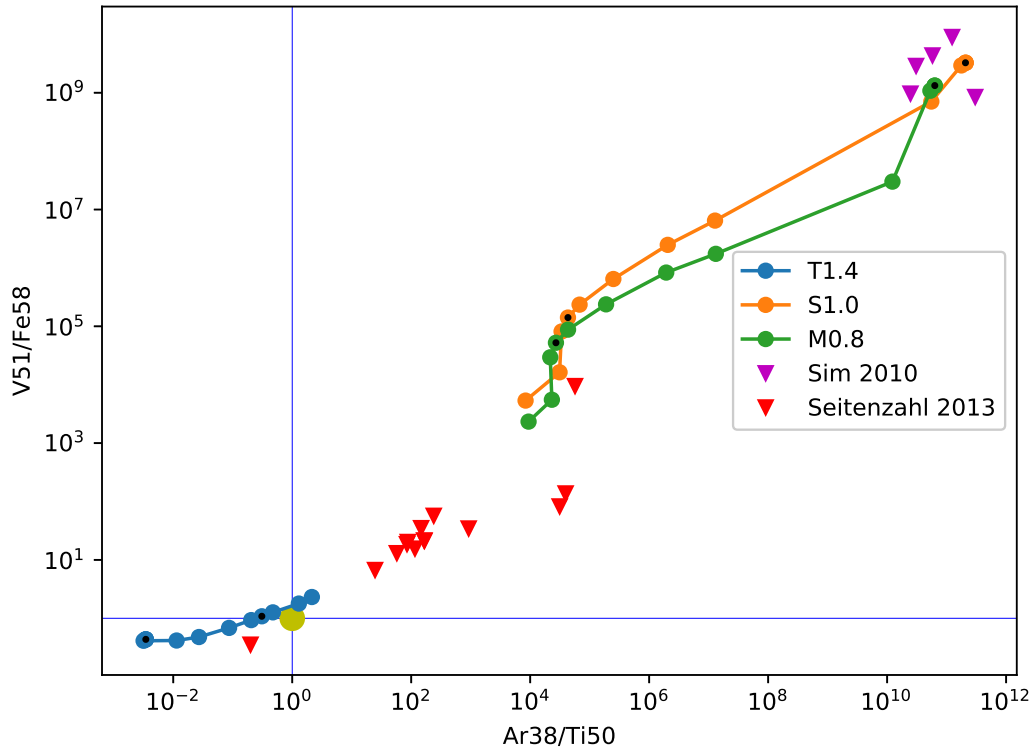


FIGURE 5.21: Example diagnostic plot showing the large spread in isotopic ratios between T1.4 and S1.0 in both $^{38}\text{Ar}/^{50}\text{Ti}$ and $^{51}\text{V}/^{58}\text{Fe}$.

be found at the low metallicity end of the sub-Chandrasekhar mass SNIa models. This suggests that the production of ^{50}Ti is a strong constraint on the progenitor of SNIa, providing that accurate contributions from SNIa sources can be verified for the solar value.

Here ^{58}Fe has a similar dependence on progenitor mass, with production in the T1.4Z0.014 model being over 5 orders of magnitude larger than in the S1.4Z0.01 model. We see a large production in the densest, hottest regions of the model, with production in the sub-Chandrasekhar mass models only occurring due to metallicity effects. ^{58}Fe is dominated in the T1.4 models by the hot contribution above 7.5 GK.

Some isotopes provide a potential constraint if the initial metallicity of the progenitor is known. An example of this is given in figure 5.22 where, due to the low scatter of the T1.4 with respect to metallicity, and the high

scatter in the S1.0 and M0.8 models, a clear distinction between sub- and Chandrasekhar mass progenitors can be drawn. As initial metallicity approaches super solar values, however, the models converge on a near solar value for $^{41}\text{K}/^{50}\text{V}$. A good understanding of the physical constraints on progenitor metallicity would potentially allow the use of a wider range of isotopic ratios as diagnostic tools.

One model in particular from Seitzzahl et al. (2013b), the N100H model, consistently matches the T1.4 models much more closely than their other models, including their recommended N100 model. Indeed, Seitzzahl et al. (2013b) cite the overproduction of ^{54}Cr in these models (a factor of 1000 larger than solar) as evidence for the relative rarity of these high density explosions ($\rho_{\text{cent}} \gtrsim 5.5 \times 10^9$). Seitzzahl et al. (2013b) identifies ^{54}Cr , ^{58}Fe and ^{64}Ni as the most sensitive to neutronisation in the central regions of the SNIa explosion, all of which are shown in this present work to also be highly sensitive to the central density (see the local isotopic ratio plots). We therefore argue they are a good indicator of progenitor mass if we accept the yields of T1.4. In addition to the isotopes identified by Seitzzahl et al. (2013b), we also see a strong dependence on the central density in the production of ^{50}Ti . In addition to this, we also identify ^{64}Ni as being a strong tracer of progenitor mass, where no secondary production is observed in the lower mass models. If these results do not belong to rare SN events, as suggested, the high density region is the defining characteristic of the Chandrasekhar mass model.

Figure 5.23 shows an example of another plot with large separations between the sub- and Chandrasekhar mass models. Here the isotopes are ^{58}Fe and ^{35}Cl which show a difference of over 4 orders of magnitude at solar metallicity.

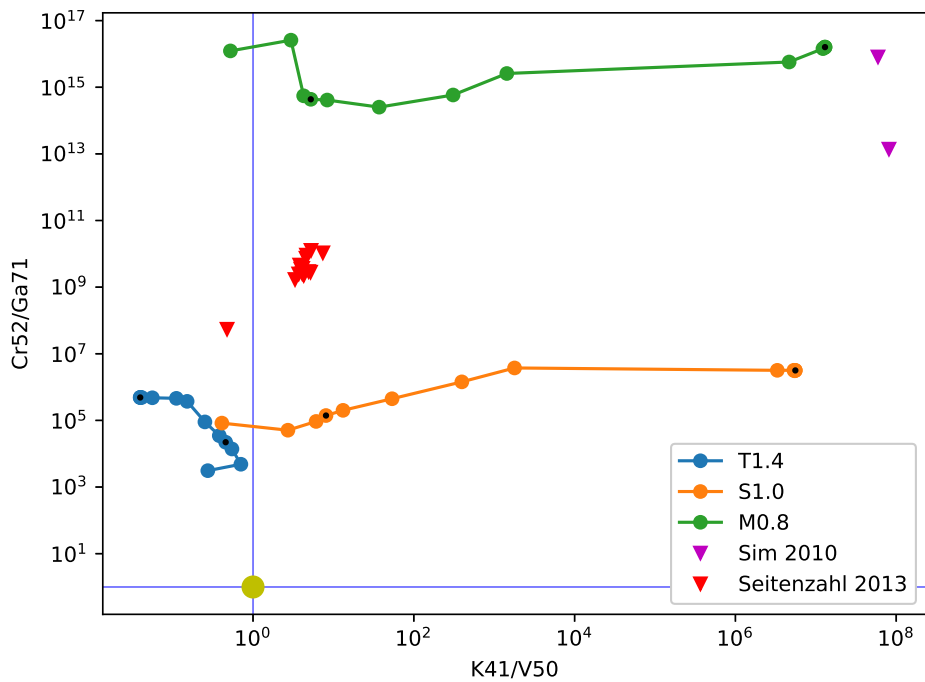


FIGURE 5.22: Example diagnostic plot showing the large spread in isotopic ratios between T1.4 and S1.0 in both $^{38}\text{Ar}/^{50}\text{Ti}$ and $^{51}\text{V}/^{58}\text{Fe}$.

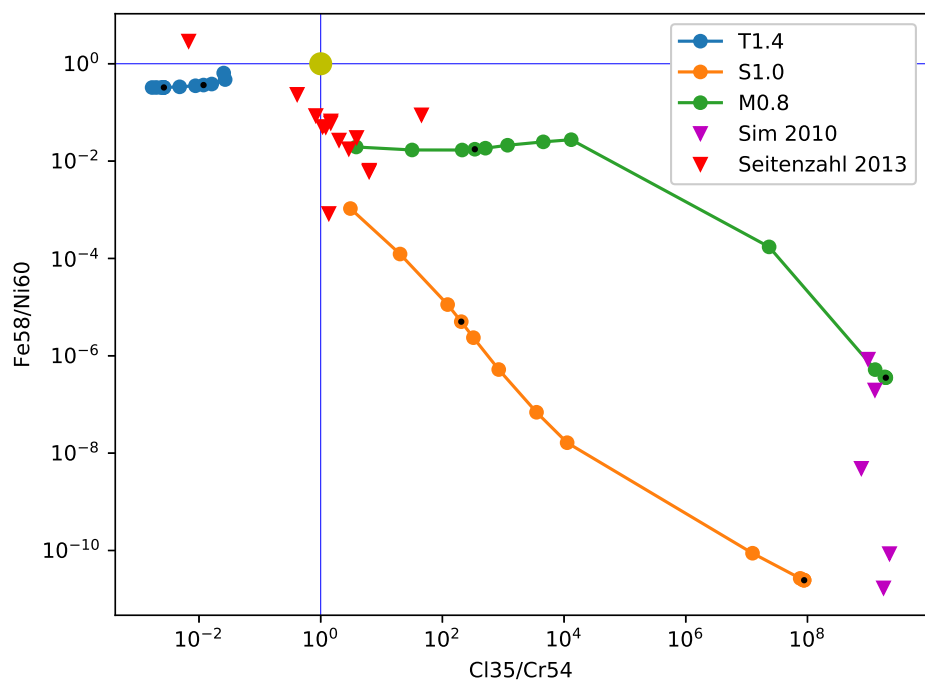


FIGURE 5.23: Example diagnostic plot showing the large spread in isotopic ratios between T1.4 and S1.0 in both $^{38}\text{Ar}/^{50}\text{Ti}$ and $^{51}\text{V}/^{58}\text{Fe}$.

5.1.4 Further Isotopic Ratios

Some isotopes produced in the T1.4 models are not produced in the S1.0 or M0.8 models.

^{64}Ni would also be an indicator of sub- to Chandrasekhar-mass progenitors. However, since there is no production of ^{64}Ni in any of the lower mass models above trace amounts, the data cannot be represented as it has been, for instance, ^{50}Ti . Similar effects for a range of isotopes can be seen in the $Z=0$ models. Travaglio, Hillebrandt, and Reinecke (2005) and Bravo et al. (2010) give realistic ranges of initial metallicity ranging from $0.1 - 3Z_{\odot}$ and $Z = 10^{-5} - 0.1$ respectively. These ranges are close to the metallicity range covered in this work, and results in low metallicity models can be seen to be roughly similar throughout these plots.

5.1.5 Summary

In this section we have identified a number of potential isotopic tracers of SNIa progenitor mass.

We note that there are some significant limitations in the application of this work. For isotopes with small contributions from SNIa to solar system abundances, accurate contributions from all other sources are necessary in order for this work to have predictive power. The exact contribution from SNIa necessary for the progenitor to be well constrained varies by isotope, by the relative difference between sub- and Chandrasekhar mass models, and by the accuracy of the contributions from other sources. As such, it is impossible in the scope of this work to accurately determine a threshold for the contribution from SNIa however it is likely to require at least 30-40% contribution for most isotopes. Certainly, a contribution of less than 10% would require very tight constraints on contributions from other sources and a large difference in the sub- and Chandrasekhar mass models.

Some of the isotopic ratios identified here may be strengthened as tracers of SNIa progenitor mass with the inclusion of a thick helium shell, as the production of some key radioactive nuclei - ^{52}Fe and ^{48}Cr being two - are increased due to production in this helium shell. Full modeling of a thick shell is therefore vital to determine the strongest constraints on SNIa progenitor mass.

Chapter 6

Conclusions

“It is a tale told by an idiot, full of sound and fury”

William Shakespeare, Macbeth

6.1 Conclusions

In this work, 39 models of SNIa explosions have been post processed. They cover a mass range of 1.4 - 0.8 M_{\odot} , with metallicities from $Z = 0$ to $Z = 0.1$. From this, a set of metallicity dependent nucleosynthetic yields for Chandrasekhar and sub-Chandrasekhar mass SNIa explosions has been produced, with consistent nuclear physics between the classes of model. These have been analysed, benchmarking the results against both the previously published yields of the three parent models, and against literature yields from a variety of research groups. The yields are then analysed to identify isotopic ratios which may provide a method of discriminating between SNIa progenitor masses.

The abundances from our models are consistent with published work and provide a suite of metallicity dependent yields with consistent nuclear reaction network over a range of masses and metallicities. These are crucial for applications in GCE investigations.

We identify the main burning regimes and the products of these, and categorise them broadly into three regions:

- A high temperature region above approximately 7 GK, present only in the Chandrasekhar mass models, where the isotopic yields are insensitive to the initial chemical composition of the WD, due to the large electron capture cross sections at high densities. Iron group isotopes are synthesised under these conditions during the freeze out from NSE.
- An intermediate temperature region present in the $1.4 M_{\odot}$, $1.0 M_{\odot}$ and $0.8 M_{\odot}$ models, between approximately 4 and 6.5 GK, although in the $0.8 M_{\odot}$ model the maximum peak temperature does not reach the upper limit of this range. In this region initial metallicity changes the isotopic distribution of the ejecta. This component produces a mixture of iron group and intermediate mass isotopes.
- A cooler outer component, with maximum peak temperatures lower than 4 GK. There is a strong metallicity effect in this component, which is similar between the three classes of model. Production is centered on intermediate mass elements between Mg and the beginning of the iron group. Conditions are similar between the three categories of model.

Due to the absence of the high temperature region from the sub-Chandrasekhar models, and the lower production of iron group isotopes in the cooler regions, there are a number of isotopes which are potential tracers of progenitor mass in the iron group. ^{62}Ni is produced predominantly in this hot component, with only a small contribution in the cool region at high metallicities, and a small contribution in the intermediate temperature region (absent from the $M0.8$ models). This presents a strong constraint on the mass of the progenitor at all metallicities, in contrast with the broad production of ^{55}Mn at higher metallicities. Similarly, ^{61}Ni presents a reasonable constraint on the

mass of the progenitor. We identify a number of isotopes, made predominantly in the 7 - 9 GK peak temperature region unique to the M_{Chand} explosion model. These are: ^{50}Ti , ^{54}Cr , ^{58}Fe , ^{64}Ni and ^{51}V . Additionally, there is a strong dependence on the ratio of intermediate mass isotopes with respect to the iron group production, with ^{38}Ar showing a large difference in production between the sub and Chandrasekhar mass models.

Isotopic ratios therefore present a valuable method of identifying SNIa progenitor, however the practicalities of investigating these may be impossible with current experimental methods. A discussion of the difficulties of using isotopic ratios is presented in the Possible Future Work section below.

6.1.1 Possible Future Work

The application of these results to GCE codes provides the opportunity to assess the impact of these new sets of yields compared with previous iterations. Correct initial abundances, particularly in the outer layers of the progenitor WD, may significantly impact the production of the intermediate mass isotopes and their relative abundances. Investigation into this and subsequent post-processing with consistent reaction networks provides an important test of these results. The inclusion of an accreted helium layer on the surface of the WD introduces the possibility of s-process nucleosynthesis during the helium detonation of the double detonation models. After the passage of the shock wave during the carbon detonation, these s-process seeds are destroyed, and may contribute to the production of p-nuclei such as ^{92}Mo through γ, p reactions. Future work expanding on these models should include fully realised hydrodynamic models of the accretion phase, preferably in 3 dimensions, in order to capture this production. Similar work has been undertaken in, for example, Travaglio et al. (2004) and should be investigated here to further validate these yields.

We note that the specific abundances of ejected material may depend sensitively on the initial composition and its stratification in the outer layers of the progenitor WD. Also in these outer layers, temperatures are such that reaction rates may influence the abundances of products more significantly than in the hot NSE or quasi-NSE burning regions in the center of the WD. Because of these considerations further work investigating the effect of seed nuclei on the ejected isotopic abundances, and a sensitivity study of weak reaction rates for the inner regions of the Chandrasekhar mass progenitors and charged particle reaction rates for the outer regions of all models

Further experimental work on isotopic ratios found in pre-solar grains or bulk solar system material may be an interesting next step in the process of identifying the progenitors of Type Ia, the accuracy of this method however requires that the isotopic contributions from other sources of enrichment - e.g. CCSN, AGB stars - be well constrained. For those isotopes with large and well constrained contributions from SNIa, the isotopic ratios both locally and between elements, in either potential SNIa grains or bulk solar material, will provide the best evidence. Local isotopic ratios are preferred, as there will be no chemical effects which separate the products however isotopic ratios between elements may also be useful as a diagnostic. While SNIa are not widely thought to produce pre-solar grains, dust formation in the SNIa ejecta may be possible (Gomez et al., 2012; Sarangi, Matsuura, and Micelotta, 2018).

Gamma ray spectroscopy of the decay of radioactive isotopes formed during the explosion may provide a further channel for investigation, as does the specific velocity distribution of the products of the explosion. Our yields provide a full distribution of stable and radioactive products for each of our models, and may be used to investigate the decay of ^{55}Fe . As the production of ^{55}Fe depends both on the initial mass and the metallicity - it being a major radiogenic contributor to the ejected ^{55}Mn mass - its distribution in the SN

remnant may provide information on its production site and the metallicity of the progenitor.

Appendices

Appendix A

Decayed Yields

Element	A	$^{22}\text{Ne} = 0$	1e-7	1e-6	1e-5	1e-4	1e-3	2e-3	5e-3	1e-2	1.4e-2	2e-2	5e-2	1e-1
C	12	1.63e-03	1.63e-03	1.63e-03	1.63e-03	1.63e-03	1.62e-03	1.62e-03	1.61e-03	1.59e-03	1.59e-03	1.58e-03	1.54e-03	1.49e-03
C	13	6.39e-10	6.37e-10	6.35e-10	6.29e-10	6.13e-10	8.70e-10	1.44e-09	4.03e-09	8.79e-09	1.29e-08	1.95e-08	6.18e-08	1.60e-07
N	14	2.53e-08	2.53e-08	2.52e-08	2.51e-08	2.85e-08	1.39e-07	2.81e-07	6.61e-07	1.19e-06	1.57e-06	2.07e-06	3.88e-06	5.65e-06
N	15	1.07e-06	1.07e-06	1.07e-06	1.04e-06	7.18e-07	5.37e-08	2.04e-08	6.49e-09	4.00e-09	3.65e-09	3.73e-09	7.25e-09	2.60e-08
O	16	5.37e-02	5.37e-02	5.37e-02	5.37e-02	5.38e-02	5.43e-02	5.48e-02	5.60e-02	5.73e-02	5.80e-02	5.87e-02	5.96e-02	5.68e-02
O	17	5.78e-10	5.79e-10	5.83e-10	6.32e-10	1.28e-09	2.65e-08	6.52e-08	1.62e-07	2.66e-07	3.22e-07	4.21e-07	4.89e-07	4.85e-07
O	18	5.74e-12	5.75e-12	5.78e-12	6.07e-12	1.01e-11	1.67e-10	4.15e-10	1.12e-09	2.19e-09	3.00e-09	4.2e-09	1.15e-08	4.14e-08
F	19	9.12e-10	9.11e-10	9.07e-10	8.67e-10	6.37e-10	1.92e-10	1.32e-10	1.43e-10	2.42e-10	3.40e-10	5.01e-10	1.34e-09	2.24e-09
NE	20	1.61e-03	1.61e-03	1.61e-03	1.61e-03	1.61e-03	1.60e-03	1.59e-03	1.56e-03	1.51e-03	1.47e-03	1.42e-03	1.22e-03	1.05e-03
NE	21	1.08e-08	1.08e-08	1.08e-08	1.10e-08	1.28e-08	6.59e-08	1.68e-07	5.39e-07	1.20e-06	1.78e-06	2.74e-06	9.09e-06	2.59e-05
NE	22	1.98e-08	1.98e-08	2.00e-08	2.22e-08	4.81e-08	3.69e-07	7.97e-07	2.41e-06	5.91e-06	9.29e-06	1.52e-05	5.70e-05	1.71e-04
NA	23	6.64e-06	6.64e-06	6.64e-06	6.63e-06	6.50e-06	5.96e-06	6.03e-06	6.75e-06	8.76e-06	1.07e-05	1.39e-05	3.60e-05	1.05e-04
MG	24	1.49e-02	1.49e-02	1.49e-02	1.49e-02	1.50e-02	1.44e-02	1.36e-02	1.16e-02	9.25e-03	7.93e-03	6.49e-03	3.67e-03	3.55e-03
MG	25	1.81e-07	1.81e-07	1.81e-07	1.83e-07	2.24e-07	2.79e-06	4.54e-06	1.03e-05	2.19e-05	3.28e-05	5.16e-05	1.91e-04	6.90e-04
MG	26	8.66e-07	8.66e-07	8.67e-07	8.77e-07	9.94e-07	2.44e-06	3.98e-06	8.55e-06	1.60e-05	2.21e-05	3.16e-05	9.61e-05	5.05e-04
AL	27	3.96e-05	3.96e-05	3.95e-05	3.95e-05	3.89e-05	8.91e-05	1.61e-04	3.00e-04	4.22e-04	4.75e-04	5.20e-04	6.04e-04	9.03e-04
SI	28	1.65e-01	1.65e-01	1.65e-01	1.65e-01	1.65e-01	1.68e-01	1.69e-01	1.69e-01	1.69e-01	1.68e-01	1.68e-01	1.64e-01	1.65e-01
SI	29	2.85e-05	2.85e-05	2.85e-05	2.84e-05	2.96e-05	1.02e-04	1.34e-04	1.99e-04	2.83e-04	3.47e-04	4.49e-04	1.35e-03	4.98e-03
SI	30	1.63e-05	1.62e-05	1.62e-05	1.54e-05	1.04e-05	1.47e-05	5.01e-05	2.08e-04	5.16e-04	7.70e-04	1.15e-03	3.14e-03	6.74e-03
P	31	4.40e-05	4.40e-05	4.39e-05	4.28e-05	3.28e-05	2.52e-05	3.87e-05	7.95e-05	1.41e-04	1.85e-04	2.44e-04	4.71e-04	5.39e-04
S	32	9.42e-02	9.42e-02	9.41e-02	9.41e-02	9.39e-02	9.30e-02	9.27e-02	9.22e-02	9.15e-02	9.08e-02	8.96e-02	8.10e-02	6.45e-02
S	33	3.33e-05	3.33e-05	3.33e-05	3.36e-05	3.55e-05	3.56e-05	3.92e-05	5.97e-05	8.80e-05	1.06e-04	1.27e-04	1.82e-04	1.91e-04
S	34	2.81e-06	2.81e-06	2.79e-06	2.64e-06	1.57e-06	1.79e-05	5.53e-05	1.81e-04	4.18e-04	6.27e-04	9.59e-04	2.59e-03	4.32e-03
S	36	3.93e-12	3.93e-12	3.93e-12	3.93e-12	3.93e-12	4.75e-11	3.38e-10	3.20e-09	1.52e-08	3.21e-08	7.48e-08	1.16e-06	1.07e-05
CL	35	7.14e-06	7.14e-06	7.12e-06	6.92e-06	5.35e-06	4.58e-06	6.44e-06	1.31e-05	2.39e-05	3.27e-05	4.49e-05	7.83e-05	8.10e-05
CL	37	1.87e-06	1.87e-06	1.87e-06	1.87e-06	1.93e-06	2.15e-06	2.57e-06	3.88e-06	5.70e-06	6.94e-06	8.58e-06	1.56e-05	2.10e-05
AR	36	2.11e-02	2.11e-02	2.11e-02	2.11e-02	2.10e-02	2.06e-02	2.04e-02	2.00e-02	1.95e-02	1.92e-02	1.87e-02	1.60e-02	1.23e-02
AR	38	2.45e-06	2.45e-06	2.42e-06	2.45e-06	2.25e-06	8.09e-06	1.93e-05	6.21e-05	1.47e-04	2.24e-04	3.47e-04	1.00e-03	1.82e-03
AR	40	9.69e-13	9.69e-13	9.69e-13	9.69e-13	9.70e-13	1.30e-12	3.03e-12	1.89e-11	9.85e-11	2.47e-10	7.37e-10	1.52e-08	7.42e-08
K	39	2.78e-06	2.78e-06	2.76e-06	2.76e-06	2.58e-06	3.25e-06	4.92e-06	1.10e-05	1.73e-05	2.14e-05	2.69e-05	4.79e-05	5.43e-05
K	40	1.57e-12	1.57e-12	1.57e-12	1.58e-12	1.89e-12	1.08e-10	2.62e-10	9.55e-10	3.22e-09	6.16e-09	1.21e-08	3.05e-08	1.43e-08
K	41	1.12e-07	1.12e-07	1.13e-07	1.17e-07	1.59e-07	3.16e-07	4.31e-07	7.21e-07	1.12e-06	1.38e-06	1.70e-06	2.83e-06	2.98e-06
CA	40	2.27e-02	2.27e-02	2.27e-02	2.27e-02	2.26e-02	2.21e-02	2.18e-02	2.13e-02	2.06e-02	2.01e-02	1.95e-02	1.66e-02	1.29e-02
CA	42	2.76e-08	2.75e-08	2.75e-08	2.75e-08	2.72e-08	1.52e-07	4.01e-07	1.54e-06	3.76e-06	5.70e-06	8.75e-06	2.33e-05	3.43e-05
CA	43	2.74e-07	2.73e-07	2.72e-07	2.73e-07	2.62e-07	2.83e-07	4.51e-07	1.14e-06	1.37e-06	1.39e-06	1.35e-06	1.04e-06	6.54e-07
CA	44	4.11e-05	4.11e-05	4.10e-05	4.11e-05	4.11e-05	4.19e-05	4.20e-05	4.12e-05	3.94e-05	3.81e-05	3.62e-05	2.83e-05	1.90e-05
CA	46	4.22e-11	4.22e-11	4.22e-11	4.22e-11	4.22e-11	4.23e-11	4.24e-11	4.27e-11	4.34e-11	4.44e-11	4.78e-11	1.39e-10	5.07e-10
CA	48	1.61e-12	1.61e-12	1.61e-12	1.61e-12	1.61e-12	1.61e-12	1.62e-12	1.63e-12	1.66e-12	1.68e-12	1.71e-12	1.92e-12	6.94e-12
SC	45	1.38e-08	1.38e-08	1.38e-08	1.44e-08	2.06e-08	4.60e-08	5.22e-08	6.98e-08	9.57e-08	1.13e-07	1.35e-07	1.93e-07	2.10e-07
TI	46	1.06e-06	1.06e-06	1.06e-06	1.06e-06	9.73e-07	4.32e-07	2.89e-07	7.95e-07	1.97e-06	3.00e-06	4.62e-06	1.31e-05	2.21e-05
TI	47	1.46e-06	1.46e-06	1.44e-06	1.46e-06	1.35e-06	6.87e-07	5.22e-07	9.56e-07	1.29e-06	1.42e-06	1.53e-06	1.65e-06	1.65e-06
TI	48	6.48e-04	6.48e-04	6.48e-04	6.48e-04	6.48e-04	6.50e-04	6.50e-04	6.32e-04	6.02e-04	5.82e-04	5.52e-04	4.37e-04	3.08e-04
TI	49	4.96e-06	4.95e-06	4.96e-06	5.11e-06	7.27e-06	1.43e-05	1.58e-05	2.00e-05	2.56e-05	2.90e-05	3.28e-05	4.14e-05	4.45e-05
TI	50	1.12e-05	1.12e-05	1.12e-05	1.12e-05	1.12e-05	1.12e-05	1.12e-05	1.13e-05	1.14e-05	1.14e-05	1.15e-05	1.22e-05	1.34e-05
V	50	1.02e-08	1.02e-08	1.02e-08	1.02e-08	1.02e-08	1.02e-08	1.02e-08	1.03e-08	1.06e-08	1.09e-08	1.12e-08	1.44e-08	3.92e-08
V	51	3.47e-05	3.47e-05	3.46e-05	3.46e-05	3.28e-05	3.32e-05	3.81e-05	5.48e-05	7.50e-05	8.77e-05	1.03e-04	1.52e-04	2.11e-04
CR	50	5.45e-05	5.45e-05	5.44e-05	5.45e-05	5.43e-05	5.55e-05	6.16e-05	9.18e-05	1.48e-04	1.97e-04	2.71e-04	6.82e-04	1.28e-03
CR	52	1.52e-02	1.52e-02	1.52e-02	1.52e-02	1.52e-02	1.50e-02	1.49e-02	1.45e-02	1.40e-02	1.36e-02	1.31e-02	1.14e-02	1.03e-02
CR	53	5.09e-04	5.09e-04	5.10e-04	5.14e-04	5.56e-04	6.57e-04	6.99e-04	8.17e-04	9.77e-04	1.08e-03	1.20e-03	1.60e-03	2.04e-03
CR	54	1.79e-04	1.79e-04	1.79e-04	1.79e-04	1.79e-04	1.80e-04	1.80e-04	1.81e-04	1.82e-04	1.83e-04	1.85e-04	1.93e-04	2.11e-04
MN	55	3.73e-03	3.73e-03	3.73e-03	3.73e-03	3.74e-03	4.28e-03	4.73e-03	5.68e-03	6.85e-03	7.61e-03	8.59e-03	1.23e-02	1.69e-02
FE	54	3.48e-02	3.48e-02	3.48e-02	3.48e-02	3.49e-02	3.57e-02	3.68e-02	4.04e-02	4.66e-02	5.16e-02	5.94e-02	9.86e-02	1.61e-01
FE	56	8.62e-01	8.62e-01	8.62e-01	8.62e-01	8.62e-01	8.59e-01	8.56e-01	8.48e-01	8.36e-01	8.26e-01	8.11e-01	7.40e-01	6.29e-01
FE	57	1.31e-02	1.31e-02	1.31e-02	1.32e-02	1.33e-02	1.43e-02	1.53e-02	1.65e-02	1.81e-02	1.93e-02	2.09e-02	2.68e-02	3.21e-02
FE	58	9.51e-04	9.51e-04	9.51e-04	9.51e-04	9.51e-04	9.52e-04	9.53e-04	9.57e-04	9.63e-04	9.68e-04	9.75e-04	1.02e-03	1.09e-03
CO	59	9.01e-04	9.02e-04	8.99e-04	9.00e-04	8.70e-04	6.10e-04	5.14e-04	6.45e-04	7.66e-04	8.33e-04	9.11e-04	1.13e-03	1.26e-03
NI	58	3.38e-02	3.38e-02	3.38e-02	3.38e-02	3.38e-02	3.39e-02	3.42e-02	3.74e-02	4.35e-02	4.85e-02	5.59e-02	9.36e-02	1.57e-01
NI	60	1.47e-02	1.47e-02	1.47e-02	1.47e-02	1.47e-02	1.48e-02	1.48e-02	1.44e-02	1.38e-02	1.34e-02	1.29e-02	1.08e-02	8.55e-03
NI	61	2.06e-04	2.06e-04	2.06e-04	2.07e-04	2.09e-04	2.38e-04	2.67e-04	2.92e-04	3.13e-04	3.28e-04	3.46e-04	3.94e-04	3.89e-04
NI	62	8.77e-04	8.77e-04	8.77e-04	8.78e-04	8.81e-04	9.53e-04	1.14e-03	1.59e-03	2.19e-03	2.65e-03	3.32e-03	6.19e-03	9.33e-03
NI	64	8.89e-07	8.89e-07	8.89e-07	8.89e-07	8.89e-07	8.91e-07	8.92e-07	8.96e-07	9.03e-07	9.09e-07	9.17e-07	9.62e-07	1.05e-06
CU	63	8.24e-06	8.25e-06	8.23e-06	8.26e-06	8.18e-06	1.01e-05	8.94e-06	1.85e-06	1.81e-06	1.88e-06	2.06e-06	3.91e-06	7.99e-06
CU	65	1.47e-06	1.47e-06	1.47e-06	1.48e-06	1.50e-06	1.68e-06	1.69e-06	1.72e-06	1.99e-06	2.21e-06	2.51e-06	3.30e-06	2.99e-06
ZN	64	2.75e-04	2.75e-04	2.74e-04	2.75e-04	2.78e-04	2.64e-04	1.56e-04	5.21e-05	3.56e-05	3.12e-05	2.73e-05	1.81e-05	1.06e-05
ZN	66	6.74e-06	6.74e-06	6.74e-06	6.76e-06	6.99e-06	9.32e-06	1.17e-05	1.78e-05	2.80e-05	3.59e-05	4.71e-0		

Element	A	$^{22}\text{Ne} = 0$	1e-7	1e-6	1e-5	1e-4	1e-3	2e-3	5e-3	1e-2	1.4e-2	2e-2	5e-2	1e-1
C	12	8.98e-04	8.98e-04	8.98e-04	8.98e-04	8.97e-04	8.92e-04	8.88e-04	8.80e-04	8.72e-04	8.68e-04	8.63e-04	8.46e-04	8.23e-04
C	13	6.05e-10	6.06e-10	6.12e-10	6.00e-10	6.05e-10	1.21e-09	2.46e-09	8.51e-09	2.06e-08	3.10e-08	4.72e-08	1.27e-07	2.43e-07
N	14	1.28e-08	1.28e-08	1.28e-08	1.28e-08	1.72e-08	9.22e-08	1.58e-07	3.04e-07	4.63e-07	5.44e-07	6.34e-07	9.85e-07	1.42e-06
N	15	6.76e-07	6.75e-07	6.72e-07	6.36e-07	3.09e-07	1.11e-06	4.08e-06	1.48e-05	1.01e-05	9.42e-05	1.03e-05	4.84e-05	2.04e-04
O	16	4.81e-02	4.81e-02	4.81e-02	4.81e-02	4.85e-02	4.98e-02	5.05e-02	5.20e-02	5.34e-02	5.41e-02	5.47e-02	5.48e-02	5.12e-02
O	17	3.35e-10	3.36e-10	3.41e-10	3.96e-10	1.39e-09	2.34e-08	4.26e-08	7.10e-08	8.66e-08	9.27e-08	9.97e-08	1.06e-07	9.60e-08
O	18	5.01e-12	5.01e-12	5.07e-12	5.65e-12	1.39e-11	1.17e-10	1.91e-10	3.65e-10	6.22e-10	7.95e-10	1.12e-09	7.37e-09	3.11e-08
F	19	1.50e-10	1.50e-10	1.49e-10	1.41e-10	9.52e-11	2.80e-11	3.47e-11	6.99e-11	1.10e-10	1.43e-10	2.16e-10	4.80e-10	5.26e-10
NE	20	5.22e-04	5.22e-04	5.22e-04	5.22e-04	5.21e-04	5.14e-04	5.07e-04	4.90e-04	4.69e-04	4.56e-04	4.39e-04	3.83e-04	3.28e-04
NE	21	3.58e-09	3.58e-09	3.60e-09	3.67e-09	4.81e-09	4.59e-08	1.28e-07	3.55e-07	6.17e-07	8.42e-07	1.36e-06	4.63e-06	1.06e-05
NE	22	6.20e-09	6.20e-09	6.21e-09	6.24e-09	8.95e-09	1.30e-07	3.44e-07	1.30e-06	3.55e-06	5.66e-06	9.27e-06	3.48e-05	9.71e-05
NA	23	2.78e-06	2.78e-06	2.78e-06	2.77e-06	2.68e-06	2.36e-06	2.38e-06	2.86e-06	3.88e-06	4.86e-06	6.78e-06	1.75e-05	4.45e-05
MG	24	7.45e-03	7.45e-03	7.45e-03	7.46e-03	7.48e-03	6.98e-03	6.26e-03	4.58e-03	3.01e-03	2.32e-03	1.71e-03	9.06e-04	1.19e-03
MG	25	7.99e-08	7.99e-08	8.07e-08	8.15e-08	1.12e-07	1.26e-06	2.00e-06	4.46e-06	9.19e-06	1.37e-05	2.12e-05	7.10e-05	2.23e-04
MG	26	3.26e-07	3.26e-07	3.26e-07	3.31e-07	3.92e-07	1.04e-06	1.68e-06	3.46e-06	6.28e-06	8.48e-06	1.18e-05	3.42e-05	1.32e-04
AL	27	1.74e-05	1.74e-05	1.74e-05	1.73e-05	1.61e-05	4.21e-05	7.16e-05	1.20e-04	1.48e-04	1.56e-04	1.59e-04	1.78e-04	3.01e-04
SI	28	1.89e-01	1.89e-01	1.89e-01	1.89e-01	1.89e-01	1.92e-01	1.94e-01	1.95e-01	1.94e-01	1.94e-01	1.93e-01	1.91e-01	1.85e-01
SI	29	2.54e-05	2.54e-05	2.54e-05	2.52e-05	2.62e-05	9.40e-05	1.19e-04	1.60e-04	1.98e-04	2.23e-04	2.62e-04	5.92e-04	2.37e-03
SI	30	1.32e-05	1.32e-05	1.31e-05	1.21e-05	5.46e-06	1.16e-05	3.82e-05	1.36e-04	2.99e-04	4.22e-04	6.02e-04	1.82e-03	5.76e-03
P	31	2.92e-05	2.92e-05	2.91e-05	2.80e-05	1.97e-05	2.31e-05	3.57e-05	6.91e-05	1.14e-04	1.44e-04	1.83e-04	3.54e-04	5.35e-04
S	32	1.10e-01	1.10e-01	1.10e-01	1.10e-01	1.09e-01	1.07e-01	1.07e-01	1.06e-01	1.05e-01	1.04e-01	1.02e-01	9.06e-02	7.14e-02
S	33	1.58e-05	1.58e-05	1.58e-05	1.62e-05	1.95e-05	3.34e-05	4.31e-05	6.81e-05	9.91e-05	1.19e-04	1.44e-04	2.30e-04	4.45e-04
S	34	2.03e-06	2.03e-06	2.01e-06	1.84e-06	7.15e-07	3.58e-05	1.05e-04	3.32e-04	7.38e-04	1.08e-03	1.59e-03	4.19e-03	7.64e-03
S	36	6.84e-15	6.85e-15	6.88e-15	7.19e-15	1.31e-14	4.00e-11	2.38e-10	1.88e-09	7.90e-09	1.70e-08	3.96e-08	5.92e-07	5.30e-06
CL	35	5.26e-06	5.26e-06	5.24e-06	5.04e-06	3.74e-06	6.71e-06	1.09e-05	2.18e-05	3.81e-05	5.02e-05	6.65e-05	1.15e-04	1.29e-04
CL	37	1.34e-06	1.34e-06	1.34e-06	1.39e-06	1.76e-06	3.30e-06	4.43e-06	7.17e-06	1.07e-05	1.31e-05	1.62e-05	2.60e-05	2.96e-05
AR	36	2.37e-02	2.37e-02	2.37e-02	2.37e-02	2.36e-02	2.28e-02	2.24e-02	2.18e-02	2.11e-02	2.06e-02	1.99e-02	1.64e-02	1.23e-02
AR	38	5.56e-07	5.61e-07	5.65e-07	5.36e-07	4.67e-07	1.80e-05	4.67e-05	1.48e-04	3.50e-04	5.29e-04	8.09e-04	2.14e-03	3.57e-03
AR	40	1.77e-16	1.77e-16	1.78e-16	1.85e-16	2.81e-16	5.47e-13	2.82e-12	1.97e-11	9.77e-11	2.39e-10	6.73e-10	1.09e-08	6.34e-08
K	39	1.67e-06	1.67e-06	1.67e-06	1.62e-06	1.44e-06	5.73e-06	1.00e-05	2.01e-05	3.35e-05	4.28e-05	5.48e-05	8.94e-05	8.87e-05
K	40	4.46e-13	4.46e-13	4.47e-13	4.65e-13	8.19e-13	2.32e-10	5.29e-10	1.72e-09	4.90e-09	8.45e-09	1.48e-08	3.38e-08	2.67e-08
K	41	2.00e-07	2.00e-07	2.01e-07	2.10e-07	2.99e-07	6.20e-07	8.67e-07	1.47e-06	2.23e-06	2.73e-06	3.33e-06	4.82e-06	4.37e-06
CA	40	2.43e-02	2.43e-02	2.43e-02	2.43e-02	2.41e-02	2.31e-02	2.26e-02	2.17e-02	2.08e-02	2.02e-02	1.93e-02	1.59e-02	1.21e-02
CA	42	4.59e-09	4.59e-09	4.59e-09	4.45e-09	2.60e-09	3.23e-07	9.31e-07	3.32e-06	8.39e-06	1.30e-05	2.04e-05	5.18e-05	7.03e-05
CA	43	7.18e-08	7.16e-08	7.07e-08	6.87e-08	4.96e-08	8.44e-08	1.88e-07	3.26e-07	3.57e-07	3.45e-07	3.31e-07	2.32e-07	1.60e-07
CA	44	2.46e-05	2.44e-05	2.45e-05	2.48e-05	2.44e-05	2.39e-05	2.35e-05	2.20e-05	2.06e-05	1.96e-05	1.84e-05	1.37e-05	9.14e-06
CA	46	6.31e-22	6.32e-22	6.40e-22	7.33e-22	2.91e-21	2.85e-17	4.86e-16	1.70e-14	2.61e-13	1.06e-12	4.61e-12	9.42e-11	6.21e-10
CA	48	5.82e-30	5.84e-30	5.98e-30	7.69e-30	7.71e-29	1.75e-23	1.21e-21	1.08e-19	3.78e-18	3.11e-17	1.81e-16	4.78e-14	4.63e-12
SC	45	1.59e-08	1.59e-08	1.60e-08	1.70e-08	2.81e-08	5.72e-08	6.77e-08	9.25e-08	1.21e-07	1.39e-07	1.59e-07	1.98e-07	1.96e-07
TI	46	1.48e-07	1.50e-07	1.52e-07	1.43e-07	1.32e-07	1.62e-07	4.34e-07	1.69e-06	4.36e-06	6.68e-06	1.02e-05	2.47e-05	3.44e-05
TI	47	2.65e-07	2.68e-07	2.69e-07	2.57e-07	2.33e-07	1.29e-07	1.85e-07	3.32e-07	4.68e-07	5.43e-07	6.44e-07	9.76e-07	1.42e-06
TI	48	5.27e-04	5.26e-04	5.27e-04	5.27e-04	5.26e-04	5.20e-04	5.14e-04	4.97e-04	4.72e-04	4.55e-04	4.31e-04	3.39e-04	2.39e-04
TI	49	3.06e-06	3.06e-06	3.08e-06	3.21e-06	5.56e-06	1.12e-05	1.25e-05	1.61e-05	2.07e-05	2.35e-05	2.66e-05	3.34e-05	3.62e-05
TI	50	4.22e-20	4.22e-20	4.27e-20	4.77e-20	1.33e-19	2.22e-14	3.58e-13	9.33e-12	8.13e-11	1.93e-10	3.78e-10	1.08e-09	6.71e-09
V	50	1.29e-16	1.30e-16	1.33e-16	1.42e-16	3.24e-16	1.25e-12	7.90e-12	9.85e-11	6.11e-10	1.22e-09	1.97e-09	6.39e-09	3.84e-08
V	51	7.90e-06	7.93e-06	7.96e-06	7.77e-06	6.16e-06	1.07e-05	1.73e-05	3.19e-05	4.92e-05	6.00e-05	7.32e-05	1.15e-04	1.75e-04
CR	50	2.15e-06	2.17e-06	2.21e-06	2.13e-06	2.30e-06	6.79e-06	1.59e-05	4.77e-05	1.07e-04	1.57e-04	2.37e-04	6.76e-04	1.72e-03
CR	52	1.14e-02	1.14e-02	1.14e-02	1.14e-02	1.14e-02	1.12e-02	1.11e-02	1.07e-02	1.03e-02	9.94e-03	9.51e-03	8.04e-03	7.64e-03
CR	53	2.03e-04	2.04e-04	2.04e-04	2.08e-04	2.53e-04	3.23e-04	3.60e-04	4.63e-04	5.99e-04	6.85e-04	7.88e-04	1.13e-03	1.57e-03
CR	54	3.96e-15	3.98e-15	4.10e-15	4.41e-15	1.99e-14	3.97e-11	2.06e-10	1.72e-09	7.84e-09	1.64e-08	3.62e-08	3.80e-07	2.78e-06
MN	55	1.19e-04	1.19e-04	1.20e-04	1.20e-04	1.32e-04	6.67e-04	1.05e-03	1.88e-03	2.86e-03	3.48e-03	4.25e-03	6.97e-03	1.02e-02
FE	54	4.55e-05	4.55e-05	4.60e-05	4.67e-05	5.93e-05	8.29e-04	1.86e-03	5.15e-03	1.09e-02	1.55e-02	2.25e-02	5.64e-02	1.05e-01
FE	56	5.67e-01	5.67e-01	5.67e-01	5.67e-01	5.67e-01	5.65e-01	5.63e-01	5.57e-01	5.47e-01	5.40e-01	5.30e-01	4.82e-01	4.09e-01
FE	57	4.63e-03	4.63e-03	4.61e-03	4.65e-03	4.71e-03	5.56e-03	6.15e-03	6.92e-03	8.10e-03	8.95e-03	1.01e-02	1.43e-02	1.83e-02
FE	58	2.89e-14	2.90e-14	2.93e-14	3.16e-14	1.04e-13	1.97e-11	8.32e-11	5.90e-10	2.50e-09	5.07e-09	1.07e-08	8.44e-08	3.90e-07
CO	59	2.87e-04	2.88e-04	2.91e-04	2.81e-04	2.60e-04	7.84e-05	8.21e-05	1.56e-04	2.27e-04	2.68e-04	3.17e-04	4.43e-04	4.79e-04
NI	58	7.11e-04	7.14e-04	7.23e-04	7.04e-04	6.98e-04	4.84e-04	6.53e-04	2.88e-03	6.68e-03	9.80e-03	1.45e-02	3.91e-02	8.21e-02
NI	60	5.96e-03	5.95e-03	5.97e-03	5.96e-03	5.98e-03	6.07e-03	6.07e-03	5.70e-03	5.34e-03	5.10e-03	4.80e-03	3.46e-03	1.86e-03
NI	61	8.85e-05	8.81e-05	8.80e-05	8.89e-05	9.03e-05	1.10e-04	1.22e-04	1.30e-04	1.41e-04	1.49e-04	1.59e-04	1.75e-04	1.47e-04
NI	62	4.49e-05	4.51e-05	4.08e-05	4.53e-05	4.46e-05	1.39e-04	2.51e-04	4.64e-04	8.00e-04	1.06e-03	1.43e-03	2.84e-03	3.59e-03
NI	64	3.68e-23	3.65e-23	3.72e-23	3.71e-23	3.93e-23	8.17e-20	1.68e-18	2.26e-17	2.57e-17	2.77e-17	3.36e-17	2.53e-16	4.62e-15
CU	63	5.10e-06	5.10e-06	4.89e-06	5.12e-06	5.18e-06	6.82e-06	7.04e-07	3.13e-07	3.25e-07	3.76e-07	4.93e-07	1.30e-06	2.39e-06
CU	65	6.59e-07	6.54e-07	6.64e-07	6.61e-07	6.75e-07	6.55e-07	5.97e-07	6.27e-07	7.21e-07	7.82e-07	8.67e-07	9.10e-07	5.01e-07
ZN	64	1.51e-04	1.50e-04	1.55e-04	1.51e-04	1.55e-04	9.22e-05	3.64e-05	1.85e-05	1.34e-05	1.16e-05	1.01e-05	5.65e-06	2.08e-06
ZN	66	2.39e-06	2.37e-06	2.37e-06	2.41e-06	2.49e-06	3.42e-06	4.29e-06	6.89e-06	1.12e-05	1.43e-05	1.87e-		

Element	A	²² Ne = 0	1e-7	1e-6	1e-5	1e-4	1e-3	2e-3	5e-3	1e-2	1.4e-2	2e-2	5e-2	1e-1
C	12	7.08e-03	7.08e-03	7.08e-03	7.08e-03	7.08e-03	7.05e-03	7.03e-03	6.98e-03	6.93e-03	6.89e-03	6.85e-03	6.69e-03	6.47e-03
C	13	6.53e-11	6.52e-11	6.51e-11	6.39e-11	7.94e-11	1.47e-09	3.95e-09	1.25e-08	2.85e-08	4.25e-08	6.59e-08	2.22e-07	5.94e-07
N	14	7.50e-08	7.50e-08	7.49e-08	7.43e-08	8.36e-08	4.04e-07	7.84e-07	1.79e-06	3.24e-06	4.28e-06	5.70e-06	1.12e-05	1.71e-05
N	15	2.98e-06	2.98e-06	2.97e-06	2.87e-06	1.87e-06	1.44e-07	5.62e-08	1.93e-08	1.16e-08	1.04e-08	1.06e-08	2.31e-08	8.85e-08
O	16	1.79e-01	1.79e-01	1.79e-01	1.79e-01	1.79e-01	1.81e-01	1.82e-01	1.87e-01	1.92e-01	1.95e-01	1.98e-01	2.00e-01	1.91e-01
O	17	1.87e-09	1.87e-09	1.88e-09	2.01e-09	3.81e-09	7.45e-08	1.74e-07	4.16e-07	6.86e-07	8.36e-07	1.00e-06	1.32e-06	1.31e-06
O	18	1.82e-11	1.82e-11	1.83e-11	1.92e-11	3.23e-11	4.94e-10	1.13e-09	2.94e-09	5.93e-09	8.37e-09	1.22e-08	3.79e-08	1.46e-07
F	19	2.63e-09	2.63e-09	2.61e-09	2.49e-09	1.77e-09	5.07e-10	3.53e-10	4.22e-10	8.10e-10	1.18e-09	1.78e-09	5.03e-09	8.28e-09
NE	20	6.42e-03	6.42e-03	6.42e-03	6.42e-03	6.42e-03	6.38e-03	6.33e-03	6.19e-03	5.97e-03	5.81e-03	5.59e-03	4.83e-03	4.17e-03
NE	21	3.63e-08	3.63e-08	3.64e-08	3.70e-08	4.39e-08	2.18e-07	5.46e-07	1.78e-06	4.21e-06	6.38e-06	1.00e-05	3.53e-05	1.01e-04
NE	22	6.82e-08	6.86e-08	7.13e-08	9.91e-08	3.80e-07	3.36e-06	6.90e-06	1.86e-05	4.06e-05	6.02e-05	9.24e-05	3.00e-04	8.24e-04
NA	23	2.72e-05	2.72e-05	2.72e-05	2.71e-05	2.66e-05	2.46e-05	2.47e-05	2.69e-05	3.39e-05	4.11e-05	5.35e-05	1.41e-04	4.07e-04
MG	24	3.78e-02	3.78e-02	3.78e-02	3.78e-02	3.79e-02	3.64e-02	3.42e-02	2.83e-02	2.15e-02	1.80e-02	1.44e-02	7.96e-03	7.59e-03
MG	25	5.16e-07	5.16e-07	5.17e-07	5.28e-07	6.80e-07	6.98e-06	1.26e-05	3.30e-05	7.65e-05	1.18e-04	1.92e-04	7.51e-04	2.51e-03
MG	26	3.47e-06	3.47e-06	3.47e-06	3.51e-06	3.97e-06	9.35e-06	1.49e-05	3.06e-05	5.73e-05	8.02e-05	1.17e-04	3.79e-04	1.56e-03
AL	27	1.40e-04	1.40e-04	1.40e-04	1.39e-04	1.38e-04	2.83e-04	4.75e-04	8.48e-04	1.16e-03	1.29e-03	1.39e-03	1.61e-03	2.45e-03
SI	28	3.04e-01	3.04e-01	3.04e-01	3.04e-01	3.05e-01	3.11e-01	3.14e-01	3.19e-01	3.21e-01	3.21e-01	3.21e-01	3.16e-01	3.05e-01
SI	29	6.04e-05	6.04e-05	6.04e-05	6.10e-05	7.47e-05	2.73e-04	3.46e-04	5.10e-04	7.32e-04	9.11e-04	1.21e-03	3.57e-03	1.35e-02
SI	30	2.95e-05	2.95e-05	2.94e-05	2.84e-05	2.24e-05	4.34e-05	1.42e-04	5.67e-04	1.39e-03	2.05e-03	3.04e-03	8.48e-03	1.98e-02
P	31	8.92e-05	8.91e-05	8.88e-05	8.57e-05	5.93e-05	6.00e-05	1.06e-04	2.36e-04	4.27e-04	5.62e-04	7.44e-04	1.42e-03	1.63e-03
S	32	1.56e-01	1.56e-01	1.56e-01	1.56e-01	1.55e-01	1.53e-01	1.52e-01	1.51e-01	1.50e-01	1.49e-01	1.46e-01	1.28e-01	9.52e-02
S	33	9.39e-05	9.39e-05	9.39e-05	9.47e-05	1.02e-04	1.16e-04	1.35e-04	2.06e-04	2.99e-04	3.56e-04	4.22e-04	5.80e-04	5.30e-04
S	34	4.32e-06	4.32e-06	4.29e-06	4.07e-06	2.54e-06	7.79e-05	2.34e-04	7.31e-04	1.63e-03	2.39e-03	3.59e-03	9.36e-03	1.47e-02
S	36	3.74e-14	3.74e-14	3.76e-14	3.91e-14	6.20e-14	1.50e-10	1.00e-09	8.64e-09	3.97e-08	8.58e-08	2.14e-07	3.87e-06	3.5e-05
CL	35	1.02e-05	1.02e-05	1.02e-05	9.71e-06	6.19e-06	1.27e-05	2.14e-05	4.52e-05	8.64e-05	1.19e-04	1.64e-04	2.59e-04	2.25e-04
CL	37	5.91e-06	5.92e-06	5.92e-06	5.98e-06	6.51e-06	7.39e-06	8.99e-06	1.37e-05	2.02e-05	2.46e-05	3.02e-05	4.81e-05	5.73e-05
AR	36	3.03e-02	3.03e-02	3.03e-02	3.02e-02	3.00e-02	2.86e-02	2.77e-02	2.64e-02	2.50e-02	2.40e-02	2.28e-02	1.73e-02	1.14e-02
AR	38	3.97e-07	3.97e-07	3.96e-07	3.87e-07	2.84e-07	3.69e-05	9.57e-05	2.97e-04	6.96e-04	1.05e-03	1.61e-03	4.30e-03	6.97e-03
AR	40	6.21e-16	6.21e-16	6.23e-16	6.46e-16	9.46e-16	1.65e-12	9.21e-12	6.81e-11	3.47e-10	8.83e-10	2.17e-09	5.99e-08	3.21e-07
K	39	1.33e-06	1.33e-06	1.33e-06	1.27e-06	1.03e-06	1.00e-05	1.73e-05	3.47e-05	5.97e-05	7.76e-05	1.01e-04	1.66e-04	1.58e-04
K	40	1.53e-12	1.53e-12	1.54e-12	1.58e-12	2.30e-12	5.19e-10	1.13e-09	3.64e-09	1.20e-08	2.29e-08	4.48e-08	1.11e-07	4.28e-08
K	41	3.73e-07	3.73e-07	3.75e-07	3.93e-07	5.68e-07	1.18e-06	1.58e-06	2.57e-06	3.88e-06	4.75e-06	5.82e-06	8.41e-06	7.34e-06
CA	40	2.71e-02	2.71e-02	2.71e-02	2.71e-02	2.68e-02	2.48e-02	2.36e-02	2.16e-02	1.96e-02	1.84e-02	1.69e-02	1.20e-02	7.55e-03
CA	42	4.74e-09	4.73e-09	4.70e-09	4.33e-09	6.78e-10	6.64e-07	1.89e-06	6.65e-06	1.70e-05	2.66e-05	4.21e-05	1.10e-04	1.45e-04
CA	43	2.37e-08	2.37e-08	2.33e-08	1.94e-08	1.61e-10	7.06e-10	1.98e-09	8.61e-09	2.68e-08	4.52e-08	7.44e-08	1.75e-07	2.35e-07
CA	44	1.24e-05	1.24e-05	1.24e-05	1.24e-05	1.22e-05	1.10e-05	1.03e-05	9.08e-06	8.01e-06	7.42e-06	6.75e-06	4.71e-06	3.14e-06
CA	46	2.39e-21	2.40e-21	2.43e-21	2.75e-21	9.64e-21	1.81e-16	2.97e-15	9.00e-14	1.15e-12	4.30e-12	1.82e-11	4.47e-10	2.55e-09
CA	48	4.90e-27	4.95e-27	5.30e-27	8.82e-27	3.06e-26	3.55e-23	1.97e-21	2.08e-19	7.61e-18	5.25e-17	5.08e-16	2.32e-13	2.31e-11
SC	45	2.23e-08	2.23e-08	2.26e-08	2.53e-08	4.86e-08	7.72e-08	9.39e-08	1.27e-07	1.66e-07	1.89e-07	2.18e-07	2.49e-07	2.06e-07
TI	46	1.60e-09	1.60e-09	1.61e-09	1.66e-09	3.56e-09	2.77e-07	8.22e-07	3.18e-06	8.31e-06	1.29e-05	1.98e-05	4.83e-05	6.26e-05
TI	47	1.98e-08	1.98e-08	1.96e-08	1.81e-08	4.30e-09	1.86e-08	3.34e-08	7.99e-08	1.77e-07	2.67e-07	4.10e-07	1.12e-06	2.05e-06
TI	48	2.25e-04	2.25e-04	2.25e-04	2.25e-04	2.24e-04	2.13e-04	2.04e-04	1.85e-04	1.61e-04	1.46e-04	1.28e-04	7.70e-05	4.86e-05
TI	49	4.26e-07	4.27e-07	4.37e-07	5.50e-07	4.27e-06	5.80e-06	6.75e-06	8.91e-06	1.11e-05	1.21e-05	1.29e-05	1.25e-05	1.22e-05
TI	50	9.89e-20	9.90e-20	1.00e-19	1.14e-19	3.64e-19	4.40e-14	7.78e-13	2.48e-11	2.53e-10	6.11e-10	1.17e-09	2.92e-09	1.17e-08
V	50	1.03e-16	1.03e-16	1.04e-16	1.15e-16	4.39e-16	2.96e-12	1.85e-11	2.50e-10	1.67e-09	3.27e-09	4.92e-09	1.02e-08	5.06e-08
V	51	2.93e-06	2.93e-06	2.93e-06	2.89e-06	4.92e-07	6.29e-06	1.02e-05	1.82e-05	2.72e-05	3.26e-05	3.88e-05	5.65e-05	1.07e-04
CR	50	2.00e-07	2.00e-07	2.03e-07	2.32e-07	3.13e-07	7.46e-06	1.77e-05	5.29e-05	1.20e-04	1.78e-04	2.72e-04	8.06e-04	1.49e-03
CR	52	3.17e-03	3.17e-03	3.17e-03	3.17e-03	3.16e-03	3.04e-03	2.93e-03	2.67e-03	2.36e-03	2.17e-03	1.95e-03	1.60e-03	3.68e-03
CR	53	4.71e-05	4.72e-05	4.75e-05	5.09e-05	8.63e-05	1.10e-04	1.30e-04	1.75e-04	2.20e-04	2.44e-04	2.70e-04	4.00e-04	8.60e-04
CR	54	3.51e-16	3.52e-16	3.63e-16	4.98e-16	1.76e-14	6.46e-11	3.13e-10	2.55e-09	1.13e-08	2.32e-08	5.15e-08	5.42e-07	3.90e-06
MN	55	2.24e-05	2.24e-05	2.22e-05	2.02e-05	2.28e-05	2.74e-04	4.22e-04	7.06e-04	1.00e-03	1.17e-03	1.37e-03	2.05e-03	3.32e-03
FE	54	1.29e-05	1.29e-05	1.29e-05	1.29e-05	1.52e-05	7.50e-04	1.64e-03	4.38e-03	9.04e-03	1.28e-02	1.83e-02	4.28e-02	6.81e-02
FE	56	4.87e-02	4.87e-02	4.87e-02	4.87e-02	4.86e-02	4.70e-02	4.55e-02	4.21e-02	3.79e-02	3.53e-02	3.22e-02	2.41e-02	2.32e-02
FE	57	1.56e-04	1.56e-04	1.56e-04	1.56e-04	1.62e-04	2.05e-04	2.44e-04	3.14e-04	4.24e-04	4.74e-04	5.27e-04	6.42e-04	7.45e-04
FE	58	2.64e-14	2.64e-14	2.69e-14	3.19e-14	1.96e-13	4.31e-11	1.46e-10	9.14e-10	3.70e-09	7.43e-09	1.57e-08	1.22e-07	5.50e-07
CO	59	2.64e-07	2.64e-07	2.62e-07	2.41e-07	1.84e-08	2.06e-08	4.91e-08	1.94e-07	5.82e-07	9.98e-07	1.78e-06	8.46e-06	1.86e-05
NI	58	2.47e-05	2.47e-05	2.47e-05	2.55e-05	3.21e-05	8.12e-05	1.37e-04	3.10e-04	6.01e-04	8.29e-04	1.16e-03	2.42e-03	3.66e-03
NI	60	3.75e-07	3.74e-07	3.68e-07	3.10e-07	5.72e-09	7.91e-09	2.97e-08	2.18e-07	1.01e-06	2.14e-06	4.70e-06	3.64e-05	1.42e-04
NI	61	6.86e-10	6.85e-10	6.76e-10	5.89e-10	3.55e-11	6.52e-12	1.46e-11	6.66e-11	2.57e-10	5.33e-10	1.19e-09	9.71e-09	4.84e-08
NI	62	5.76e-12	5.77e-12	5.78e-12	5.97e-12	7.73e-12	1.42e-11	2.79e-11	8.07e-11	1.84e-10	3.05e-10	5.80e-10	4.91e-09	3.65e-08
NI	64	2.94e-26	2.95e-26	2.98e-26	3.38e-26	1.43e-25	4.28e-19	6.16e-18	6.62e-17	5.89e-17	5.81e-17	6.72e-17	2.85e-16	5.13e-15
CU	63	7.49e-15	7.50e-15	7.61e-15	8.87e-15	3.62e-14	2.36e-14	5.45e-14	2.54e-13	1.16e-12	2.75e-12	6.94e-12	7.07e-11	3.37e-10
CU	65	3.86e-17	3.85e-17	3.79e-17	3.19e-17	3.54e-18	8.11e-17	1.77e-16	5.52e-16	1.30e-15	2.82e-15	6.78e-15	5.94e-14	2.38e-13
ZN	64	2.28e-15	2.28e-15	2.28e-15	2.32e-15	6.07e-15	4.58e-14	1.21e-13	7.19e-13	3.29e-12	6.91e-12	1.49e-11	9.45e-11	2.60e-10
ZN	66	3.70e-18	3.70e-18	3.66e-18	3.31e-18	1.56e-18	1.10e-15	6.38e-15	2.18e-14	9.51e-15	9.05e-15			

Appendix B

Rates

Element	A	Reaction	Element	A	Reaction
H	1	(n,g)	CA	43	(n,g)
H	2	(n,g)	CA	44	(n,g)
LI	7	(n,g)	CA	45	(n,g)
BE	9	(n,g)	CA	46	(n,g)
C	12	(n,g)	CA	48	(n,g)
C	13	(n,g)	SC	45	(n,g)
C	14	(n,g)	TI	46	(n,g)
N	14	(n,g)	TI	47	(n,g)
N	15	(n,g)	TI	48	(n,g)
O	16	(n,g)	TI	49	(n,g)
O	17	(n,g)	TI	50	(n,g)
O	18	(n,g)	V	50	(n,g)
F	19	(n,g)	V	51	(n,g)
NE	20	(n,g)	CR	50	(n,g)
NE	21	(n,g)	CR	51	(n,g)
NE	22	(n,g)	CR	52	(n,g)
NA	23	(n,g)	CR	53	(n,g)
MG	24	(n,g)	CR	54	(n,g)
MG	25	(n,g)	MN	55	(n,g)
MG	26	(n,g)	FE	54	(n,g)
AL	26	(n,g)	FE	55	(n,g)
AL	27	(n,g)	FE	56	(n,g)
SI	28	(n,g)	FE	57	(n,g)
SI	29	(n,g)	FE	58	(n,g)
SI	30	(n,g)	FE	60	(n,g)
P	31	(n,g)	CO	59	(n,g)
S	32	(n,g)	NI	58	(n,g)
S	33	(n,g)	NI	59	(n,g)
S	34	(n,g)	NI	60	(n,g)
S	36	(n,g)	NI	61	(n,g)
CL	35	(n,g)	NI	62	(n,g)
CL	36	(n,g)	NI	63	(n,g)
CL	37	(n,g)	NI	64	(n,g)
AR	36	(n,g)	CU	63	(n,g)
AR	38	(n,g)	CU	65	(n,g)
AR	39	(n,g)	ZN	64	(n,g)
AR	40	(n,g)	ZN	65	(n,g)
K	39	(n,g)	ZN	66	(n,g)
K	40	(n,g)	ZN	67	(n,g)
K	41	(n,g)	ZN	68	(n,g)
CA	40	(n,g)	ZN	70	(n,g)

TABLE B.1: Selection of KADONIS rates comprising of (n, γ)

Bibliography

- Aasi, J et al. (2015). "Characterization of the LIGO detectors during their sixth science run". In: *Classical and Quantum Gravity* 32.11, p. 115012.
- Abt, Helmut A and Saul G Levy (1976). "Multiplicity among solar-type stars". In: *The Astrophysical Journal Supplement Series* 30, pp. 273–306.
- Anders, Edward and Mitsuru Ebihara (1982). "Solar-system abundances of the elements". In: *Geochimica et Cosmochimica Acta* 46.11, pp. 2363–2380.
- Angulo, Carmen et al. (1999). "A compilation of charged-particle induced thermonuclear reaction rates". In: *Nuclear Physics A* 656.1, pp. 3–183.
- Arnett, David and Eli Livne (1994). "The delayed-detonation model of a type IA supernovae. 1: The deflagration phase". In: *The Astrophysical Journal* 427, pp. 315–329.
- Arnett, W David (1969). "A possible model of supernovae: detonation of ^{12}C ". In: *Astrophysics and Space Science* 5.2, pp. 180–212.
- Arnett, W David, JW Truran, and Stanford E Woosley (1971). "Nucleosynthesis in Supernova Models. II. The ^{12}C Detonation Model". In: *The Astrophysical Journal* 165, p. 87.
- Arnett, William David (1996). *Supernovae and nucleosynthesis: an investigation of the history of matter, from the big bang to the present*. Princeton University Press.
- Asplund, Martin et al. (2009). "The chemical composition of the Sun". In: *Annual Review of Astronomy and Astrophysics* 47, pp. 481–522.
- Baade, Walter and Fritz Zwicky (1934). "On super-novae". In: *Proceedings of the National Academy of Sciences* 20.5, pp. 254–259.

- Battino, Umberto et al. (2020). "Heavy elements nucleosynthesis on accreting white dwarfs: building seeds for the p-process". In: *Monthly Notices of the Royal Astronomical Society* 497.4, pp. 4981–4998.
- Belczynski, Krzysztof et al. (2007). "On the rarity of double black hole binaries: consequences for gravitational wave detection". In: *The Astrophysical Journal* 662.1, p. 504.
- Botyánszki, János, Daniel Kasen, and Tomasz Plewa (2017). "Multidimensional models of type Ia supernova nebular spectra: strong emission lines from stripped companion gas rule out classic single-degenerate systems". In: *The Astrophysical Journal Letters* 852.1, p. L6.
- Brachwitz, Franziska et al. (2000). "The role of electron captures in Chandrasekhar-mass models for Type Ia supernovae". In: *The Astrophysical Journal* 536.2, p. 934.
- Branch, David et al. (1995). "In search of the progenitors of type Ia supernovae". In: *Publications of the Astronomical Society of the Pacific* 107.717, p. 1019.
- Bravo, E, C Badenes, and D García-Senz (2005). "Thermonuclear supernova models, and observations of Type Ia supernovae". In: *AIP Conference Proceedings*. Vol. 797. 1. American Institute of Physics, pp. 453–462.
- Bravo, E et al. (2010). "Metallicity as a source of dispersion in the SNIa bolometric light curve luminosity-width relationship". In: *The Astrophysical Journal Letters* 711.2, p. L66.
- Calder, AC et al. (2007). "Capturing the fire: Flame energetics and neutronization for Type Ia supernova simulations". In: *The Astrophysical Journal* 656.1, p. 313.
- Cashmore, Claire R et al. (2017). "Too small to succeed: the difficulty of sustaining star formation in low-mass haloes". In: *Monthly Notices of the Royal Astronomical Society* 468.1, pp. 451–468.

- Caughlan, Georgeanne R and William A Fowler (1988). "Thermonuclear reaction rates V". In: *Atomic Data and Nuclear Data Tables* 40.2, pp. 283–334.
- Cyburt, Richard H et al. (2010). "The JINA REACLIB database: its recent updates and impact on type-I X-ray bursts". In: *The Astrophysical Journal Supplement Series* 189.1, p. 240.
- Da Silva, LAL (1993). "The classification of supernovae". In: *Astrophysics and space science* 202.2, pp. 215–236.
- Della Valle, Massimo et al. (2005). "Why are radio galaxies prolific producers of type Ia supernovae?" In: *The Astrophysical Journal* 629.2, p. 750.
- Dillmann, I et al. (2006). "KADoNiS-The Karlsruhe Astrophysical Database of Nucleosynthesis in Stars". In: *AIP conference proceedings*. Vol. 819. 1. American Institute of Physics, pp. 123–127.
- Doherty, Carolyn L et al. (2015). "Super-and massive AGB stars–IV. Final fates–initial-to-final mass relation". In: *Monthly Notices of the Royal Astronomical Society* 446.3, pp. 2599–2612.
- Domínguez, Inma, Peter Höflich, and Oscar Straniero (2001). "Constraints on the progenitors of type Ia supernovae and implications for the cosmological equation of state". In: *The Astrophysical Journal* 557.1, p. 279.
- Duchêne, Gaspard and Adam Kraus (2013). "Stellar multiplicity". In: *Annual Review of Astronomy and Astrophysics* 51, pp. 269–310.
- Eitner, Philipp et al. (2020). "Observational constraints on the origin of the elements-III. Evidence for the dominant role of sub-Chandrasekhar SN Ia in the chemical evolution of Mn and Fe in the Galaxy". In: *Astronomy & Astrophysics* 635, A38.
- Fadlisyah, Muhammad (2014). "A Rewriting-Logic-Based Approach for the Formal Modeling and Analysis of Interacting Hybrid Systems". PhD thesis. University of Oslo, Norway.

- Fink, M et al. (2010). "Double-detonation sub-Chandrasekhar supernovae: can minimum helium shell masses detonate the core?" In: *Astronomy & Astrophysics* 514, A53.
- Fryer, CL, SE Woosley, and A Heger (2001). "Pair-instability supernovae, gravity waves, and gamma-ray transients". In: *The Astrophysical Journal* 550.1, p. 372.
- Fuller, George M, William A Fowler, and Michael J Newman (1982). "STELLAR WEAK INTERACTION RATES FOR INTERMEDIATE-MASS NUCLEI. 2. A= 21 TO A= 60". In: *Astrophysical Journal* 252.2, pp. 715–740.
- Fuller, GM, WA Fowler, and MJ Newman (1985). "STELLAR WEAK INTERACTION RATES FOR INTERMEDIATE-MASS NUCLEI. 4. INTERPOLATION PROCEDURES FOR RAPIDLY VARYING LEPTON CAPTURE RATES USING EFFECTIVE LOG (FT)-VALUES". In: *Astrophysical Journal* 293.1, pp. 1–16.
- García Senz, Domingo, Eduardo Bravo Guil, and S Woosley (1999). "Single and multiple detonations in white dwarfs". In: *Astronomy and astrophysics* 349.1, pp. 177–188.
- Gibson, Brad K et al. (2003). "Galactic chemical evolution". In: *Publications of the Astronomical Society of Australia* 20.4, pp. 401–415.
- Gomez, Haley Louise et al. (2012). "A COOL DUST FACTORY IN THE CRAB NEBULA: A HERSCHEL* STUDY OF THE FILAMENTS". In: *The Astrophysical Journal* 760.1, p. 96.
- Goriely, Stéphane (1999). "Uncertainties in the solar system r-abundance distribution". In: *Astronomy and Astrophysics* 342, pp. 881–891.
- Greggio, L and A Renzini (1983). "The binary model for type I supernovae-Theoretical rates". In: *Astronomy and Astrophysics* 118, pp. 217–222.
- Greggio, Laura (2005). "The rates of type Ia supernovae-I. Analytical formulations". In: *Astronomy & Astrophysics* 441.3, pp. 1055–1078.

- Gronow, Sabrina et al. (2020). "SNe Ia from double detonations: Impact of core-shell mixing on the carbon ignition mechanism". In: *Astronomy & Astrophysics* 635, A169.
- Hamers, Adrian S et al. (2013). "Population synthesis of triple systems in the context of mergers of carbon–oxygen white dwarfs". In: *Monthly Notices of the Royal Astronomical Society* 430.3, pp. 2262–2280.
- Hamuy, Mario et al. (2003). "An asymptotic-giant-branch star in the progenitor system of a type Ia supernova". In: *Nature* 424.6949, pp. 651–654.
- Hansen, Brad MS (2003). "Type Ia Supernovae and High-Velocity White Dwarfs". In: *The Astrophysical Journal* 582.2, p. 915.
- Heger, Alexander et al. (2003). "How massive single stars end their life". In: *The Astrophysical Journal* 591.1, p. 288.
- Hillebrandt, Wolfgang and Jens C Niemeyer (2000). "Type Ia supernova explosion models". In: *Annual Review of Astronomy and Astrophysics* 38.1, pp. 191–230.
- Hillman, Yael et al. (2016). "Growing white dwarfs to the Chandrasekhar limit: the parameter space of the single degenerate SN Ia channel". In: *The Astrophysical Journal* 819.2, p. 168.
- Hoeflich, Peter et al. (1996). "Maximum brightness and postmaximum decline of light curves of type supernovae ia: A comparison of theory and observations". In: *The Astrophysical Journal Letters* 472.2, p. L81.
- Höflich, Peter et al. (2002). "Infrared spectra of the subluminous Type Ia supernova SN 1999by". In: *The Astrophysical Journal* 568.2, p. 791.
- Hosseinzadeh, Griffin et al. (2017). "Early Blue Excess from the Type Ia Supernova 2017cbv and Implications for Its Progenitor". In: *The Astrophysical Journal Letters* 845.2, p. L11.
- Howell, D Andrew (2001). "The progenitors of subluminous type Ia supernovae". In: *The Astrophysical Journal* 554.2, p. L193.

- Howell, D Andrew et al. (2009). "The effect of progenitor age and metallicity on luminosity and ^{56}Ni yield in Type Ia supernovae". In: *The Astrophysical Journal* 691.1, p. 661.
- Hoyle, Fred and William A Fowler (1960). "Nucleosynthesis in Supernovae." In: *The Astrophysical Journal* 132, p. 565.
- Hurley, Jarrod R, Christopher A Tout, and Onno R Pols (2002). "Evolution of binary stars and the effect of tides on binary populations". In: *Monthly Notices of the Royal Astronomical Society* 329.4, pp. 897–928.
- Iben Jr, Icko and Alexander V Tutukov (1985). "On the evolution of close binaries with components of initial mass between 3 solar masses and 12 solar masses". In: *The Astrophysical Journal Supplement Series* 58, pp. 661–710.
- Iliadis, Christian (2015). *Nuclear physics of stars*. John Wiley & Sons.
- Iliadis, Christian et al. (2001). "Proton-induced thermonuclear reaction rates for $A=20\text{--}40$ nuclei". In: *The Astrophysical Journal Supplement Series* 134.1, p. 151.
- Iwamoto, Koichi et al. (1999). "Nucleosynthesis in Chandrasekhar mass models for type IA supernovae and constraints on progenitor systems and burning-front propagation". In: *The Astrophysical Journal Supplement Series* 125.2, p. 439.
- Janka, H-Th et al. (2007). "Theory of core-collapse supernovae". In: *Physics Reports* 442.1-6, pp. 38–74.
- Janka, Hans-Thomas (2012). "Explosion mechanisms of core-collapse supernovae". In: *Annual Review of Nuclear and Particle Science* 62, pp. 407–451.
- Jerkstrand, A et al. (2015). "Constraints on explosive silicon burning in core-collapse supernovae from measured Ni/Fe ratios". In: *The Astrophysical Journal* 807.1, p. 110.
- Joglekar, Hrishikesh et al. (2011). "Oldest sky-chart with Supernova record". In: *Puratattva-Bulletin of the Indian Archaeological Society* 41, pp. 207–211.

- Jones, Samuel W et al. (2019). “ ^{60}Fe in core-collapse supernovae and prospects for X-ray and gamma-ray detection in supernova remnants”. In: *Monthly Notices of the Royal Astronomical Society* 485.3, pp. 4287–4310.
- Justham, Stephen et al. (2009). “Type Ia supernovae and the formation of single low-mass white dwarfs”. In: *Astronomy & Astrophysics* 493.3, pp. 1081–1091.
- Karakas, Amanda I and John C Lattanzio (2014). “The Dawes review 2: nucleosynthesis and stellar yields of low-and intermediate-mass single stars”. In: *Publications of the Astronomical Society of Australia* 31.
- Katz, Boaz and Subo Dong (2012). “The rate of WD-WD head-on collisions may be as high as the SNe Ia rate”. In: *arXiv preprint arXiv:1211.4584*.
- Keegans, J et al. (2019). “Nucleosynthetic yields from neutron stars accreting in binary common envelopes”. In: *Monthly Notices of the Royal Astronomical Society* 485.1, pp. 620–639.
- Khokhlov, AM (1989). “The structure of detonation waves in supernovae”. In: *Monthly Notices of the Royal Astronomical Society* 239.3, pp. 785–808.
- (1991). “Delayed detonation model for type Ia supernovae”. In: *Astronomy and Astrophysics* 245, pp. 114–128.
- Kippenhahn, Rudolf, Alfred Weigert, and Achim Weiss (1990). *Stellar structure and evolution*. Springer.
- Kobayashi, Chiaki, Amanda I Karakas, and Maria Lugaro (2020). “The Origin of Elements from Carbon to Uranium”. In: *The Astrophysical Journal* 900.2, p. 179.
- Kobayashi, Chiaki, Shing-Chi Leung, and Ken’ichi Nomoto (2020). “New Type Ia Supernova Yields and the Manganese and Nickel Problems in the Milky Way and Dwarf Spheroidal Galaxies”. In: *The Astrophysical Journal* 895.2, p. 138.
- Kobayashi, Chiaki et al. (2006). “Galactic chemical evolution: carbon through zinc”. In: *The Astrophysical Journal* 653.2, p. 1145.

- Kozyreva, Alexandra, S-C Yoon, and Norbert Langer (2014). "Explosion and nucleosynthesis of low-redshift pair-instability supernovae". In: *Astronomy & Astrophysics* 566, A146.
- Kratter, Kaitlin M (2011). "The formation of close binaries". In: *Evolution of Compact Binaries*. Vol. 447, p. 47.
- Kromer, Markus et al. (2010). "Double-detonation sub-Chandrasekhar supernovae: synthetic observables for minimum helium shell mass models". In: *The Astrophysical Journal* 719.2, p. 1067.
- Kushnir, Doron, Nahliel Wygoda, and Amir Sharon (2020). "Sub-Chandrasekhar-mass detonations are in tension with the observed $t_0 - M_{\text{Ni}56}$ relation of type Ia supernovae". In: *Monthly Notices of the Royal Astronomical Society* 499.4, pp. 4725–4747.
- Kushnir, Doron et al. (2013). "Head-on collisions of white dwarfs in triple systems could explain type Ia supernovae". In: *The Astrophysical Journal Letters* 778.2, p. L37.
- Lach, F et al. (2020). "Nucleosynthesis imprints from different Type Ia supernova explosion scenarios and implications for galactic chemical evolution". In: *arXiv preprint arXiv:2010.14084*.
- Langanke, Karlheinz and G Martínez-Pinedo (2000). "Shell-model calculations of stellar weak interaction rates: II. Weak rates for nuclei in the mass range $A = 45 - 65$ in supernovae environments". In: *Nuclear Physics A* 673.1-4, pp. 481–508.
- Langanke, Karlheinz and G Martínez-Pinedo (2001). "Rate tables for the weak processes of pf-shell nuclei in stellar environments". In: *Atomic Data and Nuclear Data Tables* 79.1, pp. 1–46.
- Leibundgut, Bruno and Nicholas B Suntzeff (2003). "Optical light curves of supernovae". In: *Supernovae and gamma-ray bursters*. Springer, pp. 77–90.

- Leung, Shing-Chi and Ken'ichi Nomoto (2020). "Explosive Nucleosynthesis in Sub-Chandrasekhar-mass White Dwarf Models for Type Ia Supernovae: Dependence on Model Parameters". In: *The Astrophysical Journal* 888.2, p. 80.
- Livio, Mario (2000). "The progenitors of type ia supernovae". In: *Type Ia Supernovae, theory and cosmology* 33.
- Livio, Mario and Paolo Mazzali (2018). "On the progenitors of Type Ia supernovae". In: *Physics Reports* 736, pp. 1–23.
- Livio, Mario and Adam G Riess (2003). "Have the elusive progenitors of type Ia supernovae been discovered?" In: *The Astrophysical Journal Letters* 594.2, p. L93.
- Lodders, Katharina (2003). "Solar system abundances and condensation temperatures of the elements". In: *The Astrophysical Journal* 591.2, p. 1220.
- Magkotsios, Georgios et al. (2010). "Trends in ^{44}Ti and ^{56}Ni from Core-collapse Supernovae". In: *The Astrophysical Journal Supplement Series* 191.1, p. 66.
- Maguire, Kate et al. (2013). "A statistical analysis of circumstellar material in Type Ia supernovae". In: *Monthly Notices of the Royal Astronomical Society* 436.1, pp. 222–240.
- Maiolino, Roberto and F Mannucci (2019). "De re metallica: the cosmic chemical evolution of galaxies". In: *The Astronomy and Astrophysics Review* 27.1, p. 3.
- Mannucci, Filippo, M Della Valle, and N Panagia (2006). "Two populations of progenitors for Type Ia supernovae?" In: *Monthly Notices of the Royal Astronomical Society* 370.2, pp. 773–783.
- Mannucci, Filippo et al. (2005). "The supernova rate per unit mass". In: *Astronomy & Astrophysics* 433.3, pp. 807–814.
- Maoz, Dan and Filippo Mannucci (2012). "Type-Ia supernova rates and the progenitor problem: a review". In: *Publications of the Astronomical Society of Australia* 29.4, pp. 447–465.

- Marion, GH et al. (2016). "SN 2012cg: Evidence for interaction between a normal SN Ia and a non-degenerate binary companion". In: *The Astrophysical Journal* 820.2, p. 92.
- Matteucci, F and L Greggio (1986). "Relative roles of type I and II supernovae in the chemical enrichment of the interstellar gas". In: *Astronomy and Astrophysics* 154, pp. 279–287.
- Matteucci, F et al. (2006). "A new formulation of the Type Ia supernova rate and its consequences on galactic chemical evolution". In: *Monthly Notices of the Royal Astronomical Society* 372.1, pp. 265–275.
- Matteucci, F et al. (2009). "The effect of different type Ia supernova progenitors on Galactic chemical evolution". In: *Astronomy & Astrophysics* 501.2, pp. 531–538.
- Meng, Xiangcun and Philipp Podsiadlowski (2013). "Constraining the Spin-down Timescale of the White Dwarf Progenitors of Type Ia Supernovae". In: *The Astrophysical Journal Letters* 778.2, p. L35.
- Mennekens, Nicki et al. (2010). "The delay-time distribution of Type Ia supernovae: a comparison between theory and observation". In: *Astronomy & Astrophysics* 515, A89.
- Miles, Broxton J et al. (2019). "Quantifying How Density Gradients and Front Curvature Affect Carbon Detonation Strength During Type Ia Supernovae". In: *arXiv preprint arXiv:1806.07820*.
- Minkowski, Rudolph (1941). "Spectra of supernovae". In: *Publications of the Astronomical Society of the Pacific* 53, p. 224.
- Nimmo, Francis et al. (2020). "Radiogenic Heating and Its Influence on Rocky Planet Dynamos and Habitability". In: *The Astrophysical Journal Letters* 903.2, p. L37.
- Nomoto, K (1982). "Accreting white dwarf models for type 1 supernovae. II-Off-center detonation supernovae". In: *The Astrophysical Journal* 257, pp. 780–792.

- Nomoto, K, F-K Thielemann, and JC Wheeler (1984). "Explosive nucleosynthesis and type I supernovae. Erratum". In: *The Astrophysical Journal* 283.1.
- Nomoto, K, F-K Thielemann, and K Yokoi (1984). "Accreting white dwarf models of Type I supernovae. III-Carbon deflagration supernovae". In: *The Astrophysical Journal* 286, pp. 644–658.
- Nomoto, Ken and Daiichiro Sugimoto (1977). "Rejuvenation of helium white dwarfs by mass accretion". In: *Publications of the Astronomical Society of Japan* 29, pp. 765–780.
- Nomoto, Ken'ichi and Yoji Kondo (1991). "Conditions for accretion-induced collapse of white dwarfs". In: *The Astrophysical Journal* 367, pp. L19–L22.
- Nomoto, Ken'ichi and Shing-Chi Leung (2018). "Single degenerate models for type Ia supernovae: progenitor's evolution and nucleosynthesis yields". In: *Space Science Reviews* 214.4, p. 67.
- Oda, Takeshi et al. (1994). "Rate tables for the weak processes of sd-shell nuclei in stellar matter". In: *Atomic Data and Nuclear Data Tables* 56.2, pp. 231–403.
- Pakmor, Rüdiger et al. (2010). "Sub-luminous type Ia supernovae from the mergers of equal-mass white dwarfs with mass $0.9 M_{\odot}$ ". In: *Nature* 463.7277, pp. 61–64.
- Phillips, MM et al. (1987). "THE TYPE IA SUPERNOVA 1986G IN NGC 5128: OPTICAL PHOTOMETRY AND SPECTRA." In: *Publications of the Astronomical Society of the Pacific* 99.617, p. 592.
- Pignatari, M et al. (2016). "NuGrid stellar data set. I. Stellar yields from H to Bi for stars with metallicities $Z=0.02$ and $Z=0.01$ ". In: *The Astrophysical Journal Supplement Series* 225.2, p. 24.
- Polin, Abigail, Peter Nugent, and Daniel Kasen (2021). "Nebular models of sub-Chandrasekhar mass type Ia supernovae: Clues to the origin of Ca-rich transients". In: *The Astrophysical Journal* 906.1, p. 65.

- Rauscher, Thomas and F-K Thielemann (2000). "Astrophysical reaction rates from statistical model calculations". In: *arXiv preprint astro-ph/0004059*.
- Ritter, C et al. (2018). "NuGrid stellar data set-II. Stellar yields from H to Bi for stellar models with $M_{\text{ZAMS}} = 1\text{--}25 M_{\odot}$ and $Z = 0.0001\text{--}0.02$ ". In: *Monthly Notices of the Royal Astronomical Society* 480.1, pp. 538–571.
- Roelofs, Gijs HA et al. (2010). "Spectroscopic evidence for a 5.4 minute orbital period in HM Cancri". In: *The Astrophysical Journal Letters* 711.2, p. L138.
- Romano, Donatella et al. (2017). "The evolution of CNO isotopes: a new window on cosmic star formation history and the stellar IMF in the age of ALMA". In: *Monthly Notices of the Royal Astronomical Society* 470.1, pp. 401–415.
- Röpke, FK (2007). "Flame-driven deflagration-to-detonation transitions in type Ia supernovae?" In: *The Astrophysical Journal* 668.2, p. 1103.
- Röpke, FK et al. (2007). "A three-dimensional deflagration model for type Ia supernovae compared with observations". In: *The Astrophysical Journal* 668.2, p. 1132.
- Ruiter, Ashley J et al. (2014). "The effect of helium accretion efficiency on rates of Type Ia supernovae: double detonations in accreting binaries". In: *Monthly Notices of the Royal Astronomical Society: Letters* 440.1, pp. L101–L105.
- Sarangi, A, Mikako Matsuura, and ER Micelotta (2018). "Dust in supernovae and supernova remnants I: Formation scenarios". In: *Space Science Reviews* 214.3, pp. 1–48.
- Schwarzschild, M and R Härm (1965). "Thermal Instability in Non-Degenerate Stars." In: *The Astrophysical Journal* 142, p. 855.
- Seitenzahl, Ivo R et al. (2013a). "Solar abundance of manganese: a case for near Chandrasekhar-mass Type Ia supernova progenitors". In: *Astronomy & Astrophysics* 559, p. L5.

- Seitenzahl, Ivo R et al. (2013b). "Three-dimensional delayed-detonation models with nucleosynthesis for Type Ia supernovae". In: *Monthly Notices of the Royal Astronomical Society* 429.2, pp. 1156–1172.
- Shapiro, Stuart L and Saul A Teukolsky (2008). *Black holes, white dwarfs, and neutron stars: The physics of compact objects*. John Wiley & Sons.
- Shen, Ken J et al. (2018). "Sub-Chandrasekhar-mass white dwarf detonations revisited". In: *The Astrophysical Journal* 854.1, p. 52.
- Sim, SA et al. (2010). "Detonations in sub-Chandrasekhar-mass C+ O white dwarfs". In: *The Astrophysical Journal Letters* 714.1, p. L52.
- Southwell, KA et al. (1996). "The nature of the supersoft X-ray source RX J0513–69". In: *arXiv preprint astro-ph/9605090*.
- Stephenson, F Richard (2010). "SN 1006: the brightest supernova". In: *Astronomy & Geophysics* 51.5, pp. 5–27.
- Takahashi, K and K Yokoi (1987). "Beta-decay rates of highly ionized heavy atoms in stellar interiors". In: *Atomic Data and Nuclear Data Tables* 36.3, pp. 375–409.
- Thielemann, FK and WD Arnett (1985). "Hydrostatic nucleosynthesis-part two-core neon to silicon burning and presupernova abundance yields of massive stars". In: *The Astrophysical Journal* 295, p. 604.
- Thielemann, Friedrich-Karl, Ken'ichi Nomoto, and Koichi Yokoi (1986). "Explosive nucleosynthesis in carbon deflagration models of Type I supernovae". In: *Nucleosynthesis and Its Implications on Nuclear and Particle Physics*. Springer, pp. 131–142.
- Timmes, Frank X, Edward F Brown, and JW Truran (2003). "On variations in the peak luminosity of Type Ia supernovae". In: *The Astrophysical Journal Letters* 590.2, p. L83.
- Timmes, FX and SE Woosley (1992). "The conductive propagation of nuclear flames. I-Degenerate C+ O and O+ NE+ MG white dwarfs". In: *The Astrophysical Journal* 396, pp. 649–667.

- Toloza, Odette et al. (2019). "Understanding the evolution of close white dwarf binaries". In: *Bulletin of the American Astronomical Society* 51.3, p. 168.
- Toonen, S, HB Perets, and AS Hamers (2018). "Rate of WD-WD head-on collisions in isolated triples is too low to explain standard type Ia supernovae". In: *Astronomy & Astrophysics* 610, A22.
- Townsley, Dean M et al. (2007). "Flame evolution during Type Ia supernovae and the deflagration phase in the gravitationally confined detonation scenario". In: *The Astrophysical Journal* 668.2, p. 1118.
- Townsley, Dean M et al. (2016). "A Tracer Method for Computing Type Ia Supernova Yields: Burning Model Calibration, Reconstruction of Thickened Flames, and Verification for Planar Detonations". In: *The Astrophysical Journal Supplement Series* 225.1, p. 3.
- Townsley, Dean M et al. (2019). "Double detonations with thin, modestly enriched helium layers can make normal Type Ia supernovae". In: *The Astrophysical Journal Letters* 878.2, p. L38.
- Travaglio, Claudia, W Hillebrandt, and M Reinecke (2005). "Metallicity effect in multi-dimensional SNIa nucleosynthesis". In: *Astronomy & Astrophysics* 443.3, pp. 1007–1011.
- Travaglio, Claudia et al. (2004). "Nucleosynthesis in multi-dimensional SN Ia explosions". In: *Astronomy & Astrophysics* 425.3, pp. 1029–1040.
- Truran, James W, William David Arnett, and Alastair Graham Walter Cameron (1967). "Nucleosynthesis in supernova shock waves". In: *Canadian Journal of Physics* 45.7, pp. 2315–2332.
- Wheeler, J Craig and Robert P Harkness (1990). "Type I supernovae". In: *Reports on Progress in Physics* 53.12, p. 1467.
- Woosley, SE, RONALD E Taam, and THOMAS A Weaver (1986). "Models for Type I supernova. I-Detonations in white dwarfs". In: *The Astrophysical Journal* 301, pp. 601–623.

- Woosley, SE and Thomas A Weaver (1994). "Sub-Chandrasekhar mass models for Type IA supernovae". In: *The Astrophysical Journal* 423, pp. 371–379.
- Woosley, Stanford E, Alex Heger, and Thomas A Weaver (2002). "The evolution and explosion of massive stars". In: *Reviews of modern physics* 74.4, p. 1015.
- Wyse, Rosemary FG and Gerard Gilmore (1988). "The Galactic spheroidal- What is Population II?" In: *The Astronomical Journal* 95, pp. 1404–1414.
- Yungelson, Lev R and Mario Livio (2000). "Supernova rates: A cosmic history". In: *The Astrophysical Journal* 528.1, p. 108.
- Zinner, E (2014). "Presolar grains". In: *Meteorites and cosmochemical processes* 1, pp. 181–213.
- Zwicky, F (1964). "NGC 1058 and its Supernova 1961." In: *The Astrophysical Journal* 139, p. 514.
- Zwicky, Fritz. "Supernovae." In: *Stellar structure*. Ed. by Lawrence Hugh Aller and Dean Benjamin McLaughlin.